

**UCLA**

**UCLA Electronic Theses and Dissertations**

**Title**

Characterization, Simulation, and Measurement of the Far Field Error Vector Magnitude of Millimeter-Wave Antennas and Phased Arrays using Compact and Planar Near Field Ranges

**Permalink**

<https://escholarship.org/uc/item/06m185sd>

**Author**

Brown, Dustin

**Publication Date**

2023

Peer reviewed|Thesis/dissertation

UNIVERSITY OF CALIFORNIA

Los Angeles

Characterization, Simulation, and Measurement of the Far Field Error Vector Magnitude of  
Millimeter-Wave Antennas and Phased Arrays using Compact and Planar Near Field Ranges

A dissertation submitted in partial satisfaction  
of the requirements for the degree  
Doctor of Philosophy in Electrical Engineering

by

Dustin Connor Brown

2023

© Copyright by  
Dustin Connor Brown  
2023

## ABSTRACT OF THE DISSERTATION

Characterization, Simulation, and Measurement of the Far Field Error Vector Magnitude of Millimeter-Wave Antennas and Phased Arrays using Compact and Planar Near Field Ranges

by

Dustin Connor Brown

Doctor of Philosophy in Electrical Engineering

University of California, Los Angeles, 2023

Professor Yahya Rahmat-Samii, Chair

A proliferation of large active electronically-scanned arrays (AESA) is enabling precise beam steering in wireless communication links at millimeter wave carrier frequencies. In addition to radiated power, linear and nonlinear distortion from the transceivers and array elements must also be examined to discern their relative effects on received signal quality in the far field. For digital signals, error vector magnitude (EVM) represents a complete measure of the amplitude and phase distortion in a wireless channel. This work focuses on the analysis, simulation, and measurement of the EVM resulting from transmission by millimeter-wave antennas and phased arrays. An ultra-wideband (UWB) model of antenna transmission based on the vector effective length is presented and applied to EVM simulation of over-the-air (OTA) links for a microstrip patch and conical horn antenna at two different 5G FR2 bands. The EVM for the conical horn link is measured using a multi-port vector network analyzer (VNA) and compact antenna test range (CATR) provided by Keysight Technologies in Santa Rosa, CA. The same simulation and measurement techniques are then applied to analysis of phased array transmission to understand the effects of beam squint and embedded element frequency response. The EVM of individual active array element channels and the fully-active 8x8 phased array are measured as a function of RF carrier power, far field observation angles, beam scan angles, and modulation rates using MATLAB instrument control scripts. The feasibility of estimating the EVM of far field antenna links from the planar near fields (PNF) is also investigated. A theoretical framework for calculating EVM from wideband far fields

derived through PNF transformations and results from PNF simulations and measurements of a Ka-band conical horn and 8x8 phased array are presented. Finally, the effective range of a vehicle-to-infrastructure antenna link at 5.9 GHz is estimated by calculating received power along a linear highway using the Friis free space transmission equation and full-wave simulations of base station and vehicular antenna arrays.

The dissertation of Dustin Connor Brown is approved.

Omid Abari

Aydin Babakhani

Yuanxun Ethan Wang

Yahya Rahmat-Samii, Committee Chair

University of California, Los Angeles

2023

*To my sweet wife Lauren and family . . .  
for all of their steadfast love and support.*

## TABLE OF CONTENTS

<b>1</b>	<b>Introduction</b>	<b>1</b>
1.1	Entering an Era of Highly-Integrated Millimeter-Wave Phased Arrays	1
1.2	Link-Level Performance Analysis with Error Vector Magnitude (EVM)	5
1.3	Outline of this Dissertation	8
<b>2</b>	<b>Error Vector Magnitude Measurement Methods</b>	<b>11</b>
2.1	Digital Signal Generation, Distortion, and Equalization	11
2.1.1	Signal Generation and Modulation Schemes	11
2.1.2	Signal Impairments from a Device Under Test	14
2.1.3	Channel Estimation and Equalization Methods	15
2.2	EVM Measurements via Time Domain Demodulation	16
2.3	EVM Measurements via Frequency Domain Spectral Correlation	18
2.4	EVM Measurements via Continuous Wave Stimulation	21
2.5	Summary	23
<b>3</b>	<b>Far Field EVM Characterization of Millimeter-Wave Antennas</b>	<b>24</b>
3.1	Review of an UWB Transmission Model for Far Field Antenna Links	24
3.2	EVM Simulation of Amplitude Distortion from a Microstrip Patch Antenna	31
3.2.1	Introduction	31
3.2.2	Far Field Signal Transmission and Reception	31
3.2.3	Antenna Transfer Function Derivation	34
3.2.4	EVM Results for Microstrip Patch Antenna	34
3.3	EVM Simulation of Linear Distortion from a Far Field Ka-Band Conical Horn Link	36



3.4	EVM Measurement of a Ka-Band Conical Horn Link with a Compact Antenna Test Range and Network Analyzer . . . . .	52
3.5	Summary . . . . .	69
<b>4</b>	<b>Far Field EVM Characterization of Millimeter-Wave Phased Arrays . .</b>	<b>71</b>
4.1	Review of Phased Array Modeling Methods for Far Field EVM Analysis . . .	71
4.2	EVM Simulation of an 8x8 Microstrip Patch Phased Array . . . . .	77
4.2.1	Introduction . . . . .	77
4.2.2	Simulation Model and EVM Results for Beam Scanning with Beam Squint and Embedded Element Patterns . . . . .	79
4.2.3	Simulation Model and EVM Results for Beam Scanning with Individual Element Patterns, Amplitude Taper, and Phase Quantization . . . .	83
4.3	Review of Indirect Far Field Measurement Methods for Phased Array EVM Analysis . . . . .	89
4.4	EVM Measurement of an 8x8 Microstrip Patch Phased Array with a Compact Antenna Test Range and Network Analyzer . . . . .	93
4.4.1	CATR Measurement System and Phased Array Calibration . . . . .	94
4.4.2	EVM Measurement of Individual Phased Array Elements . . . . .	95
4.4.3	EVM Measurement of Fully-Activated Phased Array . . . . .	100
4.5	Summary . . . . .	105
<b>5</b>	<b>Far Field EVM Characterization via Planar Near Field to Far Field Transformation . . . . .</b>	<b>107</b>
5.1	Review of Planar Near Field to Far Field Transformation for Far Field EVM Analysis . . . . .	107
5.2	Planar Near Field Simulation and Far Field EVM Prediction for a Ka-band Conical Horn Antenna . . . . .	113

5.2.1	Introduction . . . . .	113
5.2.2	Planar Near Field Simulation . . . . .	114
5.2.3	Broadband Far Field and EVM Results . . . . .	116
5.3	Planar Near Field Measurement and Far Field Pattern Estimation for a Ka-band Conical Horn Antenna . . . . .	121
5.4	Planar Near Field Measurement, Far Field Pattern Estimation, and EVM Prediction for an 8x8 Microstrip Patch Phased Array . . . . .	128
5.5	Summary . . . . .	139
<b>6</b>	<b>Vehicle-to-Infrastructure Link Budget Analysis . . . . .</b>	<b>140</b>
6.1	Introduction . . . . .	140
6.2	RSU and OBU Antenna Array Coordinate Systems . . . . .	142
6.3	RSU and OBU Antenna Array Design Specifications . . . . .	142
6.4	OBU Received Power for Multi-Lane Linear Highway . . . . .	145
6.5	Summary . . . . .	147
<b>7</b>	<b>Conclusion . . . . .</b>	<b>149</b>
	<b>References . . . . .</b>	<b>152</b>

## LIST OF FIGURES

1.1	Examples of PCB-integrated millimeter wave phased arrays designed for SATCOM [14, 25, 26]. Each one operates over a frequency range of 27-31 GHz and features 1024 dual-polarized microstrip patch elements integrated with 256 beamforming RFICs on opposite sides of the PCBs. . . . .	3
1.2	Three categories of phased array performance metrics: (a) radiated power, beam pattern, and polarization, (b) angular beam scan range, loss, and execution speed, and (c) received signal quality. Examples of the (a) co-polarized and cross-polarized radiation patterns, (b) beam scan loss, and (c) EVM vs. data rate of the 1024-element Ka-band active phased array from [25] are shown. . . . .	6
1.3	Outline of this Dissertation: Chapters 2-5 cover topics related to the modeling, simulation, and measurement of EVM resulting from transmission by antennas and phased arrays. Chapter 6 addresses the simulation of received signal power for a V2I antenna link. . . . .	10
2.1	Block diagram of a generic EVM measurement system. In this single-carrier QAM representation, a QAM-modulated baseband signal $x(t)$ is generated, upconverted to carrier $f_c$ , transmitted through a device or OTA channel under test, and demodulated at the receiver to obtain $y(t)$ with frequency spectrum $Y(f)$ . This spectrum is represented as a sum of linear component $H(f)X(f)$ , nonlinear distortion $D(f)$ , and noise $N(f)$ as described in Section 2.3. . . . .	12
2.2	EVM far field measurement system based on the demodulation method. An AWG generates a baseband IQ signal which is upconverted to the carrier frequency via the VSG and applied to the AUT port. A VSA is used to demodulate and equalize the signal measured by the probe before computing EVM. . . . .	16

2.3	EVM far field measurement system based on the spectral correlation method. The VNA spectrum analyzer is used to compute the spectral correlation components ( $S_{XX}$ , $S_{YY}$ , $S_{XY}$ ) and perform frequency domain equalization $E(f) \approx 1/H(f)$ for the signal measured by the probe before computing EVM. . . . .	18
2.4	Decomposition of output signal spectrum $Y(f)$ of a power amplifier into linear part $H(f)X(f)$ and nonlinear part $D(f)$ using a PNA-X Vector Network Analyzer [63].	20
2.5	Compact test signal generation on a PNA-X Vector Network Analyzer. The CTS (blue) is extracted from a longer original time domain signal (yellow) and filtered to eliminate spectral leakage. The PSD and CCDF of the original signal and CTS are shown to be very similar [63]. See details in Section 2.2. . . . .	20
2.6	RF transmitter model and closed form EVM expression from [66]. It includes the distortion effects from an IQ modulator ( $M$ ) with gain ( $g$ ) and phase ( $\varphi$ ) imbalance and DC offset ( $\alpha_{DC}$ ) in the $I$ and $Q$ paths, a voltage-controlled oscillator ( $R$ ) with phase noise ( $\varphi_C$ ), and additive noise source ( $N_0$ ). . . . .	22
3.1	An UWB antenna transmitter and receiver model with transfer function $H(f) = H_{tx}(f)H_{ch}(f)H_{rx}$ based on (3.1), (3.2), and (3.3) from [54]: Thevenin equivalent circuit model of the (a) transmitter and (b) receiver, and (c) two-port S-parameter network with incident and reflected voltage waves. . . . .	25
3.2	EVM simulation for far field antenna link based on FIR filter models matching measured two-port S-parameters [78]: (a) block diagram of the digital communication system modeling process, (b) FIR filter and (c) antenna link simulation models, and (d) constellation diagrams of scattered symbols from the simulated transmission of 16-QAM signals at 2.0 GHz (left) and 6.0 GHz (right). . . . .	29

3.3	EVM simulation for a far field antenna link based on the grid impulse response (GIR) method [83]: (a) GIR error relative to direct FDTD simulation, which is less than $10^{-6}$ for time steps less than or equal to the number used in the full FDTD simulation (GIR Limit), and (b) EVM as a function of antenna separation distance for free space propagation and propagation with an infinite ground plane placed beneath the two dipoles. . . . .	30
3.4	MATLAB transmitter and receiver block diagram illustrating EVM of a 16-QAM signal resulting from transmitting antenna frequency response $H(f)$ . Error vectors point from transmitted symbols (red) to received symbols (blue) in the complex IQ plane highlighting the in-phase and quadrature components. . . . .	32
3.5	(a) Spectrum of the transmitted and received signals (blue and green respectively) and transfer function normalized to its magnitude at carrier frequency $f_c = 27.4$ GHz. (b) Antenna realized gain (blue), transfer function normalized by its magnitude at $f_c = 28.0$ GHz (red), and $ S_{11} $ of microstrip patch antenna (green). (c)-(d) In-phase and quadrature components of the 16-QAM transmitted and received voltage signals (blue and green) and resulting errors (red) after ideal down-conversion and transmission through the matched filter. . . . .	33
3.6	Constellation diagrams and EVM of 16-QAM signals with bandwidths and carrier frequencies $f_c$ representative of 5G FR2. The carrier frequencies are selected such that rows form a continuous band with 28 GHz upper limit. . . . .	35
3.7	Group delay and EVM comparison of a microstrip patch and conical horn antenna, where $x(t)$ is the input voltage signal applied to the transmitting antenna and $y(t)$ is the received voltage signal of the ideal far field receiver described in section 3.2. . . . .	37
3.8	Transmitting test antennas simulated in CST Studio for the far field link EVM simulations in this dissertation with coordinate systems and co-to-cross polarization ratio $20\log( \vec{E}_H(f_c) / \vec{E}_V(f_c) )$ vs. far field angle $(\theta, \phi)$ : (a) spline-profiled conical horn antenna [85] used in section 3.3-3.4, (b) inset-fed microstrip patch antenna used in section 3.2, and (c) coax-fed microstrip patch antenna used in section 4.2. . . . .	38

- 3.9 Line-of-sight far field link between the two Ka-band conical horn antennas used for the EVM simulation. For each far field observation angle of the transmitting horn  $(\theta_t, \phi_t)$ , the receiving horn is oriented to match the polarization of the radiated  $\vec{E}_V$  component from the transmitting antenna along its boresight direction  $(\hat{z}_r)$ . A distance of  $r = 1.0$  m, approximately  $20D^2/\lambda_c$  with  $\lambda_c = 7.7$  mm, separates the antennas. The vector effective lengths (VEL) of the antennas  $(H_{tx}, H_{rx})$  are obtained through independent full-wave simulations to determine the complete input voltage  $(x_{rf}(t))$  to output voltage  $(y_{rf}(t))$  transfer function  $H(f, r, \theta_t, \phi_t)$ . 39
- 3.10 Steps 1-3 of the EVM simulation process implemented for the Ka-band conical horn of Fig. 3.8(a): (1) full-wave simulation of test antenna in CST Microwave Studio, where the frequency response of radiated Ludwig 3 E-field components are captured at various far field angles  $(\theta, \phi)$ , (2) computation of the antenna link voltage transfer function  $H(f, r, \theta_t, \phi_t)$  from the VEL of the transmit and receive antennas obtained in step (1), and (3) synthesis of symmetric  $(S_{11} = S_{22} = 0, S_{21} = S_{12} = H(f, r, \theta_t, \phi_t))$  two-port s-parameters in MATLAB, which provide a complete description of the linear distortion from the far field antenna link. The  $S_{21}(f)$  for the E-plane observation angles  $\theta_t = [-60^\circ : 15^\circ : 60^\circ], \phi_t = 0^\circ, 180^\circ$  are shown. . . . . 41
- 3.11 Comparison of the antenna link transfer functions estimated from the inset-fed microstrip patch far field probes using equation 3.15c (blue) and simulated directly in CST Microwave Studio with both transmitting and receiving antennas (green). The antennas were separated by  $r = 63.0$  mm and positioned to transmit and receive along boresight as shown. . . . . 43

3.12	Steps 4-6 of the EVM simulation process implemented for the Ka-band conical horn of Fig. 3.8(a): (4) rational function of the form $H(s)$ fitted to the complex data of the voltage transfer function $H(f)$ over a 34-44 GHz frequency range with good agreement between the transfer function (blue) and rational fit (green), (5) up-conversion of the baseband 16-QAM test signal $x(t)$ to carrier frequency $f_c = 39.0$ GHz, transmission through the channel filter $H(s)$ , and down-conversion to retrieve the baseband data of the received signal $y(t)$ , and (6) estimation of the average group delay $\tau_{avg}$ and residual phase error $\Delta\phi_{res}$ for $E_{un}(f)$ . . . . .	45
3.13	Ka-band horn link transfer function estimated from CST far field probe simulations for the boresight direction $H_{est}(f)$ and corresponding rational fit frequency response $H_{rat}(f)$ obtained through the MATLAB algorithm with $n = 82$ poles and a tolerance level of $-60$ dB. . . . .	46
3.14	Time response of microstrip patch antenna link to a Gaussian pulse voltage signal applied to the transmitting antenna port $x_{rf}(t) = V_{Gtx}(t)$ (red). The receiving antenna load voltage signals $y_{rf}(t) = V_L(t)$ resulting from full-wave simulation performed in CST (blue) and application of the transfer function rational fit $H_{rat}(f)$ in MATLAB (green) are shown to be nearly-identical. . . . .	47
3.15	Histogram (left) and constellation diagram (right) showing the phase error $\Delta\phi$ between the $N_{bins} = 3600$ transmitted 16-QAM symbols $x(t_n)$ and delay-corrected received symbols $y(t_n)$ . The $0.1^\circ$ -wide error bins containing the most symbols $N_{sym}$ are concentrated near the residual phase error $\Delta\phi_{res} \approx -5^\circ$ computed from equation (3.17). . . . .	48

3.16	Steps 7-9 of the EVM simulation process implemented for the Ka-band conical horn of Fig. 3.8(a): (7) design and application of an equalization filter $E(f)$ which is applied to the received signal $y(t)$ , (8) addition of AWGN to equalized received signal based on SNR estimated from the applied test signal power $P_{x(t)}$ , channel power gain $ H(f) ^2$ , and thermal noise power $P_{n(t)}$ calculated for the test signal bandwidth $B = 400$ MHz and approximate room temperature $T = 300$ K, and finally (9) plotting of the signal constellation diagrams and calculation of EVM for both the equalized and un-equalized cases, where $x(t_n)$ represent the symbols of the 16-QAM voltage signal applied to the transmit antenna port and $y(t_n - \tau_{avg})$ represent the symbols of the voltage signal at the receive antenna port following equalization. . . . .	50
3.17	Compact test range EVM measurement system diagram for the Ka-band horn link highlighting the RF (green), control (blue), and OTA (red) signal paths between the test instruments and antennas. A 10 MHz reference signal (black) is used for synchronization of the AWG, VSG, and VNA. A single port VSA (green dotted line) could be utilized as an alternative to the VNA to measure EVM if it had adequate dynamic range. . . . .	53
3.18	Images of a millimeter-wave compact antenna test range and instruments provided by Keysight in Santa Rosa, CA: (a) Ka-band horn antenna mounted with customized 3D-printed bracket that extends it to quiet zone center, (b) roll/azimuth AUT positioner and feed horn enclosure, and (c) CATR exterior and instruments. Reflector is shown in Fig. 4.13(b). . . . .	54
3.19	MATLAB IQ Tools dialog box (left) showing parameters of the digital modulation format used for the test signal and resulting time-domain voltage signal and power spectrum (bottom right). The 16-QAM signal has a length of 3200 symbols, a sampling rate of 3200 Msym/s and a symbol rate of 400 Mbaud. A root-raised cosine filter with $\alpha=0.15$ is applied, and the resulting waveform file is uploaded to an AWG with two baseband IQ output ports. . . . .	55



3.20	Measured modulated channel gain $ H(f) $ and normalized group delay $t_d(f)$ of the Ka-band horn link for different E-plane (a),(c),(e) and H-plane (b),(d),(f) angles of the AUT. In addition to the gain degradation with $\theta_t$ angles further off boresight ( $\theta_t = 0^\circ$ ), an increase in peak-to-peak $ H(f) $ passband ripple and group delay variation is also observed. . . . .	57
3.21	Power spectral densities of the modulated stimulus applied to the AUT $S_{XX}(f)$ (blue) and measured on the PNA-X reference receiver $R1$ , the received signal from the CATR feed horn $S_{YY}(f)$ (green) measured on receiver $B$ , and the distortion spectrum $S_{DD}(f)$ (red) described in section 2.3, with the corresponding modulated gain $ H(f) $ (magenta) overlaid. These results are for the AUT E-plane angles ( $\phi_t = 0^\circ$ ) (a) $\theta_t = 0^\circ$ , (b) $\theta_t = 15^\circ$ , (c) $\theta_t = 30^\circ$ , and (d) $\theta_t = 45^\circ$ . . . . .	58
3.22	Power spectral densities of the modulated stimulus applied to the AUT $S_{XX}(f)$ (blue) and measured on the PNA-X reference receiver $R1$ , the received signal from the CATR feed horn $S_{YY}(f)$ (green) measured on receiver $B$ , and the distortion spectrum $S_{DD}(f)$ (red) described in section 2.3, with the corresponding modulated gain $ H(f) $ (magenta) overlaid. These results are for the AUT H-plane angles ( $\phi_t = 90^\circ$ ) (a) $\theta_t = 0^\circ$ , (b) $\theta_t = 15^\circ$ , (c) $\theta_t = 30^\circ$ , and (d) $\theta_t = 45^\circ$ . . . . .	59
3.23	Measured (blue) and simulated (green) un-equalized (a)-(b) and equalized (c)-(d) EVM for the Ka-band horn link. Results are shown for E-plane $\theta_t$ angles in (a) and (c) and for H-plane angles in (b) and (d). Equalized EVM results show good agreement, indicating a good match between measured and simulated horn gains. Unequalized EVM results show the same dependency on $\theta_t$ with some residual error that is likely due to the vector calibration. . . . .	61

3.24	(a) Estimated linear distortion component of the Ka-band horn link's un-equalized EVM due to $H(f)$ only as a function of E-plane $\theta_t$ angles: simulated EVM of the Ka-band horn link without AWGN (green) and calculated from measured quantities (blue). (b) Linear distortion EVM component calculated from measurements with (red) and without (blue) the preamplifier in series with the transmitting Ka-band horn antenna. . . . .	63
3.25	WR-28 broadband dual-polarized scalar feed horn model used in the F9650A compact antenna test range: (a) Image of corrugated feed horn with an integrated orthomode transducer and (b) simulated gain vs. frequency with a dotted line at the integration band centered at $f_c = 39.0$ GHz from the manufacturer data sheet [86]. . . . .	63
3.26	(a) Un-equalized EVM (blue), equalized EVM (green), and RF carrier gain (red) of the Keysight U7227F pre-amplifier versus RF carrier power from the VSG, (b) Estimated noise (blue) and non-linear distortion (red) components of the pre-amplifier's equalized EVM (green), and un-equalized EVM of the Ka-band horn link with (red) and without (blue) the pre-amplifier on transmitting antenna side for $\theta_t$ angles in the (c) E-plane and (d) H-plane. . . . .	65
3.27	Power spectral densities of the modulated stimulus applied to the pre-amplifier in front of the AUT $S_{XX}(f)$ (blue) and measured on the PNA-X reference receiver $R1$ , the received signal from the CATR feed horn $S_{YY}(f)$ (green) measured on receiver $B$ , and the distortion spectrum $S_{DD}(f)$ (red) described in section 2.3, with the corresponding modulated gain $ H(f) $ (magenta) overlaid. These results are for the AUT E-plane angles ( $\phi_t = 0^\circ$ ) (a) $\theta_t = 0^\circ$ , (b) $\theta_t = 15^\circ$ , (c) $\theta_t = 30^\circ$ , and (d) $\theta_t = 45^\circ$ . The distortion spectrum and modulated gain are elevated relative to those of Fig. 3.21 due to inclusion of the transmit pre-amplifier. . . . .	67
3.28	Typical gain (a) and noise figure (b) of the U7227A pre-amplifier versus frequency. The gain and noise figure at $f_c = 39$ GHz are approximately 33 dB and 6 dB respectively [94]. . . . .	68

3.29	(a) $ S_{21} $ at $f_c = 39$ GHz as a function of PNA-X RF output power level where PNA-X attenuation settings are shown to change at -25 dBm, (b) $ S_{21}(f) $ for a 10 GHz span centered at $f_c = 39$ GHz plotted for PNA-X RF output power levels [-25 dBm:2.5 dBm:10 dBm], and (c)-(d) EVM of the Ka-band horn link without pre-amplifier measured in a CATR as a function of VSG RF output power for 16-QAM test signals with 400 and 800 Mbaud symbol rates respectively. Both $ S_{21} $ and $EVM_{H(f)}$ stabilize at high RF output power levels. . . . .	70
4.1	A digital beamforming array EVM simulation based on random amplitude and phase errors $\delta_n$ and $\psi_n$ in equations (4.1) and (4.2) [95]: (a) phased array dimensions and element $n$ cylindrical coordinates $(\rho_n, \phi_n)$ and (b) EVM simulation results for amplitude (left) and phase (right) error ranges with $SNR = 23$ dB. .	72
4.2	A model of phased array 64-QAM signal transmission implemented in MATLAB and EVM simulation results [98]: (a) phased array model and plots of memoryless power amplifier AM-AM (left) and AM-PM (right) vs. $P_{in}$ , (b) EVM vs. RMS amplitude and phase error for 5 dB backoff ( $P_{in} = -19$ dB), and (c) EVM vs. number of elements for 5 dB backoff, 1 dB RMS amplitude error, and $10^\circ$ RMS phase error (for 60 iterations). . . . .	74
4.3	A model of phased array signal transmission implemented in MATLAB with linear equalizer compensating for beam scanning ISI and EVM results [106]: (a) block diagram of 16x16 array model and linear equalizer, (b) array diagram showing the time delay differences between elements at a $60^\circ$ scan angle, and (c) EVM results for different scan angles (x-axis) and modulation rates (curves). . . . .	76
4.4	MATLAB model for 16-QAM signal transmission from the phased array transmitter (blue) to the single antenna receiver (green). Each phased array element is connected to an ideal phase shifter and fed through a lossless $1/N$ divider, where $N$ is the number of elements. EVM represents the difference between transmitted and received symbols after normalization. . . . .	78

4.5	(a) $ \vec{H}_{44}(f_c, \theta, \phi) $ : $ \vec{E}_H $ field pattern for embedded element $(m, n) = (4, 4)$ in an 8x8 microstrip patch array at $f_c = 39$ GHz. (b) Normalized beam squint amplitude versus frequency offset from $f_c$ for $N$ isotropic elements with a 100 MHz bandwidth centered at $f_0$ highlighted in gray. (c)-(d) $ \vec{H}_{44}(f, \theta, \phi) $ at various E- and H-field plane angles respectively. . . . .	80
4.6	(a)-(b) EVM of the 16-QAM test signal for azimuth plane beam scan angles $\theta_s$ in the E-plane and H-plane respectively for the 32x32 (blue), 16x16 (green), and 8x8 (red) phased arrays. (c)-(d) Constellation diagrams showing the ideal transmitted symbols (red) and simulated received symbols (blue) for the beam scan angles $(\theta_s, \phi_s) = (60^\circ, 0^\circ)$ in the E-plane and $(\theta_s, \phi_s) = (60^\circ, 90^\circ)$ in the H-plane respectively.	81
4.7	Design specifications for the 8x8 coax-fed microstrip patch phased array used in EVM simulations of section 4.2, E-plane far field probe positions, and $\vec{E}_H(f)$ and $S_{11}(f)$ for embedded element $(m, n) = (4, 4)$ . The resonant frequency of this patch element is 39 GHz. . . . .	84
4.8	Gain of the far field link voltage transfer functions $ H_{mn}(f) $ for each array element $(m, n) = (1, 1) \dots (8, 8)$ at E-plane beam scan angles $(\theta_s, \phi_s) =$ <b>(a)</b> $(60^\circ, 180^\circ)$ , <b>(b)</b> $(45^\circ, 180^\circ)$ , <b>(c)</b> $(30^\circ, 180^\circ)$ , <b>(d)</b> $(15^\circ, 180^\circ)$ , <b>(e)</b> $(0^\circ, 0^\circ)$ , <b>(f)</b> $(15^\circ, 0^\circ)$ , <b>(g)</b> $(30^\circ, 0^\circ)$ , <b>(h)</b> $(45^\circ, 0^\circ)$ , and <b>(i)</b> $(60^\circ, 0^\circ)$ . . . . .	85
4.9	Normalized group delay $\tau_{mn}$ of the far field link voltage transfer functions $H_{mn}(f)$ for each array element $(m, n) = (1, 1) \dots (8, 8)$ at E-plane beam scan angles $(\theta_s, \phi_s) =$ <b>(a)</b> $(60^\circ, 180^\circ)$ , <b>(b)</b> $(45^\circ, 180^\circ)$ , <b>(c)</b> $(30^\circ, 180^\circ)$ , <b>(d)</b> $(15^\circ, 180^\circ)$ , <b>(e)</b> $(0^\circ, 0^\circ)$ , <b>(f)</b> $(15^\circ, 0^\circ)$ , <b>(g)</b> $(30^\circ, 0^\circ)$ , <b>(h)</b> $(45^\circ, 0^\circ)$ , and <b>(i)</b> $(60^\circ, 0^\circ)$ . . . . .	86
4.10	In-phase component of the 400 Mbaud 16-QAM signals transmitted by each array element and received at the E-plane beam scan angles $(\theta_s, \phi_s) =$ <b>(a)</b> $(60^\circ, 180^\circ)$ , <b>(b)</b> $(45^\circ, 180^\circ)$ , <b>(c)</b> $(30^\circ, 180^\circ)$ , <b>(d)</b> $(15^\circ, 180^\circ)$ , <b>(e)</b> $(0^\circ, 0^\circ)$ , <b>(f)</b> $(15^\circ, 0^\circ)$ , <b>(g)</b> $(30^\circ, 0^\circ)$ , <b>(h)</b> $(45^\circ, 0^\circ)$ , and <b>(i)</b> $(60^\circ, 0^\circ)$ . . . . .	87

4.11	(a) Un-equalized EVM of the 400 Mbaud 16-QAM test signal resulting from superposition of the simulated array element channels at E-plane beam scan angles $\theta_s$ with uniform amplitude and no phase error (blue), the 10 dB Taylor amplitude taper shown in (b), and a 6-bit ( $5.6^\circ$ ) phase quantization error (green) shown in (c). Received signals from array elements at $(\theta_s, \phi_s) = (60^\circ, 180^\circ)$ for the blue, red, and green cases are shown in (d)-(f). . . . .	88
4.12	Far field EVM measurement system for a 39 GHz 8x8 phased array and probe separated by $D = 1.0$ m [98]: (a) block diagram of measurement system with AWG and external upconverter for signal generation and real-time scope with VSA software for demodulation of the received signal, and (b) EVM vs. EIRP plot demonstrating the (1) SNR, (2) measurement system, and (3) power amplifier linearity dominated regions. . . . .	90
4.13	Images of a millimeter-wave compact antenna test range and instruments provided by Keysight in Santa Rosa, CA: (a) 39 GHz 8x8 phased array [98] mounted to a roll/azimuth positioner with a custom-designed, 3D-printed bracket that extends the array to quiet zone center, (b) reflector and feed horn enclosure, and (c) exterior view of CATR and instruments. . . . .	91
4.14	Compact test range EVM measurement system diagram highlighting RF signal (green), control (blue), DC power supply (orange), and OTA (red) paths between the PC and test instruments. A 10 MHz reference signal (black) is used for synchronization of the AWG, VSG, and VNA. An Arduino is used as a digital interface between the PC and array. . . . .	92
4.15	Phase calibration of array performed at $f_c = 39$ GHz: (a) enumeration of elements 1-64, which excludes dummy elements, and (b) calibrated (green) and uncalibrated (blue) $S_{21}$ phase of the array elements with peak-to-peak variations of $28.5^\circ$ and $87.5^\circ$ respectively. . . . .	95

4.16	RF carrier gain (a)-(b), $EVM_{UN}$ (c)-(d), and $EVM_{EQ}$ (e)-(f) of all sixty-four phased array elements. In [(a),(c),(e)], results are plotted at boresight as a function of RF carrier power $P_{RF}$ from the VSG, and colors represent array elements. In [(b),(d),(f)], results are plotted as a function of array element number with $P_{RF} = 15$ dBm, and colors represent far field observation angles $\theta_t$ in the azimuth plane. The anomaly from element 34 for angle $\theta_t = 15^\circ$ (light blue) in [(b),(d),(f)] is conjectured to result from an Arduino activation failure. . . . .	96
4.17	Power spectral densities of the modulated stimulus applied to the AUT $S_{XX}(f)$ (blue) and measured on the PNA-X reference receiver $R1$ , the received signal from the CATR feed horn $S_{YY}(f)$ (green) measured on receiver $B$ , and the distortion spectrum $S_{DD}(f)$ (red) described in section 2.3, with the corresponding modulated gain $ H(f) $ (magenta) overlaid. These results are for array elements (a) 13, (b) 46, (c) 50, and (d) 57. . . . .	97
4.18	Equalized $EVM_{EQ}$ (green), un-equalized $EVM_{UN}$ (blue), and carrier gain $ H(f_c) $ (red) as a function of RF output power from the VSG for elements (a) 13, (b) 46, (c) 50, and (d) 57. . . . .	98
4.19	Equalized $EVM_{EQ}$ (green), noise component $EVM_{SNR}$ (blue), and intermodulation distortion component $EVM_{IMD}$ (red) from equation (3.22) as a function of VSG RF output power for elements (a) 13 and (b) 46. . . . .	99
4.20	Equalized $EVM_{EQ}$ (green), un-equalized $EVM_{UN}$ (blue), and carrier gain $ H(f_c) $ (red) for all 64 array elements with $P_{RF} = 15$ dBm. Results for the four array elements from Figs. 4.17 and 4.18 are highlighted for comparison. . . . .	99
4.21	Images of another millimeter-wave compact antenna test range and instruments provided by Keysight in Santa Rosa, CA: (a) 39 GHz 8x8 phased array [98] mounted to a roll/azimuth positioner with a custom-designed, 3D-printed bracket that extends the array to quiet zone center, (b) reflector and CATR, and (c) exterior view of CATR and instruments. . . . .	101

4.22	Measured modulated channel gain $ H(f) $ (a)-(c) and normalized group delay $t_d(f)$ (d)-(e) of the 8x8 phased array link for a 100 MHz-wide flat tone signal with 1.0 MHz tone spacing [(a),(d)] and 16-QAM signal with 400 Mbaud [(b),(e)] and 800 Mbaud [(c),(f)] symbol rates as a function of E-plane beam scan angle, which is represented by trace color. . . . .	102
4.23	Power spectral densities of the modulated stimulus applied to the AUT $S_{XX}(f)$ (blue) and measured on the PNA-X reference receiver $R1$ , the received signal from the CATR feed horn $S_{YY}(f)$ (green) measured on receiver $B$ , and the distortion spectrum $S_{DD}(f)$ (red) described in section 2.3, with the corresponding modulated gain $ H(f) $ (magenta) overlaid. Results are for a 100 MHz-wide flat tone signal (a)-(c), and a 16-QAM signal with 400 Mbaud (d)-(f) and 800 Mbaud (g)-(i) symbol rates measured at beam scan angles $(\theta_s, \phi_s) = (45^\circ, 270^\circ)$ [(a),(d),(g)]; $(\theta_s, \phi_s) = (0^\circ, 0^\circ)$ [(b),(e),(h)]; and $(\theta_s, \phi_s) = (45^\circ, 90^\circ)$ [(c),(f),(i)]. . . . .	103
4.24	Equalized $EVM_{EQ}$ (green), un-equalized $EVM_{UN}$ (blue), and carrier gain $ H(f_c) $ (red) as a function of RF output power from the VSG (a)-(c) and elevation beam scan angle $\theta_s = [0^\circ : 15^\circ : 45^\circ]$ , $\phi_s = [90^\circ, 270^\circ]$ (d)-(e) for a 100 MHz-wide flat tone signal [(a),(d)] and 16-QAM signals with 400 Mbaud [(b),(e)] and 800 Mbaud [(c),(f)] symbol rates. . . . .	104
5.1	A patented procedure for far field EVM estimation from wideband PNF-to-FF transformation [120] based on time advancing the digitized PNF waveforms using eqn. (5.5). . . . .	109
5.2	A patented procedure for far field EVM estimation from wideband PNF-to-FF transformation [120] based on Fourier transforming multiple PNF waveform time segments and frequency bins. . . . .	109
5.3	Far field EVM estimation from a multi-probe PNF measurement [124]: (a) diagrams of far field calibration and near field measurements and (b) wideband application for EVM. . . . .	111

5.4	Ka-band conical horn antenna model with $N_x N_y = 4096$ ideal planar near field probes (green) in CST Microwave Studio. Ideal probes have a linear spacing $\Delta x = \Delta y = \lambda/2$ over the $32\lambda \times 32\lambda$ scan plane positioned $z_0 = 5\lambda$ above the horn aperture, where $\lambda = 6.82$ mm at $f_{max} = 44$ GHz. . . . .	113
5.5	Simulated $\vec{E}_y$ planar near field magnitude (dBV/m) [(a)-(c)] and phase (degrees) [(d)-(f)] at 35 GHz [(a),(d)], 39 GHz [(b),(e)] and 43 GHz [(c),(f)] for Ka-band horn model. . . . .	115
5.6	Simulated $\vec{E}_x$ planar near field magnitude (dBV/m) [(a)-(c)] and phase (degrees) [(d)-(f)] at 35 GHz [(a),(d)], 39 GHz [(b),(e)] and 43 GHz [(c),(f)] for Ka-band horn model. . . . .	115
5.7	Magnitude of vertical Ludwig-3 far field component ( $ \vec{E}_V $ ) from ideal far field probes (blue) and planar near field to far field transform (green) as a function of the far field angle $\theta$ in the E-plane [(a)-(b)] and H-plane [(d)-(f)] at 35 GHz [(a),(d)], 39 GHz [(b),(e)] and 43 GHz [(c),(f)]. All $\theta$ angles are positive (in upper hemisphere): Negative to positive $\theta$ shifts indicate a $\phi$ shift of $(180^\circ, 0^\circ)$ for E-plane and $(270^\circ, 90^\circ)$ for H-plane. . . . .	116
5.8	Magnitude of vertical Ludwig-3 far field component ( $ \vec{E}_V $ ) from ideal far field probes (blue) and planar near field to far field transform (green) as a function of frequency at far field angles $(\theta, \phi) =$ (a) $(60^\circ, 0^\circ)$ , (b) $(45^\circ, 0^\circ)$ , (c) $(30^\circ, 0^\circ)$ , (d) $(15^\circ, 0^\circ)$ , (e) $(0^\circ, 0^\circ)$ , (f) $(15^\circ, 90^\circ)$ , (g) $(30^\circ, 90^\circ)$ , (h) $(45^\circ, 90^\circ)$ , and (i) $(60^\circ, 90^\circ)$ . . . . .	118
5.9	Measured (blue) and CST-simulated far field (red), and transformed PNF (green) un-equalized $EVM_{UN}$ (a)-(b) and linear distortion $EVM_{H(f)}$ (c)-(d) for Ka-band horn link. Results are shown for E-plane angles ( $\phi = 0^\circ$ ) in (a) and (c) and H-plane angles ( $\phi = 90^\circ$ ) in (b) and (d). $EVM_{UN}$ results show good agreement except at largest far field angles ( $\theta \geq 45^\circ$ ), while linear distortion $EVM_{H(f)}$ results only show good agreement for small angles ( $\theta \leq 30^\circ$ ). . . . .	119



5.10	Planar near field measurement system for the spline-profiled Ka-band horn: (a) front view of measurement system placed in a shielded millimeter-wave compact antenna test range provided by Keysight in Santa Rosa, CA, with the reflector and AUT positioner covered in absorber, (b) side view of the PNF scanning machine with WR-28 open-ended waveguide probe, and (c) top view of probe and Ka-band horn mounting bracket with absorber covers. This custom PNF measurement system was invented by Dan Slater and presented in [129]. . . . .	121
5.11	Measured $S_{21_y}$ planar near field magnitude (dB) [(a)-(c)] and phase (degrees) [(d)-(f)] at 35 GHz [(a),(d)], 39 GHz [(b),(e)] and 43 GHz [(c),(f)] for Ka-band horn antenna. . . . .	122
5.12	Measured $S_{21_x}$ planar near field magnitude (dB) [(a)-(c)] and phase (degrees) [(d)-(f)] at 35 GHz [(a),(d)], 39 GHz [(b),(e)] and 43 GHz [(c),(f)] for Ka-band horn antenna. . . . .	122
5.13	Magnitude of vertical Ludwig-3 far field component ( $ \vec{E}_V $ ) from CST far field ideal probes (red) and simulated (green) and measured (blue) planar near field to far field transforms as a function of the far field angle $\theta$ in the E-plane [(a)-(b)] and H-plane [(d)-(f)] at 35 GHz [(a),(d)], 39 GHz [(b),(e)] and 43 GHz [(c),(f)]. All $\theta$ angles are positive (in upper hemisphere): Negative to positive $\theta$ shifts indicate a $\phi$ shift of $(180^\circ, 0^\circ)$ for E-plane and $(270^\circ, 90^\circ)$ for H-plane. . . . .	124
5.14	Magnitude of vertical Ludwig-3 far field component ( $ \vec{E}_V $ ) from CST far field ideal probes (red) and simulated (green) and measured (blue) planar near field to far field transforms as a function of frequency at far field angles $(\theta, \phi) =$ (a) $(60^\circ, 0^\circ)$ , (b) $(45^\circ, 0^\circ)$ , (c) $(30^\circ, 0^\circ)$ , (d) $(15^\circ, 0^\circ)$ , (e) $(0^\circ, 0^\circ)$ , (f) $(15^\circ, 90^\circ)$ , (g) $(30^\circ, 90^\circ)$ , (h) $(45^\circ, 90^\circ)$ , and (i) $(60^\circ, 90^\circ)$ . . . . .	125

5.15	Estimate of the normalized WR-28 waveguide probe pattern in the E-plane: (a) as a function of the far field elevation angle $\theta$ at each of nine frequencies spanning 35-43 GHz, and (b) as a function of frequency at nine elevation angles. Estimates in (a)-(b) are calculated from the difference between $ \vec{E}_V(f, \theta, \phi) $ derived from PNF simulation and measurement of the Ka-band conical horn. For comparison, the (c) WR-28 waveguide probe patterns and (d) gain versus frequency profile published in the manufacturer data sheet [130] are also shown. . . . .	127
5.16	Un-equalized $EVM_{UN}$ (a), equalized $EVM_{EQ}$ (b), and carrier gain $ H(f_c) $ (c) measured at the PNF scan plane center as a function of RF output power from the VSG and equalized $EVM_{EQ}$ as function of PNF probe position for a 100 MHz-wide flat tone signal (d) and 16-QAM signals with 400 Mbaud (e), and 800 Mbaud (f) symbol rates. In (a)-(c), these three test signals are shown in blue, green, and red respectively. EVM is expressed as a %. . . . .	128
5.17	Planar near field measurement system for the 8x8 phased array [98]: (a) front view of measurement system placed in a shielded millimeter-wave compact antenna test range provided by Keysight in Santa Rosa, CA, with the Arduino microcontroller and breakout board taped to cardboard box behind the array, (b) side view of PNF scanning machine with WR-28 open-ended waveguide probe, and (c) top view of probe and array mounting bracket. This custom PNF measurement system was invented by Dan Slater and presented in [129]. . . . .	129
5.18	Carrier gain $ H(f_c) $ of 8x8 phased array transmitting a 16-QAM signal with 400 Mbaud symbol rate, with a VSG output power of -9 dBm and a VNA noise bandwidth of 312 Hz, measured at PNF probe positions with beam scanned to far field angles (a) $(45^\circ, 180^\circ)$ , (b) $(30^\circ, 180^\circ)$ , (c) $(15^\circ, 180^\circ)$ , (d) $(15^\circ, 0^\circ)$ , (e) $(30^\circ, 0^\circ)$ , and (f) $(45^\circ, 0^\circ)$ at $f_c = 39$ GHz. . . . .	130

5.19	Carrier gain $ H(f_c) $ of 8x8 phased array transmitting a 16-QAM signal with 400 Mbaud symbol rate, with a VSG output power of -9 dBm and a VNA noise bandwidth of 312 Hz, measured at PNF probe positions with beam scanned to far field angles (a) $(45^\circ, 270^\circ)$ , (b) $(30^\circ, 270^\circ)$ , (c) $(15^\circ, 270^\circ)$ , (d) $(15^\circ, 90^\circ)$ , (e) $(30^\circ, 90^\circ)$ , and (f) $(45^\circ, 90^\circ)$ at $f_c = 39$ GHz. . . . .	131
5.20	Carrier gain $ H(f_c) $ in dB [(a)-(c)], un-equalized $EVM_{UN}$ [(d)-(f)], and equalized $EVM_{EQ}$ [(g)-(h)] of 8x8 phased array transmitting a 16-QAM signal with 400 Mbaud symbol rate, with a VSG output power of -9 dBm and a VNA noise bandwidth of 312 Hz, measured at PNF probe positions with beam scanned to far field angles [(a),(d),(g)] $(45^\circ, 180^\circ)$ , [(b),(e),(h)] $(0^\circ, 0^\circ)$ , and [(c),(f),(i)] $(45^\circ, 0^\circ)$ . EVM is expressed as a %. . . . .	132
5.21	Carrier gain $ H(f_c) $ in dB [(a)-(c)], un-equalized $EVM_{UN}$ [(d)-(f)], and equalized $EVM_{EQ}$ [(g)-(h)] of 8x8 phased array transmitting a 16-QAM signal with 400 Mbaud symbol rate, with a VSG output power of -9 dBm and a VNA noise bandwidth of 312 Hz, measured at PNF probe positions with beam scanned to far field angles [(a),(d),(g)] $(45^\circ, 270^\circ)$ , [(b),(e),(h)] $(0^\circ, 0^\circ)$ , and [(c),(f),(i)] $(45^\circ, 90^\circ)$ . EVM is expressed as a %. . . . .	133
5.22	Carrier gain $ H(f_c) $ in dB [(a)-(c)], un-equalized $EVM_{UN}$ [(d)-(f)], and equalized $EVM_{EQ}$ [(g)-(h)] of 8x8 phased array transmitting a 100 MHz-wide flat tone signal [(a),(d),(g)] and 16-QAM signals with 400 Mbaud [(b),(e),(h)] and 800 Mbaud [(c),(f),(i)] symbol rates, measured at PNF probe positions with the beam scanned to far field angle $(45^\circ, 0^\circ)$ . EVM is expressed as a %. . . . .	134
5.23	Un-equalized $EVM_{UN}$ (a), equalized $EVM_{EQ}$ (b), and carrier gain $ H(f_c) $ (c) of 8x8 phased array measured at the PNF scan plane center as a function of RF output power from VSG for a 100 MHz-wide flat tone signal (blue), and 16-QAM signals with 400 Mbaud (green), and 800 Mbaud (red) symbol rates. . . . .	135

5.24	Measured spectrum of 16-QAM test signal with 800 Mbaud symbol rate transmitted to the 8x8 phased array port from VNA port #1 (a1, blue) and measured spectrum of the signal received by the probe on VNA port #2 (b2, green) at each of five probe positions along the diagonal of the PNF scan (a), with the beam scanned to boresight $(\theta_s, \phi_s) = (0^\circ, 0^\circ)$ . . . . .	136
5.25	Normalized far field patterns $ \vec{E}_V(\theta) $ of 8x8 phased array with beams scanned to angles $\theta_s = [-45^\circ : 15^\circ : 45^\circ]$ in azimuth [(a)-(c)] and elevation [(c)-(f)] at 35 GHz [(a),(d)], 39 GHz [(b),(e)], and 43 GHz [(c),(f)], where negative to positive $\theta$ shifts indicate $\phi$ shift of $(180^\circ, 0^\circ)$ for azimuth and $(270^\circ, 90^\circ)$ for elevation. Far field patterns are obtained from Fourier transforms of measured modulated complex gain at the specified frequency, as described in section 5.1. Phase gradients are calculated for $f_c = 39$ GHz, so beam squint effects are shown. . . . .	137
5.26	Measured spectrum of 16-QAM test signal with 800 Mbaud symbol rate transmitted to the 8x8 phased array port from VNA port #1 (a1, blue) and estimated spectrum of the far field signal received at $(1.0 \text{ m}, 0^\circ, 0^\circ)$ , with the beam scanned to boresight (b, red). . . . .	138
6.1	Front view (a) and side view (b) of the RSU and OBU coordinate systems and (c) top view of the vehicle-mounted OBU circular monopole array beam states at each of the three linear highway segments: $-500\text{m} \leq x_o < 20\text{m}$ , $-20\text{m} \leq x_o \leq 20\text{m}$ , and $20\text{m} < x_o \leq 500\text{m}$ . See Table 6.1 for linear highway dimensions and RSU and OBU antenna positions. . . . .	141
6.2	(a) RSU linear microstrip patch array with $N = 4$ elements spaced apart by $l_{sp}$ and gain patterns with peak $G_{RSU} = 13.0$ dB at $\theta_{RSU} = 0^\circ$ and first nulls at $\theta_{RSU} = \theta_{fn} = 21.0^\circ$ in $\phi_{RSU} = 90^\circ$ plane. (b) OBU circular monopole array with $N = 16$ elements spaced apart by $R\Delta\phi(\pi/180^\circ) = 15.97$ mm along a circle centered at $\hat{z}_o$ with radius $R$ and gain pattern in $\theta_{OBU} = 90^\circ$ plane with peak $G_{OBU} = 9.5$ dB. The OBU gain pattern shown represents the monopole array state when the vehicle's position along the highway is $-500\text{m} \leq x_o < -20\text{m}$ . . .	144

6.3	<i>P</i> <sub>OB<sub>U</sub></sub> at $f_0 = 5.90$ GHz calculated via equation (6.2) for grid points on a linear highway segment for cases in which (a) OBU has a single monopole antenna and an RSU range of 325 m with a -68 dBm threshold and (c) OBU has a circular monopole array that switches between three beam states as shown in Fig. 6.1(b)-(c) and an RSU range of 961 m with a -68 dBm threshold. The highway is 1.0 km long (along $\hat{x}_o$ ) and 11.0 m wide (along $\hat{y}_o$ ). . . . .	146
6.4	<i>P</i> <sub>OB<sub>U</sub></sub> at $f_0 = 5.90$ GHz calculated via equation (6.2) for grid points on a linear highway segment in (a) near, (b) center, and (c) far lanes with $\theta_{tilt} = 50.25^\circ$ . See Fig. 6.1(a). . . . .	148
6.5	<i>P</i> <sub>OB<sub>U</sub></sub> at $f_0 = 5.90$ GHz calculated via equation (6.2) for grid points on a linear highway segment in all three lanes with different RSU tilt angles $\theta_{tilt}$ . See Fig. 6.1(a). . . . .	148

## LIST OF TABLES

1.1	EVM Requirements for 5G NR Base Stations (3GPP TS 38.104) . . . . .	2
2.1	Types of Signal Impairments in Communication Systems ( [38]) . . . . .	15
6.1	RSU Antenna Positions and Highway Dimensions . . . . .	142
6.2	RSU and OBU Phased Array Dimensions . . . . .	144

## LIST OF ACRONYMS

- 3GPP** 3rd Generation Partnership Project. xxviii, 2, 13, 34
- ACPR** Adjacent Channel Power Ratio. 74
- ADC** Analog-to-Digital Converter. 15
- AESA** Active Electronically-Scanned Array. 105
- AM-AM** Amplitude-to-Amplitude Distortion. xvii, 23, 73–75
- AM-PM** Amplitude-to-Phase Distortion. xvii, 23, 73–75
- AUT** Antenna Under Test. ix, 16, 40, 52, 54–56, 60, 62, 64, 66, 68, 91, 93, 94, 100, 101, 107, 110–113, 120, 121, 123, 125, 126, 129, 130, 135–137, 139, 150
- AWG** Arbitrary Waveform Generator. ix, xiv, xix, 16, 52–55, 90, 92
- AWGN** Additive White Gaussian Noise. xiv, xvi, 13, 15, 50, 51, 62–64, 66
- BER** Bit Error Rate. 7, 8, 29, 89, 107
- BLA** Best Linear Approximation. 19–21
- CATR** Compact Antenna Test Range. xiv, xvii, xx, 9, 40, 51, 52, 54–56, 60, 62, 64, 66, 68–70, 77, 91–94, 100–102, 106, 107, 119, 123, 126, 128, 135, 150, 151
- CCDF** Complimentary Cumulative Distribution Function. x, 20
- CMOS** Complimentary Metal-Oxide Semiconductor. 4
- CTS** Compact Test Signal. x, 20
- CW** Continuous Wave. 8, 22, 23, 66, 89, 150
- DPD** Digital Pre-Distortion. 14, 73, 74

**DSRC** Dedicated Short Range Communications. 10, 143, 145

**DUT** Device Under Test. 7, 8, 11, 16–21, 23, 64, 91, 149, 150

**EIRP** Effective Isotropic Radiated Power. xix, 4, 6–8, 14, 90, 105, 143

**EVM** Error Vector Magnitude. ix–xii, xvii–xix, xxviii, 2, 5–24, 28–32, 34–39, 52, 54–56, 60, 62, 64, 66, 68–79, 81–84, 88–95, 97, 98, 100, 104–107, 110–112, 118–120, 126, 129, 131, 135–139, 149–151

**FDTD** Finite Difference Time Domain. 30

**FF** Far Field. 108, 110, 112

**FFT** Fast Fourier Transform. 17, 31, 107, 108, 110, 113, 114

**FIR** Finite Impulse Response. 15, 28, 29

**FR** Frequency Range. xi, 34, 35, 38, 111

**GIR** Grid Impulse Response. 30

**IC** Integrated Circuit. ix, 2–5, 8, 89, 94, 98, 104, 106, 149

**IF** Intermediate Frequency. 106, 110, 123, 150

**IFFT** Inverse Fast Fourier Transform. 28, 32

**IM** Intermodulation Distortion. 2

**IQ** In-Phase and Quadrature. ix–xi, 2, 7, 8, 12, 16, 17, 21–23, 32, 36, 48, 54, 56, 72, 149

**ISI** Inter-Symbol Interference. 12, 13, 15, 17, 32, 75, 79

**LO** Local Oscillator. 22, 90

**LPF** Low Pass Filter. 22



**LTI** Linear Time-Invariant. 14, 24, 27, 28

**MIMO** Multiple Input Multiple Output. 92

**NBW** Noise Bandwidth. 55, 56, 106

**NPR** Noise to Power Ratio. 8

**NR** New Radio. xxviii, 1, 2, 13

**OBU** On-board Unit. xxvi–xxviii, 10, 140–147

**OFDM** Orthogonal Frequency Division Multiplexing. 13, 15, 21, 22, 89, 92, 93, 108, 145

**OTA** Over The Air. ix, xiv, xix, 2, 12, 14, 15, 23, 47, 52, 53, 55, 56, 84, 89–93, 101, 135, 149

**P1dB** 1 dB Output Power Compression Point. 73, 74

**PA** Power Amplifier. 73–75

**PAE** Power-Added Efficiency. 14

**PAPR** Peak-to-Average Power Ratio. 13, 101, 104, 130

**PCB** Printed Circuit Board. ix, 3, 4, 94

**PDF** Probability Density Function. 21

**PN** Phase Noise. 22

**PNF** Planar Near Field. 9, 107, 108, 110–114, 116–121, 123–126, 128–131, 135–139, 150, 151

**PSD** Power Spectral Density. x, 20, 21, 60, 68, 95, 102

**PWC** Plane Wave Converter. 77, 93

**QAM** Quadrature Amplitude Modulation. ix, xi, xiv, xvii, xviii, 2, 7, 9–13, 17, 28–36, 40, 48–50, 52, 54, 69, 70, 72–75, 77–79, 81, 82, 84, 87, 88, 90, 94, 100, 101, 105, 106, 112, 119, 128–131, 135, 136, 138, 150

**QPSK** Quadrature Phase Shift Keying. 2

**RBW** Resolution Bandwidth. 55

**RF** Radio Frequency. ix, x, xiv, xvii, xix–xxi, xxiv, xxv, 2, 3, 5, 6, 8, 19, 21, 22, 53, 55, 69, 70, 72, 77, 89, 90, 92, 95, 97–100, 104, 106, 110, 126, 128, 135

**RMS** Root Mean Square. xvii, 2, 7, 8, 16, 17, 31, 73, 74

**RRC** Root-Raised Cosine. 12, 31, 32, 75, 79, 84, 101, 128

**RSU** Roadside Unit. xxvi–xxviii, 10, 140–148

**SATCOM** Satellite Communication. ix, 3

**SC-FDE** Single Carrier Frequency Domain. 15

**SCPI** Standard Commands for Programmable Instruments. 52, 94

**SiGe** Silicon-Germanium. 4

**SNR** Signal to Noise Ratio. xiv, xix, 4, 6–8, 13, 14, 39, 50, 60, 64, 66, 68, 74, 84, 90, 95, 97, 98, 100, 105, 110, 113, 135, 139, 147, 151

**SPI** Serial Peripheral Interface. 94

**UWB** Ultra-Wideband. x, 8, 24, 25, 28, 30, 69, 100, 150

**V2I** Vehicle-to-Infrastructure. 10, 140, 142, 145, 147, 149

**VEL** Vector Effective Length. xii, 8, 9, 39, 41

**VGA** Variable Gain Amplifier. 94, 104, 105

**VNA** Vector Network Analyzer. x, xiv, xix, 8, 9, 18–20, 23, 51–53, 56, 60, 64, 66, 69, 92, 94, 105, 106, 136, 137, 139, 150

**VSA** Vector Signal Analyzer. ix, xiv, xix, 15–17, 53, 90, 91, 149

**VSG** Vector Signal Generator. ix, xiv, xvi, xvii, xix–xxi, xxiv, xxv, 16, 52–56, 64, 65, 68, 70, 92, 95, 96, 98, 99, 104, 105, 126, 128, 130, 135

## ACKNOWLEDGMENTS

Furthering my education as a graduate student and member of the UCLA Antenna Research, Analysis, and Measurement (ARAM) Laboratory has been a tremendous honor and privilege. I have so many to thank for providing this opportunity and helping me to make the most of it. First, I would like to express my sincere gratitude to my advisor, Prof. Yahya Rahmat-Samii, for allowing me to join his research group in spite of my early struggles in his electromagnetics courses. His steady leadership, technical expertise, and words of encouragement helped me to persevere through the many challenges of this research topic and complete this dissertation. He inspired me to match his attention to detail and uncompromising commitment to excellence in all aspects of my research, from concept validation to conference presentation. I would also like to thank Professors Yuanxun Wang, Aydin Babakhani, and Omid Abari for their helpful feedback and dedication of time as members of my committee. I am deeply thankful for Prof. Tatsuo Itoh's contributions to my work and for his enduring legacy as a pioneer in this field.

The fifteen quarters of teaching experience that I acquired in the undergraduate engineering ethics courses have played a critical role in my personal and professional development here at UCLA. I thank Professors Don Browne and John Villasenor for providing that opportunity and helping me to improve the quality of my teaching. I also want to thank my classmates and lab colleagues at UCLA for the friendships, collaborations, and conversations that made this work possible: Raju Manthena, Srinivas Prasad, Jordan Budhu, Vignesh Manohar, Lingnan Song, Daisong Zhang, Yubin Cai, Anastasios Papathanasopolous, Junbo Wang, Botian Zhang, and Tianjian Huang. Additionally, I acknowledge my colleagues at Keysight, Santa Rosa for providing technical assistance and allowing me to use their OTA test ranges and instruments. Thanks to Phil Lorch, Joel Dunsmore, Tuan Tang, Abhi Mahadevan, and Cherisa Kmetovicz.

Finally, I would like to acknowledge my dear family: My wife Lauren and her family, father Steven, mother Desiree, brother Zach, and sister Jessica have been the source of constant love, support, and encouragement that I have needed to relentlessly pursue this life-long goal and maintain a healthy balance in my life throughout this process. I could not have achieved this milestone without them, and I celebrate the completion of this long journey with them.

## VITA

### EDUCATION

- 2011–2015 **LeTourneau University**, Longview, TX 75602, USA
- B.S. in Engineering with Electrical Concentration
  - Final GPA: 3.70/4.00
- 2015–2017 **University of California, Los Angeles (UCLA)**, Los Angeles, CA 90095, USA
- M.S. in Electrical Engineering
  - Advisor: Professor Yahya Rahmat-Samii
  - Final GPA: 3.66/4.00

### TEACHING EXPERIENCE

- 2016–2017 **Teaching Assistant**, UCLA Dept. of Engineering and Applied Science, ENGR 185EW Art of Engineering Endeavors
- 2017–2020 **Teaching Associate**, UCLA Dept. of Engineering and Applied Science, ENGR 182EW Technology and Society, ENGR 183EW Engineering and Society
- 2021 **Teaching Fellow**, UCLA Dept. of Engineering and Applied Science, ENGR 183EW Engineering and Society

### PROFESSIONAL AND RESEARCH EXPERIENCE

- 2016–2023 **Graduate Student Researcher**, UCLA Antenna Research, Analysis, and Measurement Laboratory
- 06/2016–09/2016 **RF/Antenna Engineer Intern**, GoPro Inc., San Mateo, CA
- 06/2017–09/2017 **Antenna Products Division Intern**, Northrop Grumman Aerospace Systems, Redondo Beach, CA
- 06/2019–09/2019 **Phased Array Measurement Intern**, Keysight Technologies, Santa Rosa, CA
- 06/2020–09/2020 **Graduate Satellite Antenna Intern**, The Aerospace Corp., El Segundo, CA
- 09/2022–Present **Application Development Engineer**, Keysight Technologies, Santa Rosa, CA

### HONORS and AWARDS

- 2011–2022 **Almanor Scholarship (Almanor Scholarship Fund)**
- 2011–2015 **Heritage Scholarship (LeTourneau University)**
- 2021 **Summer Mentored Research Fellowship (UCLA)**
- 2022 **Student Paper Competition Finalist (2022 IEEE International Symposium on Phased Array Systems and Technology)**

## PUBLICATIONS

**D. Brown** and Y. Rahmat-Samii, “Link Budget Analysis for a Vehicle-to-Infrastructure System with a Switchable Circular Monopole Array”, *2020 IEEE International Symposium on Antennas and Propagation and North American Radio Science Meeting*, Montreal, QC, Canada, 2020, pp. 1375-1376.

**D. Brown** and Y. Rahmat-Samii, “Far Field EVM Characterization of Antenna Frequency Response via Full-Wave Analysis”, *2021 IEEE International Symposium on Antennas and Propagation and USNC-URSI Radio Science Meeting (APS/URSI)*, Singapore, Singapore, 2021, pp. 1251-1252.

**D. Brown** and Y. Rahmat-Samii, “Far Field EVM Estimation for Large Phased Arrays using Embedded Elements and Beam Squint Model”, *2022 United States National Committee of URSI National Radio Science Meeting (USNC-URSI NRSM)*, Boulder, CO, USA, 2022, pp. 112-113.

**D. Brown** and Y. Rahmat-Samii, “Compact Antenna Test Range EVM Measurements of a Millimeter-Wave Phased Array using a VNA”, *2022 IEEE International Symposium on Phased Array System & Technology (PAST)*, Waltham, MA, USA, 2022, pp. 01-05. **(Among top ten finalists in the student paper competition.)**

**D. Brown** and Y. Rahmat-Samii, “Error Vector Magnitude as a Performance Standard for Antennas in the Millimeter-Wave Era, Part 1: Metric Comparisons and Measurement Concepts”, *IEEE Antennas and Propagation Magazine*, pp. 01-14. **(Accepted for publication in March 2023.)**

**D. Brown** and Y. Rahmat-Samii, “Error Vector Magnitude as a Performance Standard for Antennas in the Millimeter-Wave Era, Part 2: Modeling, Simulation, and Measurement Methods”, *IEEE Antennas and Propagation Magazine*, pp. 01-14. **(Accepted for publication in March 2023.)**

**D. Brown** and Y. Rahmat-Samii, “Calculating Wideband Far Fields at Wide Angles via Planar Near Fields from Time Domain Simulations”, *2023 IEEE International Symposium on Antennas and Propagation and USNC-URSI Radio Science Meeting (APS/URSI)*. **(Accepted for publication in March 2023.)**

# CHAPTER 1

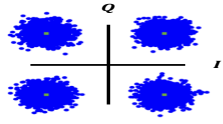
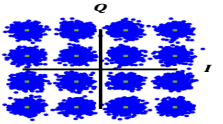
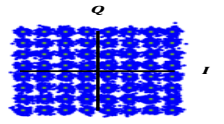
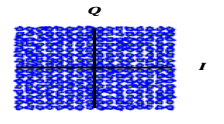
## Introduction

### 1.1 Entering an Era of Highly-Integrated Millimeter-Wave Phased Arrays

Improving the performance of mobile wireless communication systems has required us to transition from the congested spectrum at microwave carrier frequencies (300 MHz-3GHz) to higher millimeter wave carrier frequencies (30 GHz-300 GHz), where tens of GHz of additional spectrum is available to support a larger number of connections and enable multi-Gbps data rates at low latencies on the order of a few milliseconds. [1–3]. These advancements in network capacity are critical for accommodating the rapidly-expanding number of internet-connected devices across the world and for realizing a variety of new applications such as intelligent transportation systems and smart factories. This transition to millimeter-wave spectrum was initiated with adoption of the 28 and 39 GHz bands for 5G NR and will likely continue with 6G, as researchers investigate the potential for ultra-high data rate wireless systems at THz frequencies [4–6].

One of the main challenges of maintaining reliable wireless millimeter-wave communication links is the significant signal attenuation at these high frequencies. The shorter wavelengths promote increased absorption from atmospheric gasses such as oxygen and scattering from precipitation, buildings, trees, and other such obstacles. Millimeter-wave channel models and measurements for indoor and outdoor propagation environments have provided valuable insights on these propagation characteristics [7–9]. High data rate millimeter-wave wireless links will depend on the widespread deployment of high-gain active phased arrays that offer adaptive beamforming and compensation for high path loss [2, 10, 11]. Antenna engineers

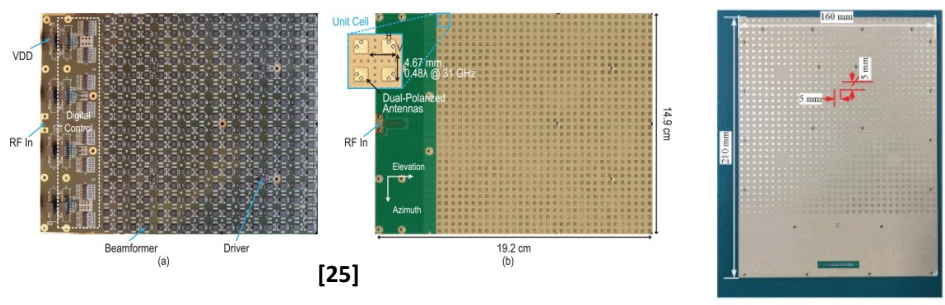
Table 1.1: EVM Requirements for 5G NR Base Stations (3GPP TS 38.104)

QPSK	16-QAM	64-QAM	256-QAM
17.5%	12.5%	8.0%	3.5%
			

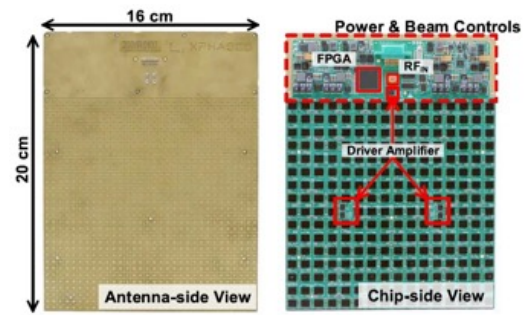
have been leveraging the down-scaled size of the radiating elements and silicon integrated circuit (IC) packaging technologies to design highly-integrated millimeter-wave phased array architectures with digitally-controlled amplitude and phase states for hundreds and thousands of printed antennas [12–18].

While this emerging class of millimeter-wave phased arrays is becoming an essential component of modern terrestrial and satellite communication systems, it is also challenging the conventional methods of antenna simulation and measurement, which have generally evaluated the radiation and impedance-matching characteristics of passive antennas in isolation from the RF transceivers with which they are integrated. The reduced size and spacing between the radiating elements and lack of direct access to RFIC ports precludes the installation of RF connectors and consequently the independent measurement of antenna radiation and RF performance characteristics such as power amplifier linearity or intermodulation (IM) distortion [4, 6, 19–22]. This has increased interest in the adoption of updated performance metrics which account for the combined response of the transceiver components and radiating elements to an applied voltage signal as a function of the beam scan angle [23]. One such metric which has been applied in performance characterization of transmitting millimeter-wave phased arrays is error vector magnitude (EVM), a measure of IQ-modulated signal quality that is calculated as the root-mean-square (RMS) value of the vector difference between transmitted and received symbols in the complex plane. In over-the-air (OTA) measurements of active arrays, EVM represents the net amplitude and phase distortion produced by the RF circuits and antenna elements. [23, 24] It is therefore a function of both the signal modulation characteristics and phased array linearity.

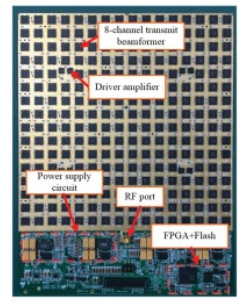




[25]



[14]



[26]

Figure 1.1 Examples of PCB-integrated millimeter wave phased arrays designed for SATCOM [14,25,26]. Each one operates over a frequency range of 27-31 GHz and features 1024 dual-polarized microstrip patch elements integrated with 256 beamforming RFICs on opposite sides of the PCBs.

High gain and precise beam scan control over a large angular scan range are required to maintain high capacity links with mobile users in lossy and dispersive millimeter-wave channels. Parabolic reflector and multi-feed lens antennas have received consideration for deployment in millimeter-wave base stations and satellite platforms, but they are limited by a small number of switchable beam states, commensurate with the number of antenna feeds, as well as a high scan loss at large angles [27–30]. Large flat-panel active phased arrays integrated on printed circuit boards (PCBs) have become an attractive alternative due to their lower profile, superior beamforming flexibility, and scalability [16]. Three examples of 1024-element arrays designed for Ka-band satellite communication are presented in Fig. 1.1 [14, 25, 26]. The past decade of enhancements in silicon integrated circuit and packaging technologies has led to the commercialization and miniaturization of beamforming ICs that contain switches, power amplifiers, phase shift units, and attenuators [14–16, 18]. There are numerous incentives for continued research and development of scalable planar phased arrays which have been described in recent publications [14–16]. One of these is the effect of frequency scaling on the radiating element size: The number of radiating elements  $N$  that can be fabricated on a fixed square substrate increases as the square of the frequency scaling factor when array elements are spaced apart by half of a wavelength [14]. Increasing the number of elements by a factor of  $N$  leads to an  $N$ -times higher EIRP, and a corresponding increase in SNR at the receiver [16]. Another incentive is the development of low cost, low footprint SiGe and CMOS integrated circuits. At millimeter-wave frequencies, these beamforming ICs can be seamlessly integrated with microstrip antennas on PCBs to facilitate digital control of the radiating element amplitude and phase, providing precise and adaptable beamforming that maximizes the SNR. Minimizing silicon IC size to match the frequency scaling of antenna size has challenged the continued development of integrated phased arrays, as carrier frequencies in the THz regime are under consideration for 6G applications [15, 16, 31]. If researchers can continue to make progress in addressing these design challenges, integrated phased arrays will remain a critical component of millimeter-wave systems, enabling the high spatial selectivity and beamforming flexibility required for supporting multiple multi-Gbps wireless links.

However, these modern millimeter-wave phased arrays have also introduced new mea-

surement challenges that are having a profound impact on the tools and metrics that are used to validate their far field performance. Due to the increasingly-small size and spacing between array elements at millimeter-wave frequencies, it is no longer possible to add separate RF-connectors for each element to enable isolated measurements of radiating elements and RFICs. Therefore, the performance of the entire active array from the RF common port to the far field probe has to be measured through over-the-air techniques [4, 6, 19–22]. Even if the array elements were independently accessible, the use of a large number of highly lossy millimeter-wave cables would make passive measurements of the phased array prohibitively time-consuming and expensive [21, 22]. Consequently, link-level performance metrics that can account for not only the radiated power and impedance-matching characteristics of the antennas but also the linearity of RFICs have received increasing attention in recent years, as all of these have an impact on the quality of the wideband radiated far field signals. Error vector magnitude (EVM) is one such metric which has been recommended as a figure of merit for highly-integrated millimeter-wave active beamforming arrays [23]. In the next section, EVM is compared with other metrics used to characterize the beam-scanning performance of phased arrays.

## **1.2 Link-Level Performance Analysis with Error Vector Magnitude (EVM)**

Highly-integrated phased arrays will play an essential role in maximizing the reliable range and data throughput rates of millimeter-wave communication systems, in part by maximizing radiated power in the direction of intended receivers while simultaneously minimizing it in other directions. However, due to the presence of nonlinear distortion from active transceiver components such as power amplifiers, they must also minimize nonlinear distortion to prevent degradation of received signal quality. Fig. 1.2 shows three broad categories of metrics for phased array performance: (a) radiated power and polarization purity, (b) beam-scanning speed and versatility, and (c) signal quality.

When radiating elements are integrated with beamforming ICs in active phased arrays,

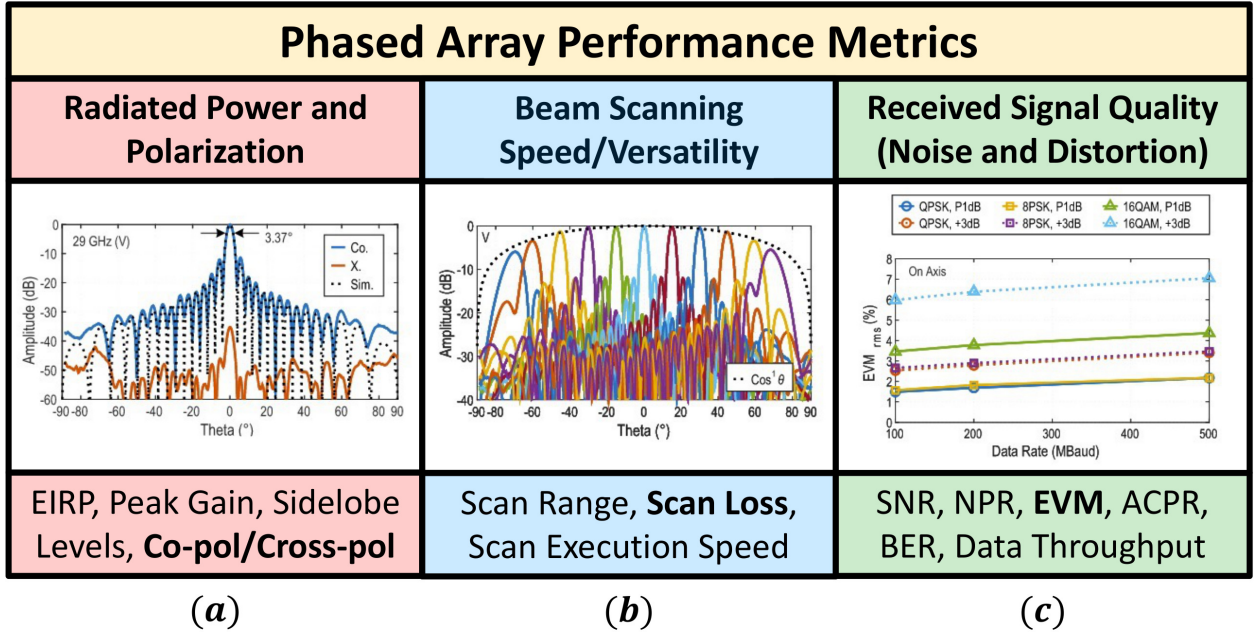


Figure 1.2 Three categories of phased array performance metrics: (a) radiated power, beam pattern, and polarization, (b) angular beam scan range, loss, and execution speed, and (c) received signal quality. Examples of the (a) co-polarized and cross-polarized radiation patterns, (b) beam scan loss, and (c) EVM vs. data rate of the 1024-element Ka-band active phased array from [25] are shown.

radiated power depends on the spatial power combining of array elements and RF power supplied to each element. Effective isotropic radiated power (EIRP) accounts for both as shown in (1.1) from [23]:

$$EIRP = P_t + G_t + 10 * \log_{10}(N) - L \quad (1.1)$$

where  $P_t$  is the transmit power per array element,  $G_t$  is the total array directivity (dBi),  $N$  is the number of array elements, and  $L$  is the loss measured from the power amplifier output to the radiating surface. Increasing EIRP results in higher SNR at a polarization-matched receiver in the far field, resulting in higher data rates over a larger antenna link range. The independent amplitude and phase control of each array element is also leveraged to maximize the angular beam scan range and minimize beam scan loss, both of which can be defined with

respect to EIRP reduction [23]. Phased array engineers must exercise caution and ensure that element spacing and mutual coupling mitigation measures are sufficient to avoid grating lobes and scan blindness [32, 33].

While EIRP is a helpful metric for estimating SNR of a far field antenna link and has been used to characterize the bandwidth and beam scan range of phased arrays, it has limited utility for estimating modulated signal quality and data throughput rate at the receiver. This is because the data throughput rate depends not only on the SNR but also the wideband signal distortion that is generated from the far field transmission of the phased array and not compensated via equalization. Link level metrics such as error vector magnitude and bit error rate (BER), which are more directly correlated with the data throughput rate, supplement traditional antenna metrics which only account for the radiated power and field polarization properties [23, 34]. EVM is a comprehensive measure of IQ-modulated signal quality that quantifies amplitude and phase distortion from a device under test (DUT). A block diagram of the EVM measurement process is shown in Fig. 2.1. EVM is calculated as the RMS value of the difference between input signal  $x(t_n)$  and demodulated output signal  $y(t_n)$  equalized by the filter impulse response  $e(t_n)$  as highlighted in (1.2) from [35], where  $N$  is the number of data symbols and  $t_n$  are the symbol time instances.

$$EVM = \frac{\sqrt{\sum_{n=1}^N |x(t_n) - y(t_n) * e(t_n)|^2}}{\sqrt{\sum_{n=1}^N |x(t_n)|^2}} \quad (1.2)$$

In general,  $N$  is a large multiple of the signal modulation order  $M$  (e.g.  $M=16$  for a 16-QAM input signal), so the normalization in (1.2) becomes that of the average reference signal power [36]. However, normalization can alternatively be based on the peak reference power [37]. Unlike EVM, BER only permits a simple pass-fail test of the modulated signal quality [36, 38]. Observation of the error vectors in the complex IQ plane as shown in Fig. 2.1 yields greater insight on the nature of signal impairments caused by the DUT [38, 39]. Power amplifier intermodulation distortion adds harmonics that fall within the test signal bandwidth and cannot be removed via equalization, so power amplifier nonlinearity tends to

dominate the EVM from millimeter-wave active phased arrays [34, 40]. However, because the beamforming IC ports are not accessible for conducted testing in highly-integrated millimeter-wave arrays, EVM must be measured over-the-air. Fig. 1.2(c) shows the measured EVM of a 1024-element phased array [25], plotted as a function of symbol rate for three different digital modulation formats. The EVM versus beam scan range has been identified as an sensible figure of merit for millimeter-wave active arrays that can provide a linearity constraint for setting maximum EIRP [23]. Furthermore, other link-level metrics such as SNR and BER can be mathematically derived from EVM [41–45], and EVM is equivalent to the reciprocal of the noise power ratio (NPR) when specific signal formatting and test conditions are implemented [46, 47]. Thermal noise  $N(f)$  and in-band harmonic distortion  $D(f)$  both contribute to EVM, making it a valuable metric for millimeter-wave phased arrays.

### 1.3 Outline of this Dissertation

A high-level overview of this dissertation is presented in the outline of Fig. 1.3. Chapter 2 presents a review of digital modulation concepts, linear and nonlinear RF signal impairments, channel equalization, and methods of determining the error vector magnitude. Traditionally, EVM has been measured in the time domain and computed as the root-mean-square (RMS) value of the complex difference between symbols of the transmitted and received IQ-modulated signals, normalized by either the peak or average voltage of the transmitted signal applied to the DUT input port. However, an equivalent frequency domain version of the EVM formula can be derived and applied when certain modulated test signal conditions are satisfied. This spectral correlation method, its implementation with a multi-port vector network analyzer (VNA), and its advantages over the time domain demodulation method are discussed. This method is applied to EVM measurements of a conical horn antenna and 8x8 microstrip patch phased arrays in chapters 3, 4, and 5. A method of estimating EVM from the root-sum-square of assumably-uncorrelated RF impairments measured with a continuous wave stimulus (CW) is also addressed. Chapter 3 presents an UWB model of passive antenna signal transmission based on normalized vector effective length (VEL), a useful property that relates the applied

voltage at the antenna terminals to a polarized electric far field as a function of frequency and angle:  $\vec{H}_N(f, \theta, \phi)$ . This model is used to simulate the EVM from the linear distortion of two passive antennas, a 28 GHz microstrip patch and Ka-band spline-profiled conical horn antenna designed and fabricated by a colleague from the UCLA Antenna Lab. The VELs of these two antennas are obtained directly from full-wave simulations of the broadband radiated far fields and used to estimate the voltage transfer function of the far field antenna link. For the conical horn, a pole-zero model of the link transfer function is synthesized in MATLAB and applied to single-carrier QAM signals to estimate the corresponding EVM, and EVM of a 16-QAM signal is directly measured using a multi-port VNA and compact antenna test range (CATR). Chapter 4 extends the analysis from chapter 3 to an 8x8 phased array of microstrip patch elements. Following a brief review of phased array EVM modeling methods from the literature, a simulation of EVM from square patch arrays of various sizes transmitting a 16-QAM test signal at various beam scan angles is presented. The relative effects of embedded element frequency response, beam squint, amplitude tapering, and phase quantization on the far field EVM are studied. The EVM of independently-activated elements of an 8x8 phased array transmitting a 16-QAM test signal is measured as a function of RF carrier power and far field angle using the same CATR test system that was used for the Ka-band horn, and the EVM of the fully-activated array is measured as a function of RF carrier power and beam scan angle. Chapter 5 reviews the theory of planar near field to far field transformation and how it could be applied in a wideband sense to estimate far field antenna or array link EVM. While computationally-demanding, this approach would benefit from a lower test volume and higher dynamic range, making it an attractive option if it is proven to be feasible and accurate. A PNF-to-far field transformation iterated for a set of discrete frequencies spanning the desired test signal bandwidth was implemented in MATLAB and applied to near fields captured by ideal probes in full-wave time domain simulations of the Ka-band conical horn. The resulting link transfer function and EVM is compared with results obtained directly from the simulated far fields and CATR measurements in chapter 3. The potential effects of planar near field measurement errors from probe positioning, scan plane truncation, and lack of probe compensation on the far field EVM are discussed. Planar

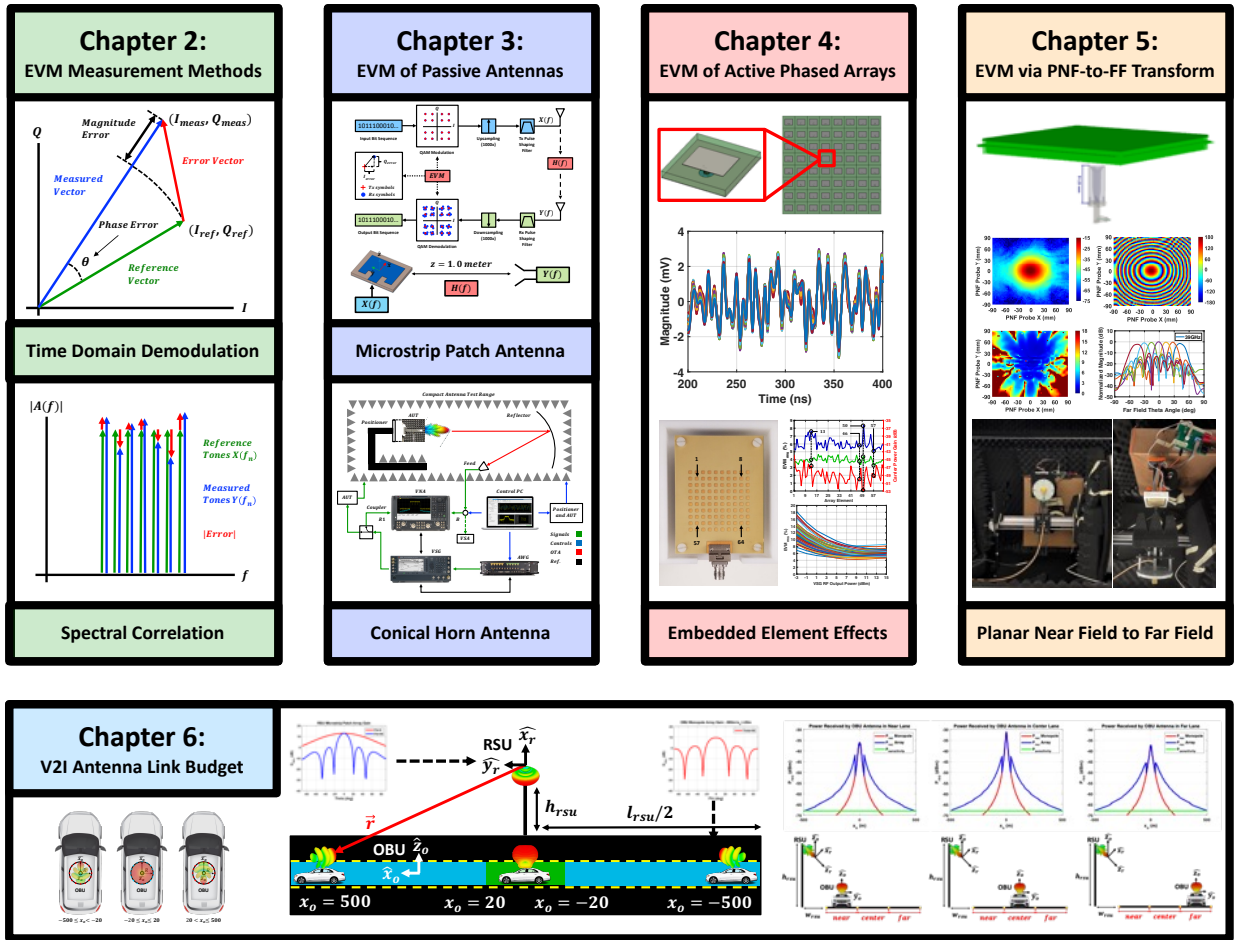


Figure 1.3 Outline of this Dissertation: Chapters 2-5 cover topics related to the modeling, simulation, and measurement of EVM resulting from transmission by antennas and phased arrays. Chapter 6 addresses the simulation of received signal power for a V2I antenna link.

near field measurements of the Ka-band conical horn and phased array transmitting 16-QAM test signals were also performed with a low-cost robotic scanner and a WR-28 waveguide probe using specially-designed MATLAB instrument control scripts. Chapter 6 presents a link budget analysis for a DSRC vehicle-to-infrastructure (V2I) system with linear microstrip patch and circular monopole arrays deployed at the roadside unit base stations (RSU) and vehicular on-board units (OBU) respectively. Full-wave simulations of the antenna arrays are integrated with a MATLAB script that projects the radiated fields onto a linear highway and calculates received signal power from the Friis free space transmission equation, enabling estimation of V2I link range and RSU array tilt sensitivity. Chapter 7 presents the conclusions of this work.



## CHAPTER 2

### Error Vector Magnitude Measurement Methods

#### 2.1 Digital Signal Generation, Distortion, and Equalization

The following section reviews the three stages of the EVM measurement process highlighted in Fig. 2.1 and their influence on EVM. These stages are (a) generation of a modulated test signal, (b) transmission and distortion of the signal by a DUT, and (c) demodulation and equalization of the measured signal  $y(t)$ . These stages precede EVM calculation using  $x(t)$ ,  $y(t)$ , and  $e(t)$  in (1.2).

##### 2.1.1 Signal Generation and Modulation Schemes

The EVM measurement process first requires the generation of a modulated reference signal  $x(t)$  that the measured signal  $y(t)$  is compared with, where the modulation format is selected to maximize the data throughput rate based on channel conditions and the constraints of the communication system protocol. Quadrature amplitude modulation (QAM) format is commonly-used in digital communication systems, and a QAM voltage signal  $v(t)$  has two components, in-phase  $v_i(t)$  and quadrature  $v_q(t)$ , which are modulated by orthogonal carriers as shown in (2.1) from [37].

$$v(t) = v_i(t)\cos(2\pi f_c t) - v_q(t)\sin(2\pi f_c t) \quad (2.1)$$

A digital bit sequence is mapped to a discrete set of amplitude states for  $v_i(t)$  and  $v_q(t)$  that correspond to unique amplitude and phase states of  $v(t)$ . These represent a collection of

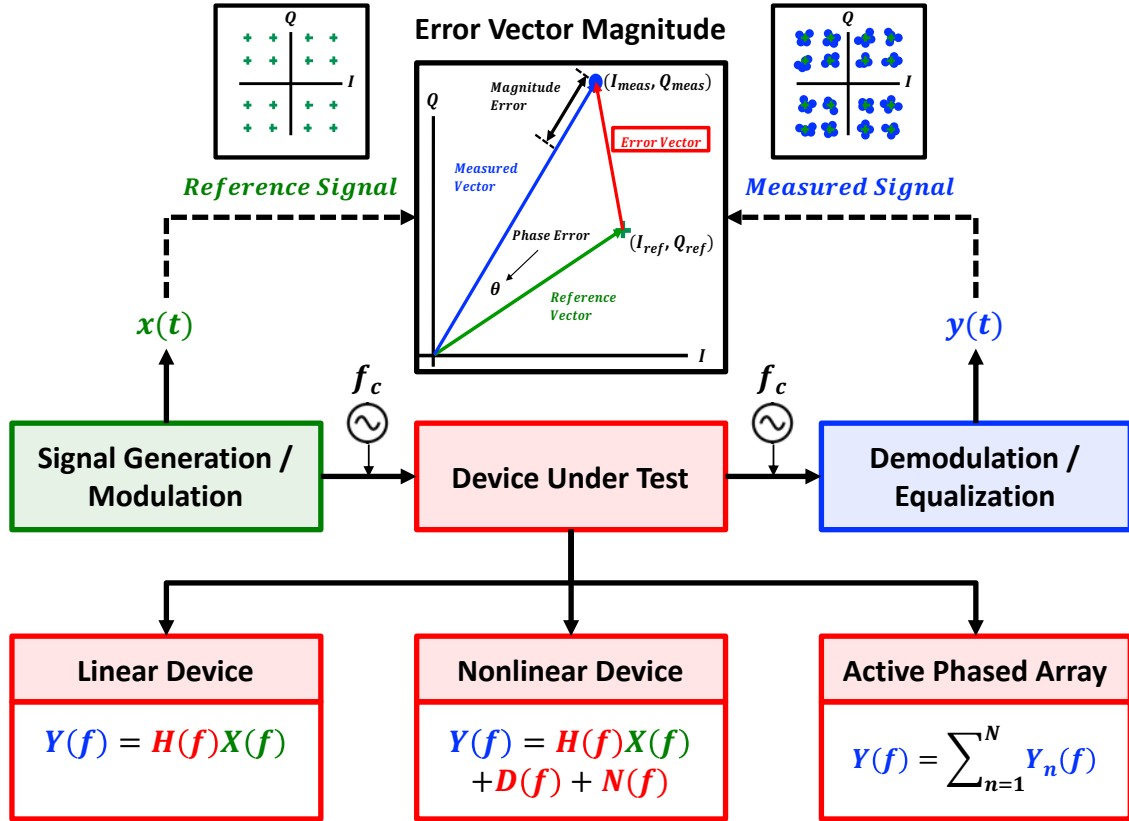


Figure 2.1 Block diagram of a generic EVM measurement system. In this single-carrier QAM representation, a QAM-modulated baseband signal  $x(t)$  is generated, upconverted to carrier  $f_c$ , transmitted through a device or OTA channel under test, and demodulated at the receiver to obtain  $y(t)$  with frequency spectrum  $Y(f)$ . This spectrum is represented as a sum of linear component  $H(f)X(f)$ , nonlinear distortion  $D(f)$ , and noise  $N(f)$  as described in Section 2.3.

symbols in the complex IQ plane as shown in Fig. 2.1. The number of unique symbols is modulation order  $M = 2^{N_b}$ , where  $N_b$  is the number of bits represented by each symbol. A 16-QAM signal has  $M = 16$  symbols, each corresponding to a different sequence of  $N_b = 4$  bits. Allowing  $v_i(t)$  and  $v_q(t)$  to take the form of rectangular pulses, with amplitude states held constant over each symbol period, would result in sharp edges and large bandwidths. Pulse-shaping filters such as the root-raised cosine filter (RRC) are generally used to reduce bandwidth and adjacent channel power. The impulse response of a root-raised cosine filter has an amplitude of zero at integer multiples of the symbol period, eliminating inter-symbol interference (ISI) [11, 39]. Maximum achievable data rate  $R_{max}$  is limited by bandwidth  $B$  and  $SNR$  in accordance with Shannon's capacity theorem (2.2) from [11]:

$$R_{max} = B \log_2(1 + SNR) \quad (2.2)$$

Increasing bandwidth allows a modulated test signal to make more-refined amplitude and phase transitions at a fixed symbol rate, and enables the use of higher-ordered modulation formats which maximize data throughput rate and spectral efficiency. The maximum permissible modulation order is limited by the SNR however, because decreasing amplitude and phase differences between the unique symbols increases the probability of error in the demodulated symbols. As a result, 3GPP has standardized EVM limits for 5G NR based on modulation order [48], as shown in Table 1.1. When the received symbols are only corrupted by additive white Gaussian noise (AWGN) and the number of measured symbols  $N$  is very large, the EVM and can be approximated from SNR as shown in (2.3) [41–44]:

$$EVM \approx \sqrt{\frac{1}{SNR}} \quad (2.3)$$

Transmitting a QAM signal with hundreds of MHz or GHz of bandwidth on a single carrier  $f_c$  is not practical, however: Frequency-selective fading from multipath in millimeter-wave channels results in nonuniform amplification of the frequency components and causes ISI that cannot be compensated without complex and expensive equalizers. Instead, multicarrier modulation schemes such as orthogonal-frequency division multiplexing (OFDM) are utilized to transmit parallel streams of QAM symbols on multiple orthogonal subcarriers, each occupying a small fraction of the complete OFDM signal bandwidth. Each of the subcarriers experiences flat-fading with a uniform frequency amplification, which can be compensated with a simple, single-tap equalizer [49]. This resilience against multipath fading and tolerance of simplified receiver circuits has led to widespread adoption of OFDM for wideband digital communication systems [49, 50]. However, OFDM signals also have certain undesirable properties, such as their large peak-to-average power ratios (PAPR) [49–51]. Power amplifiers transmitting OFDM signals must have large dynamic range or operate at a large back-off to limit nonlinear

distortion as a result. Operating at a large back-off reduces power-added efficiency (PAE) and EIRP, but is at times necessary to reduce EVM [17, 23, 51]. Researchers are proactively addressing this problem by designing advanced millimeter-wave power amplifiers that balance linearity and power efficiency demands [51], analyzing linearity with alternative multicarrier modulation formats [52], and applying digital pre-distortion (DPD) techniques [53].

### 2.1.2 Signal Impairments from a Device Under Test

The amplitude and phase of modulated reference symbols  $x(t_n)$  differ from those of the measured symbols  $y(t_n)$  as a result of measurement system noise and other types of signal impairments. Six types of impairments in communication systems are described in [38] and listed in Table 2.1, each of which can be categorized as either a linear or nonlinear form of distortion. Because passive antennas behave as linear and time-invariant (LTI) systems, their wideband response to an applied voltage signal  $x(t)$  with frequency spectrum  $X(f)$  can be modeled as a transfer function  $H(f)$  or impulse response  $h(t)$  [54–57]. The far field spectrum  $Y(f)$  of a transmitting antenna can be represented as shown for the linear DUT in Fig. 2.1:  $Y(f) = H(f)X(f)$ , where  $H(f)$  is the antenna’s normalized vector effective length. Antennas cause linear distortion when transfer function amplitude  $|H(f)|$  and group delay  $t_d$  are not constant across the channel bandwidth. Nonlinear devices such as power amplifiers create an additional distortion component  $D(f)$  which, like noise  $N(f)$ , is not linearly-correlated with input signal spectrum  $X(f)$  [35, 39]. In the absence of external sources of interference,  $D(f)$  represents intermodulation products of  $X(f)$  due to nonlinear amplification or mixing in transceiver circuits, as indicated in Table 2.1. The absorber materials lining the interior of OTA antenna test chambers are designed to minimize reflections, such that multipath effects are negligible. However, in indoor and outdoor propagation environments, reflections and diffractions from electrically-large objects will cause multiple copies of the transmitted signal to take different physical paths from the transmitter to the receiver, each with its own complex frequency response  $H_n(f)$ . Linear distortion from passive antenna transmission and multipath is typically removed by an equalizer before calculating EVM. Thus, maximizing SNR and limiting nonlinear distortion are of primary concern.

Table 2.1: Types of Signal Impairments in Communication Systems ( [38])

<b>Distortion</b>	<b>Expression</b>	<b>Example Sources</b>	<b>Description</b>
Linear	$ H(f)  \neq K$	Antennas, Filters	Non-uniform amplitude frequency response
Linear	$\angle H(f) \neq -\omega t_d$	Antennas, Filters	Non-uniform group delay versus frequency
Nonlinear	$D(f) \neq 0$	Amplifiers, Mixers	Intermodulation distortion from single channel
Nonlinear	$D(f) \neq 0$	External Sources	Intermodulation distortion from other channels
Nonlinear	$N(f) \neq 0$	Thermal ( $T \geq 0K$ )	Additive White Gaussian Noise (AWGN)
Linear	$\sum H_n(f)X(f)$	OTA Propagation	Multipath Signal Transmission

### 2.1.3 Channel Estimation and Equalization Methods

An equalization filter  $E(f) \approx 1/H(f)$  is obtained by estimating channel response  $H(f)$  and implemented in either the time domain or frequency domain. Time domain equalizers such as minimum mean square error and decision feedback equalizers are realized in digital signal processing with finite impulse response (FIR) filters, consisting of a series of delay units and complex weighting coefficients which are periodically updated in response to dynamic channel conditions [11, 50, 58]. Time domain equalizers face challenges in the era of wideband millimeter-wave communication systems. In multipath channels with high delay spread, a larger number of channel taps are required to eliminate ISI, raising demand for memory and processing power [11]. Furthermore, the ADC sampling rate must be increased proportionally with the signal data rate, and the equalizer must perform the time delays and multiplication operations faster [50]. In frequency domain equalizers, the channel response estimate is generally obtained with the aid of cyclic prefix, symbols repeated at the beginning and end of each data sequence, and intermittent transmission of pilot subcarriers. Two commonly-applied methods are OFDM and single-carrier frequency domain equalization (SC-FDE) [11, 50]. In general, channel equalization is performed with a receiver which has no awareness of the applied input signal  $x(t)$ . Such is the case for the single channel vector signal analyzers (VSAs) used to demodulate the measured signal in some EVM measurements, as described in Section 2.2 and shown in Fig. 2.2. However, EVM measurements can also be performed with a multi-channel vector network analyzer which measures input and output signals

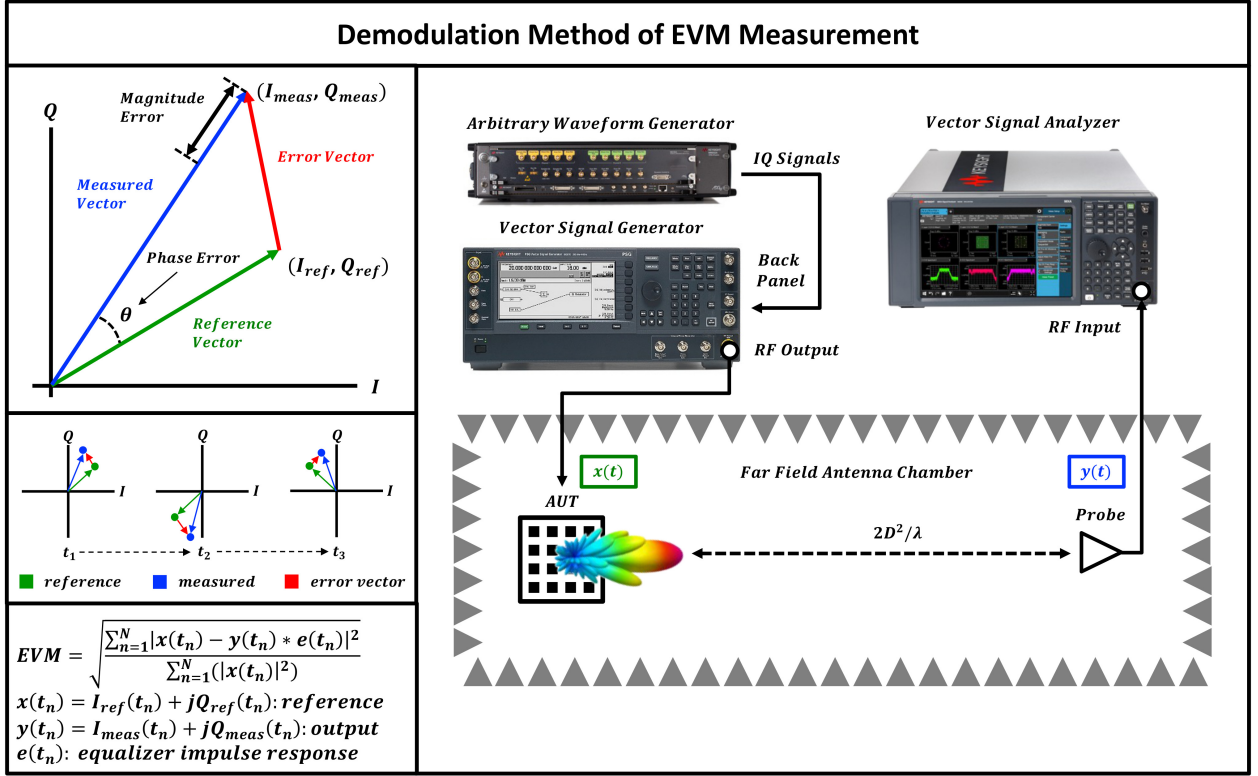


Figure 2.2 EVM far field measurement system based on the demodulation method. An AWG generates a baseband IQ signal which is upconverted to the carrier frequency via the VSG and applied to the AUT port. A VSA is used to demodulate and equalize the signal measured by the probe before computing EVM.

simultaneously and leverages awareness of the input signal to perform frequency domain equalization, as described in Section 2.3 and shown in Fig. 2.3. An ideal equalizer removes the linear distortion from channel response  $H(f)$  entirely, leaving only noise  $N(f)$  and nonlinear distortion  $D(f)$ . If the signal is not equalized, the amplitude and delay distortion shown in Table 2.1 (with constants  $K$  and  $t_d$ ) will remain and result in a higher EVM.

## 2.2 EVM Measurements via Time Domain Demodulation

The EVM of a two port network representing the DUT is classically defined as a time domain measurement representing the RMS value of error vectors evaluated from the difference between the DUT output signal  $y(t)$  and input signal  $x(t)$  at  $N$  symbol instances, as shown in (1.2), and is expressed as either a percentage or ratio on a dB scale. An example of an

error vector within the constellation diagram of a 16-QAM signal is shown in Fig. 2.1. A VSA is often used to demodulate the measured signal  $y(t)$  as shown in Fig. 2.2 [36–39]. For the case of a single-carrier QAM test signal, the  $I$  and  $Q$  amplitude pulses corresponding to data symbols are first filtered to reduce the signal bandwidth, resulting in  $x_i(t)$  and  $x_q(t)$  that only pass through the symbol amplitude states at specific time instances  $t_n$ . An IQ modulator generates passband signal  $x(t)$ , which is passed through a DUT that introduces noise and distortion, and an IQ demodulator obtains baseband signals  $y_i(t)$  and  $y_q(t)$ . These signals are sampled at the symbol rate, filtered to eliminate ISI and out-of-band distortion, and normalized by their peak or RMS amplitudes to compensate for the linear channel gain. Because it lacks direct access to the DUT input signal, the VSA estimates applied input signal  $x(t)$  from measured signal  $y(t)$ , such that reference symbols  $x(t_n)$  become the ideal  $M - QAM$  symbols nearest to the demodulated symbols  $y(t_n)$  [34, 38]. Time-alignment of input and output signals is performed by cross-correlation [39], and a uniform phase shift is typically applied to  $y(t)$  to derotate the constellation [36]. Further corrections such as compensating for IQ imbalance and frequency offset can also be implemented [39]. After time-alignment and equalization, EVM is calculated as shown in (1.2). Thus far, the EVM measurements of millimeter-wave phased arrays reported in the literature have been based on digital demodulation with VSAs as shown in Fig. 2.2, but demodulation of the wideband modulated signals deployed in millimeter-wave systems is difficult to achieve because digitizing such signals and computing fast Fourier transforms (FFT) for frequency domain analysis requires significant memory and processing power [35, 36, 40]. Increasing signal bandwidth also raises the noise floor and the minimum distortion EVM component that can be measured [59]. Because the ideal reference signal generated from by the VSA is only an estimate of the DUT input signal  $x(t)$ , vector errors resulting from the signal generator and DUT distortions cannot be distinguished. Therefore, EVM measurements with a VSA should not be considered an accurate characterization of DUT distortion unless signal generator errors are negligible. Finally, if signal distortion is high enough to yield error vectors spanning multiple symbols, the registered EVM will be erroneously low due to reference estimation from nearest ideal symbols [35, 39]. Consequently, researchers have explored alternative methods of measuring

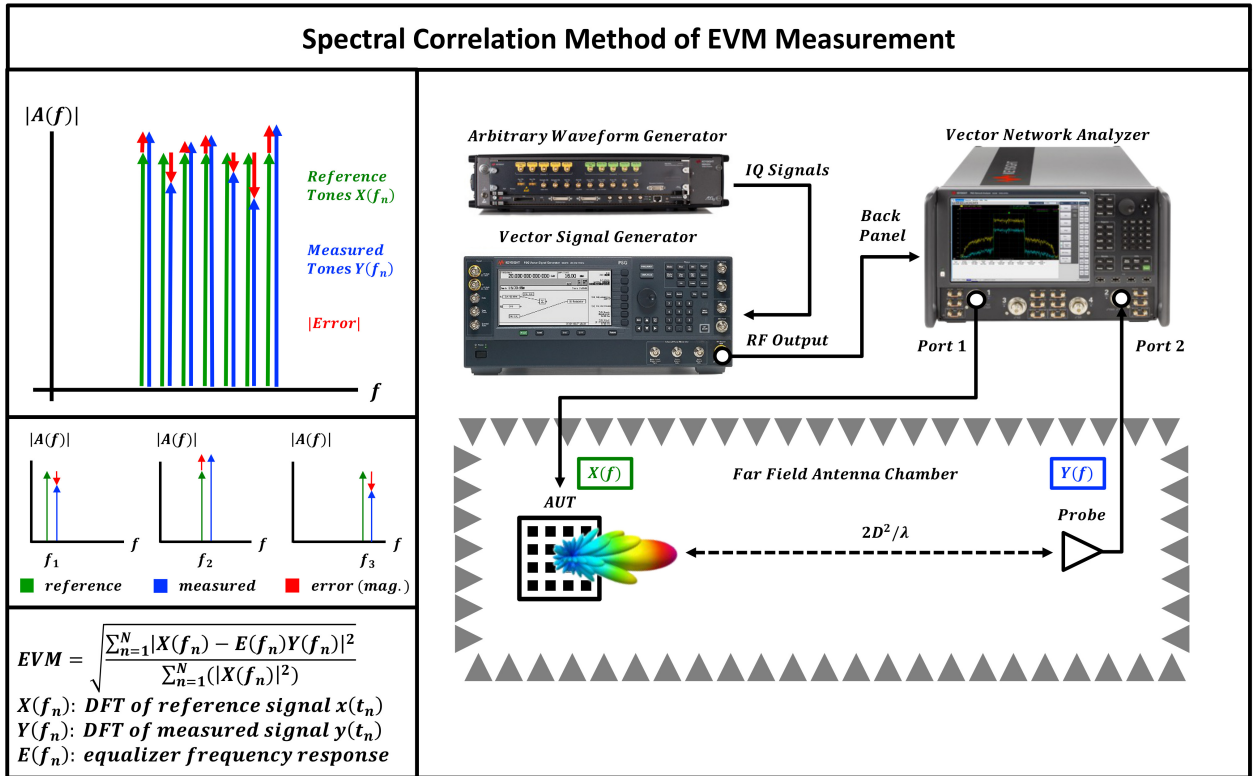


Figure 2.3 EVM far field measurement system based on the spectral correlation method. The VNA spectrum analyzer is used to compute the spectral correlation components ( $S_{XX}$ ,  $S_{YY}$ ,  $S_{XY}$ ) and perform frequency domain equalization  $E(f) \approx 1/H(f)$  for the signal measured by the probe before computing EVM.

or estimating EVM in the frequency domain.

## 2.3 EVM Measurements via Frequency Domain Spectral Correlation

A method of estimating EVM based on frequency domain analysis of DUT input and output signal spectra has recently been proposed and implemented in VNA-based measurements of nonlinear devices such as power amplifiers and mixers [34,35,60]. A modulated test signal with specific properties is required to facilitate EVM estimation directly in the frequency domain: The test signal  $x(t)$  must be periodic and measured over an integer multiple of the periods. It must also satisfy the Nyquist sampling condition, such that  $x(t)$  has a band-limited frequency

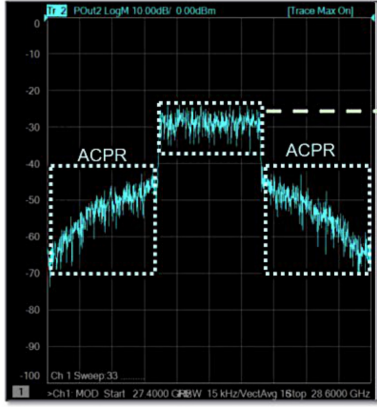


spectrum  $X(f)$  which can be represented as a discrete Fourier series. This allows for the application of Parseval's power theorem to formulate a frequency domain EVM equation (2.4) that is equivalent to the time domain equation (1.2), where  $E(f_n)$  is the equalization filter [35, 39].

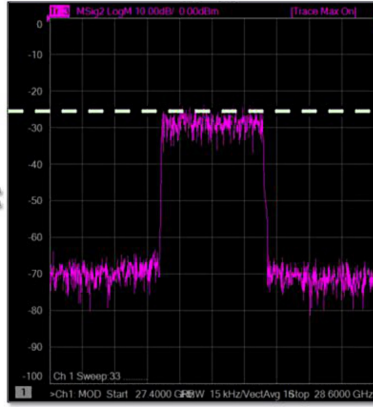
$$EVM = \frac{\sqrt{\sum_{n=1}^N |X(f_n) - E(f_n)Y(f_n)|^2}}{\sqrt{\sum_{n=1}^N |X(f_n)|^2}} \quad (2.4)$$

The summation of (2.4) is for  $N$  tones spanning the bandwidth of input signal spectrum  $X(f)$ , rather than for  $N$  symbol times in (1.2). Using a multi-channel VNA to capture both the DUT input signal spectrum  $X(f)$  and output signal spectrum  $Y(f)$  simultaneously removes the burden of accurate time alignment and resampling that exists in the demodulation process. Fig. 2.3 shows a far field EVM measurement system based on spectral correlation with a VNA. Because the VNA spectrum analyzer measures the signal applied to the DUT  $x(t)$  directly on one of its receivers rather than estimating the ideal reference symbols from the DUT output signal  $y(t)$ , signal generator errors will not be embedded in the EVM. This, combined with the application of VNA calibration techniques that eliminate RF cables and connector errors, leads to more accurate characterization of the DUT distortion [34, 35, 38, 39]. Moreover, VNAs can acquire the frequency spectrum of wideband signals over multiple coherent acquisitions with a narrowband filter as long as the test signal period is known, as demonstrated in [61]. The VNA measurement noise floor can therefore be lowered by either reducing the filter bandwidth or applying vector averaging techniques at the expense of longer frequency sweeps [35, 39]. An equalization filter  $E(f) \approx 1/H(f)$  compensating for DUT linear distortion is acquired by decomposing output signal spectrum  $Y(f)$  into a part  $H(f)$  that is linearly-correlated with the input signal spectrum  $X(f)$  and a nonlinear part  $D(f)$ , as shown in Fig. 2.4. In this model,  $H(f)$  is the best linear approximation (BLA) of the DUT frequency response and  $D(f)$  is an independently-distributed random noise source with zero mean and standard deviation  $\sigma_D$  that represents the DUT nonlinear stochastic distortion. A separate nonlinear component  $N(f)$  can also be included to represent additive measurement noise

*Output Signal Spectrum:*  
 $Y(f)$



*Linear Component:*  
 $H(f)X(f)$



*Nonlinear Component:*  
 $D(f)$

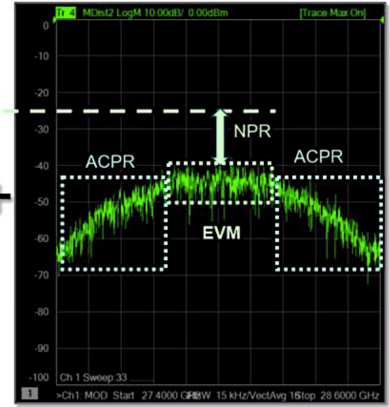
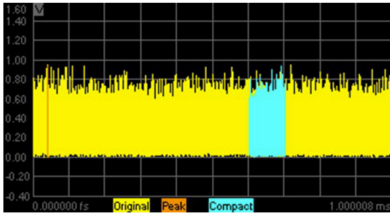
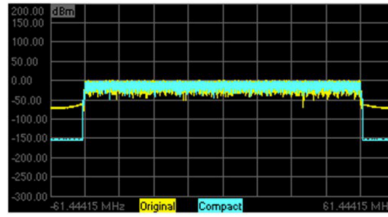


Figure 2.4 Decomposition of output signal spectrum  $Y(f)$  of a power amplifier into linear part  $H(f)X(f)$  and nonlinear part  $D(f)$  using a PNA-X Vector Network Analyzer [63].

*Original Test Signal:* ■  
*Compact Test Signal (CTS):* ■



*Power Spectral Density (PSD)*



*Complimentary Cumulative Distribution Function (CCDF)*

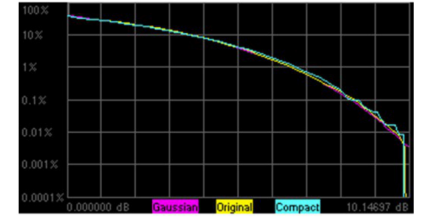


Figure 2.5 Compact test signal generation on a PNA-X Vector Network Analyzer. The CTS (blue) is extracted from a longer original time domain signal (yellow) and filtered to eliminate spectral leakage. The PSD and CCDF of the original signal and CTS are shown to be very similar [63]. See details in Section 2.2.

as shown in Fig. 2.1 [41,62]. The separation of linear and nonlinear frequency components is achieved by calculating the following spectral correlation quantities from [35]:  $S_{XY}$ , the cross-spectral density of  $X(f)$  and  $Y(f)$ ;  $S_{XX}$ , the PSD of input signal spectrum  $X(f)$ ; and  $S_{YY}$ , the PSD of output signal spectrum  $Y(f)$ . Then  $H(f) = S_{XY}(f)/S_{XX}(f)$  is the BLA of the DUT frequency response and  $D(f) = Y(f) - H(f)X(f)$  is the nonlinear distortion spectrum with PSD  $S_{DD}(f) = S_{YY}(f) - |S_{XY}(f)|^2/S_{XX}(f)$ . The EVM is calculated as shown in (2.5), which is equivalent to (2.4) with an equalization filter  $E(f) = 1/H(f)$ :

$$EVM = \frac{\sqrt{\sum_{n=1}^N S_{DD}(f_n)}}{\sqrt{\sum_{n=1}^N |H(f_n)|^2 S_{XX}(f_n)}} \quad (2.5)$$

When the modulation format does not require equalization, an un-equalized version of EVM can be obtained by letting  $E(f) = Ge^{-2\pi f_n \tau}$ , where  $G$  is the reciprocal of the average linear gain, and  $\tau$  is the group delay [35]. A BLA model with linear gain  $H(f)$ , nonlinearity variance  $\sigma_D^2(f)$ , and noise variance  $\sigma_N^2(f)$  provides an accurate characterization of the DUT frequency response in the mean-squared sense for test signals with the same power spectral density (PSD) and probability density function (PDF) [35, 62, 64]. Periodic, random-phase, signals having a sufficient number of tones can thus be designed with a PSD and PDF matching those of a specific modulation format such as OFDM [59]. This enables standard-independent EVM measurement and the supplementation of compact test signals, which can be generated by extracting a small segment of a longer periodic signal that has fewer tones but approximately the same PSD and PDF, as shown in Fig. 2.5. Compact signals have already been utilized to emulate the PSD and PDF of OFDM signals in power amplifier EVM simulations and measurements [35, 65]. Spectral correlation therefore presents an attractive alternative to the conventional demodulation method for wideband millimeter-wave measurements.

## 2.4 EVM Measurements via Continuous Wave Stimulation

Finally, some researchers have attempted to develop closed-form expressions summing the estimated EVM contributions of independent transceiver impairments such as IQ imbalance, phase noise, and third-order nonlinearity. In [66] and [67], the transmitter model and EVM equation presented in Fig. 2.6 were used to examine the effects of different RF impairments such as gain, phase noise, and phase imbalance on the EVM. The effect of IQ imbalance and phase noise distributions based on both Gaussian and Tikhonov probability distribution functions were investigated in [66]. Another analytical expression for the EVM of a wideband OFDM transmitter that encompasses the frequency-dependent signal distortion caused

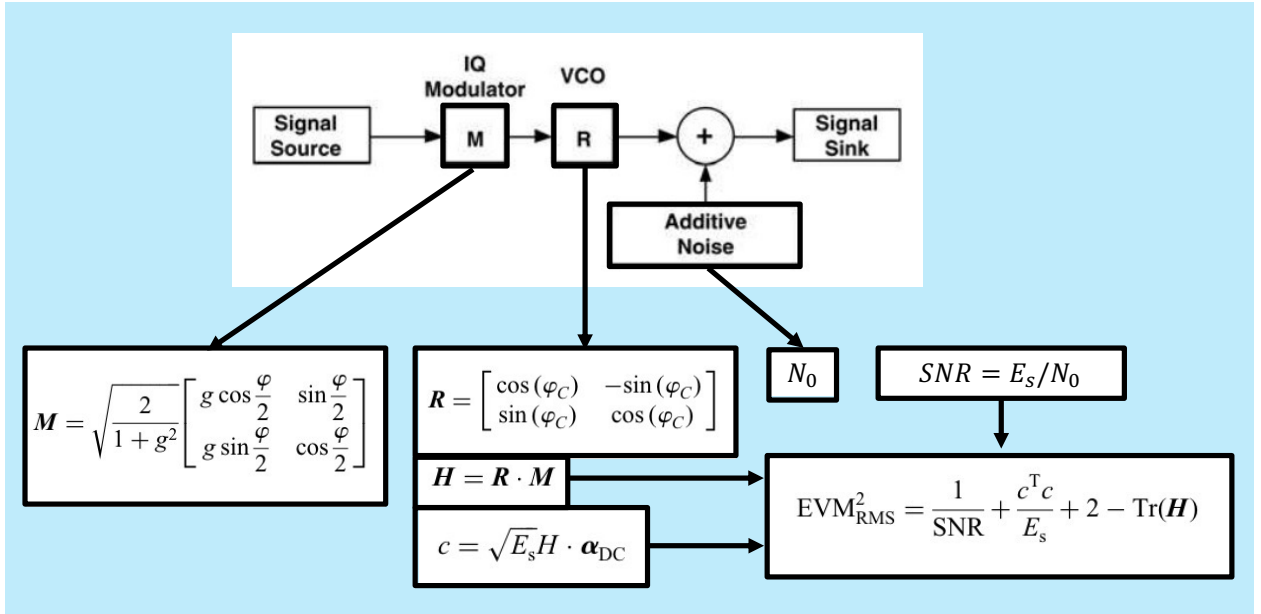


Figure 2.6 RF transmitter model and closed form EVM expression from [66]. It includes the distortion effects from an IQ modulator ( $M$ ) with gain ( $g$ ) and phase ( $\varphi$ ) imbalance and DC offset ( $\alpha_{DC}$ ) in the  $I$  and  $Q$  paths, a voltage-controlled oscillator ( $R$ ) with phase noise ( $\varphi_C$ ), and additive noise source ( $N_0$ ).

by IQ imbalance, phase noise, and power amplifier nonlinearity was derived in [68]. A statistical analysis of EVM due to phase noise, gain imbalance, and other signal distortions in OFDM systems was presented in [69]. A closed-form expression for the EVM of multicarrier modulated signals based on a memory polynomial power amplifier model with a clipping threshold was derived in [70]. The EVM expressions for RF transceivers are often root sum squares of multiple terms representing uncorrelated forms of signal distortion [67, 71]. This has motivated some researchers to determine if continuous wave (CW) signals can be substituted for wideband modulated signals to estimate each EVM component independently and reduce measurement cost [72–74]. In [73], for example, CW signals were used to estimate four EVM components representing group delay and amplitude distortion of the low-pass filter (LPF), IQ amplitude and phase imbalance (IR), and the local oscillator (LO) phase noise (PN) and leakage (LSR) as shown in (2.6):

$$EVM = [(1/SNR) + EVM_{LPF}^2 + EVM_{IR}^2 + EVM_{PN}^2 + EVM_{LSR}^2]^{1/2} \quad (2.6)$$

The total EVM in (2.6) is the sum of these EVM components squared. The DUT is assumed to operate linearly such that EVM contributions from amplitude-to-amplitude (AM-AM), amplitude-to-phase (AM-PM) and intermodulation distortion are negligible. In [75], the vector gain of a transistor as a function of both power and frequency was measured with CW signals and used to estimate EVM. While simulation and measurement results have shown good agreement with these closed-form EVM expressions, accurate analytical expressions for EVM of antennas and large active beamforming arrays are difficult to synthesize due to the OTA propagation and dynamic load modulation of the power amplifiers from mutual coupling.

## 2.5 Summary

This chapter presented a review of three fundamental signal processing steps embedded in all EVM measurements: generation of digital IQ-modulated signals, linear and nonlinear distortion of the modulated signal as it passes through the device under test, and channel estimation and equalization that can eliminate linear distortion effects. Three techniques for calculating the EVM were also reviewed: time domain demodulation, frequency domain spectral correlation, and CW stimulus estimation. While EVM is most often measured by demodulating the output signal of the DUT and calculating the complex difference between these measured symbols and those of an ideal constellation for the modulation format, an alternative is to calculate the EVM from the spectral correlation of input and output signal spectrums, which can be measured synchronously on a multi-port VNA. The advantages of the latter method were outlined and will be demonstrated in chapters 3, 4, and 5. EVM can also be estimated from the root sum square of uncorrelated CW-stimulated error components.

## CHAPTER 3

# Far Field EVM Characterization of Millimeter-Wave Antennas

### 3.1 Review of an UWB Transmission Model for Far Field Antenna Links

The far field radiation properties that are traditionally used to define the performance of passive antennas are not sufficient for characterizing their transient behavior and influence on the EVM of the received signal. One approach to modeling ultra-wideband (UWB) antenna transmission and reception in a free space link is to treat it as a linear and time-invariant (LTI) system with a transfer function  $H(f) = Y(f)/X(f)$  [54–57]. The complete transfer function of this link is represented in [54] as  $H(f) = H_{tx}(f)H_{ch}(f)H_{rx}(f)$  as shown in Fig. 3.1, where  $H_{tx}(f)$  relates generator output voltage  $V_G(f)$  across impedance  $Z_G$  to the radiated field of the transmitting antenna  $\vec{E}_{rad}$ ,  $H_{ch}(f)$  relates  $\vec{E}_{rad}$  to the incident field  $\vec{E}_{inc}$  at the receiving antenna, and  $H_{rx}(f)$  relates  $\vec{E}_{inc}$  to the voltage  $V_L(f)$  measured across the load impedance  $Z_L$ . These three transfer functions are expressed in (3.1)–(3.3) and cascaded for the complete transfer function  $H(f) = H_{tx}(f)H_{ch}(f)H_{rx}(f) = V_L(f)/V_G(f)$  from [54], where  $d$  is the antenna separation distance,  $c_0$  is the speed of light,  $R_0$  is a reference impedance typically equal to  $50\Omega$ , and the harmonic time dependence  $e^{-j\omega t}$  is assumed.

$$\vec{H}_{tx}(f) = \frac{j\omega}{c_0} \sqrt{\frac{R_0}{Z_G}} \vec{H}_{N_{tx}}(f, \theta_t, \phi_t) \quad (3.1)$$

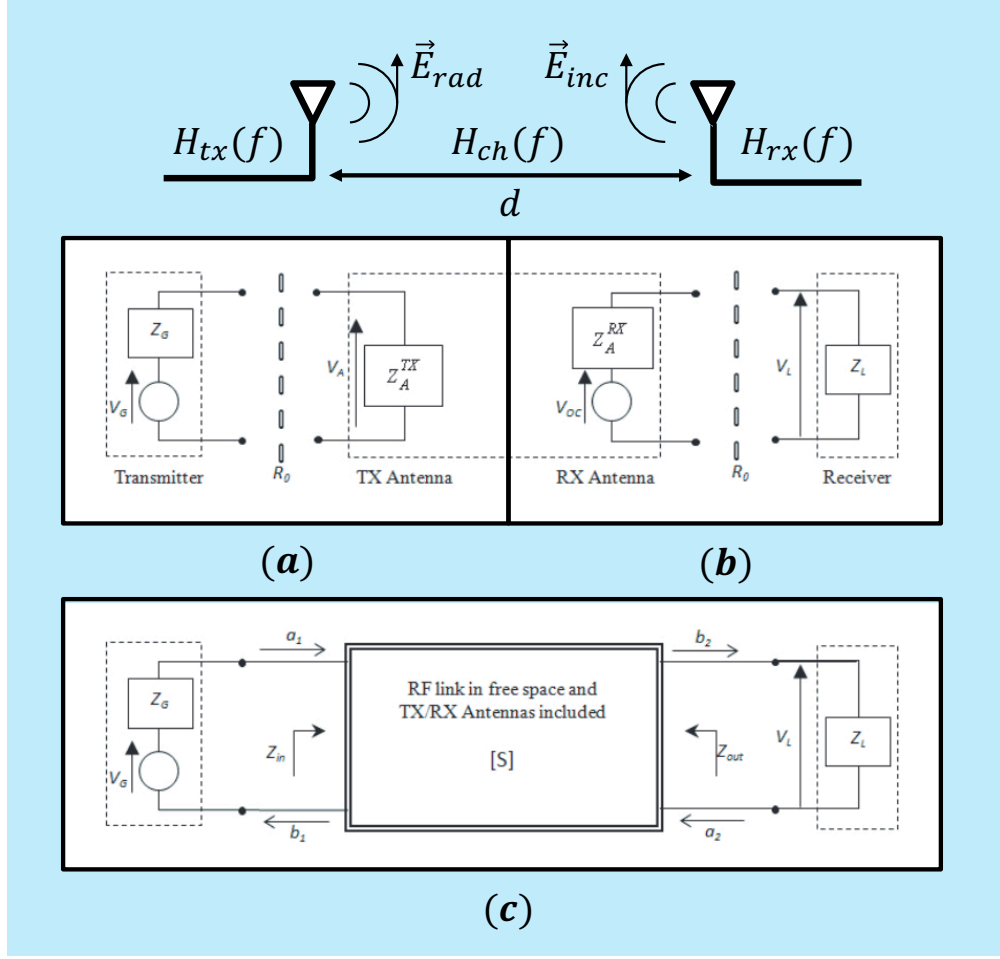


Figure 3.1 An UWB antenna transmitter and receiver model with transfer function  $H(f) = H_{tx}(f)H_{ch}(f)H_{rx}$  based on (3.1), (3.2), and (3.3) from [54]: Thevenin equivalent circuit model of the (a) transmitter and (b) receiver, and (c) two-port S-parameter network with incident and reflected voltage waves.

$$\vec{H}_{ch}(f) = \frac{e^{-j\omega d/c_0}}{4\pi d} \quad (3.2)$$

$$\vec{H}_{rx}(f) = \sqrt{\frac{Z_L}{R_0}} \vec{H}_{N_{rx}}(f, \theta_r, \phi_r) \quad (3.3)$$

In (3.1) and (3.3),  $\vec{H}_{N_{tx}}(f, \theta_t, \phi_t)$  and  $\vec{H}_{N_{rx}}(f, \theta_r, \phi_r)$  are normalized vector effective lengths

for the transmitting and receiving antennas respectively, which are defined in terms of vector effective lengths  $\vec{H}_{E_{tx}}(f)$  and  $\vec{H}_{E_{rx}}(f)$  and antenna reflection coefficients  $\Gamma_{tx}(f)$  and  $\Gamma_{rx}(f)$  as shown in (3.4)-(3.7) from [54].

$$\vec{H}_{N_{tx}}(f, \theta_t, \phi_t) = \frac{1 - \Gamma_{tx} \sqrt{Z_G Z_0}}{2} \frac{\vec{H}_{E_{tx}}(f, \theta_t, \phi_t)}{R_G} \quad (3.4)$$

$$\vec{H}_{N_{rx}}(f, \theta_r, \phi_r) = \frac{1 - \Gamma_{rx} \sqrt{Z_L Z_0}}{2} \frac{\vec{H}_{E_{rx}}(f, \theta_r, \phi_r)}{R_L} \quad (3.5)$$

$$\Gamma_{tx}(f) = \frac{Z_A^{TX} - Z_G^*}{Z_A^{TX} + Z_G^*} \quad (3.6)$$

$$\Gamma_{rx}(f) = \frac{Z_A^{RX} - Z_L^*}{Z_A^{RX} + Z_L^*} \quad (3.7)$$

In (3.4)-(3.7),  $Z_0$  represents free space impedance ( $377\Omega$ ) and \* is used to denote the complex conjugate. Vector effective length is generally defined for a receiving antenna, and relates the electric field vector of an incident plane wave  $\vec{E}_{inc}$  to the open circuit voltage  $V_{OC}$  generated at the receiving antenna as shown in (3.8). However, the reciprocity principle can be applied to derive an equivalent vector effective length expression for a transmitting antenna that relates input current  $I(f)$  to the radiated electric field  $\vec{E}_{rad}$  at far field distance  $d$ , as shown in (3.9) [54, 55].

$$\vec{H}_{E_{rx}}(f, \theta_r, \phi_r) = \frac{V_{OC}(f)}{\vec{E}_{inc}(f, \theta_r, \phi_r)} \quad (3.8)$$



$$\vec{H}_{E_{tx}}(f, \theta_t, \phi_t) = \frac{\vec{E}_{rad}(f, \theta_t, \phi_t)}{I(f)} \left[ \frac{j\omega Z_0}{4\pi d c_0} e^{-j\omega d/c_0} \right]^{-1} \quad (3.9)$$

The free space antenna link transfer function  $H(f)$ , based on the complex and directionally-dependent vector effective length functions, is a comprehensive model of the signal transmission between two passive antennas separated by a far field distance  $d$  that characterizes changes in both the amplitude and phase of the voltage signal frequency components between the transmitting antenna terminals  $V_G(f)$  and the receiving antenna terminals  $V_L(f)$ . It includes the effect of the antenna polarizations, orientations  $(\theta_t, \phi_t, \theta_r, \phi_r)$ , and impedance matching characteristics. The vector effective lengths should be defined as a sum of two orthogonal polarizations  $\vec{H}_{tx,rx}(f, \theta, \phi) = \vec{H}_{co}(f) + \vec{H}_{cr}(f)$  to model the superposition of plane waves for any polarization. The link transfer function can also be defined in terms of the scattering parameters of the equivalent circuit model from Fig. 3.1(c), as presented in (3.10), (3.11), and (3.12) from [54].

$$H(f) = \frac{1 - \Gamma_G(f)}{1 - S_{11}(f)\Gamma_G(f)} \frac{S_{21}(f, \theta, \phi)}{2} \frac{1 + \Gamma_L(f)}{1 - S_{22}(f)\Gamma_L(f)} \quad (3.10)$$

$$\Gamma_G(f) = \frac{Z_G(f) - R_0}{Z_G(f) + R_0} \quad (3.11)$$

$$\Gamma_L(f) = \frac{Z_L(f) - R_0}{Z_L(f) + R_0} \quad (3.12)$$

An equivalent time domain representation of a far field antenna link can be acquired by simply calculating the inverse Fourier transform of  $H(f)$  to derive the link impulse response  $h(t)$ . The LTI system model provides a unified frequency and time domain approach to far field antenna link characterization. It was used in [55] to determine the transient performance of

three antenna designs in terms of envelope width and ringing duration from S21 measurements. In [57], a pole-residue model of a Vivaldi antenna's vector effective length was synthesized and used to estimate the gain at multiple frequencies spanning 1-12 GHz.

However, the greatest utility of this LTI antenna link model is the opportunity that it affords for the joint optimization of wideband modulation schemes and antenna designs capable of transmitting such signals with minimal distortion, as suggested in [55]. Linear distortion results from variations in the amplitude response  $|H(f)|$  for frequency components of the applied voltage signal  $V_G(f)$  and deviations of the phase response  $\angle H(f)$  from negative linear slope  $-\omega t_d$  as shown in 2.1.2. Researchers have developed LTI antenna link simulation models to estimate the effects of one or both of these linear distortion components on the un-equalized EVM of single-carrier QAM signals. Amplitude distortion of a 16-QAM signal transmitted by the 28 GHz microstrip patch antenna from [76] and captured by a far field receiver at a distance of 1.0 meter was demonstrated in [77] and is presented in section 3.2.

While it was not applied to EVM estimation of a modulated signal, a similar simulation model for wideband linear signal distortion of a free space antenna link was developed in [79]. First, the unit step responses  $u_t(t)$  of a printed Vivaldi antenna were acquired by applying a unit step excitation current to the discrete port and simulating the time-domain radiated fields for two orthogonal polarizations at far field probe positions. The impulse responses  $h_t(t)$  for each far field probe position and polarization were then found by differentiating  $u_t(t)$ , and the impulse responses for the antenna in receive mode were found by applying the reciprocity principle. These impulse response functions were used to predict the transmission of a Gaussian pulse by two nearly-identical Vivaldi antennas, and the results compared well with measurements. An extension of the UWB free space antenna link model from [79] to multipath channels was demonstrated in [80], where ray-tracing simulations were used to estimate a superposition of weighted impulse responses representing a group of dominant signal paths.

Another technique for simulating the EVM of a far field link between nearly-identical antennas, based on the finite impulse response (FIR) filter models derived from two port S-parameter measurements, was demonstrated in [78], [81], and [82]. In [78], the IFFT of

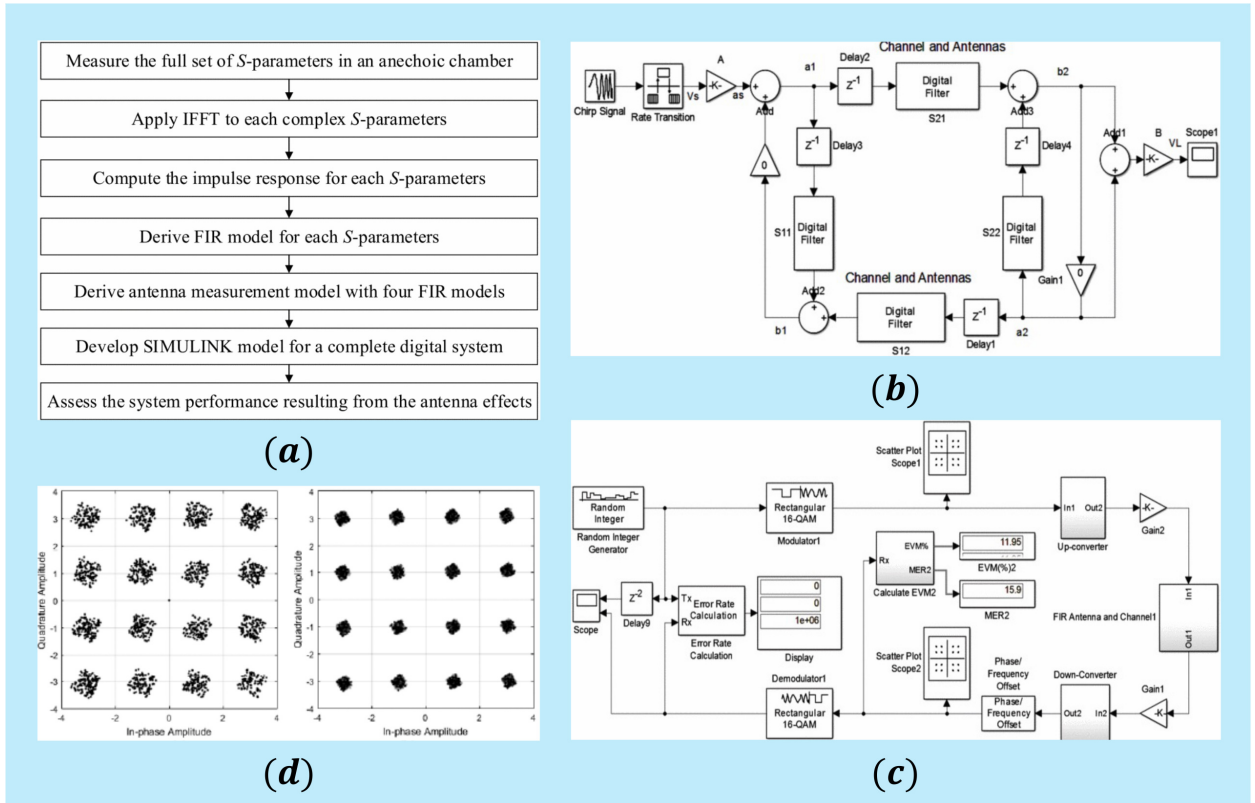


Figure 3.2 EVM simulation for far field antenna link based on FIR filter models matching measured two-port  $S$ -parameters [78]: (a) block diagram of the digital communication system modeling process, (b) FIR filter and (c) antenna link simulation models, and (d) constellation diagrams of scattered symbols from the simulated transmission of 16-QAM signals at 2.0 GHz (left) and 6.0 GHz (right).

the antenna link  $S$ -parameters measured in an anechoic test range was used to synthesize FIR filter models that were imported into a SIMULINK model of a 16-QAM communication system to determine how variations in the antenna gain and group delay across the signal bandwidth influenced un-equalized EVM and BER performance, as shown in Fig. 3.2. The same approach was used to compare simulated EVM of far field antenna links for different propagation environments [81], frequency bands [78], and antenna orientations [82]. For two antennas with low loss and negligible nonlinear phase,  $S$ -parameters can also be estimated from equivalent circuit models designed and optimized to match the measured  $S_{11}$  results [78, 82].

Full-wave simulations can be used to determine the radiation characteristics of antenna designs without making the kinds of simplifying assumptions required for the synthesis of a

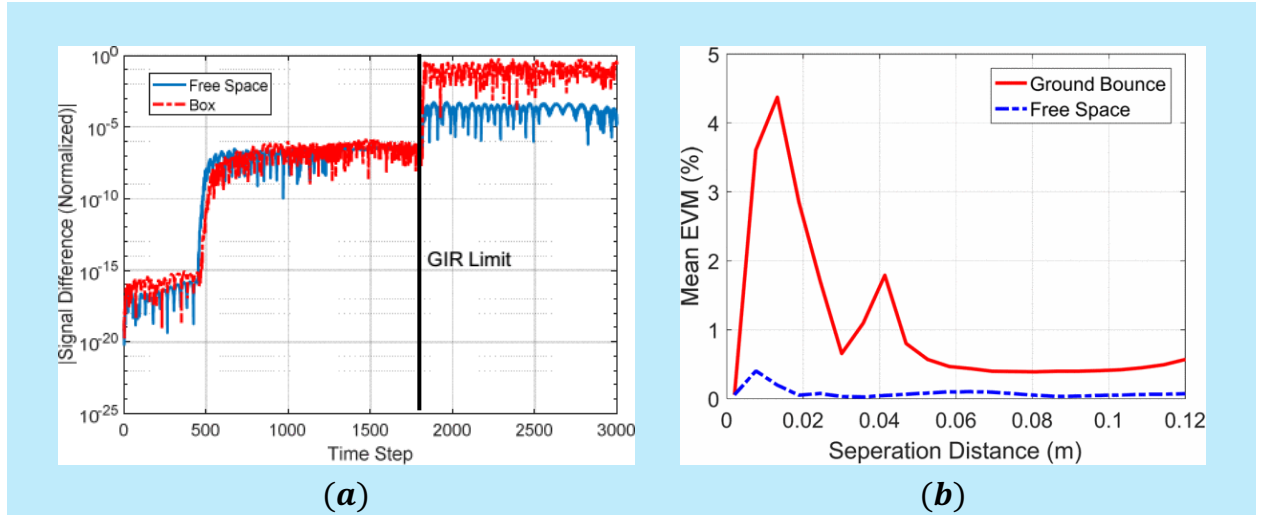


Figure 3.3 EVM simulation for a far field antenna link based on the grid impulse response (GIR) method [83]: (a) GIR error relative to direct FDTD simulation, which is less than  $10^{-6}$  for time steps less than or equal to the number used in the full FDTD simulation (GIR Limit), and (b) EVM as a function of antenna separation distance for free space propagation and propagation with an infinite ground plane placed beneath the two dipoles.

circuit model. The authors of [82] used CST Microwave Studio to simulate S-parameters of two wideband printed monopoles separated by 50 cm, but they also acknowledged that the computational resource requirements for adaptive meshing could limit the accuracy of such electrically-large simulations. One potential solution was presented in [83]: The grid impulse response (GIR) of a finite difference time domain (FDTD) solver was obtained via simulations with delta function excitation signals and subsequently convolved with a 16-QAM signal to estimate the EVM of a link between two identical 90 GHz dipole antennas as a function of the separation distance, both in free space and over an infinite ground plane. The resulting EVM was then calculated for these cases as shown in Fig. 3.3. The main advantage of this method is that the FDTD simulation used to obtain the GIR can be performed much faster than one in which a modulated source signal is used. The development of computationally-efficient full-wave simulation schemes such as these improves the accuracy and efficiency of estimating UWB amplitude and phase response from far field antenna links. While this linear distortion is generally removed with an equalizer, as described in 2.1.3, the combined effects of antennas, phase shifters, and nonlinear components such as power amplifiers embedded in active phased

arrays are not easily distinguished and must be examined with advanced simulation models. Section 4.1 focuses on the design and application of such models by representative researchers for far field EVM analysis.

## 3.2 EVM Simulation of Amplitude Distortion from a Microstrip Patch Antenna

### 3.2.1 Introduction

In this section, we describe a method for determining the effect of antenna frequency response on EVM using full-wave analysis and apply it to far field transmission of 16-QAM signals by a microstrip patch antenna as a representative array element. EVM is a measure of modulated signal distortion and is calculated as shown in (1.2), where  $x(t_n)$  represents the complex voltage signal applied to the transmitting antenna input terminals and  $y(t_n)$  represents the voltage signal generated at the terminals of a lossless and co-polarized receiving antenna having a vector effective length magnitude of one, such that radiated electric far field  $|\vec{E}_{rad}|$  in V/m at receiving antenna location  $(x_r, y_r, z_r)$  is converted directly to voltage [35]. The far field polarization is represented as *rad* and symbol time instances as  $t_n$ . The process used to obtain  $x(t)$  and  $y(t)$  is detailed in the following subsections.

### 3.2.2 Far Field Signal Transmission and Reception

The transmitter and receiver models that were implemented in MATLAB are presented in the block diagram of figure 3.4. A random bit sequence is generated and 16-QAM modulated to obtain ideal input signal  $x(t_n)$  with  $N = 1000$  data symbols. This large number of symbols relative to the signal modulation order  $M = 16$  ensures that the EVM from equation (1.2) is normalized to approximately the RMS value of the 16-QAM constellation. The input signal is up-sampled by a factor of 1000 and passed through an RRC transmit filter with a roll-off factor of  $\alpha = 0.4$ . The FFT of input signal  $x(t)$  yields frequency spectrum  $X(f)$ , as shown in figure 3.4, which is multiplied by the normalized antenna transfer function amplitude response

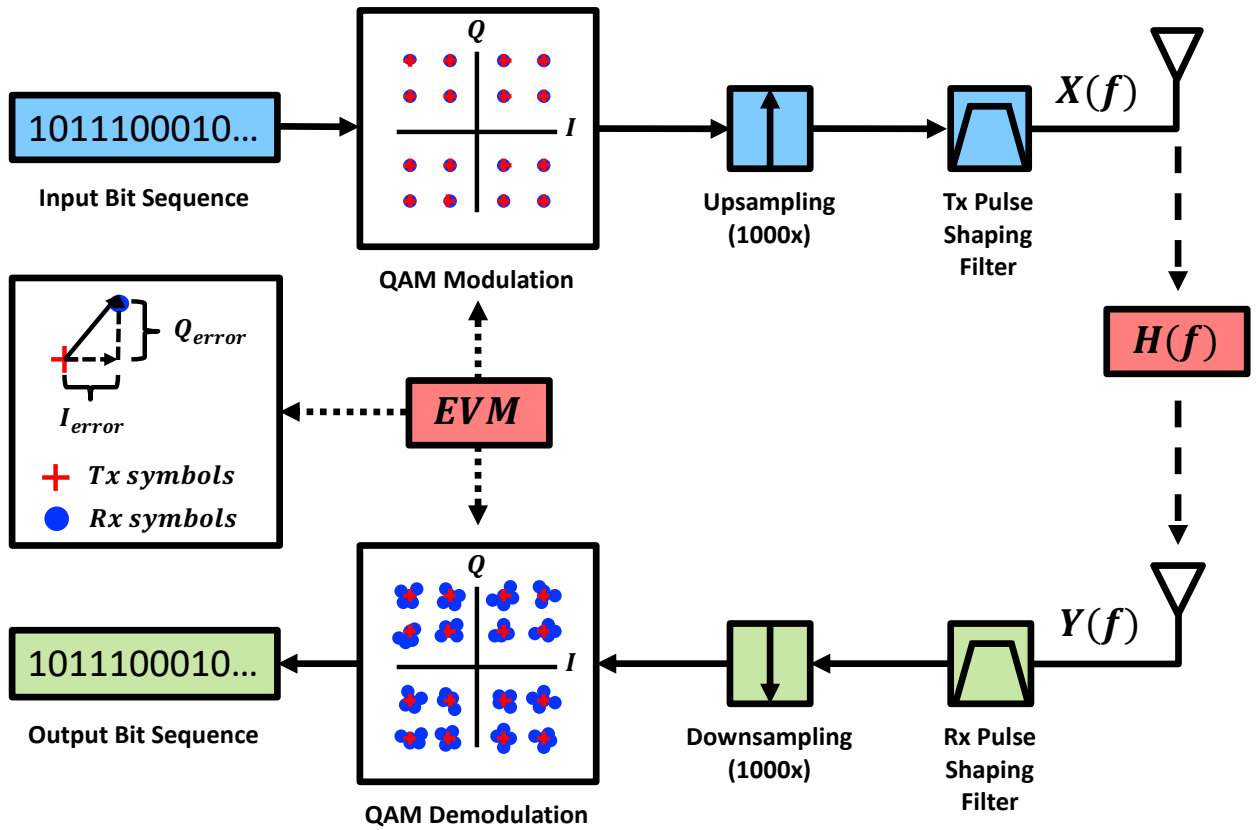


Figure 3.4 MATLAB transmitter and receiver block diagram illustrating EVM of a 16-QAM signal resulting from transmitting antenna frequency response  $H(f)$ . Error vectors point from transmitted symbols (red) to received symbols (blue) in the complex IQ plane highlighting the in-phase and quadrature components.

$|H(f)|$  to obtain the frequency spectrum  $Y(f)$  of the voltage signal received by the virtual antenna described in subsection 3.2.1, which is located one meter above the top surface of the microstrip patch centered at the coordinate system origin: That is,  $(x_r, y_r, z_r) = (0, 0, 1.0 \text{ m})$ . The IFFT of  $Y(f)$  provides the distorted complex voltage signal of the receiving antenna  $y(t)$ , which is passed through a RRC receive filter with the same properties as the transmit filter. The combined response of both filters is a raised cosine filter with zero ISI. The transmitted and received signals and normalized antenna transfer function are shown in Fig. 3.5.

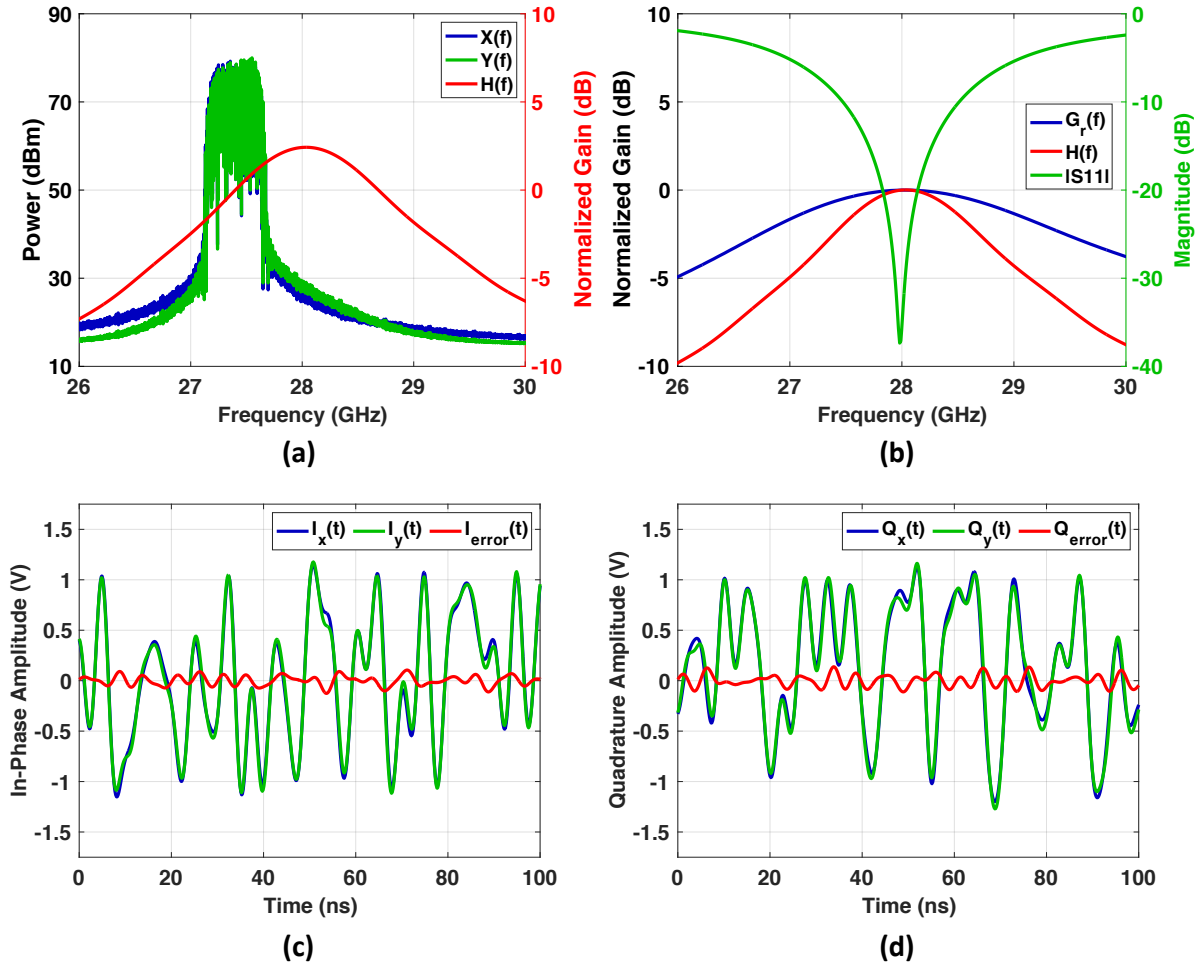


Figure 3.5 (a) Spectrum of the transmitted and received signals (blue and green respectively) and transfer function normalized to its magnitude at carrier frequency  $f_c = 27.4$  GHz. (b) Antenna realized gain (blue), transfer function normalized by its magnitude at  $f_c = 28.0$  GHz (red), and  $|S_{11}|$  of microstrip patch antenna (green). (c)-(d) In-phase and quadrature components of the 16-QAM transmitted and received voltage signals (blue and green) and resulting errors (red) after ideal down-conversion and transmission through the matched filter.

### 3.2.3 Antenna Transfer Function Derivation

The antenna transfer function amplitude response  $|H(f)|$  is defined as the magnitude of the output voltage spectrum at the receiving antenna terminals  $|Y(f)|$  divided by the magnitude of the input voltage spectrum applied to the transmitting patch antenna terminals  $|X(f)|$ :  $|H(f)| = |Y(f)|/|X(f)|$ . The transfer function is assumed to be independent of the excitation signal  $x(t)$ . In the analysis of section 3.2.4, it is always normalized to its magnitude at the carrier frequency  $f_c$ . While it is generally a function of receiving antenna position, only the boresight position described in section 3.2.2 is used in this analysis. Transfer function  $H(f)$  is obtained by performing a time domain simulation of the microstrip patch antenna in CST Microwave Studio and applying a Gaussian pulse voltage signal to the discrete port at the antenna feed. Since the microstrip patch antenna is linearly polarized in the  $\hat{x}$  direction, the magnitude of the spectrum of the  $\hat{x}$ -polarized radiated far field component  $|Y(f)| = |\vec{E}_x(f)|$  is used to determine the antenna transfer function amplitude response  $|H(f)| = |Y(f)|/|X(f)|$ .

### 3.2.4 EVM Results for Microstrip Patch Antenna

The EVM was calculated for 16-QAM signals with varying bandwidths and carrier frequencies as highlighted in figure 3.6. Carriers were selected to form a continuous band with an upper frequency limit of 28 GHz and a lower frequency limit that is offset by an integer multiple of the signal bandwidth (e.g. 27.9 GHz for bandwidth of 100 MHz) The EVM increases with signal bandwidth as expected because, as shown in Fig. 3.5(a), the peak-to-peak variation of  $|H(f)|$  is greater over larger frequency bands. Additionally, the EVM increases with carrier frequency offset from the 28 GHz resonant frequency of the microstrip patch antenna, due to the steeper slope of  $|H(f)|$  at these frequencies. While current 3GPP standards limit the channel bandwidth to 400 MHz in 5G FR2 bands [84], the expansion of channel bandwidth to multi-GHz has been considered for 5G and future high data rate wireless communication systems. Fig. 3.6 indicates that antenna bandwidth limits may impose significant distortion of digitally-modulated signals with large bandwidths and carrier frequencies far from that of the antenna resonance. Full wave analysis can therefore be used to determine the link voltage



Bandwidth	50 MHz	100 MHz	200 MHz	400 MHz
Carrier Frequencies $f_c$ (GHz): $f_{c_{50}} = 27.975$ $f_{c_{100}} = 27.95$ $f_{c_{200}} = 27.9$ $f_{c_{400}} = 27.8$				
<b>EVM</b>	<b>0.1%</b>	<b>0.3%</b>	<b>0.9%</b>	<b>3.1%</b>
Carrier Frequencies $f_c$ (GHz): $f_{c_{50}} = 27.925$ $f_{c_{100}} = 27.85$ $f_{c_{200}} = 27.7$ $f_{c_{400}} = 27.4$				
<b>EVM</b>	<b>0.2%</b>	<b>0.6%</b>	<b>2.1%</b>	<b>5.9%</b>
Carrier Frequencies $f_c$ (GHz): $f_{c_{50}} = 27.875$ $f_{c_{100}} = 27.75$ $f_{c_{200}} = 27.5$ $f_{c_{400}} = 27.0$				
<b>EVM</b>	<b>0.3%</b>	<b>0.9%</b>	<b>2.8%</b>	<b>5.4%</b>
Carrier Frequencies $f_c$ (GHz): $f_{c_{50}} = 27.825$ $f_{c_{100}} = 27.65$ $f_{c_{200}} = 27.3$ $f_{c_{400}} = 26.6$				
<b>EVM</b>	<b>0.3%</b>	<b>1.1%</b>	<b>3.1%</b>	<b>4.9%</b>

Figure 3.6 Constellation diagrams and EVM of 16-QAM signals with bandwidths and carrier frequencies  $f_c$  representative of 5G FR2. The carrier frequencies are selected such that rows form a continuous band with 28 GHz upper limit.

gain versus frequency for the desired transmitting antenna and receiving antenna orientations. This voltage gain function can then be used to estimate the EVM of a modulated test signal transmitted and received by the two antennas modeled in this far field free space antenna link.

### 3.3 EVM Simulation of Linear Distortion from a Far Field Ka-Band Conical Horn Link

The EVM simulation approach applied to far field transmission of a 16-QAM test signal by a linear microstrip patch antenna in section 3.2 provides insight on the effects of amplitude distortion on received signal quality for narrow-band antennas. However, this EVM analysis, based on the normalized vector effective length derived from full-wave simulation, is limited by a few simplifying assumptions. First, it only accounts for the amplitude response of the port voltage to radiated far field transfer function, equivalent to  $|\vec{H}_{tx}(f)|$  from equation (3.1). However, this transfer function is complex, and variations in group delay versus frequency can cause significant signal distortion if uncorrected at a far field receiver. This is demonstrated by comparing the EVM of a 16-QAM signal resulting from the boresight phase response of a spline-profiled, Ka-band conical horn antenna with that of the microstrip patch antenna from section 3.2, as shown in Fig. 3.7. The group delay  $t_d$  is calculated from the complex transmitting antenna transfer function  $|\vec{H}_{tx}(f)|e^{-j\phi_{tx}(f)}$ , which is extracted directly from a full-wave time domain simulation of the antenna, and normalized to its magnitude at carrier frequency  $f_c$  as shown in (3.13). The steeper slope of the group delay response at frequencies near the patch resonance causes the EVM of the 16-QAM signal to increase dramatically, such that received symbols cannot be distinguished in the complex IQ-plane. In contrast, the conical horn has a more-uniform group delay response across the 400 MHz signal bandwidth, which results in a lower distortion and EVM, such that demodulated symbols of the 16-QAM signal received in the far field are discernible in the constellation diagram as shown in Fig. 3.7.

$$t_d(f) = \frac{-d\phi_{tx}(f)}{df} \frac{1}{360^\circ} \quad (3.13)$$

While the complete transmitting antenna transfer function is a superposition of two orthogonal radiated far field components, as described in section 3.1, we assume a high linear polarization

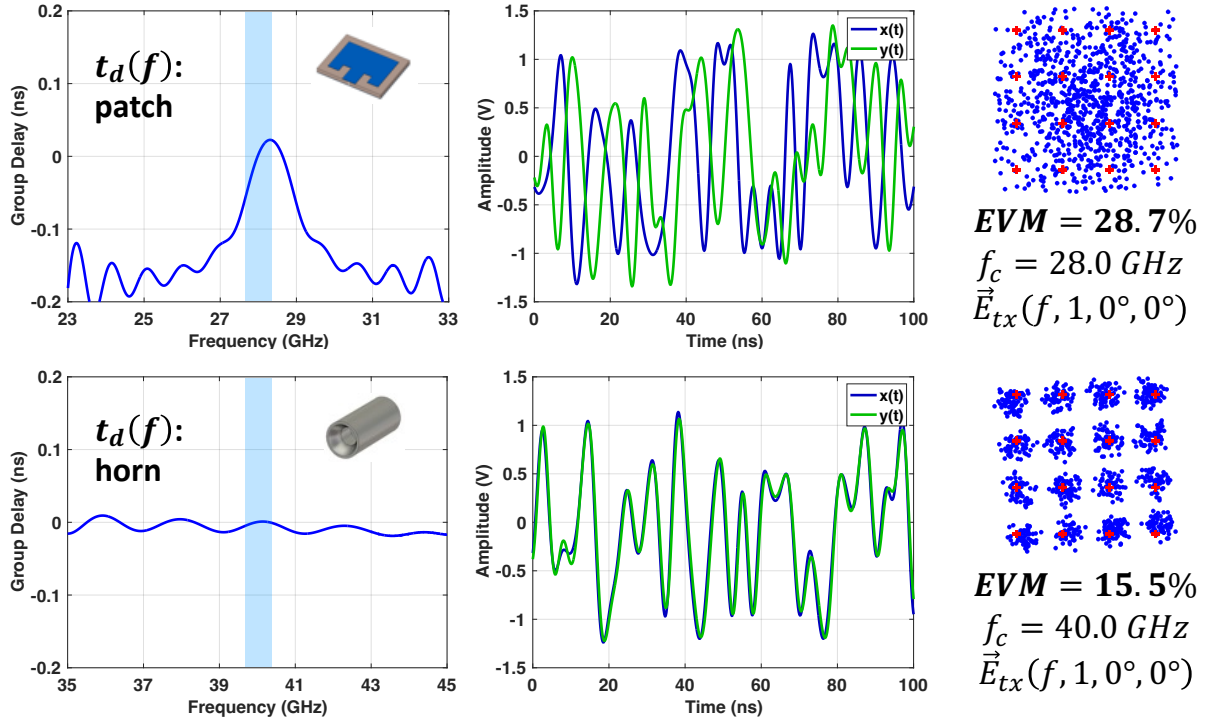


Figure 3.7 Group delay and EVM comparison of a microstrip patch and conical horn antenna, where  $x(t)$  is the input voltage signal applied to the transmitting antenna and  $y(t)$  is the received voltage signal of the ideal far field receiver described in section 3.2.

purity for all three of the transmitting test antennas and only account for the co-polarized far field component such that  $\vec{H}_{tx}(f) = \vec{H}_{co}(f)$  and  $|\vec{H}_{cr}(f)| = 0$ . For all of the EVM simulations except those for the Ka-band conical horn in Fig. 3.8(a), the co-polarized and cross-polarized components of the antenna transfer functions correspond to the Ludwig 3 horizontal and vertical far field components respectively, which are defined in terms of the antennas' spherical coordinates  $(\theta, \phi)$  as shown in equations (3.14a) and (3.14b). This assumption of negligible cross-polarization contribution to the far field received signal quality was maintained for all of the following EVM simulations, and was justified on the basis of the co-to-cross polarization ratio  $|\vec{E}_H(f_c, 0^\circ, 0^\circ)|/|\vec{E}_V(f_c, 0^\circ, 0^\circ)| \geq 20$  dB for most far field observation angles  $\theta \leq 60^\circ$  in the two principle planes  $\phi = 0^\circ, 90^\circ$  for all three of the linearly-polarized antennas utilized in these simulations. These antennas are highlighted in Fig. 3.8 with their reference coordinate systems and co-to-cross polarization ratio over the full spherical range ( $0^\circ \leq \theta \leq 180^\circ, 0^\circ \leq \phi \leq 360^\circ$ ).

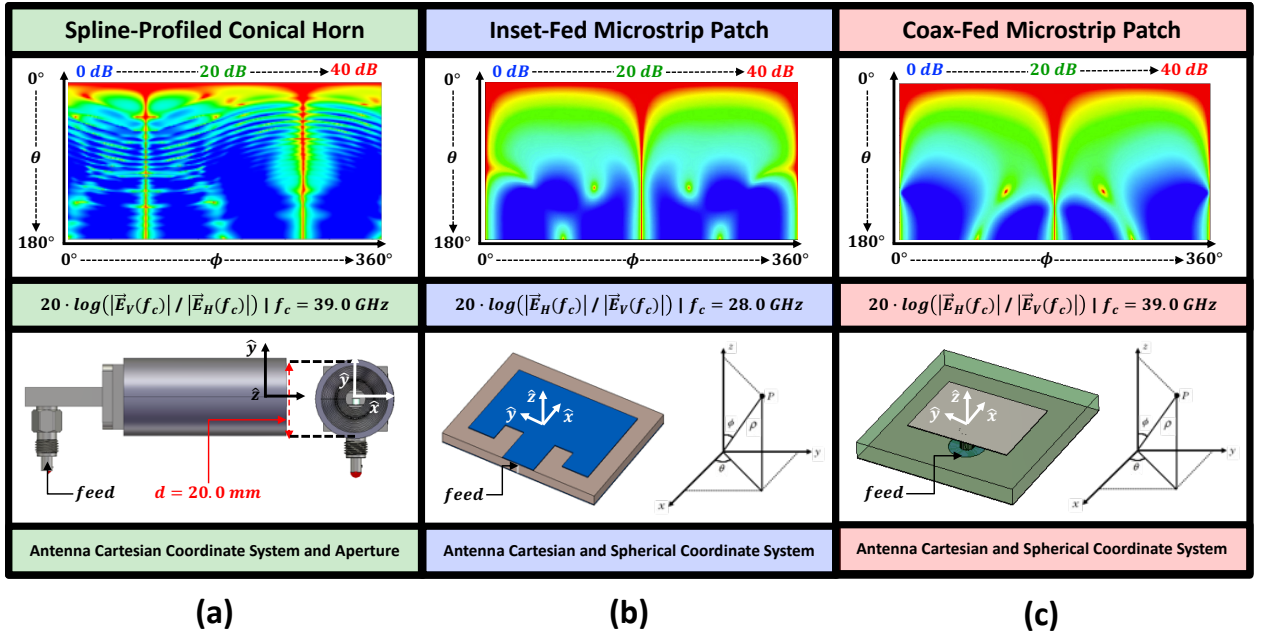


Figure 3.8 Transmitting test antennas simulated in CST Studio for the far field link EVM simulations in this dissertation with coordinate systems and co-to-cross polarization ratio  $20 \log(|\vec{E}_H(f_c)| / |\vec{E}_V(f_c)|)$  vs. far field angle  $(\theta, \phi)$ : (a) spline-profiled conical horn antenna [85] used in section 3.3-3.4, (b) inset-fed microstrip patch antenna used in section 3.2, and (c) coax-fed microstrip patch antenna used in section 4.2.

$$\vec{E}_H(\theta, \phi) = \cos \phi \vec{E}_\theta - \sin \phi \vec{E}_\phi \quad (3.14a)$$

$$\vec{E}_V(\theta, \phi) = \sin \phi \vec{E}_\theta + \cos \phi \vec{E}_\phi \quad (3.14b)$$

The carrier frequencies of 28 and 39 GHz correspond to two different 5G FR2 bands as well as the resonant frequencies of the patch antennas shown in Fig. 3.8(b) and (c) respectively. An additional limitation of the EVM simulations for the microstrip patch of Fig. 3.8(b) from section 3.2 is that the analysis was limited to a far field receiver located at boresight. The EVM simulations for the conical horn of Fig. 3.8(a) presented in this section will include other far field angles to show how variation in the transmitting antenna frequency response with respect to far field observation angle  $(\theta_t, \phi_t)$  affects the received signal quality. Finally, the EVM simulation from section 3.2 does not include the receiving antenna response  $H_{rx}(f)$ .

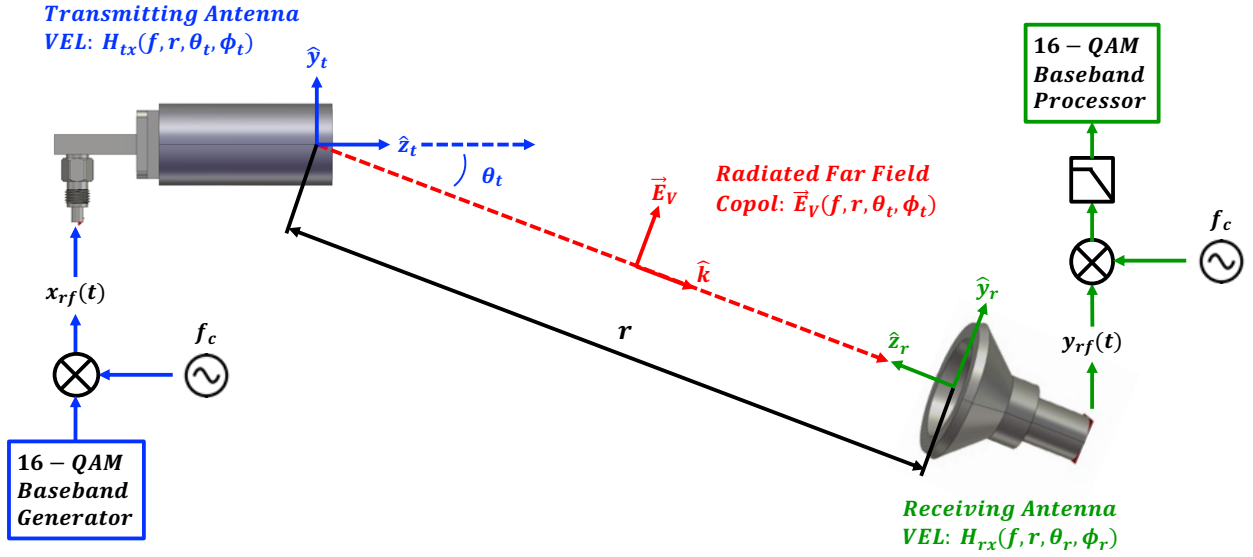


Figure 3.9 Line-of-sight far field link between the two Ka-band conical horn antennas used for the EVM simulation. For each far field observation angle of the transmitting horn ( $\theta_t, \phi_t$ ), the receiving horn is oriented to match the polarization of the radiated  $\vec{E}_V$  component from the transmitting antenna along its boresight direction ( $\hat{z}_r$ ). A distance of  $r = 1.0$  m, approximately  $20D^2/\lambda_c$  with  $\lambda_c = 7.7$  mm, separates the antennas. The vector effective lengths (VEL) of the antennas ( $H_{tx}, H_{rx}$ ) are obtained through independent full-wave simulations to determine the complete input voltage ( $x_{rf}(t)$ ) to output voltage ( $y_{rf}(t)$ ) transfer function  $H(f, r, \theta_t, \phi_t)$ .

This section describes a more-advanced simulation model for the EVM resulting from both the amplitude and phase distortion of a far field link between two passive antennas. This is achieved by deriving the complete voltage transfer function  $H(f, r, \theta_t, \phi_t)$  from complex, broadband far field probe data acquired via independent full-wave analysis of the transmitting and receiving antennas.

In addition to the linear distortion introduced by this far field antenna link, the nonlinear distortion from finite SNR at the receiver and its influence on the EVM with and without channel equalization are also demonstrated. Moreover, an estimate of the transfer function  $H_{est}(f)$  is acquired via the spectral cross-correlation method described in section 2.3, and its reciprocal is applied as an equalization filter  $E(f)$  to determine the equalized-EVM of the received signal. In all of these respects, the simulation model for far field antenna links from this section represents an improvement on the simplified model that was applied in section

3.2. An overview of this enhanced EVM simulation procedure is presented as a sequence of nine steps that are illustrated in Figs. 3.10, 3.12, and 3.16. The 16-QAM signal modulation, matched filtering, and demodulation components of the MATLAB link model shown in Fig. 3.4 were adopted for EVM simulations of transmission and reception by the Ka-band conical horn antennas shown in Fig. 3.9. The main differences between the far field antenna link models from Fig. 3.4 and Figs. 3.10, 3.12, and 3.16 pertain to the derivation of the complex voltage transfer function  $H(f, r, \theta_t, \phi_t)$ . The spline-profiled conical horn from Fig. 3.8(a), which was designed and manufactured by colleagues from the UCLA Antenna Lab [85], was used as the transmitting antenna under test (AUT). The receiving conical horn shown in Fig. 3.9 was designed in accordance with the data sheet dimensions for the WR-28 scalar feed horn model [86] that was used in the CATR measurements described in section 3.4, in order to facilitate a comparison of the simulated and measured EVM data for a single-carrier 16-QAM test signal. A virtual link between these two horn antennas, showing their coordinate systems and relative orientations for a single E-plane far field probe position, is presented in Fig. 3.9.

The first step of the process is to perform independent time domain full-wave simulations for the two antennas using CST Microwave Studio in order to characterize their respective vector effective length functions  $H_{tx}(f, r, \theta_t, \phi_t)$  and  $H_{rx}(f, r, \theta_r, \phi_r)$ . For the transmitting horn, a group of ideal far field probes is generated and used to extract the amplitude and phase of the Ludwig 3 field components from equations (3.14b) and (3.14a) at each probe position. The ideal probes were positioned  $r = 1.0$  m away from the origin of the antenna's coordinate system at elevation angles  $\theta_t = 0^\circ : 5^\circ : 60^\circ$  and azimuth angles  $\phi_t = 0^\circ, 90^\circ$  in the two principle planes. A customized CST Studio control script was developed to automate the generation of ideal far field probes and the extraction of complex field data from these ideal probes. The far field probe results were automatically normalized by the complex spectrum of the default Gaussian pulse voltage signal that was applied to the antenna discrete port, which yields the transfer function shown in equation 3.15a. For the receiving horn, the transfer function from equation 3.15b is the voltage spectrum at the load impedance  $V_L(f)$  divided by the incident co-polarized electric field radiated by the transmitting antenna  $E_{Vtx}(f, r, \theta_t, \phi_t)$ , such that the antenna link voltage spectrum transfer function  $V_L(f)/V_{Gtx}(f)$  is obtained by

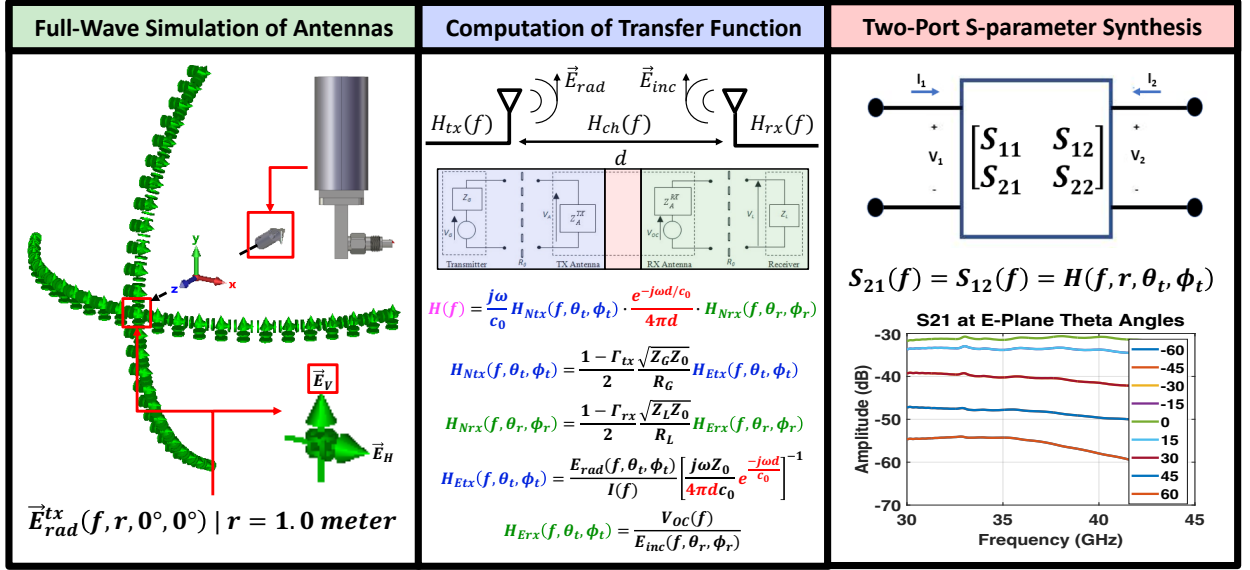


Figure 3.10 Steps 1-3 of the EVM simulation process implemented for the Ka-band conical horn of Fig. 3.8(a): (1) full-wave simulation of test antenna in CST Microwave Studio, where the frequency response of radiated Ludwig 3 E-field components are captured at various far field angles  $(\theta, \phi)$ , (2) computation of the antenna link voltage transfer function  $H(f, r, \theta_t, \phi_t)$  from the VEL of the transmit and receive antennas obtained in step (1), and (3) synthesis of symmetric ( $S_{11} = S_{22} = 0, S_{21} = S_{12} = H(f, r, \theta_t, \phi_t)$ ) two-port s-parameters in MATLAB, which provide a complete description of the linear distortion from the far field antenna link. The  $S_{21}(f)$  for the E-plane observation angles  $\theta_t = [-60^\circ : 15^\circ : 60^\circ], \phi_t = 0^\circ, 180^\circ$  are shown.

cascading transmitting and receiving antenna transfer functions as shown in equation 3.15c.

$$H_{tx}(f, r, \theta_t, \phi_t) = \frac{E_{Vtx}(f, r, \theta_t, \phi_t)}{V_{Gtx}(f)} \quad (3.15a)$$

$$H_{rx}(f, r, \theta_r, \phi_r) = \frac{V_L(f)}{E_{Vtx}(f, r, \theta_r, \phi_r)} = \frac{E_{Vrx}(f, r, \theta_r, \phi_r)}{V_{Grx}(f)} \frac{Z_{Grx}}{Z_0} \frac{4\pi r c_0}{j\omega e^{-j\omega r/c_0}} \quad (3.15b)$$

$$H(f, r, \theta_t, \phi_t) = H_{tx}(f, r, \theta_t, \phi_t) \cdot H_{rx}(f, r, \theta_r, \phi_r) \quad (3.15c)$$

Transfer function  $H_{rx}(f)$  from equation 3.15b is not acquired directly from the full-wave simulation, since the receiving horn is excited with a generator voltage  $V_{Grx}(f)$  supplied by the discrete port object. Instead, it is acquired through an application of the reciprocity principle,

which relates the generator voltage to radiated far field transfer function of an antenna in the transmitting mode to the incident plane wave to load voltage transfer function of the same antenna operating in the receiving mode. This relationship is highlighted in equations 3.1 and 3.3 from [54] and described in [55]. The  $j\omega/c_0$  term introduced to the transmitting mode equivalent of the vector effective length, which is conventionally defined in the receive mode, and the channel response from equation 3.2 are therefore removed as shown in equation 3.15b. This equation holds true under the assumption that the generator impedance  $Z_{Grx} = 50\Omega$  used for the full-wave simulation of the receiving horn in the transmitting mode does not vary with frequency and is equivalent to a fictitious load impedance  $Z_L$  for the virtual antenna link. To isolate the effect of variation in the transmitting horn's transfer function  $H_{tx}(f, r, \theta_t, \phi_t)$  on the EVM of the signal received by the WR-28 feed horn, the latter antenna is assumed to always be oriented toward the transmitting horn such that it is  $\vec{E}_V$  polarization-matched to the transmitting horn and aligned to receive along its boresight direction  $(\theta_r, \phi_r) = (0^\circ, 0^\circ)$  as shown in Fig. 3.9. Consequently, the transfer function in equation 3.15c only varies as a function of the far field angle of the vector pointing from the transmitting antenna to the receiving antenna  $(\theta_t, \phi_t)$ . The calculation of this transfer function from 3.15c for the far field probe data constitutes the second step of this EVM simulation process as shown in Fig. 3.10.



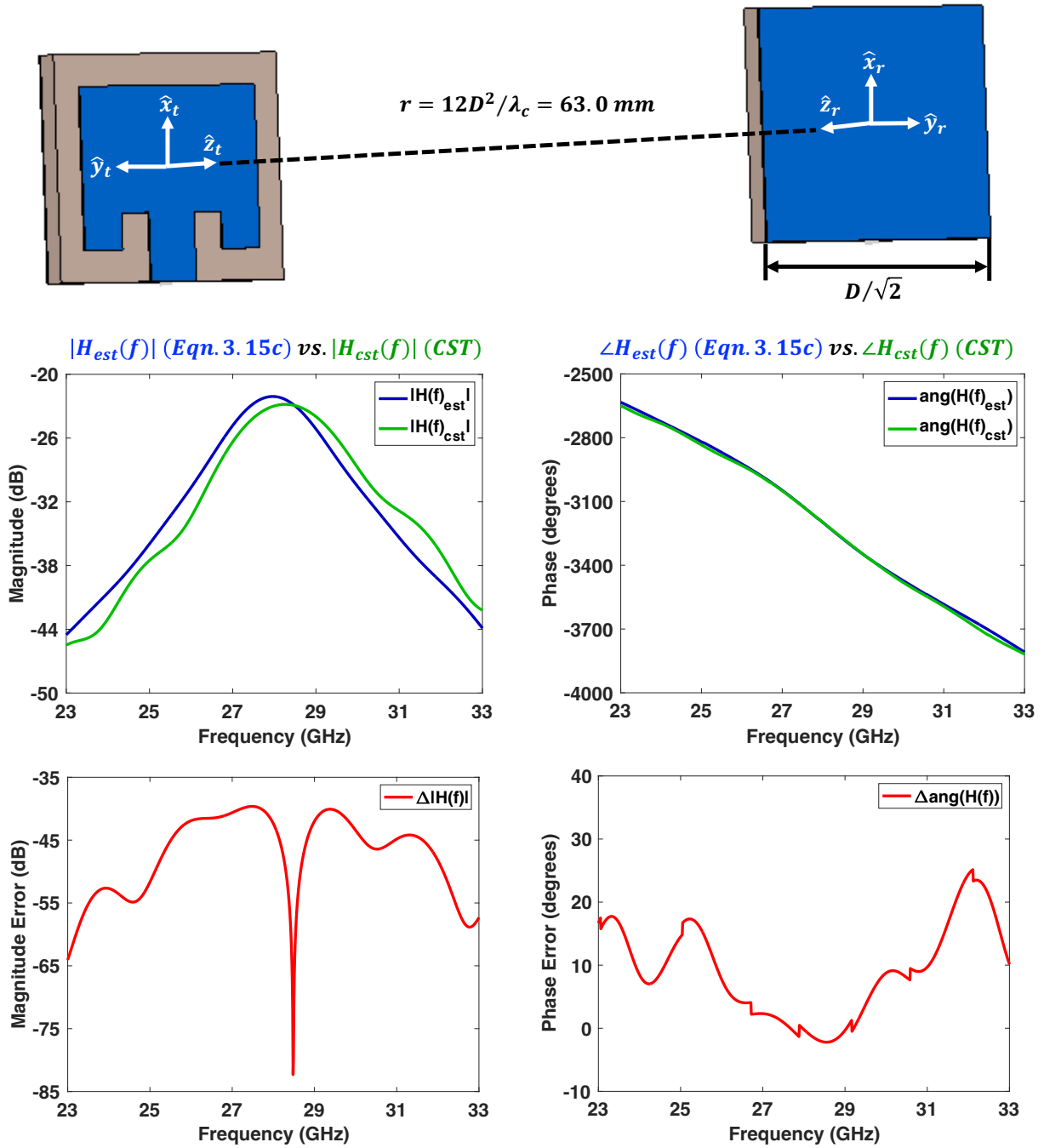


Figure 3.11 Comparison of the antenna link transfer functions estimated from the inset-fed microstrip patch far field probes using equation 3.15c (blue) and simulated directly in CST Microwave Studio with both transmitting and receiving antennas (green). The antennas were separated by  $r = 63.0 \text{ mm}$  and positioned to transmit and receive along boresight as shown.

To confirm the accuracy of the antenna link voltage gain from equation 3.15c, which was derived from independent full-wave simulations of the antennas, a single full-wave simulation of the far field link between two copies of the microstrip patch of Fig. 3.8(b) was performed. The two patch antennas were separated by  $r = 12D^2/\lambda_c = 63.0$  mm, where  $D = 7.5$  mm is the diagonal dimension of the patch substrate, and oriented to transmit and receive along boresight ( $\theta_t, \phi_t, \theta_r, \phi_r = 0^\circ$ ) as shown in Fig. 3.11. The amplitude and phase of the antenna link voltage transfer function ( $S_{21}$ ) from this complete link simulation  $H_{cst}(f)$  agreed well with the transfer function  $H_{est}(f)$  that was derived from the far field probe results for a single patch antenna using equation 3.15c, with a maximum magnitude error of  $\Delta|H(f)| = -40$  dB and phase error of  $\Delta\angle H(f) = 25^\circ$ . Some error should be anticipated because the formulation from equation 3.15c assumes that the incident field is a plane wave and does not account for any reflections between transmitting and receiving antennas with a finite separation distance. However, these results demonstrate that this approach to estimating the transfer function for a free space far field antenna link is reasonably accurate and dramatically reduces full-wave simulation time, since the bounding box for a simulation with one antenna is limited by the antenna's dimensions rather than the far field link range. These smaller inset-fed microstrip patches were substituted for the Ka-band horn antennas in this proof-of-concept simulation in order to limit the far field link range and reduce full-wave simulation time. Nonetheless, the results were considered sufficient to permit the application of this transfer function estimation method to the far field link between the two Ka-band horns shown in Fig. 3.9.

After deriving the antenna link input to output voltage transfer functions  $H(f, r, \theta_t, \phi_t)$  for each of the transmitting horn's far field probes using this methodology, the corresponding two-port S-parameter objects are generated in MATLAB as shown in step 3 of Fig. 3.10. Because the effects of mismatch between generator impedances ( $Z_{Gtx} = Z_{Grx} = 50\Omega$ ) and the transmitting and receiving antenna impedances ( $Z_{Atx}, Z_{Arx}$ ) have already been taken into account through the full-wave simulation models and use of equations 3.15a, 3.15b, and 3.15c, the forward and reverse reflection coefficients are set to zero for all frequencies spanning the simulated far field antenna link bandwidth of 10.0 GHz:  $S_{11}(f) = S_{22}(f) = 0$ . This passive antenna link is further assumed to be reciprocal such that  $S_{21}(f) = S_{12}(f) = H(f, r, \theta_t, \phi_t)$ .

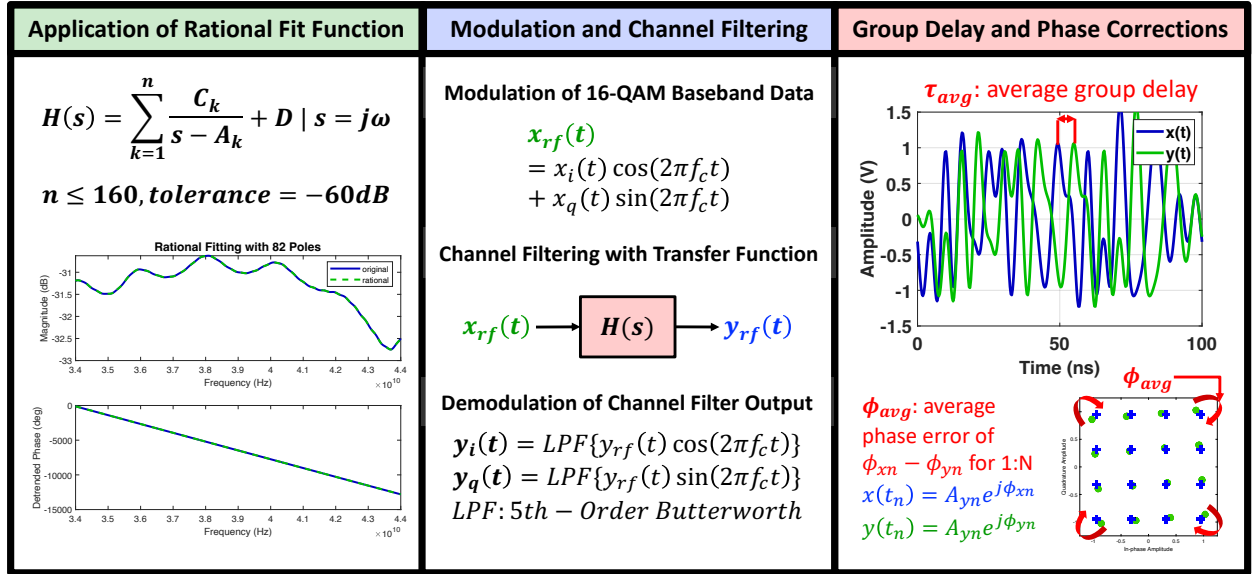


Figure 3.12 Steps 4-6 of the EVM simulation process implemented for the Ka-band conical horn of Fig. 3.8(a): (4) rational function of the form  $H(s)$  fitted to the complex data of the voltage transfer function  $H(f)$  over a 34-44 GHz frequency range with good agreement between the transfer function (blue) and rational fit (green), (5) up-conversion of the baseband 16-QAM test signal  $x(t)$  to carrier frequency  $f_c = 39.0$  GHz, transmission through the channel filter  $H(s)$ , and down-conversion to retrieve the baseband data of the received signal  $y(t)$ , and (6) estimation of the average group delay  $\tau_{avg}$  and residual phase error  $\Delta\phi_{res}$  for  $E_{un}(f)$ .

These S-parameter objects in MATLAB permit the use of other built-in functions that approximate the complex response of the antenna link transfer functions and model their response to an arbitrary applied signal, which is necessary to determine the EVM of a digitally-modulated signal that is passed through this channel filter and normalized or equalized at the receiver. This leads to the fourth step of the EVM simulation process, in which a rational fit of the form shown for  $H_{rat}(f)$  in equation 3.16 is created for each corresponding transfer function  $H_{est}(f)$ . A MATLAB function applies the adaptive Antoulas-Anderson algorithm described in [87] to compute a finite number  $n$  of poles  $A_k$  and residues  $C_k$  for the rational fit function based on the user-specified limitation for  $n$  and desired tolerance for the frequency response match of  $H(s)$ . For simulations of the Ka-band horn link, the number of poles was limited to  $n \leq 160$ , and the tolerance was set to  $-60$  dB to maintain a reasonable balance

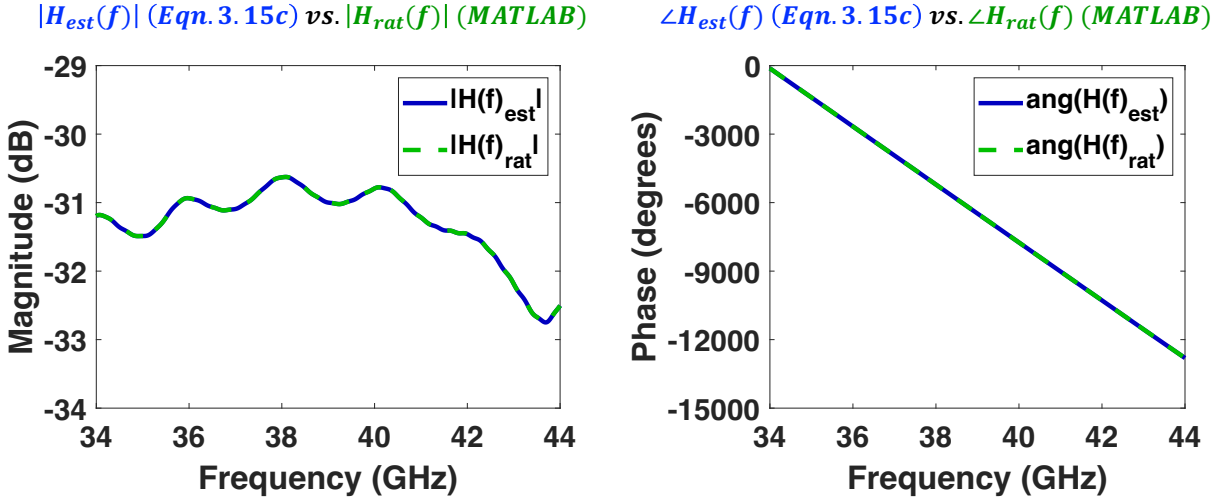
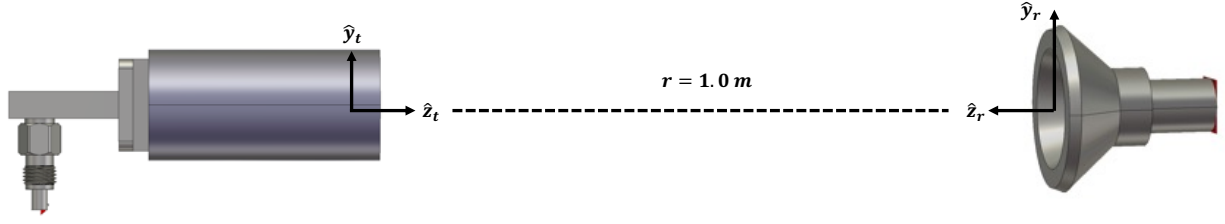


Figure 3.13 Ka-band horn link transfer function estimated from CST far field probe simulations for the boresight direction  $H_{est}(f)$  and corresponding rational fit frequency response  $H_{rat}(f)$  obtained through the MATLAB algorithm with  $n = 82$  poles and a tolerance level of  $-60$  dB.

between simulation speed and rational fit model accuracy. A comparison of the amplitude and phase of the transfer function  $H_{est}(f)$  estimated from full-wave simulations with boresight alignment and antenna link range of  $r = 1.0$  m and the corresponding rational fit function  $H_{rat}(f)$  acquired from MATLAB is shown in Fig. 3.13. An excellent agreement is observed over a 10 GHz span with center frequency  $f_c = 39$  GHz.

$$H_{rat}(f) = \sum_{k=1}^n \frac{C_k}{s - A_k}, s = j\omega = j2\pi f \quad (3.16)$$

The fifth step of the EVM simulation process is to apply this rational fit function to the modulated signal applied to the transmitting antenna port  $x_{rf}(t)$  to obtain an estimate of the signal generated at the receiving antenna port  $y_{rf}(t)$ . This step is executed with another MATLAB function that calculates the time response of the rational fit function  $H_{rat}(f)$  as

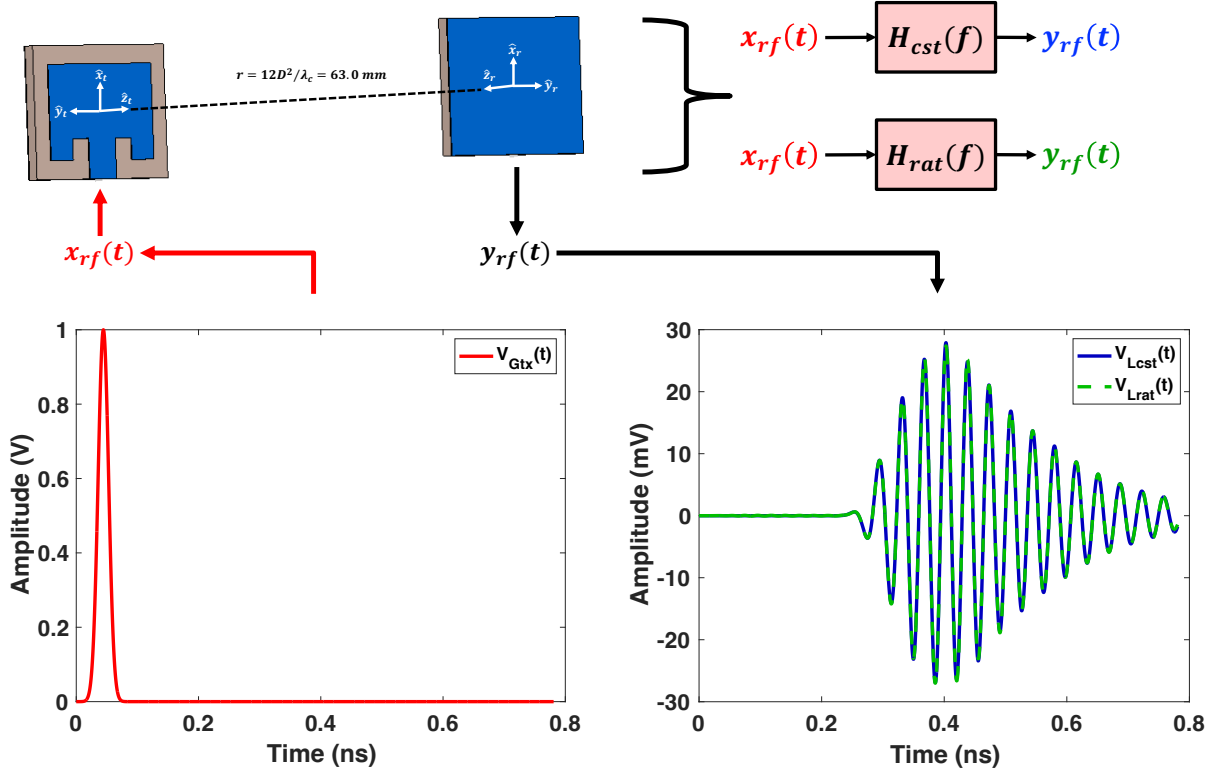


Figure 3.14 Time response of microstrip patch antenna link to a Gaussian pulse voltage signal applied to the transmitting antenna port  $x_{rf}(t) = V_{Gtx}(t)$  (red). The receiving antenna load voltage signals  $y_{rf}(t) = V_L(t)$  resulting from full-wave simulation performed in CST (blue) and application of the transfer function rational fit  $H_{rat}(f)$  in MATLAB (green) are shown to be nearly-identical.

described in [88]. To test the accuracy of this time response function, a rational fit for the simulated transfer function  $H_{cst}(f)$  of the microstrip patch far field link highlighted in Fig. 3.11 was applied to the Gaussian pulse voltage signal that was used as the default stimulus for the transmitting patch antenna discrete port within the full-wave simulation. The rational fit was designed with  $n = 62$  poles and a tolerance level of  $-60$  dB and applied with a time step  $t_s = 1.0$  ps. As shown in Fig. 3.14, the receiving antenna voltage  $y_{rf}(t)$  derived from this MATLAB function was nearly identical to that obtained directly from the receiving patch antenna's discrete port in the full-wave simulation of the entire link. One advantage of the rational fit approach to OTA channel modeling over the FIR filter synthesis approach adopted in [78], [81], and [82] is that an arbitrary time step  $t_s$  may be selected for the time response, which is convenient when simulating the EVM of wideband modulated test signals [88, 89].

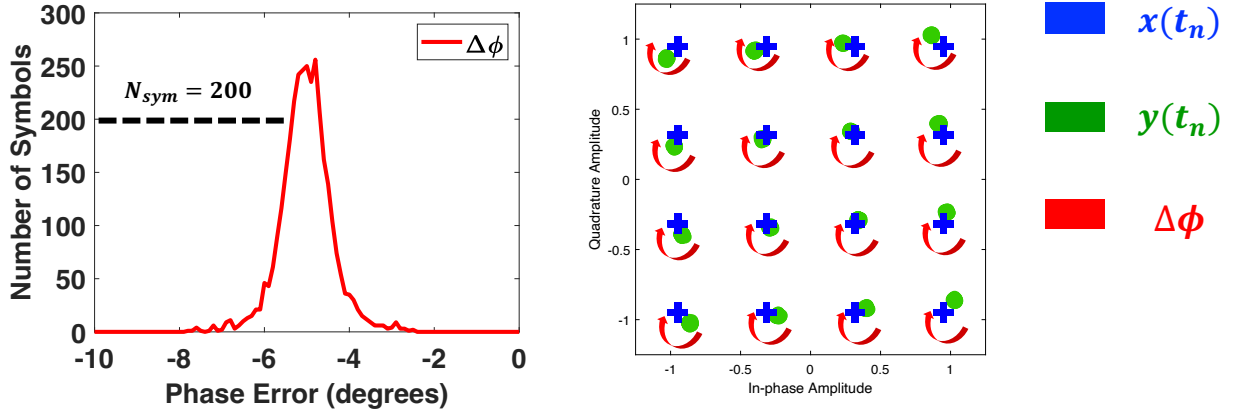


Figure 3.15 Histogram (left) and constellation diagram (right) showing the phase error  $\Delta\phi$  between the  $N_{bins} = 3600$  transmitted 16-QAM symbols  $x(t_n)$  and delay-corrected received symbols  $y(t_n)$ . The  $0.1^\circ$ -wide error bins containing the most symbols  $N_{sym}$  are concentrated near the residual phase error  $\Delta\phi_{res} \approx -5^\circ$  computed from equation (3.17).

As shown in the fifth step of Fig. 3.12, the transmitted voltage signal  $x_{rf}(t)$  that was used for EVM simulations of the Ka-band horn link was synthesized by QAM-modulating the baseband IQ data from a 16-QAM test signal  $x(t)$  at carrier frequency  $f_c = 39.0$  GHz. This modulated signal  $x_{rf}(t)$  was then applied to the rational fit function  $H_{rat}(f)$  with time step  $t_s = 1.0$  ps to obtain an estimate of the received voltage signal  $y_{rf}(t)$ . Finally,  $y_{rf}(t)$  was demodulated and low-pass filtered to obtain the baseband IQ data with embedded linear distortion from the channel filter  $y(t)$ . The modulation and demodulation from this fifth step was a prerequisite for applying the rational fit function from MATLAB. However, it should be noted that this step was not required for the EVM simulations from section 3.2, as the amplitude response from the full-wave field probe simulation was simply shifted to baseband to scale the spectral components of the applied voltage signal  $X(f)$ . Now the only remaining component of the EVM calculation from equation (1.2) is the equalization filter  $e(t_n)$ . Both the sixth and seventh steps of the EVM simulation relate to received signal corrections for the un-equalized EVM ( $EVM_{un}$ ) and equalized EVM ( $EVM_{eq}$ ) respectively. The differences between equalized and un-equalized EVM were described in section 2.3 and [90], and were applied to EVM analysis of a power amplifier with a VNA in [35]. For  $EVM_{un}$ , the received symbols  $y(t_n)$  are compensated for the average channel gain  $|H_{avg}(f)|$  and group delay  $\tau_{avg}(f)$

across the bandwidth of the test signal  $f_{min} \leq f \leq f_{max}$ . The former is calculated directly from the rational fit function, while the latter is estimated from the cross correlation of the 16-QAM input and output signals  $x(t)$  and  $y(t)$ . The residual phase error  $\Delta\phi_{res}$  is calculated from a weighted average of phase errors between transmitted symbols and delay-corrected received symbols  $\Delta\phi = \phi_x(t_n) - \phi_y(t_n + \tau_{avg})$ . A histogram of phase errors spanning the complete range  $[-180^\circ, 180^\circ]$  with bin widths  $\Delta\phi_n = 0.1^\circ$  was used to compute weighting factors for the residual phase error  $\Delta\phi_{res}$  defined in equation (3.17), where  $N_{sym}(n)$  is the number of symbols correlated with each phase error bin  $n$  and  $N_{bins} = 3600$  is the number of phase error bins. Fig. 3.15 highlights an example histogram for the residual phase error of the Ka-band horn link for the boresight orientation, where bins with the highest symbol counts are concentrated near  $\Delta\phi \approx -5^\circ$ . Tighter concentrations indicate a lower variation in the group delay  $\tau(f)$  over the signal bandwidth which results in a lower  $EVM_{un}$ . For this un-equalized EVM case, the received signal is only compensated for average group delay  $\tau_{avg}$  and residual phase error  $\Delta\phi_{res}$  by applying the equalization filter  $E_{un}(f)$  shown in equation 3.18. This is shown in the seventh step of the EVM simulation process in Fig. 3.16. Because the  $EVM_{un}$  includes error from amplitude and phase distortion in the far field antenna link, it is always higher than the equalized  $EVM_{eq}$ , as described in section 2.3. For  $EVM_{eq}$ , the equalization filter is the reciprocal of the channel estimate  $H_{est}(f)$  as shown in equation (3.19), where  $S_{XX}(f)$  and  $S_{XY}(f)$  are power spectral and cross-spectral densities of the input and output signal spectrums  $X(f)$  and  $Y(f)$  from the MATLAB transfer function estimate.

$$\Delta\phi_{res} = \frac{1}{N_{bins}} \sum_{n=1}^{N_{bins}} N_{sym}(n) \Delta\phi_n \quad (3.17)$$

$$E_{un}(f) = \frac{e^{-j\omega\tau_{avg}} e^{-j\Delta\phi_{res}}}{|H_{avg}(f)|} \quad (3.18)$$

$$E_{eq}(f) = \frac{1}{H_{est}(f)} = \frac{S_{XX}(f)}{S_{XY}(f)} \quad (3.19)$$

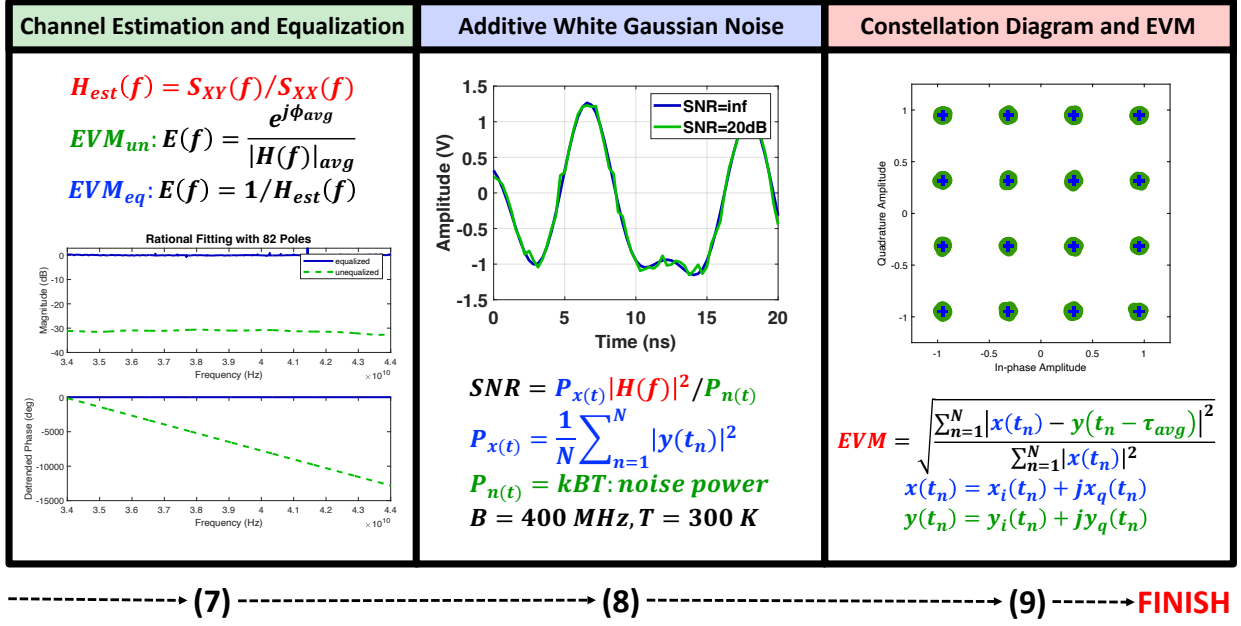


Figure 3.16 Steps 7-9 of the EVM simulation process implemented for the Ka-band conical horn of Fig. 3.8(a): (7) design and application of an equalization filter  $E(f)$  which is applied to the received signal  $y(t)$ , (8) addition of AWGN to equalized received signal based on SNR estimated from the applied test signal power  $P_{x(t)}$ , channel power gain  $|H(f)|^2$ , and thermal noise power  $P_{n(t)}$  calculated for the test signal bandwidth  $B = 400$  MHz and approximate room temperature  $T = 300$  K, and finally (9) plotting of the signal constellation diagrams and calculation of EVM for both the equalized and un-equalized cases, where  $x(t_n)$  represent the symbols of the 16-QAM voltage signal applied to the transmit antenna port and  $y(t_n - \tau_{avg})$  represent the symbols of the voltage signal at the receive antenna port following equalization.

While  $E_{un}(f)$  is applied to  $y(t)$  directly in the time domain,  $E_{eq}(f)$  is applied to  $y(t)$  in the same manner that  $H_{rat}(f)$  is applied to  $x(t)$  to model the transmission of the modulated test signal from transmitting to receiving horn antenna: A rational fit function is generated for  $E_{eq}(f)$  and applied to  $y(t)$  using the MATLAB time response function, resulting in an equalized received signal that can be used for the EVM calculations shown in equation (1.2). After the equalization from step seven of Fig. 3.16, a finite  $EVM_{un}$  resulting from the linear distortion of the antenna link could be computed for the  $N = 3600$  16-QAM symbols, but the  $EVM_{eq} \approx 0$  since  $E_{eq}(f)$  is an ideal equalizer that eliminates this distortion. However, additive thermal noise power  $P_{n(t)} = kBT$  at the receiver also corrupts the received signal and



contributes to the EVM. This effect can be modeled independently from the linear distortion using MATLAB's AWGN function as shown in the eighth step of the EVM simulation process in Fig. 3.16, where  $SNR$  is equal to the received signal power  $P_{y(t)}$  divided by the receiver's thermal noise power  $P_{n(t)}$ . For a free space link between two antennas separated by a far field distance  $r \geq 2D^2\lambda$ ,  $P_{y(t)}$  can be calculated from the Friis transmission equation presented in equation 3.20, where  $P_{x(t)}$  is the transmitted signal power,  $G_t$  and  $G_r$  are the average realized gains of the transmitting and receiving horns across the modulated test signal bandwidth  $B = 400$  MHz centered at  $f_c = 39$  GHz,  $\lambda_c = c_0/f_c = 7.7$  mm, and  $\hat{p}_t$  and  $\hat{p}_r$  are the antenna polarization vectors [91].

$$P_{y(t)} = P_{x(t)} G_t(\theta_t, \phi_t) G_r(\theta_r, \phi_r) \left( \frac{\lambda_c}{4\pi r} \right)^2 [\hat{p}_t \cdot \hat{p}_r]^2 \quad (3.20)$$

In these EVM simulations, the receiving horn is always oriented to match the Ludwig's 3rd vertical polarization component of the transmitting horn and receive along its boresight direction at a fixed distance  $r = 1.0$  m, such that  $[\hat{p}_t \cdot \hat{p}_r] = 1$  and  $(\theta_r, \phi_r) = (0^\circ, 0^\circ)$ . Therefore,  $P_{y(t)}$  only varies as a function of the transmitting antenna gain at the CST far field probe angle  $G_t(\theta_t, \phi_t)$ . The noise power  $P_{n(t)}$  is assumed to be static for bandwidth  $B = 400$  MHz and combined antenna and receiver temperatures  $T = T_a + T_r$ . While the latter could be approximated for a generic receiver based on the noise principles described in [91] and [92], a comparison of simulated and measured EVM results for the Ka-band horn link is better facilitated by assuming that the simulated horn link has the same noise floor  $P_{n(t)}$  as the VNA receiver used in the corresponding CATR measurements described in section 3.4. This measured noise floor accounts for the VNA receiver noise figure and the IF filter bandwidth and vector averaging factor applied during the measurement. After random amplitude and phase errors have been added to the received signal  $y(t)$  based on this antenna link  $SNR$  approximation, the received symbols, corrupted by additive noise and the linear distortion of the channel  $H(f, r, \theta_t, \phi_t)$ , can be visualized via the constellation diagram feature in MATLAB. Finally, the  $EVM_{un}$  and  $EVM_{eq}$  are computed for  $N = 3600$  symbols via equation (1.2), as shown in the ninth step of Fig. 3.16. These EVM simulation results are shown in section 3.4.

### 3.4 EVM Measurement of a Ka-Band Conical Horn Link with a Compact Antenna Test Range and Network Analyzer

To demonstrate the combined effects of linear and nonlinear distortion on the EVM of passive and active antenna links and evaluate the accuracy of the EVM results from the Ka-band horn link simulation presented in section 3.3, EVM measurements of a 400 Mbaud 16-QAM test signal were performed with the same two horn antennas in a millimeter-wave compact antenna test range with a multi-port VNA receiver, which computes EVM from the frequency spectrum of the modulated signals transmitted by the AUT and received by the CATR feed horn using the spectral correlation method described in section 2.3. The CATR emulates the far field test condition with a reflector that transforms the spherical wave front from a stationary feed horn to a quasi-planar wavefront which has minimal amplitude and phase ripple within a specified quiet zone surrounding the AUT. Because the chamber volume and spatial path loss are dependent on the focal length of the reflector rather than the dimensions of the AUT ( $2D^2/\lambda$ ), CATRs are typically preferred for controlled OTA measurements of millimeter-wave antennas and phased arrays. The data sheet for the F9650A CATR model used in the following measurements specifies an amplitude ripple of  $\pm 0.5$  dB and phase ripple of  $17^\circ$  at carrier frequency  $f_c = 39$  GHz, which is less than the  $22.5^\circ$  spherical phase taper at the conventional far field distance of  $2D^2/\lambda$ , and its 30 cm quiet zone diameter is large enough to accommodate the spline-profiled conical horn antenna under test ( $D = 20.0$  mm) [93]. A block diagram of the complete CATR-EVM measurement system is presented in Fig. 3.17, and images of the Ka-band horn, roll-over-azimuth positioner, and test instruments are shown in Fig. 3.18. The generation of the 16-QAM signal and synchronization of the AUT positioner with frequency sweeps and data acquisitions from the PNA-X network analyzer (a multi-port VNA) was achieved with a laptop computer running MATLAB instrument control scripts that were designed to establish connections with and send SCPI commands to the positioner and the test instruments: an arbitrary waveform generator (AWG), PNA-X network analyzer (VNA), and vector signal generator (VSG). The procedure for measuring the EVM of a 400 Mbaud 16-QAM test signal distorted by this CATR link with Ka-band horns was as follows:

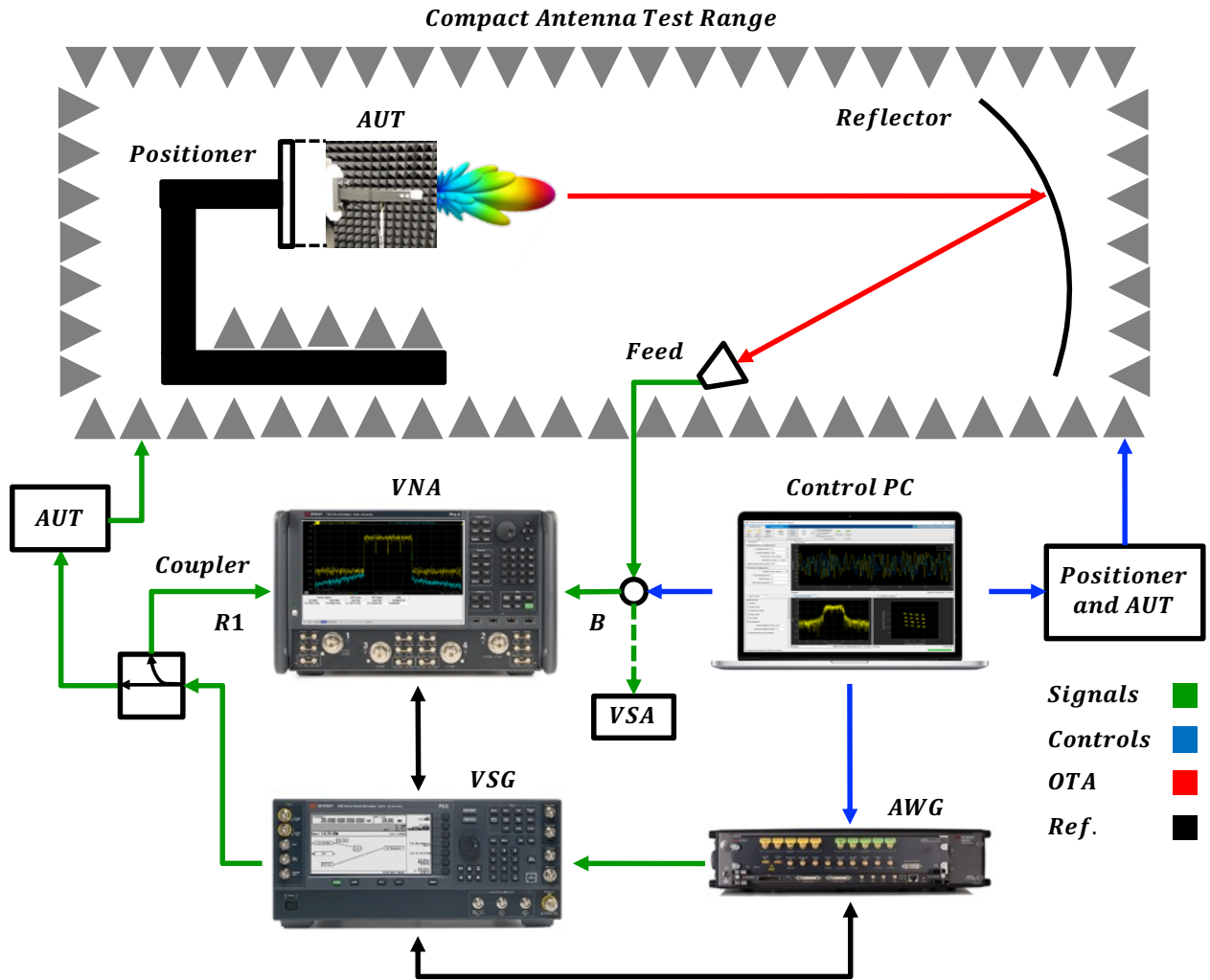


Figure 3.17 Compact test range EVM measurement system diagram for the Ka-band horn link highlighting the RF (green), control (blue), and OTA (red) signal paths between the test instruments and antennas. A 10 MHz reference signal (black) is used for synchronization of the AWG, VSG, and VNA. A single port VSA (green dotted line) could be utilized as an alternative to the VNA to measure EVM if it had adequate dynamic range.

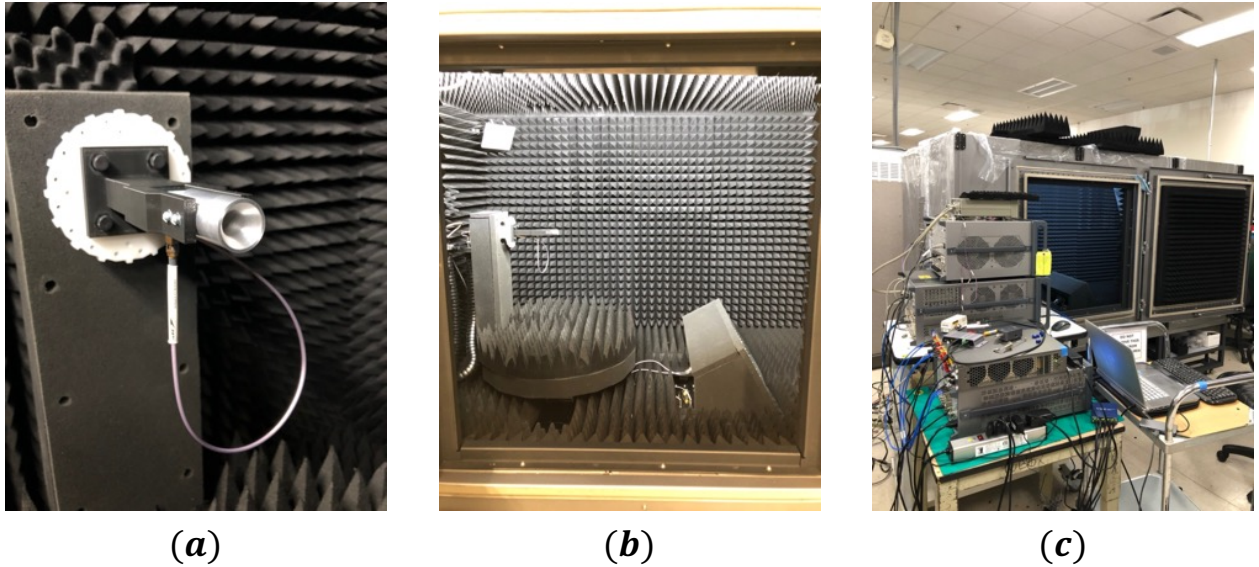


Figure 3.18 Images of a millimeter-wave compact antenna test range and instruments provided by Keysight in Santa Rosa, CA: (a) Ka-band horn antenna mounted with customized 3D-printed bracket that extends it to quiet zone center, (b) roll/azimuth AUT positioner and feed horn enclosure, and (c) CATR exterior and instruments. Reflector is shown in Fig. 4.13(b).

First, the MATLAB IQ Tools dialog box shown in Fig. 3.19 was used to create a 16-QAM test signal with a length of 3200 symbols at a symbol rate of 400 Mbaud and sampling rate of 3200 Msamples/s. A root-raised cosine pulse-shaping filter with rolloff factor  $\alpha = 0.15$  was applied to this signal to limit its bandwidth to approximately 400 MHz, and the resulting waveform file was uploaded to a two-channel M8190A AWG. This AWG was used to transmit the waveform's baseband IQ data to the E8267D VSG, which upconverted the 16-QAM test signal to a carrier frequency of  $f_c = 39.0$  GHz. A directional coupler was used to couple the resulting RF test stimulus  $x_{rf}(t)$  to PNA-X receiver  $R1$  via the coupled arm and transmit it to the AUT port via the through arm. The test signal  $x_{rf}(t)$  was radiated from the AUT to the WR-28 scalar feed horn installed in the CATR through the reflection path shown in Fig. 3.17, and the signal received by the feed horn  $y_{rf}(t)$  was measured by PNA-X receiver  $B$ . The input signal  $x_{rf}(t)$  and output signal  $y_{rf}(t)$  from the Ka-band horn link were thereby measured simultaneously on the PNA-X with the aid of the 10 MHz reference signal, enabling a precise comparison and an accurate EVM calculation from the spectral components of these two signals as detailed in section 2.3.

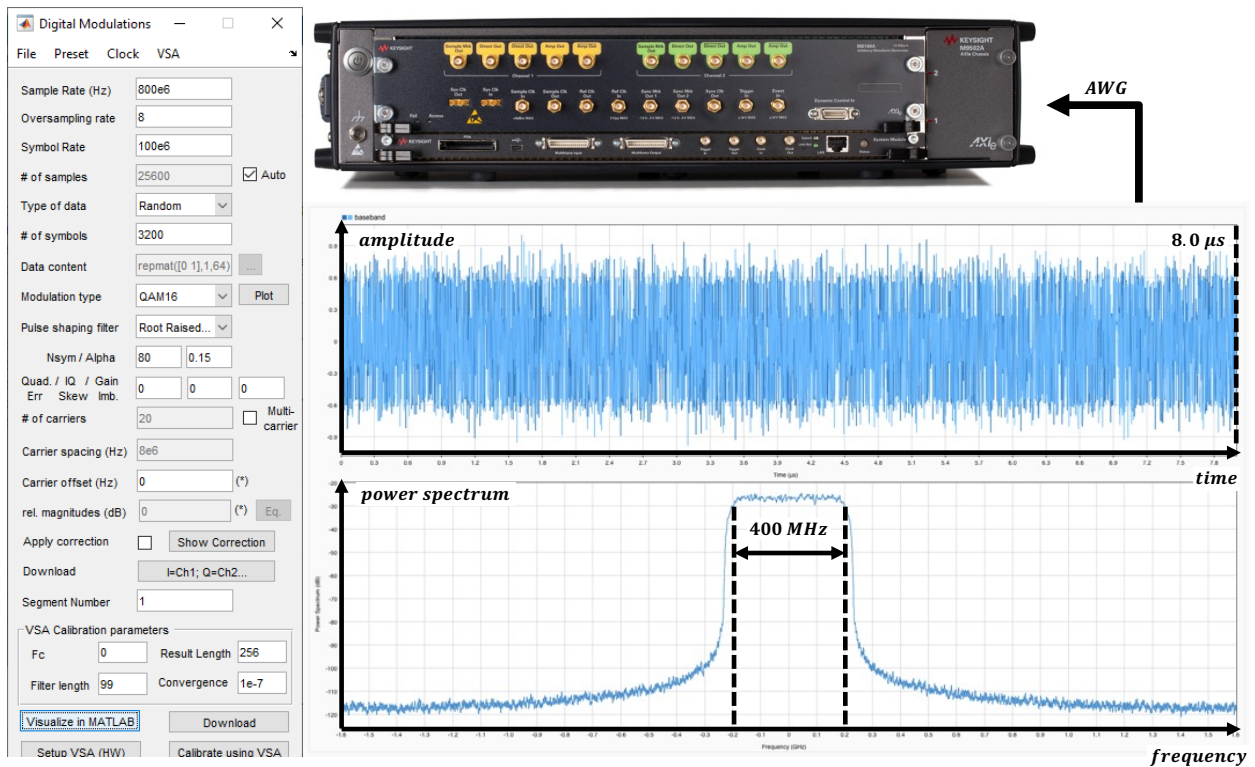


Figure 3.19 MATLAB IQ Tools dialog box (left) showing parameters of the digital modulation format used for the test signal and resulting time-domain voltage signal and power spectrum (bottom right). The 16-QAM signal has a length of 3200 symbols, a sampling rate of 3200 Msym/s and a symbol rate of 400 Mbaud. A root-raised cosine filter with  $\alpha=0.15$  is applied, and the resulting waveform file is uploaded to an AWG with two baseband IQ output ports.

Because both the transmitted and received signals are measured on synchronized receivers of the PNA-X, complex spectral error vectors resulting from imperfections in the AWG and VSG are eliminated from the EVM results. Additional errors from the linear distortion of RF test cable transmission are likewise eliminated by implementing a two-port S-parameter calibration that moves the reference planes to the ports of the AUT and WR-28 feed horn. Consequently, in this CATR measurement, EVM is purely a manifestation of linear distortion from OTA link transfer function  $H(f)$  and nonlinear distortion  $D(f)$  from the PNA-X receiver  $B$  noise. Passive intermodulation effects were assumed to be negligible, and the receiver noise floor was lowered to approximately -114 dBm for the PNA-X spectrum analyzer with a 1.0 GHz span centered at  $f_c$  by reducing the resolution filter bandwidth (RBW) and applying vector averaging. The noise bandwidth (NBW), defined as the RBW divided by the vector

averaging factor, was set to 10 Hz for all of the following EVM measurements and resulted in an average frequency sweep time of approximately 18.3 seconds. The NBW represents a key tradeoff between EVM measurement speed and dynamic range: Measurement speed suffered as a result of this long spectrum acquisition time, but the dynamic range improvement helped to compensate for the 64.4 dB of spatial path loss over the 1.02 meter focal length of this CATR [93], and was considered worthwhile due to the limited number of desired EVM points (19-25 in each of two orthogonal planes of the AUT). This tradeoff is enabled by the fact that a known periodic test signal with a deterministic FFT grid is transmitted to the AUT, which allows the received signal spectrum to be obtained over multiple coherent acquisitions [39, 61]. This can be leveraged to minimize the receiver noise contribution in EVM measurements of wideband modulated test signals at millimeter-wave carrier frequencies. Conversely, the frequency sweep time can be reduced by increasing NBW if lower dynamic range is tolerable. For example, at an NBW of 100 Hz, the sweep time is reduced to 1.9 seconds. The numerous advantages of performing OTA EVM measurements with a multi-port VNA, including vector calibration and the ability to directly measure the modulated test signal, make it a promising new methodology for evaluating the quality of OTA links with wideband modulated signals.

The equalized and unequalized EVM, as well as the corresponding spectral correlation quantities and modulated signal gain  $H(f)$ , were captured from the PNA-X using customized MATLAB measurement automation scripts as the AUT azimuth positioner shown at the bottom of Fig. 3.18(b) was rotated in  $5^\circ$  increments. For the E-plane orientation of the AUT, as shown in Fig. 3.18(a), the rotation range of the azimuth positioner was set to  $[-60^\circ, 60^\circ]$ . For the H-plane orientation of the AUT, where the roll position was rotated  $90^\circ$  with respect to the position shown in Fig. 3.18(a), the rotation range of the azimuth positioner was set to  $[-45^\circ, 45^\circ]$ . The RF carrier power from the VSG was set to 15.0 dBm, the maximum value that could be selected without the source becoming unlevel, and the integration bandwidth for the EVM calculation was set to 449.1 MHz by default, based on the properties of the uploaded IQ waveform file highlighted in Fig. 3.19. The results of these measurements for the Ka-band horn link, measured in the compact test range presented in Figs. 3.17 and 3.18, are presented in Figs. 3.20, 3.21, 3.22, and 3.23.

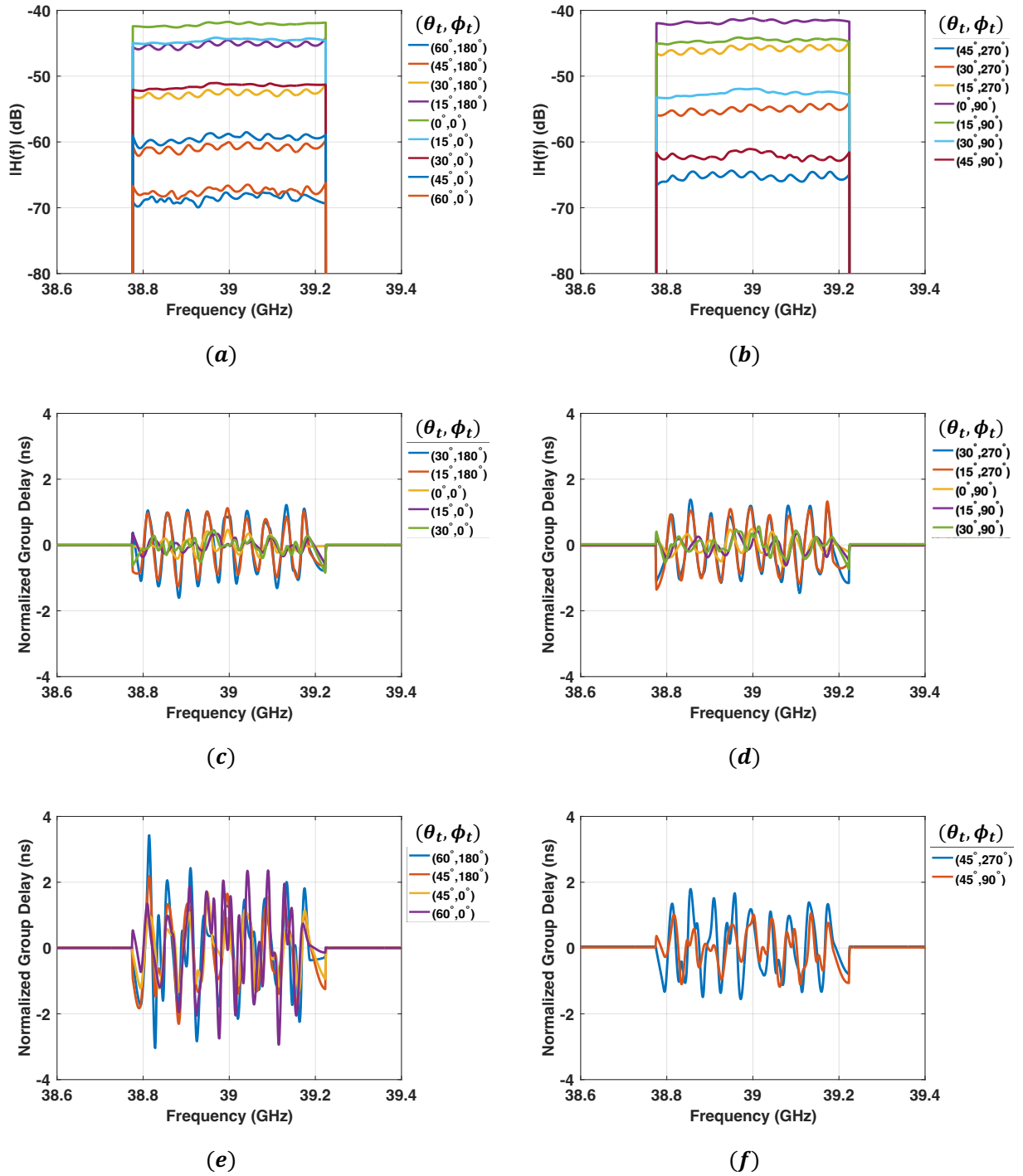


Figure 3.20 Measured modulated channel gain  $|H(f)|$  and normalized group delay  $t_d(f)$  of the Ka-band horn link for different E-plane (a),(c),(e) and H-plane (b),(d),(f) angles of the AUT. In addition to the gain degradation with  $\theta_t$  angles further off boresight ( $\theta_t = 0^\circ$ ), an increase in peak-to-peak  $|H(f)|$  passband ripple and group delay variation is also observed.

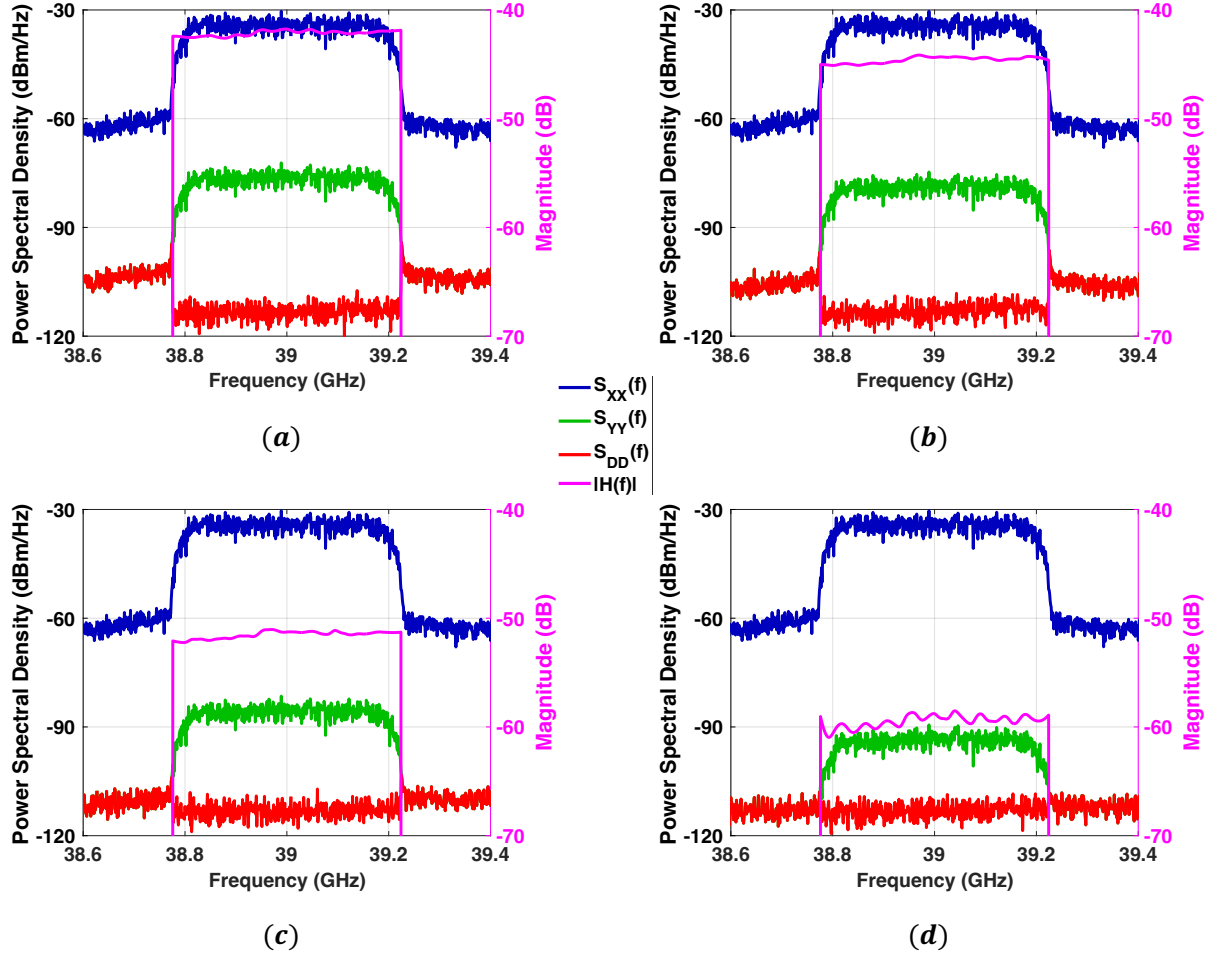


Figure 3.21 Power spectral densities of the modulated stimulus applied to the AUT  $S_{XX}(f)$  (blue) and measured on the PNA-X reference receiver  $R1$ , the received signal from the CATR feed horn  $S_{YY}(f)$  (green) measured on receiver  $B$ , and the distortion spectrum  $S_{DD}(f)$  (red) described in section 2.3, with the corresponding modulated gain  $|H(f)|$  (magenta) overlaid. These results are for the AUT E-plane angles ( $\phi_t = 0^\circ$ ) (a)  $\theta_t = 0^\circ$ , (b)  $\theta_t = 15^\circ$ , (c)  $\theta_t = 30^\circ$ , and (d)  $\theta_t = 45^\circ$ .



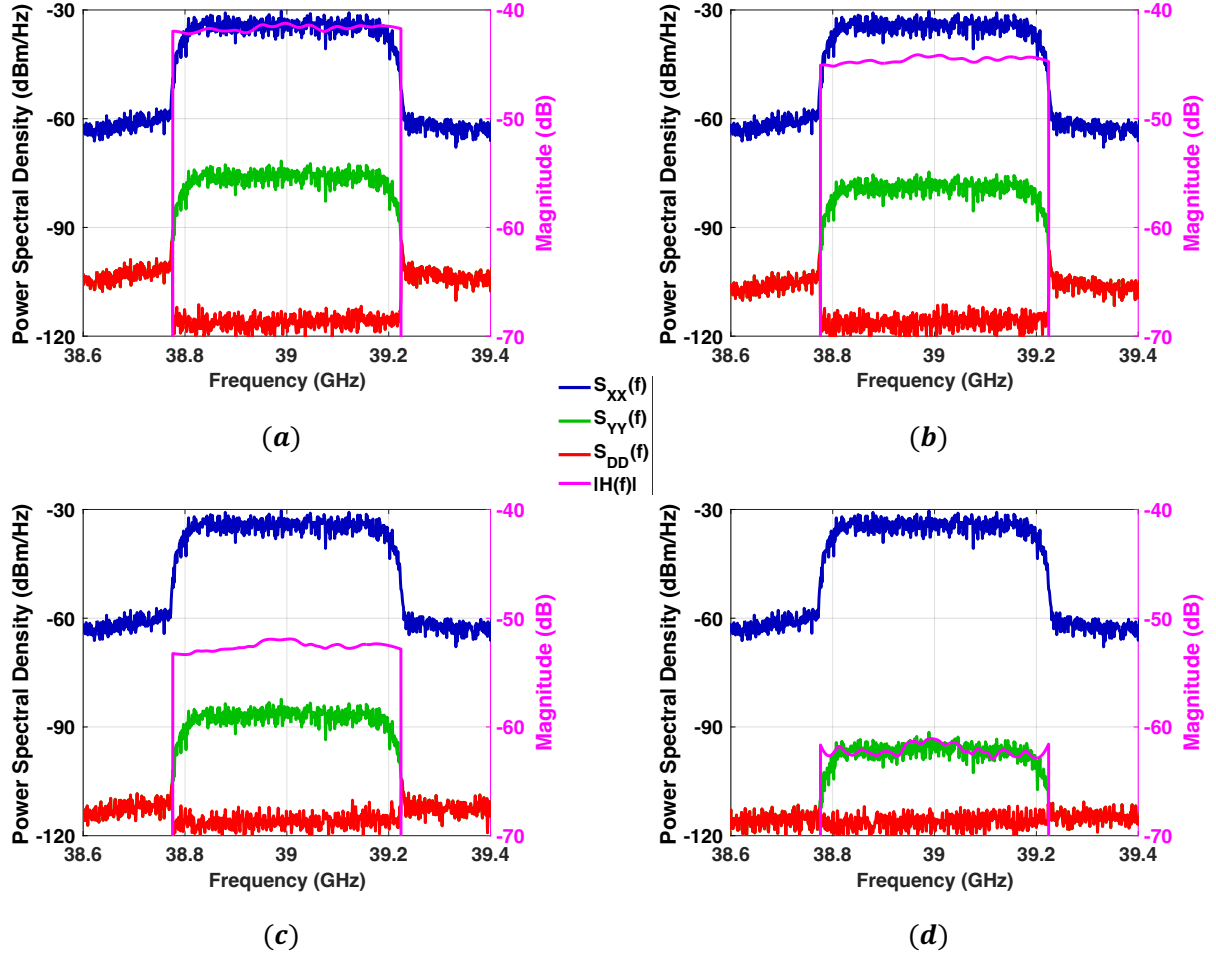


Figure 3.22 Power spectral densities of the modulated stimulus applied to the AUT  $S_{XX}(f)$  (blue) and measured on the PNA-X reference receiver  $R1$ , the received signal from the CATR feed horn  $S_{YY}(f)$  (green) measured on receiver  $B$ , and the distortion spectrum  $S_{DD}(f)$  (red) described in section 2.3, with the corresponding modulated gain  $|H(f)|$  (magenta) overlaid. These results are for the AUT H-plane angles ( $\phi_t = 90^\circ$ ) (a)  $\theta_t = 0^\circ$ , (b)  $\theta_t = 15^\circ$ , (c)  $\theta_t = 30^\circ$ , and (d)  $\theta_t = 45^\circ$ .

Fig. 3.20 shows the modulated gain of the CATR link  $|H(f)| = |S_{XY}(f)/S_{XX}(f)|$  and the corresponding normalized group delay  $t_d(f)$  across the 449.1 MHz integration bandwidth centered at  $f_c = 39.0$  GHz for each of the measured E and H-plane far field angles  $(\theta_t, \phi_t)$  in the legends. Two general observations can be made from these results: First, as the measured far field angle with respect to the AUT deviates further from boresight (e.g. as  $\theta_t$  increases from  $0^\circ$ ), the gain of the spline-profiled conical horn AUT decreases from its peak value across the entire 449.1 MHz band. A close proximity of the modulated gain values measured on opposite sides of the horn aperture's normal axis ( $\hat{z}$ ) for specific  $\theta_t$  values, especially in the E-plane ( $\phi_t = 0^\circ, 180^\circ$ ) measurements of Fig. 3.20(a), demonstrates the pattern symmetry. Due to this lower wideband antenna gain at off  $\hat{z}$ -axis angles, the SNR at VNA receiver  $B$   $|Y(f)|^2/|D(f)|^2$  is likewise lower and results in a lower equalized and un-equalized EVM as shown in the blue plots of Fig. 3.23. The PSD of the transmitted signal  $S_{XX}(f)$  measured at VNA receiver  $R1$ , received signal  $S_{YY}$  measured at VNA receiver  $B$ , and distortion component  $S_{DD}(f)$ , calculated from the spectral correlation process detailed in section 2.3 are shown for four E and H-plane observation angles spaced  $15^\circ$  apart in Fig. 3.21 and 3.22 respectively. From these two figures, the SNR reduction with increasing  $\theta_t$  is readily observed, and it is evident that the PSD of the transmitted signal (blue) and distortion (red) remain constant within the 449.1 MHz integration band as the AUT positioner is rotated, while that of the received signal (green) gradually decreases. The second observation from Fig. 3.20 is that the peak-to-peak ripple of the modulated gain and normalized group delay across the 449.1 MHz band likewise increase as the far field elevation angle of the AUT deviates further from boresight. That is, the CATR link produces a greater variation in amplitude scaling and propagation delay of the transmitted signal's spectral components at larger  $\theta_t$  angles, and the un-equalized received signal has a higher degree of linear distortion that results in higher un-equalized EVM at these angles. However, because a low SNR dominates both the equalized and un-equalized EVM at large  $\theta_t$  angles, the effect of linear distortion increasing with  $\theta_t$  is not discernible from the measured EVM results presented in Fig 3.23. The same is true for the simulated EVM results from the Ka-band horn link model described in section 3.3, which are also shown in Fig 3.23 for comparison.

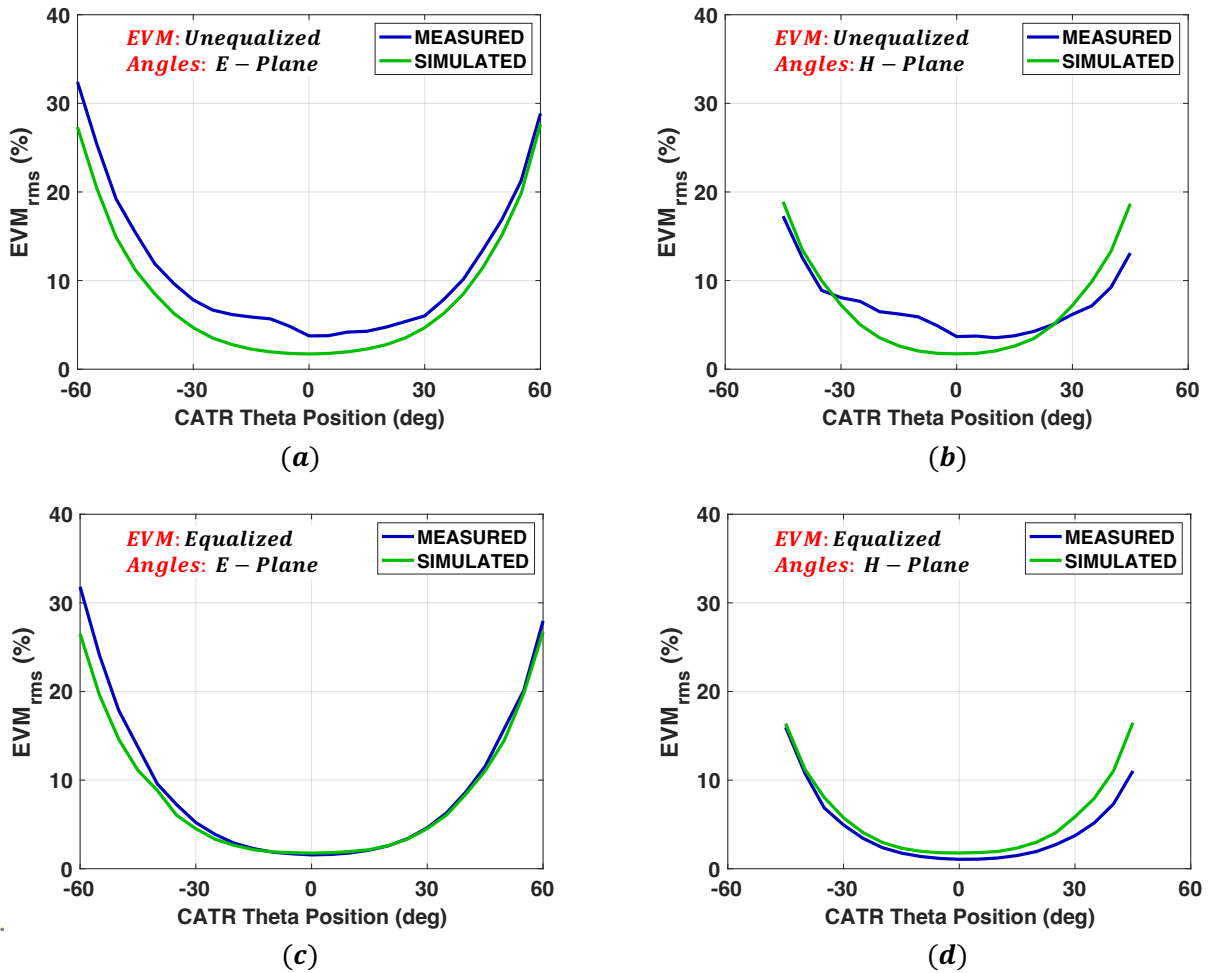


Figure 3.23 Measured (blue) and simulated (green) un-equalized (a)-(b) and equalized (c)-(d) EVM for the Ka-band horn link. Results are shown for E-plane  $\theta_t$  angles in (a) and (c) and for H-plane angles in (b) and (d). Equalized EVM results show good agreement, indicating a good match between measured and simulated horn gains. Unequalized EVM results show the same dependency on  $\theta_t$  with some residual error that is likely due to the vector calibration.

The AWGN added to the simulated horn link was based on the measured noise floor power shown as distortion spectrum of Figs. 3.21 and 3.22 and the power gain of the link transfer function derived from full-wave simulations of vector effective length. As shown in Fig. 3.16, it was added to the received signal distorted by link transfer function estimate  $H_{est}(f)$  in the final step preceding the EVM calculation. Consequently, the simulated EVM contribution due to the linear distortion only  $EVM_{H(f)}$ , caused by deviations from flat amplitude and linear phase response of modulated signal gain, was easily computed and is plotted in Fig. 3.24(a). If it is assumed that the receiver AWGN measured in  $EVM_{EQ}$  and linear distortion embedded in  $EVM_{UN}$  represent two uncorrelated random error variables,  $EVM_{H(f)}$  for the measured result can be estimated from the root-difference-square as shown in equation (3.21).

$$EVM_{H(f)} = \sqrt{EVM_{UN}^2 - EVM_{EQ}^2} \quad (3.21)$$

The resulting measured  $EVM_{H(f)}$  result is also plotted in Fig. 3.24(a). Comparing the measured and simulated results, both appear to increase with  $\theta_t$  and demonstrate that the amplitude and phase variation of the horn link transfer function is greater when the AUT is positioned to transmit the modulated test signal from large angles off the aperture normal axis  $\hat{z}$ . However, there are also some notable discrepancies: The measured  $EVM_{H(f)}$  values are consistently higher than the simulated ones and lack the smooth parabolic distribution across E-plane angles. The simulated far field link distance matched the focal length of the CATR reflector, but the  $\pm 0.5$  dB of amplitude ripple and  $17.0^\circ$  of phase variation across the 30 cm quiet zone of the CATR at  $f_c = 39.0$  GHz represents one potential source of error [93]. Another potential source of error is that the feed horn design in the full-wave simulation was not entirely identical to the model used in the CATR, since the manufacturer datasheet did not provide specific details on the corrugation dimensions or the orthomode transducer [86]. An image of the WR-28 dual-polarized feed horn and simulated gain versus frequency data from [86] are shown in Fig. 3.25, where the dotted line highlights the tested integration band. Other sources of error could include RF cable movement with the AUT positioner and failures in applying S-parameter calibration for the RF cables and adapters mating to the antennas.

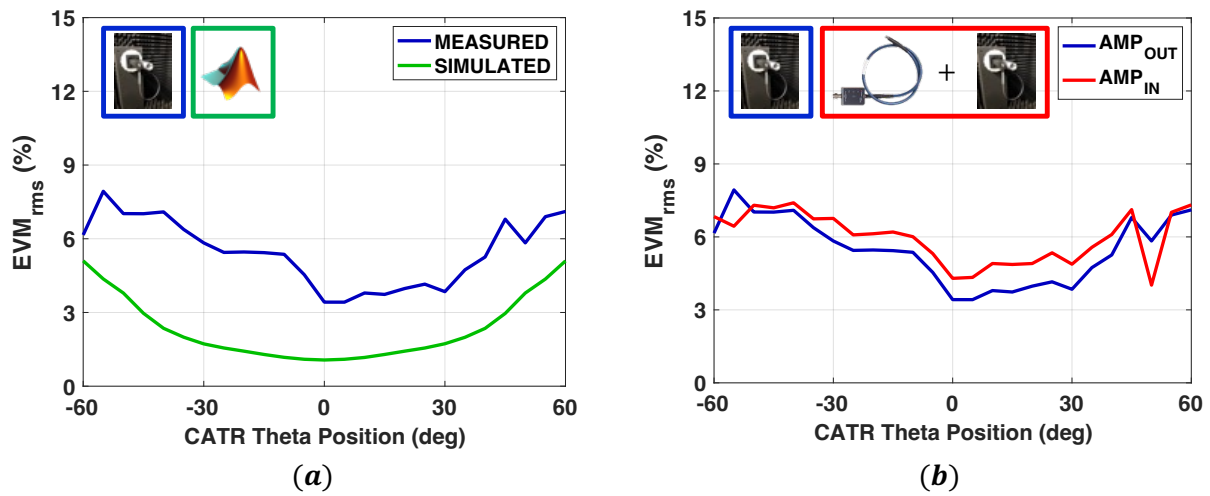


Figure 3.24 (a) Estimated linear distortion component of the Ka-band horn link's un-equalized EVM due to  $H(f)$  only as a function of E-plane  $\theta_t$  angles: simulated EVM of the Ka-band horn link without AWGN (green) and calculated from measured quantities (blue). (b) Linear distortion EVM component calculated from measurements with (red) and without (blue) the preamplifier in series with the transmitting Ka-band horn antenna.

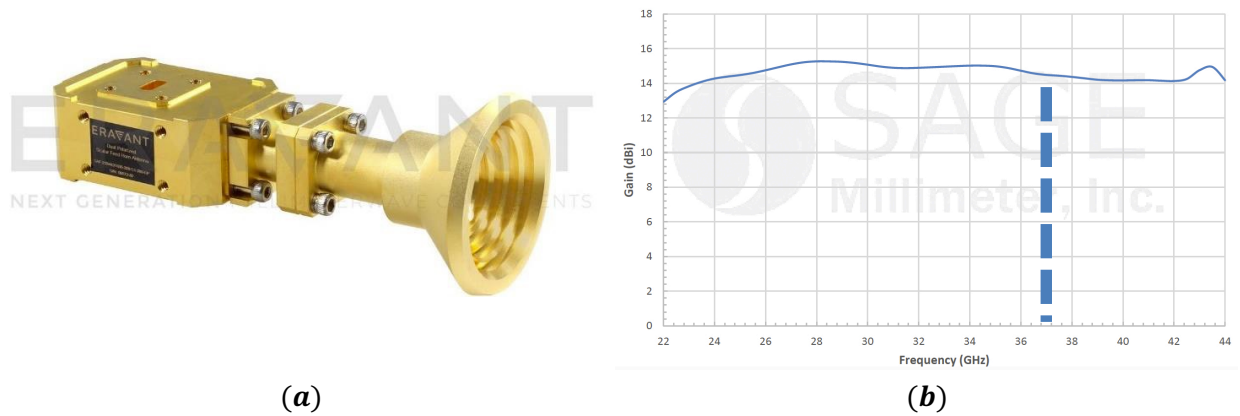


Figure 3.25 WR-28 broadband dual-polarized scalar feed horn model used in the F9650A compact antenna test range: (a) Image of corrugated feed horn with an integrated orthomode transducer and (b) simulated gain vs. frequency with a dotted line at the integration band centered at  $f_c = 39.0$  GHz from the manufacturer data sheet [86].

While measurement errors associated with surface imperfections of the CATR reflector and RF cable movement could not have been completely mitigated, the CATR path loss and feed horn frequency response could have been eliminated by implementing an S-parameter calibration with a reference antenna such as a standard gain horn. This likely would have resulted in a better match between the simulated and measured  $EVM_{H(f)}$  results for this Ka-band horn link. These differences in linear distortion between the measured and simulated results appear in the un-equalized EVM plots of Fig. 3.23(a) and (b) as well. The equalized EVM results are more closely-matched because broadband changes in the Ka-band horn link gain and SNR with far field observation angles  $(\theta_t, \phi_t)$  were more-accurately predicted by the simulation model than the specific amplitude and phase variations of  $H(f)$  at those angles, and the noise floor for the AWGN component of the received signal error was obtained directly from the VNA measurement to facilitate comparison. A slight asymmetry in measured  $EVM_{EQ}$  values in Fig. 3.23(c) and (d) suggests that there may have been an AUT alignment error that prevented better agreement between the simulated and measured  $EVM_{EQ}$  results.

To observe the effects of nonlinear distortion from an active device on EVM, another set of modulation distortion measurements were performed with the same VNA with a 50 GHz pre-amplifier as both an isolated DUT and a front end for the transmitting AUT in the CATR link. In the former, EVM was measured as a function of RF carrier power from the VSG. In the latter, it was measured as a function of the E and H-plane observation angles from Fig. 3.23 with a constant RF carrier power of -22.5 dBm from the VSG source. The RF carrier power was reduced from 15.0 dBm to -22.5 dBm for CATR measurements in which the pre-amplifier was used as a front end for the AUT in order to prevent over-compression and potential damage. At this IP1dB compression point, the equalized EVM from measurements of the pre-amplifier as an isolated DUT was approximately 10%, as shown in Fig. 3.26(a). Results from EVM measurements with the pre-amplifier are presented in Figs. 3.26 and 3.27.

The EVM measurements of the isolated pre-amplifier as a function of RF carrier power are shown in Fig. 3.26(a) and (b) and take the form of bathtub curves: EVM is high and dominated by low SNR for the VNA receiver at the low RF power levels ( $P_{RF} \leq -35$  dBm), low and limited by the VNA receiver noise floor at median power levels ( $-35$  dBm  $\leq P_{RF} \leq -25$

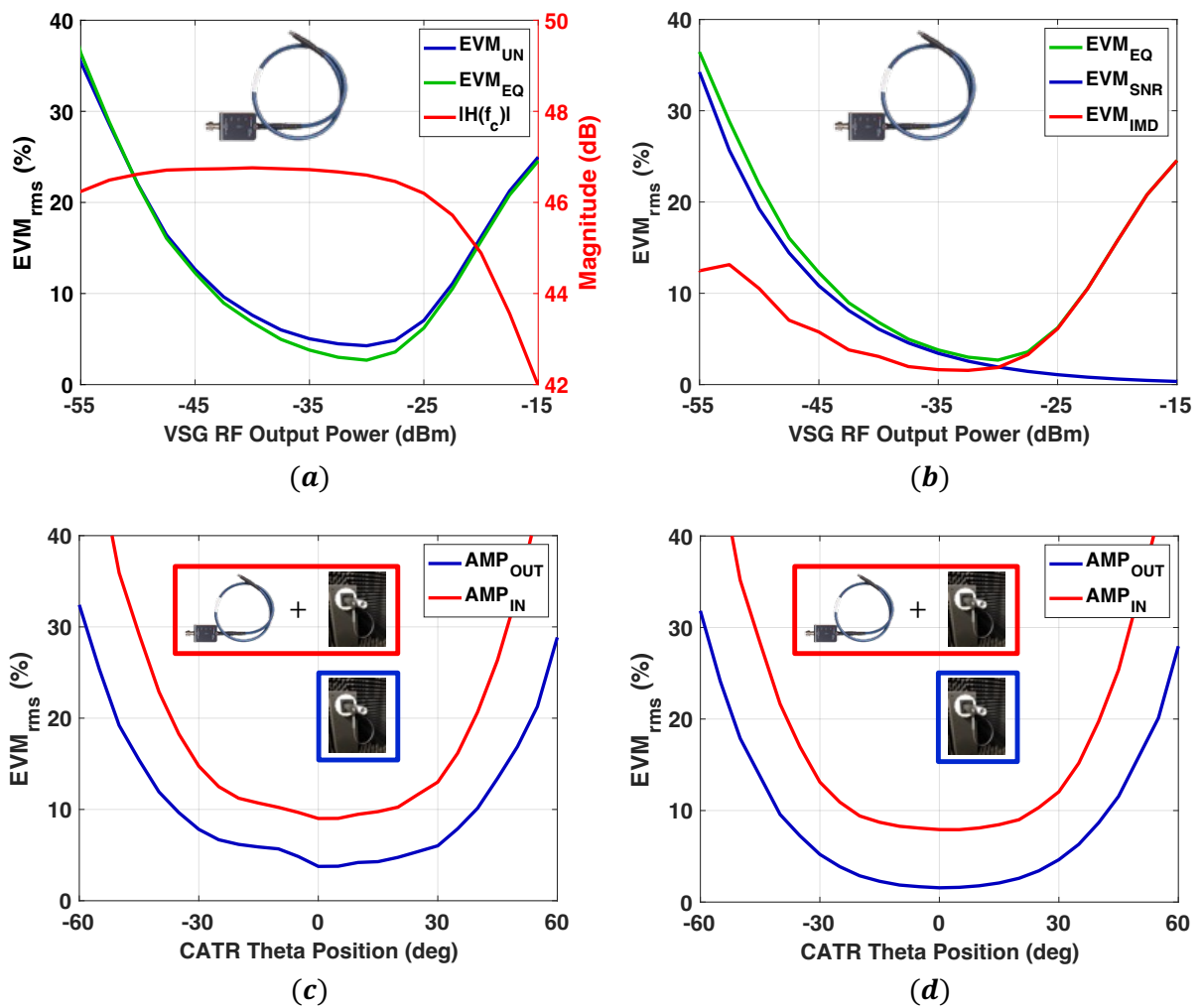


Figure 3.26 (a) Un-equalized EVM (blue), equalized EVM (green), and RF carrier gain (red) of the Keysight U7227F pre-amplifier versus RF carrier power from the VSG, (b) Estimated noise (blue) and non-linear distortion (red) components of the pre-amplifier's equalized EVM (green), and un-equalized EVM of the Ka-band horn link with (red) and without (blue) the pre-amplifier on transmitting antenna side for  $\theta_t$  angles in the (c) E-plane and (d) H-plane.

dBm), and once again high and dominated by intermodulation distortion of the pre-amplifier at high RF power levels ( $P_{RF} \geq -25$  dBm). The maximum difference between  $EVM_{UN}$  and  $EVM_{EQ}$  results in Fig. 3.26(a) is 1.6% at  $P_{RF} = -30$  dBm and demonstrates that the linear distortion of the pre-amplifier has a negligible impact on modulated signal quality except in the median RF power region, where the noise and nonlinear distortion are both minimized. If it is assumed that the VNA receiver AWGN and nonlinear distortion from intermodulation by the pre-amplifier measured in  $EVM_{EQ}$  can be modeled as two uncorrelated random error variables, the noise component  $EVM_{SNR}$  and intermodulation component  $EVM_{IMD}$  for the measured  $EVM_{EQ}$  can be estimated from the root-sum-square as shown in equation (3.22).

$$EVM_{EQ} = \sqrt{EVM_{SNR}^2 + EVM_{IMD}^2} \quad (3.22)$$

Fig. 3.26(b) shows the EVM components of equation (3.22), where  $EVM_{SNR}$  is estimated as  $EVM_{SNR} = \sqrt{1/SNR}$ , and SNR is estimated by assuming that  $EVM_{EQ} = EVM_{SNR}$  for the lowest RF power level ( $P_{RF} = -55$  dBm) and increasing this minimum SNR in direct proportion with the RF power level increase for all remaining power levels. Then  $EVM_{IMD}$  is computed from the measured  $EVM_{EQ}$  and estimated  $EVM_{SNR}$  values via equation (3.22). Note that the minimum  $EVM_{EQ}$  and maximum difference between  $EVM_{EQ}$  and  $EVM_{UN}$  in Fig. 3.26(b) occur at  $P_{RF} = -30$  dBm, where the  $EVM_{SNR}$  and  $EVM_{IMD}$  curves intersect. Furthermore, the decomposition of  $EVM_{UN}$  into three uncorrelated components  $EVM_{H(f)}$ ,  $EVM_{SNR}$ , and  $EVM_{IMD}$  in equations (3.21) and (3.22) is consistent with the methodology applied in the EVM estimation from CW stimulus presented in [73] and shown in equation (2.6). Fig. 3.26(c) and (d) show the  $EVM_{UN}$  measured for the CATR link with and without the pre-amplifier at  $P_{RF} = -22.5$  dBm for the E and H planes of the AUT respectively. The results show that pre-amplifier intermodulation distortion elevates  $EVM_{UN}$  for all far field angles (red) relative to the CATR link measurements with only the passive AUT (blue). Fig. 3.24(b) also demonstrates that the broadband impedance mismatch between the pre-amplifier and AUT results in only a slight increase (about 1.5% maximum) in  $EVM_{H(f)}$  relative to that of the AUT in isolation.



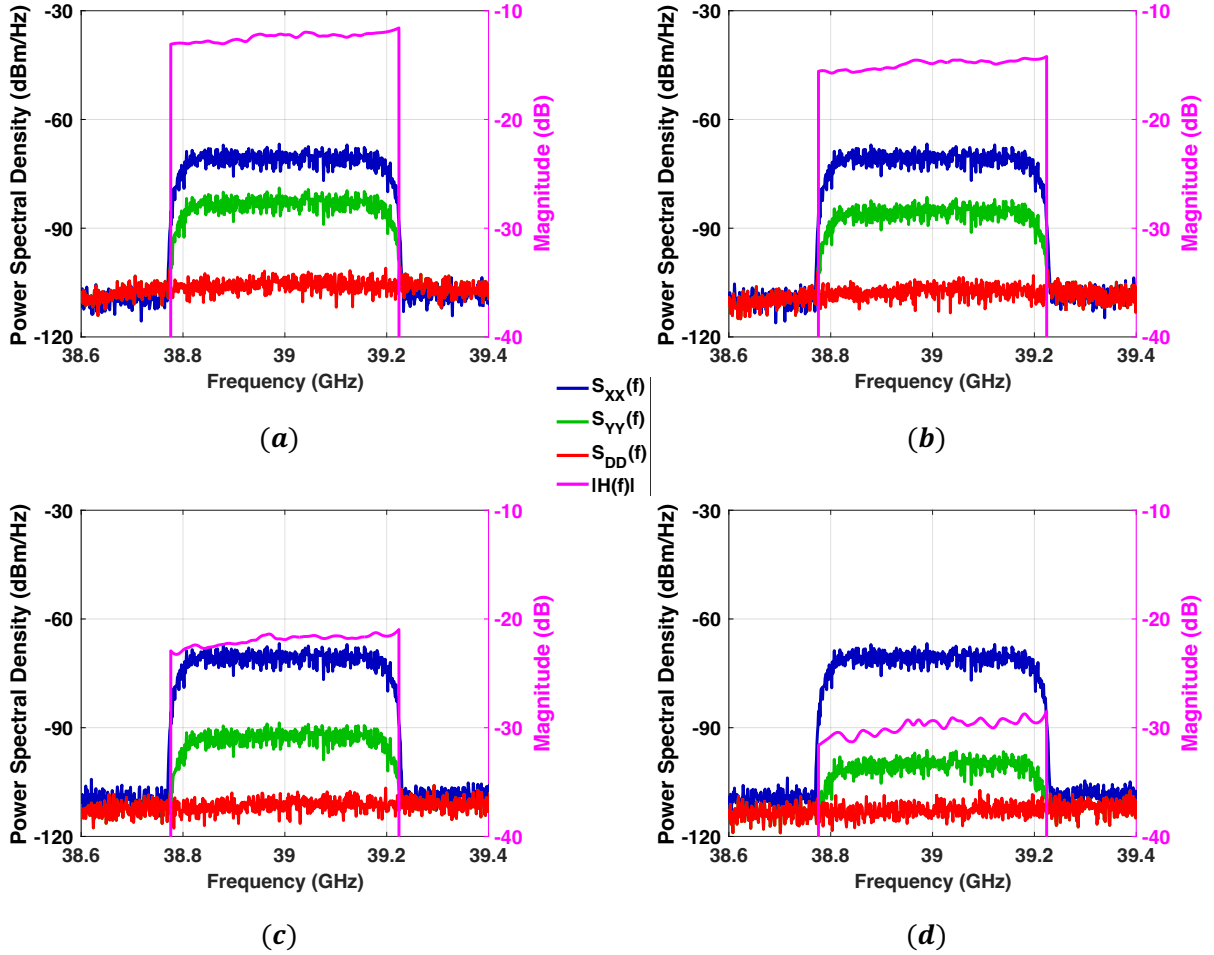


Figure 3.27 Power spectral densities of the modulated stimulus applied to the pre-amplifier in front of the AUT  $S_{XX}(f)$  (blue) and measured on the PNA-X reference receiver  $R1$ , the received signal from the CATR feed horn  $S_{YY}(f)$  (green) measured on receiver  $B$ , and the distortion spectrum  $S_{DD}(f)$  (red) described in section 2.3, with the corresponding modulated gain  $|H(f)|$  (magenta) overlaid. These results are for the AUT E-plane angles ( $\phi_t = 0^\circ$ ) (a)  $\theta_t = 0^\circ$ , (b)  $\theta_t = 15^\circ$ , (c)  $\theta_t = 30^\circ$ , and (d)  $\theta_t = 45^\circ$ . The distortion spectrum and modulated gain are elevated relative to those of Fig. 3.21 due to inclusion of the transmit pre-amplifier.

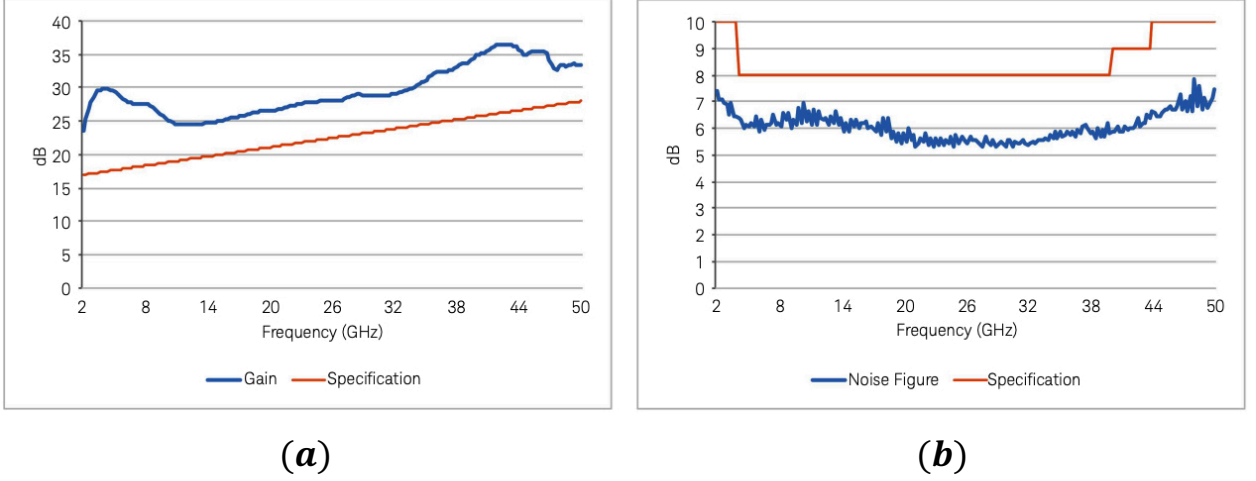


Figure 3.28 Typical gain (a) and noise figure (b) of the U7227A pre-amplifier versus frequency. The gain and noise figure at  $f_c = 39$  GHz are approximately 33 dB and 6 dB respectively [94].

The PSD of the transmitted signal  $S_{XX}(f)$ , received signal  $S_{YY}$ , distortion component  $S_{DD}(f)$ , and modulated gain  $|H(f)|$  are shown for four E-plane observation angles spaced  $15^\circ$  apart for the CATR link with pre-amplifier front end in Fig. 3.27. A few observations can be made in comparing these EVM results with those of the AUT-only CATR link presented in Fig. 3.21: First, the modulated gain of the CATR link with the pre-amplifier front end in Fig. 3.27 is approximately 33 dB higher at  $f_c = 39$  GHz than that of the CATR link with AUT only in Fig. 3.21, which is consistent with the 33 dB of gain at OP1dB specified by the U7227A pre-amplifier datasheet [94], as highlighted in Fig. 3.28(a). However, because RF carrier power from the VSG was reduced by 37.5 dB to prevent excessive compression, SNR decreased by 4.5 dB. An additional 6.0 dB of SNR degradation results from the noise figure of the pre-amplifier, which is presented in Fig. 3.28(b). Consequently, the CATR link SNR is approximately 10.5 dB lower when the pre-amplifier is included in the transmission path. If  $EVM_{EQ} = \sqrt{1/SNR}$  at  $\theta_t = 0^\circ$  in Fig. 3.26(d) for the AUT-only case (blue), then SNR is 36.1 dB for this case and would be approximately 25.6 dB when the pre-amplifier is added. This would result in  $EVM_{EQ}$  increasing from 1.56% to 5.23% in the absence of additional nonlinear distortion components ( $EVM_{EQ} = \sqrt{1/SNR}$ ). However, because the pre-amplifier was operated at its OP1dB compression point and because  $EVM_{EQ}$  was measured at 7.92% when the pre-amplifier was included, the intermodulation distortion component  $EVM_{IMD}$  is

non-zero and estimated to be 5.95% using equation (3.22) where  $EVM_{SNR} = 5.23\%$ . This increase in both  $EVM_{SNR}$  and  $EVM_{IMD}$  elevates distortion spectrum  $S_{DD}(f)$  with respect to the received signal spectrum  $S_{YY}(f)$ , which can be observed by comparing Fig. 3.21 with Fig. 3.27, and results in a higher  $EVM_{UN}$  and  $EVM_{EQ}$  at each far field angle as shown in Fig. 3.26(c) and (d). In contrast to these two EVM components, which represent nonlinear distortion of the received signal and depend on the RF output power of the source, the linear distortion component  $EVM_{H(f)}$  stabilizes as RF output power increases and the measured amplitude and phase responses of the CATR link converge across the test signal bandwidth. This is demonstrated through S21 and EVM measurements of a separate CATR link as a function of RF output power, which are presented in Fig. 3.29. A sharp discontinuity in the measured  $|S21(f_c)|$  at  $P_{RF} = -25$  dBm, due to automatic adjustment of the VNA attenuation settings, is shown in Fig. 3.29(a). However, for  $P_{RF} \geq -25$  dBm,  $|S21(f)|$  remains nearly constant, as shown in Fig. 3.29(b). Similarly, for both a 400 and 800 Mbaud 16-QAM test signal,  $EVM_{H(f)}$  remains nearly constant for  $P_{RF} \geq -15$  dBm, as shown in Fig. 3.29(c)-(d).

### 3.5 Summary

This chapter presented the modeling, simulation, and measurement of EVM resulting from the wideband modulated signal transmission of a far field passive antenna link. The voltage transfer function for an UWB model of a far field antenna link was derived in terms of the vector effective length properties of the transmitting and receiving antennas, and relevant EVM simulation methods that have been applied in the literature were reviewed. Estimates of millimeter-wave microstrip patch and conical horn antenna link voltage transfer functions  $H_{est}(f)$  were obtained using full-wave time domain simulations and the UWB model. These were applied to a 16-QAM test signal to simulate the EVM from the passive antenna link transmission. Only the amplitude distortion  $|H_{est}(f)|$  was included for the microstrip patch link, but a more robust model for both amplitude and phase distortion was presented and applied to the horn link. Indirect far field measurements of the horn link were also performed in a CATR, and a detailed comparison of simulated and measured EVM results was presented.

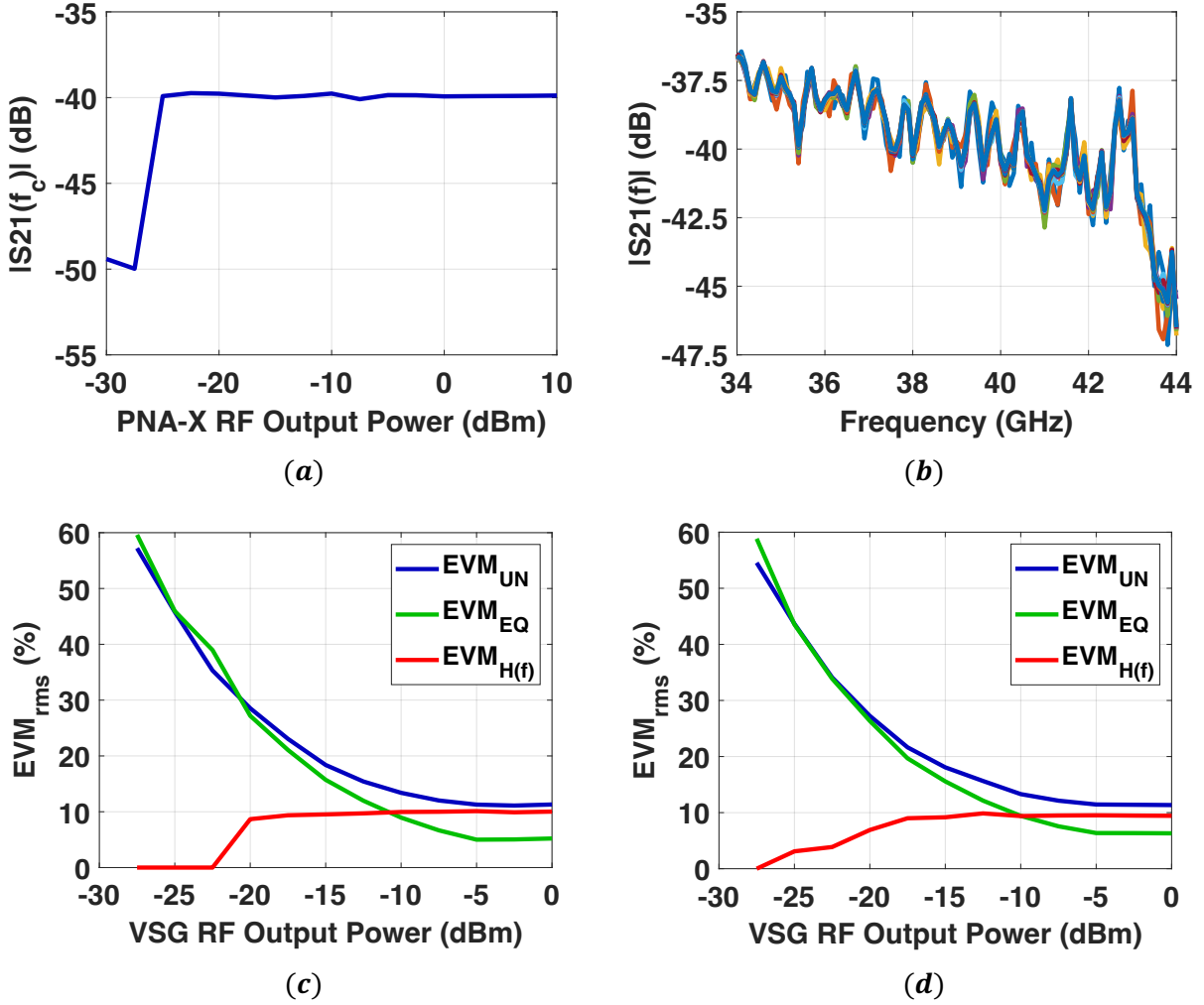


Figure 3.29 (a)  $|S_{21}|$  at  $f_c = 39$  GHz as a function of PNA-X RF output power level where PNA-X attenuation settings are shown to change at -25 dBm, (b)  $|S_{21}(f)|$  for a 10 GHz span centered at  $f_c = 39$  GHz plotted for PNA-X RF output power levels [-25 dBm:2.5 dBm:10 dBm], and (c)-(d) EVM of the Ka-band horn link without pre-amplifier measured in a CATR as a function of VSG RF output power for 16-QAM test signals with 400 and 800 Mbaud symbol rates respectively. Both  $|S_{21}|$  and  $EVM_{H(f)}$  stabilize at high RF output power levels.

## CHAPTER 4

# Far Field EVM Characterization of Millimeter-Wave Phased Arrays

### 4.1 Review of Phased Array Modeling Methods for Far Field EVM Analysis

Highly-sophisticated phased array models would be required to fully characterize simultaneous transmission and reception of wideband modulated signals by a large number of array elements, nonlinearity of active beamforming transceiver components, and mutual coupling variations for numerous beam states. As a result, most researchers develop reasonably-simplified models that only account for some of these forms of signal distortion from phased array transmission.

One technique for simulating the far field EVM of large phased arrays is to develop an analytical expression in which the array element amplitude and phase errors can be modeled as random variables [95, 96]. For example, in [95], the EVM from an  $N$ -element hexagonal phased array was calculated from equation (4.1), where  $N$  is the number of antennas,  $W_{mn}$  is the weighting coefficient for array element  $n$  and beam state  $m$ ,  $A_{mn}$  is the spatial response function (4.2),  $\sigma_\delta^2$  and  $\sigma_\psi^2$  are the variances of amplitude and phase error  $(1 + \delta_n)e^{j\psi_n}$  of each element  $n$ , and  $G_0 = \sum_{n=1}^N W_{mn}A_{mn}$  is the sum of element excitations for all  $m$  beam states. In equation (4.2),  $(\rho_n, \varphi_n)$  is the element location as shown in Fig. 4.1(a), and  $(\theta_0, \varphi_0)$  is the beam-steering angle. The phased array dimensions and EVM for the Gaussian random amplitude and phase variables  $\delta_n$  and  $\psi_n$  with different ranges are presented in Fig. 4.1(b).

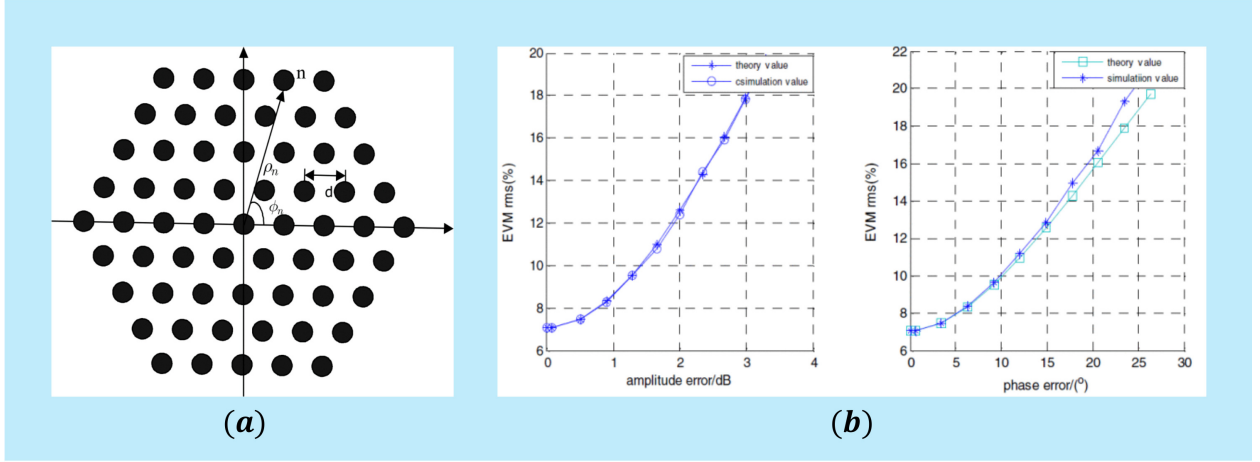


Figure 4.1 A digital beamforming array EVM simulation based on random amplitude and phase errors  $\delta_n$  and  $\psi_n$  in equations (4.1) and (4.2) [95]: (a) phased array dimensions and element  $n$  cylindrical coordinates  $(\rho_n, \phi_n)$  and (b) EVM simulation results for amplitude (left) and phase (right) error ranges with  $SNR = 23$  dB.

$$EVM = \sqrt{\sum_{n=1}^N |W_{mn} A_n|^2 \frac{(\sigma_\delta^2 + \sigma_\psi^2)}{G_0^2} + \frac{1}{SNR}} \quad (4.1)$$

$$A_n = \exp\left\{-j \frac{2\pi}{\lambda} \rho_n \sin \theta_0 \cos(\varphi_n - \varphi_0)\right\} \quad (4.2)$$

In [96], another analytical expression with random variables was used to predict how different numbers and distributions of damaged array elements would influence the EVM. In [97], IQ amplitude and phase errors were modeled as random variables and used to estimate the EVM of a 64-QAM test signal transmitted and received by identical four-element phased arrays. Modeling amplitude and phase errors of array elements as random variables can provide some insight into the statistical correlations of the far field EVM performance, but a more accurate EVM characterization requires a modeling of amplitude and phase errors which is consistent with the RF power and frequency response of the distortion-dominating active components, particularly power amplifiers. This was demonstrated in section 3.4 through a comparison of EVM measurements of a Ka-band horn antenna with and without a pre-amplifier front end.

One approach to incorporating power amplifier nonlinearity effects in phased array EVM simulations is to apply a cubic polynomial model for the AM-AM and AM-PM modulation as a function of the input signal power  $P_{in}$ , as shown in Fig. 4.2(a). For example, in [98], the active array element channels were modeled in MATLAB as linear gain segments with random amplitude and phase errors cascaded with memoryless nonlinearity segments that apply AM-AM and AM-PM modulation based on the element channel's input signal power  $P_{in}$ . The sum of the distorted signals from all array element channels is then demodulated to estimate the EVM of a receiver located in the far field of the phased array. The EVM results for a 64-element array transmitting a 64-QAM signal at 5 dB backoff from the P1dB compression point ( $P_{in} = -19$  dB) is plotted in Fig. 4.2(b) as a function of the RMS gain and phase error, and EVM is plotted in Fig. 4.2(c) for the same backoff level with an RMS gain error of 1.0 dB and phase error of  $10^\circ$  as a function of the number of array elements. These results demonstrate that EVM is more-strongly correlated with gain error than phase error because the AM-AM and AM-PM distortion depends on gain, and phase error averages out in the summation of received signals from a large number of elements [98]. This is highlighted in Fig. 4.2(c) by the convergence of sixty EVM simulations as the number of array elements increases. Beam scanning toward an angle  $(\theta_t, \phi_t)$  could have been simulated in this model by applying a progressive phase shift to each of the array element channels, based on an assumed array geometry and element spacing, and adding time delays before the ideal combiner to compensate for free space propagation.

A similar MATLAB phased array transmission model was implemented in [99] to simulate the effects of power amplifier (PA) nonlinearity variation on the far field EVM of a uniform linear array. Power amplifier AM-AM and AM-PM distortion characteristics as a function of  $P_{in}$  were based on a lookup table from measurements of a 13 GHz CMOS power amplifier (PA), and raised-cosine filtering was applied to a 100 MHz-wide 64-QAM test signal. Monte-Carlo simulations demonstrated that EVM is reduced slightly with an increase in both the number of array elements and range of random variations in PA nonlinearity in the absence of digital predistortion (DPD). They also showed that the EVM reduction is significantly enhanced when DPD is applied. Consequently, the authors of [99] suggest that it might be possible to

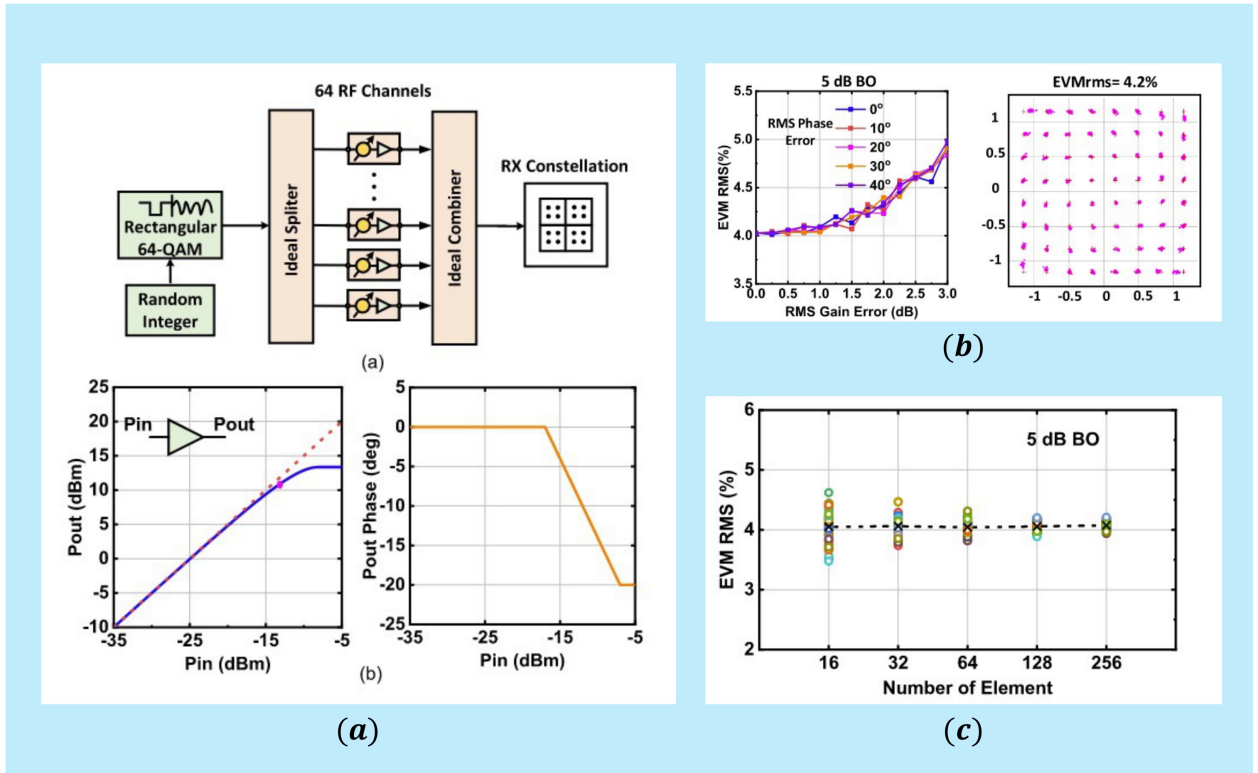


Figure 4.2 A model of phased array 64-QAM signal transmission implemented in MATLAB and EVM simulation results [98]: (a) phased array model and plots of memoryless power amplifier AM-AM (left) and AM-PM (right) vs.  $P_{in}$ , (b) EVM vs. RMS amplitude and phase error for 5 dB backoff ( $P_{in} = -19$  dB), and (c) EVM vs. number of elements for 5 dB backoff, 1 dB RMS amplitude error, and  $10^\circ$  RMS phase error (for 60 iterations).

reinforce DPD and achieve lower EVM by intentionally biasing power amplifiers in phased array element channels to generate a large initial error variation. In [100], a simulation of PA nonlinearity variation based on a Gaussian distribution of the IP1dB showed that adjacent channel power ratio (ACPR) also decreases with an increase in the number of array elements.

However, there are certain shortcomings in the baseband phased array signal transmission models of [98] and [99] that should be addressed for more accurate EVM simulations. For example, the authors of [98] acknowledged that random phase errors would reduce the phased array gain and SNR at the receiver, thereby increasing EVM. Unlike that of the Ka-band horn link simulation presented in section 3.3, this model did not include the effect of finite, gain-dependent SNR on EVM. Additionally, array element patterns and frequency response variations due to fabrication tolerances and mutual coupling effects were not included in these



two models. Because beam scanning changes the load impedances of array element power amplifiers and influences their nonlinear characteristics, it is critical that these electromagnetic effects be included in phased array signal transmission models. Finally, the cubic polynomial models do not capture power amplifier memory effects, which can also have an effect on the EVM of the signal received in the far field.

Researchers have started to address some of these challenges and have worked to develop more-advanced phased array signal transmission models that include some of these effects by deriving mathematical representations or combining power amplifiers load pull simulations with active S-parameter simulations of array elements [101–105]. In [104], a Volterra series representation of a dual-input power amplifier was designed to include nonlinearities, mutual coupling, and wideband impedance mismatch effects. The PA model coefficients for each array element channel were obtained from load pull measurements and array element S-parameter measurements. In [105], an algorithm was designed to use load-pull and S-parameter data to estimate PA nonlinearities from mutual coupling effects in phased array beam scanning, and radiated far field nonlinearity was characterized in terms of received power, AM-AM, and AM-PM distortion. In addition to these power amplifier contributions to the far field EVM, researchers have modeled and simulated the effects of large array beam scanning ISI, carrier aggregation, and beam squint. In [106], a MATLAB model of phased array signal transmission was used to show that a linear equalizer with a sufficient number of channel taps could compensate for variation in array element signal time delays during beam scanning, regardless of QAM modulation order, beam scan angle, and symbol rate. This model and the EVM results for a 64-QAM test signal are presented in Fig. 4.3. The beam scanning was modeled by applying a true time delay instead of a phase shift to each array element, and RRC filters were included at both the transmit and receive ends as highlighted in Fig. 4.3(a). When a 17-tap linear equalizer was trained on 10% of the ideal 64-QAM symbols and applied to the far field received signal from a 16x16 phased array scanned in the azimuth plane, the EVM was reduced to nearly 0.0% as shown in Fig. 4.3(c). Other phased array transmission models have been synthesized to show the combined the effects of carrier aggregation and power amplifier nonlinearities [107] and base station phased array gain and positioning within

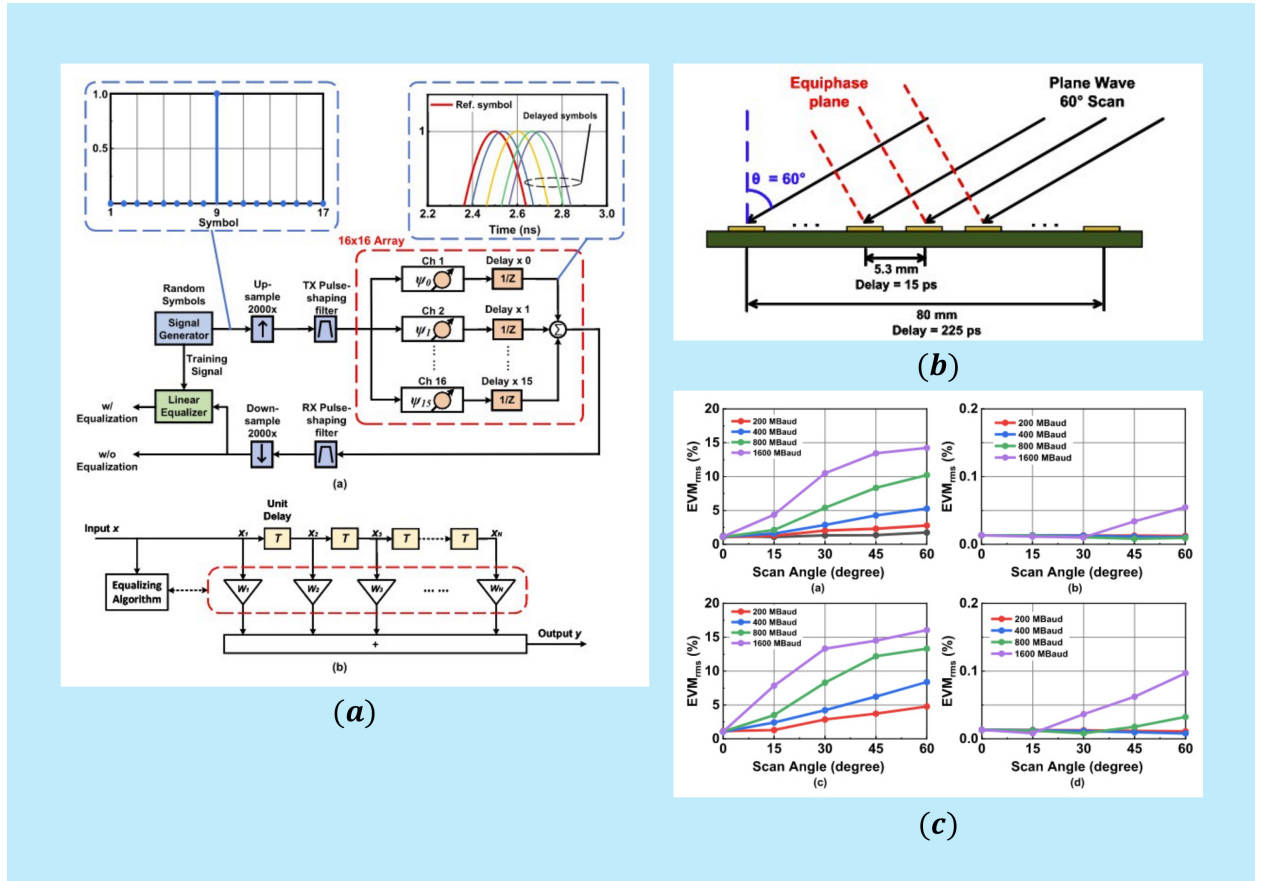


Figure 4.3 A model of phased array signal transmission implemented in MATLAB with linear equalization compensating for beam scanning ISI and EVM results [106]: (a) block diagram of 16x16 array model and linear equalizer, (b) array diagram showing the time delay differences between elements at a  $60^\circ$  scan angle, and (c) EVM results for different scan angles (x-axis) and modulation rates (curves).

indoor-to-outdoor multipath links [108] on the EVM of wideband modulated signals.

In this modern age of high data rate millimeter-wave communication systems, the development of more accurate and efficient simulation models for phased array signal transmission and EVM estimation remains a critical challenge. As previously described, one of the main deficiencies of the simulation models surveyed in the literature is that the unique frequency response of each array element and its dependence on mutual coupling is not accounted for. This can be remedied by extending techniques presented in the microstrip patch and Ka-band conical horn link simulations from sections 3.2 and 3.3 to model voltage transfer functions for the far field links between each active array element and an arbitrary receiving antenna.

Section 4.2.2 presents a phased array EVM simulation model including amplitude distortion from both the embedded element transfer functions  $|H_{mn}(f)|$  and beam squint effect resulting from slight variations in scanned beam peaks for each of the frequency components in the modulated test signal [14, 106]. This model uses far field probe data from full-wave simulations of a central element within an 8x8 microstrip patch array in precisely the same manner as the EVM simulation model for the 28 GHz microstrip patch presented in section 3.2, and it applies a phase gradient based on the element spacing and beam scan angle. Section 4.2.3 presents a more advanced model in which the complex voltage transfer functions for each element of the same 8x8 array are synthesized using the methodology described in section 3.3 and used to determine the EVM of the far field sum of element-transmitted 16-QAM signals. Amplitude tapering and phase quantization errors are also injected to observe their effects on the far field EVM of the 8x8 array. Section 4.3 provides an overview of the advantages and disadvantages of using CATRs and plane wave converters (PWCs) for indirect far field EVM measurements. Section 4.4 describes EVM measurements of the 8x8 millimeter-wave phased array from [98] using a CATR and a PNA-X network analyzer with frequency domain spectral correlation. Finally, section 4.5 summarizes the contents of this chapter.

## 4.2 EVM Simulation of an 8x8 Microstrip Patch Phased Array

### 4.2.1 Introduction

At millimeter-wave frequencies, active antenna arrays with thousands of radiating elements can be efficiently integrated with silicon RF beamforming circuits in printed circuit boards. This has led to increased interest in developing large active phased arrays for broadband 5G and satellite communication systems, as described in section 1.1. Nonetheless, because beamforming is typically achieved through narrowband RF phase shifters rather than bulky and expensive time delay control circuits, the main beam direction deviates from the targeted beam direction used to set the phase gradient at the center frequency of the channel  $f_c$ . This effect is known as beam squint, and while its influence on the EVM of a 64-QAM signal has been simulated for square arrays of isotropic radiators [14], it has not yet been simulated

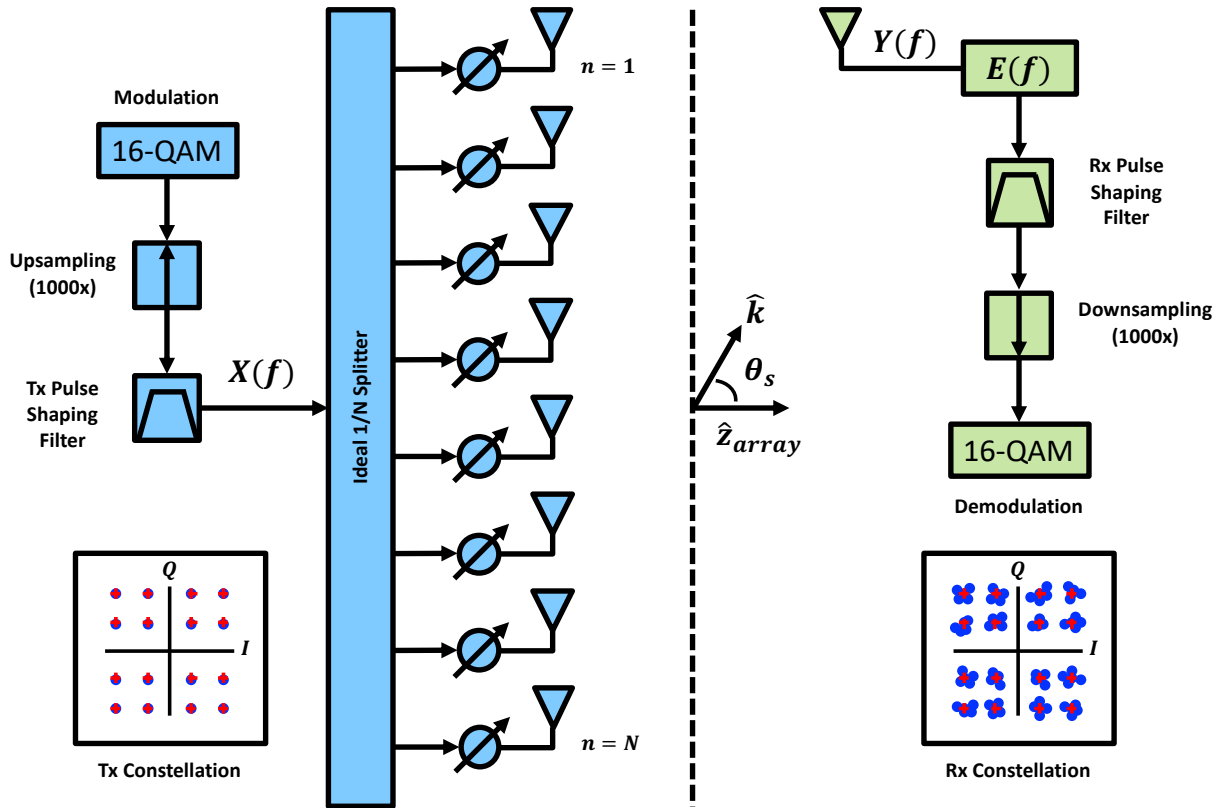


Figure 4.4 MATLAB model for 16-QAM signal transmission from the phased array transmitter (blue) to the single antenna receiver (green). Each phased array element is connected to an ideal phase shifter and fed through a lossless 1/N divider, where N is the number of elements. EVM represents the difference between transmitted and received symbols after normalization.

in conjunction with the frequency-dependent electric field pattern of the array elements at various scan angles. Since EVM is a measure of the amplitude and phase differences between the transmitted symbols  $x(t_n)$  and equalized received symbols  $y(t_n) * e(t_n)$ , as shown in equation (1.2) [35], it is related to data throughput rate in wireless links, and it has been identified as a figure of merit for 5G active antenna array systems. [23] The aim of this work is to model the far field EVM of a 5G phased array as its main beam is scanned in E and H-field planes, using MATLAB and embedded element patterns from full-wave simulation in CST Microwave Studio.

## 4.2.2 Simulation Model and EVM Results for Beam Scanning with Beam Squint and Embedded Element Patterns

The signal processing algorithm for the transmitting phased array is illustrated in the block diagram of Fig. 4.4. A sequence of 1000 random symbols is 16-QAM modulated, upsampled by a factor of 1000, and passed through a RRC filter with rolloff factor  $\alpha = 0.4$ . A second RRC filter with the same  $\alpha$  is implemented in the receiver to generate an ISI-eliminating matched filter. The frequency spectrum of the common port voltage signal  $X(f)$  is divided by the number of radiating elements  $N$ , which are arranged in a square lattice with a separation of  $d = 3.85$  mm ( $0.5\lambda$  at 39 GHz) in both  $\hat{x}$  and  $\hat{y}$  directions, such that excitation is uniform in amplitude. The radiated far field of the phased array for a specific beam scan angle  $(\theta_s, \phi_s)$  at the signal center frequency  $f_c = 39$  GHz is evaluated as shown in equation (4.3):

$$\vec{E}_{array} = \sum_{m=1}^M \sum_{n=1}^N X_{mn}(f) \vec{H}_{mn}(f, \theta, \phi) e^{j[(m-1)\psi_x + (n-1)\psi_y]} \quad (4.3)$$

where  $X_{mn}(f)$  is the spectrum of the complex voltage signal that is applied to the port of each phased array element  $(m, n)$ ,  $\vec{H}_{mn}(f, \theta, \phi)$  is the normalized vector effective length of each array element, and  $\psi_x, \psi_y$  are the beam-steering phase coefficients in (4.4a) and (4.4b).

$$\psi_x = kd \sin \theta \cos \phi - k_c d \sin \theta_s \cos \phi_s \quad (4.4a)$$

$$\psi_y = kd \sin \theta \sin \phi - k_c d \sin \theta_s \sin \phi_s \quad (4.4b)$$

In equation (4.3), the frequency can be modeled as  $f = f_c \pm \Delta f$ , where  $\Delta f$  is the frequency offset from center frequency  $f_c$ . In equations (4.4a)-(4.4b),  $k_c = 2\pi/\lambda_c$  where  $\lambda_c$  is wavelength at  $f_c$ ,  $(\theta, \phi)$  is the far field observation angle, and  $(\theta_s, \phi_s)$  is the beam scan angle. It is assumed that the phase shifts applied to array elements are continuous from 0 to 360°, with no phase quantization. Vector effective length  $\vec{H}_{mn}(f, \theta, \phi)$  is normalized by its magnitude at  $f_c$  and introduces amplitude distortion in the radiated fields of each array element. Because the EVM analysis in this section is for large planar arrays, the vector pattern of embedded

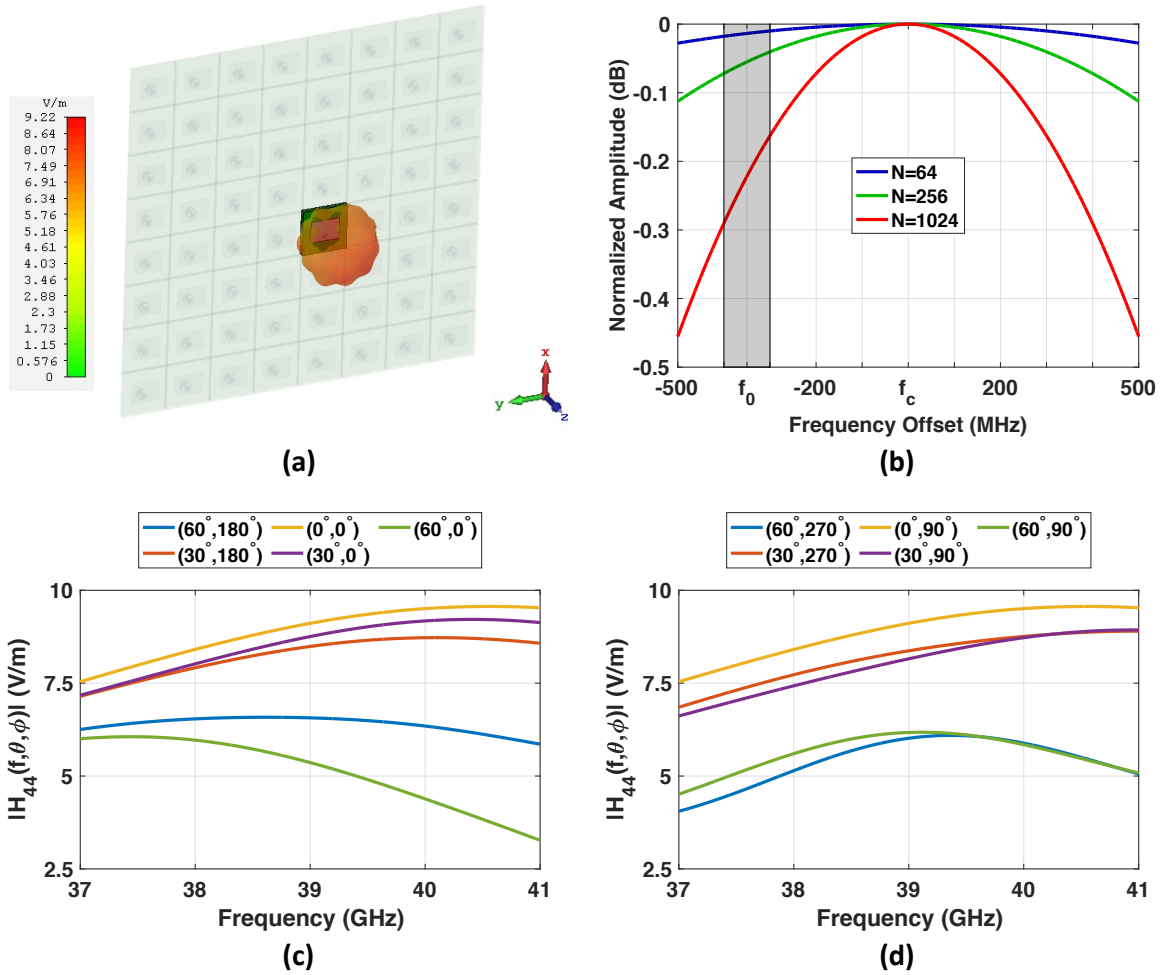


Figure 4.5 (a)  $|\vec{H}_{44}(f_c, \theta, \phi)|: |\vec{E}_H|$  field pattern for embedded element  $(m, n) = (4, 4)$  in an 8x8 microstrip patch array at  $f_c = 39$  GHz. (b) Normalized beam squint amplitude versus frequency offset from  $f_c$  for  $N$  isotropic elements with a 100 MHz bandwidth centered at  $f_0$  highlighted in gray. (c)-(d)  $|\vec{H}_{44}(f, \theta, \phi)|$  at various E- and H-field plane angles respectively.

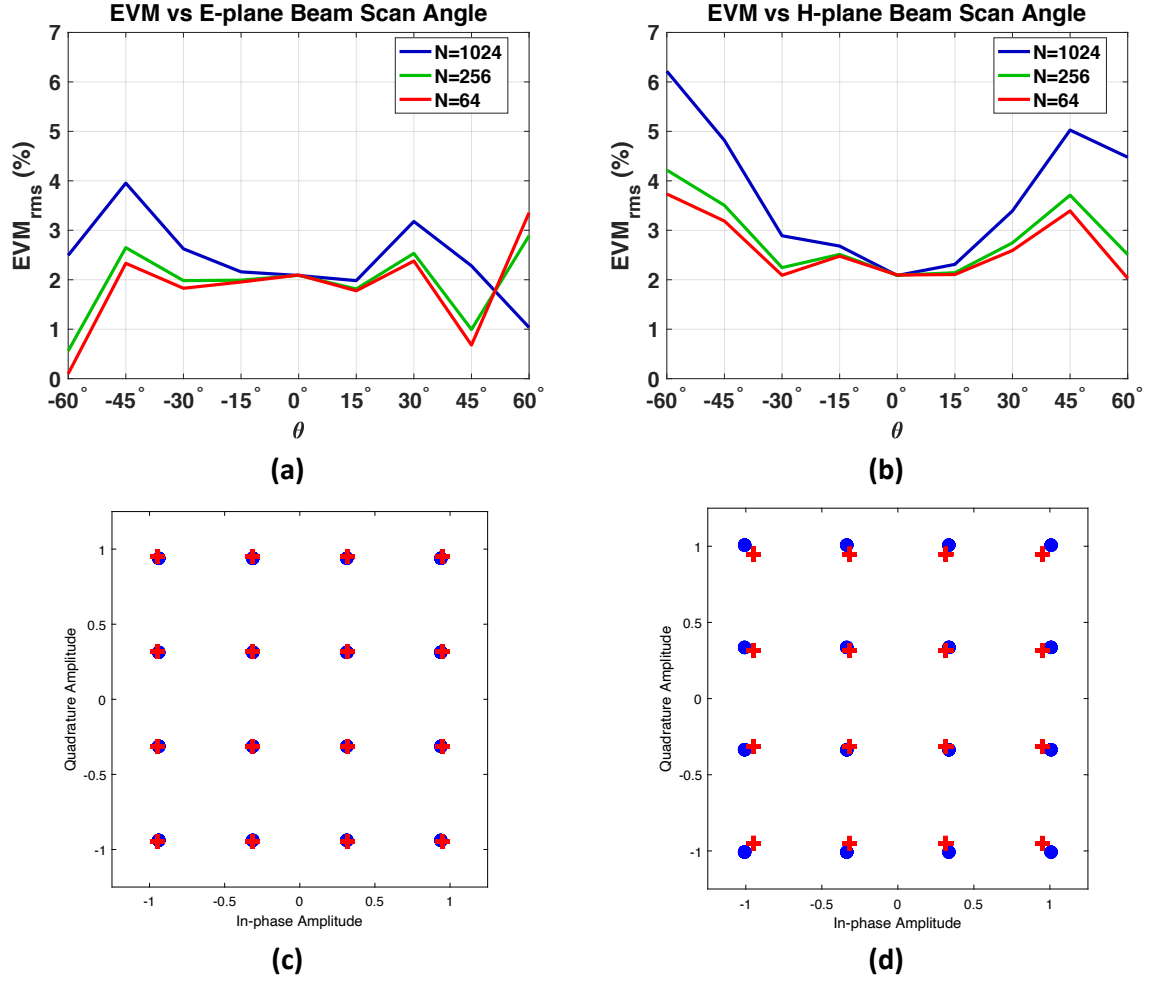


Figure 4.6 (a)-(b) EVM of the 16-QAM test signal for azimuth plane beam scan angles  $\theta_s$  in the E-plane and H-plane respectively for the 32x32 (blue), 16x16 (green), and 8x8 (red) phased arrays. (c)-(d) Constellation diagrams showing the ideal transmitted symbols (red) and simulated received symbols (blue) for the beam scan angles  $(\theta_s, \phi_s) = (60^\circ, 0^\circ)$  in the E-plane and  $(\theta_s, \phi_s) = (60^\circ, 90^\circ)$  in the H-plane respectively.

element  $(m, n) = (4, 4)$  at the center of the 8x8 microstrip patch array shown in Fig. 4.5 is used for all  $\vec{H}_{mn}(f, \theta, \phi)$  regardless of the simulated array size, and edge effects are ignored. The 8x8 array is slightly smaller than the  $5\lambda \times 5\lambda$  minimum size recommended for embedded element modeling in [109], but because the coupling between embedded element (4, 4) and the edge elements was less than  $-20$  dB, this was considered a reasonable approximation. The port of embedded element (4, 4) is excited with the default Gaussian voltage signal in CST Microwave Studio while all of the other array elements are terminated in matched loads.

The magnitude of the Ludwig's 3rd horizontal E-field component, shown in equation (3.14a), was simulated at far field probes located 1.0 meter from the center of the embedded element patch surface at all beam scan angles. Because the far field probe results are normalized with respect to applied voltage, they are used as  $\vec{H}_{mn}(f, \theta, \phi)$  in equation (4.3) and assumed to convert input voltage at element terminals directly to  $\vec{E}_H$ . These element fields are summed at far field observation angles  $(\theta, \phi) = (\theta_s, \phi_s)$  using equations (4.3) and (4.4a)-(4.4b). The receiving antenna is assumed to be co-polarized with the phased array radiated far field vector  $\vec{E}_{array}$  and have a uniform-amplitude vector effective length for all frequency components of the test signal  $X(f)$ , such that it does not further distort the received signal spectrum  $Y(f)$ .

The EVM of a 16-QAM test signal with 100 Mbaud symbol rate is calculated for  $N = 1000$  symbols using equation (1.2), where  $x(t)$  and  $y(t)$  are the IFFT of  $X(f)$  and  $\vec{E}_{array}(f, \theta, \phi)$  respectively and  $e(t)$  is a constant that represents the reciprocal of the phased array input voltage to radiated far field gain  $e(t) = |X(f_0)/\vec{E}_{array}(f_0, \theta, \phi)|$  at carrier frequency  $f_0 = 38.65$  GHz. The carrier is assumed to be one of eight independently-modulated carriers spanning an 800 MHz channel with center frequency  $f_c = 39$  GHz. In this scenario, the edge carrier  $f_0$  has the largest offset from  $f_c$ , which is the the frequency used to calculate the phase gradient applied to the array elements. Consequently, it experiences the highest degree of beam squint distortion as indicated in Fig. 4.5(b). Still, as demonstrated in Fig. 4.6, the EVM increase only exceeds 1% for large scan angles ( $\theta_s \geq 30^\circ$ ), and this increase in EVM is amplified in the H-plane of larger phased arrays due to the enhancement of the beam squint effect with a larger number of elements. However, for the large E-plane scan angles, EVM decreases for the largest phased array ( $N = 1024$ ) because  $\vec{H}_{mn}(f, \theta, \phi)$  nullifies beam squint amplitude roll-off. Therefore, in this example, embedded element frequency response is a greater contributor to the received signal linear distortion than beam squint, except when large planar phased arrays ( $N \geq 256$ ) transmit wideband signals ( $\geq 100$  Mbaud) at large scan angles ( $\theta_s \geq 30^\circ$ ).



### 4.2.3 Simulation Model and EVM Results for Beam Scanning with Individual Element Patterns, Amplitude Taper, and Phase Quantization

The phased array signal transmission model applied to the EVM simulations of subsection 4.2.2 provided some insight on the relative effects of beam squint and active element frequency response for square arrays of various sizes. However, this passive array model was subject to a few limitations: First, the group delay distortion of the embedded element at each scan angle was excluded in these simulations just as it was for the boresight EVM simulation of the 28 GHz microstrip patch antenna in section 3.2. This was resolved by adopting the complex antenna voltage transfer function modeling method implemented for the Ka-band horn link simulation of section 3.3, where the same receive horn was assumed to capture the sum of signals transmitted from all 64 array elements at a separation distance of  $r = 3.0$  m. Secondly, all of the radiating elements were assumed to have the same gain versus frequency profile for the L3 horizontal polarization as embedded element  $(m, n) = (4, 4)$ , which is highlighted in Fig. 4.5(a), regardless of the array size or the element's unique position within the array. This simplification was eliminated in the following EVM simulations by exporting the field probe results for each element in the array via a customized control script produced in MATLAB. Unique antenna link voltage transfer functions  $H_{mn}(f, \theta_s, \phi_s)$  are generated from these array element field probe results at each beam scan angle through the process outlined in section 3.3 and substituted for  $\vec{H}_{mn}$  in equation 4.3 to obtain the received signal spectrum  $Y(f)$ , rather than the received field  $\vec{E}_{array}$ : Unlike the EVM simulation of subsection 4.2.2, an ideal receiving antenna with zero amplitude and phase distortion was not assumed. The design details for the coax-fed microstrip patch elements in the 8x8 array, positioning of far field probes at E-plane beam scan angles  $(\theta_s, \phi_s)$ , and simulated  $\vec{E}_H$  and  $S_{11}$  versus frequency for central patch element  $(m, n) = (4, 4)$  are presented in Fig. 4.7. The gain and normalized group delay of the voltage transfer functions  $H_{mn}(f)$  for each element  $(m, n)$  at each E-plane scan angle in the CST and MATLAB simulations are shown in Figs. 4.8 and 4.9 respectively. It is clear from these results that the least element-to-element variation for both amplitude and phase response occurs at the scan angles in close proximity to boresight  $(\theta_s, \phi_s) = (0^\circ, 0^\circ)$ , whereas the greatest variation occurs at large scan angles such as  $\theta_s = \pm 60^\circ$ . Consequently,

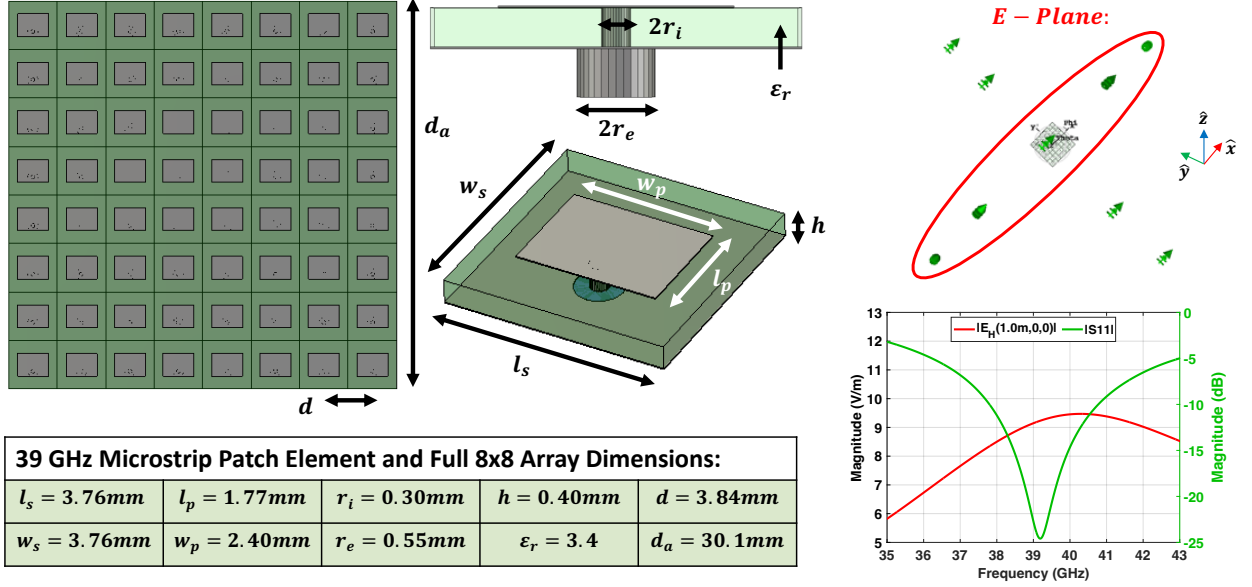


Figure 4.7 Design specifications for the 8x8 coax-fed microstrip patch phased array used in EVM simulations of section 4.2, E-plane far field probe positions, and  $\vec{E}_H(f)$  and  $S11(f)$  for embedded element  $(m, n) = (4, 4)$ . The resonant frequency of this patch element is 39 GHz.

in addition to the SNR degradation from beam scan loss at large angles, a higher degree of linear distortion should be expected to result from superposition of radiated fields of the array elements transmitting wideband single-carrier signals toward these directions. Both of these phased array beam scanning effects can degrade signal quality and result in low EVM if the received signal is un-equalized.

A 16-QAM test signal with 400 Mbaud symbol rate was generated and passed through a RRC filter with rolloff factor  $\alpha = 0.4$  and each of the array element channel filters  $H_{mn}(f)$  presented in Figs. 4.8 and 4.9 to estimate the signals received in the far field from each of the transmitting array elements at specific E-plane scan angles. The in-phase components of these signals for each beam scan angle are shown in the time domain plots of Fig. 4.10. Differences in element-to-element amplitude distortion are visible for larger scan angles such as  $\theta_s = \pm 60^\circ$ . The signals received from each array element at each beam scan angle, excluding the beam scan phase gradient factor in equation (4.3) and propagation delays to the far field receiver position, are summed together to model the same ideal OTA combination as the phased array simulation models from [98] and [106]. The un-equalized EVM is then calculated from the

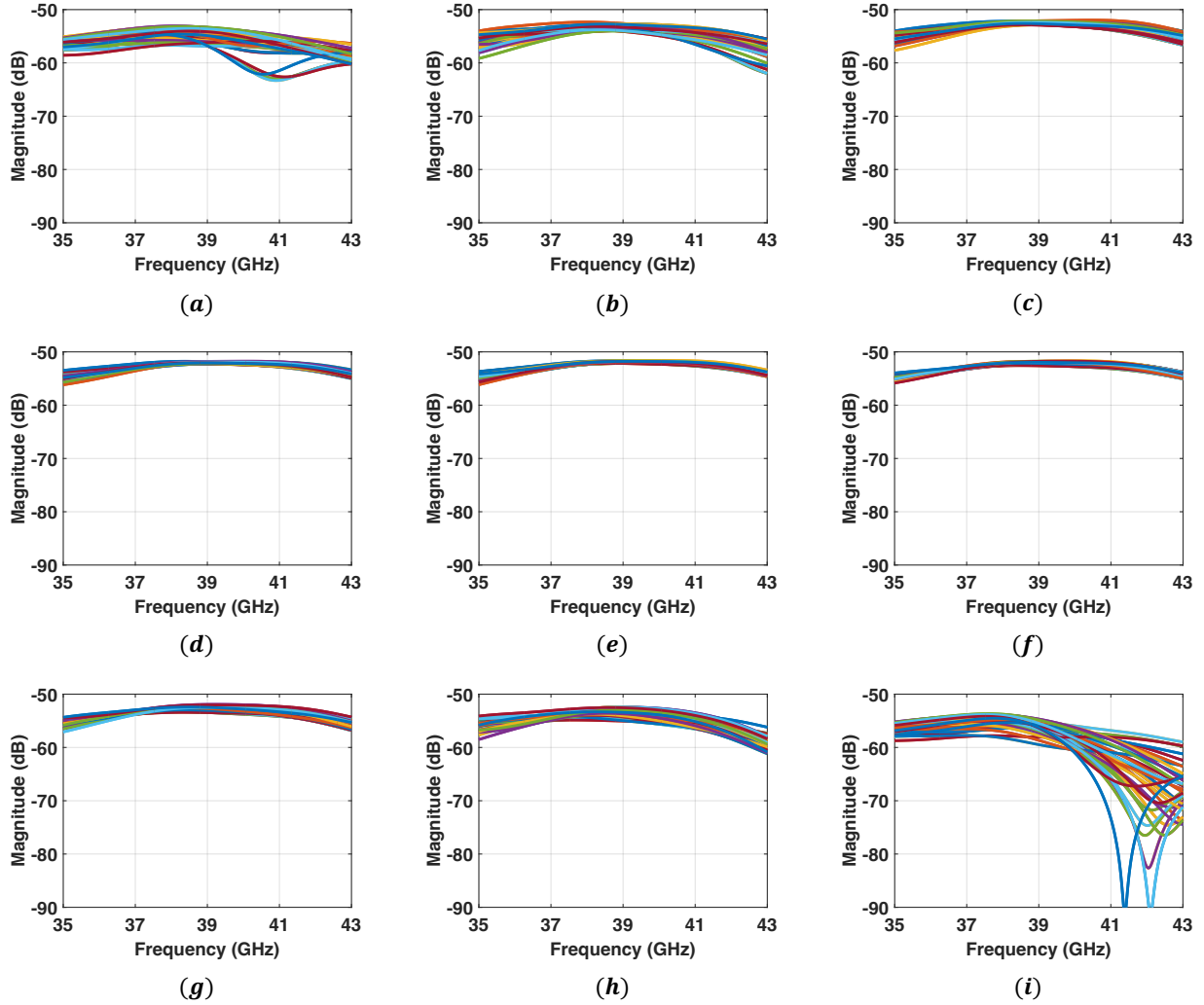


Figure 4.8 Gain of the far field link voltage transfer functions  $|H_{mn}(f)|$  for each array element  $(m, n) = (1, 1) \dots (8, 8)$  at E-plane beam scan angles  $(\theta_s, \phi_s) =$  **(a)**  $(60^\circ, 180^\circ)$ , **(b)**  $(45^\circ, 180^\circ)$ , **(c)**  $(30^\circ, 180^\circ)$ , **(d)**  $(15^\circ, 180^\circ)$ , **(e)**  $(0^\circ, 0^\circ)$ , **(f)**  $(15^\circ, 0^\circ)$ , **(g)**  $(30^\circ, 0^\circ)$ , **(h)**  $(45^\circ, 0^\circ)$ , and **(i)**  $(60^\circ, 0^\circ)$ .

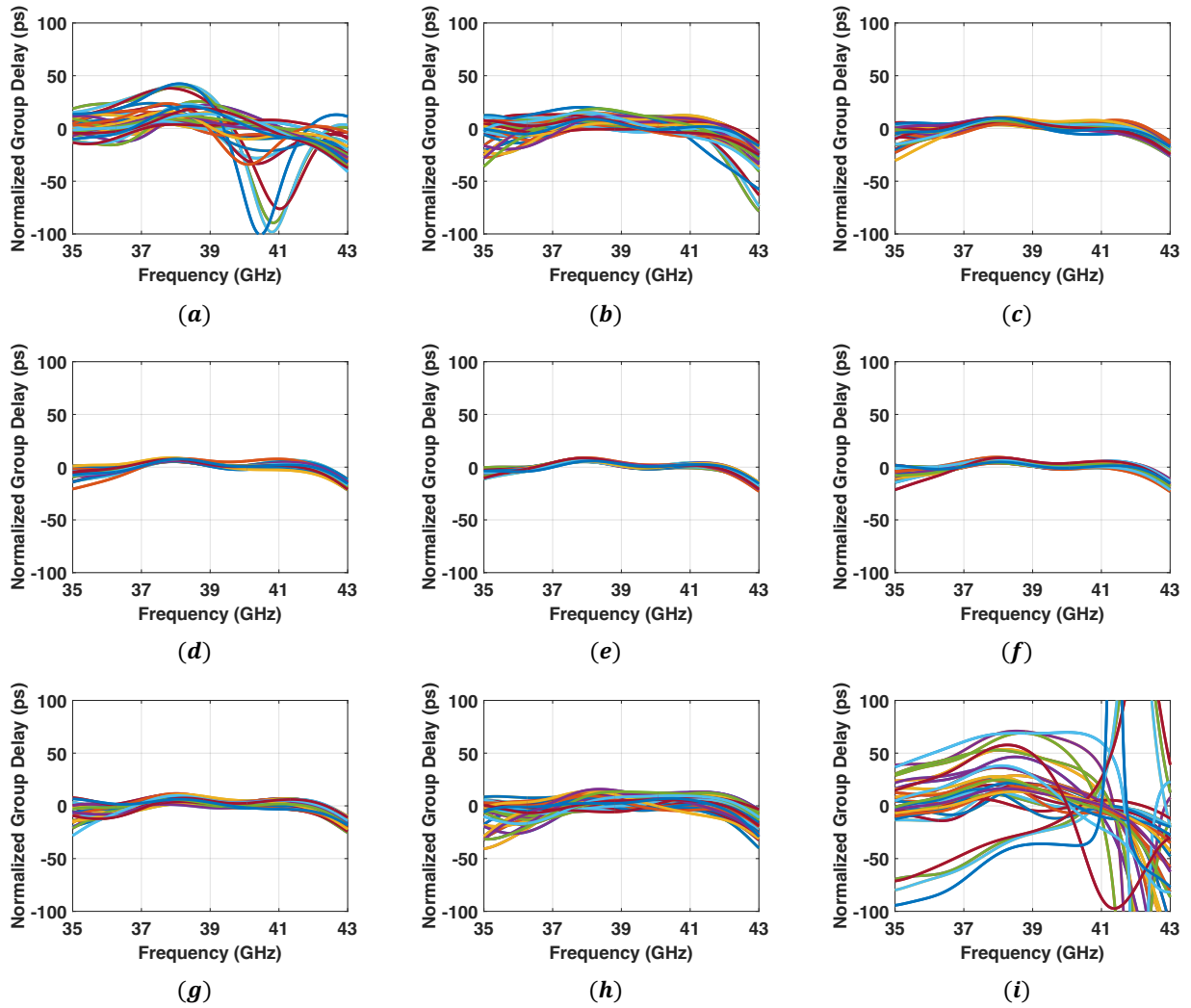


Figure 4.9 Normalized group delay  $\tau_{mn}$  of the far field link voltage transfer functions  $H_{mn}(f)$  for each array element  $(m, n) = (1, 1) \dots (8, 8)$  at E-plane beam scan angles  $(\theta_s, \phi_s) =$  **(a)**  $(60^\circ, 180^\circ)$ , **(b)**  $(45^\circ, 180^\circ)$ , **(c)**  $(30^\circ, 180^\circ)$ , **(d)**  $(15^\circ, 180^\circ)$ , **(e)**  $(0^\circ, 0^\circ)$ , **(f)**  $(15^\circ, 0^\circ)$ , **(g)**  $(30^\circ, 0^\circ)$ , **(h)**  $(45^\circ, 0^\circ)$ , and **(i)**  $(60^\circ, 0^\circ)$ .

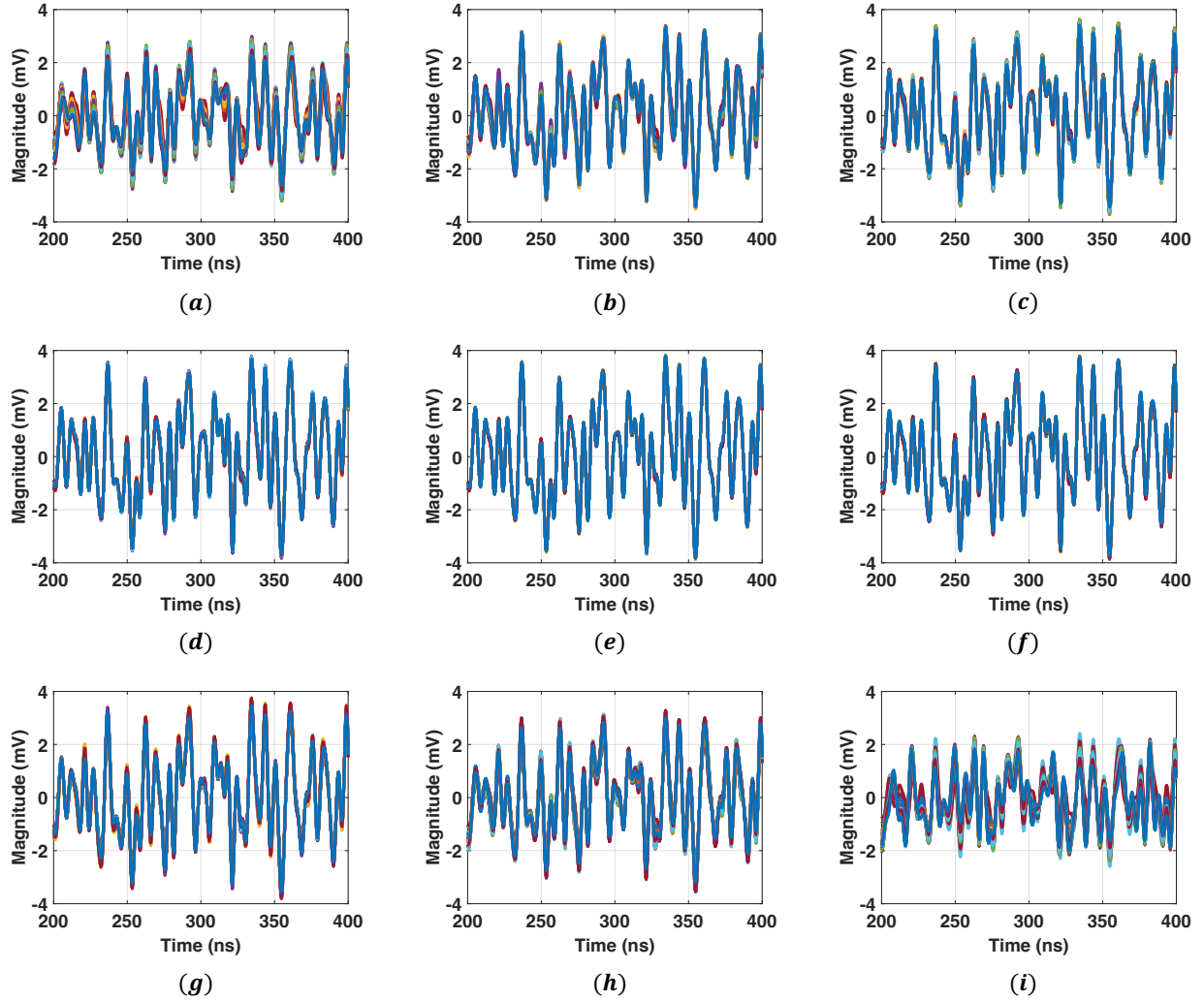


Figure 4.10 In-phase component of the 400 Mbaud 16-QAM signals transmitted by each array element and received at the E-plane beam scan angles  $(\theta_s, \phi_s) =$  **(a)**  $(60^\circ, 180^\circ)$ , **(b)**  $(45^\circ, 180^\circ)$ , **(c)**  $(30^\circ, 180^\circ)$ , **(d)**  $(15^\circ, 180^\circ)$ , **(e)**  $(0^\circ, 0^\circ)$ , **(f)**  $(15^\circ, 0^\circ)$ , **(g)**  $(30^\circ, 0^\circ)$ , **(h)**  $(45^\circ, 0^\circ)$ , and **(i)**  $(60^\circ, 0^\circ)$ .

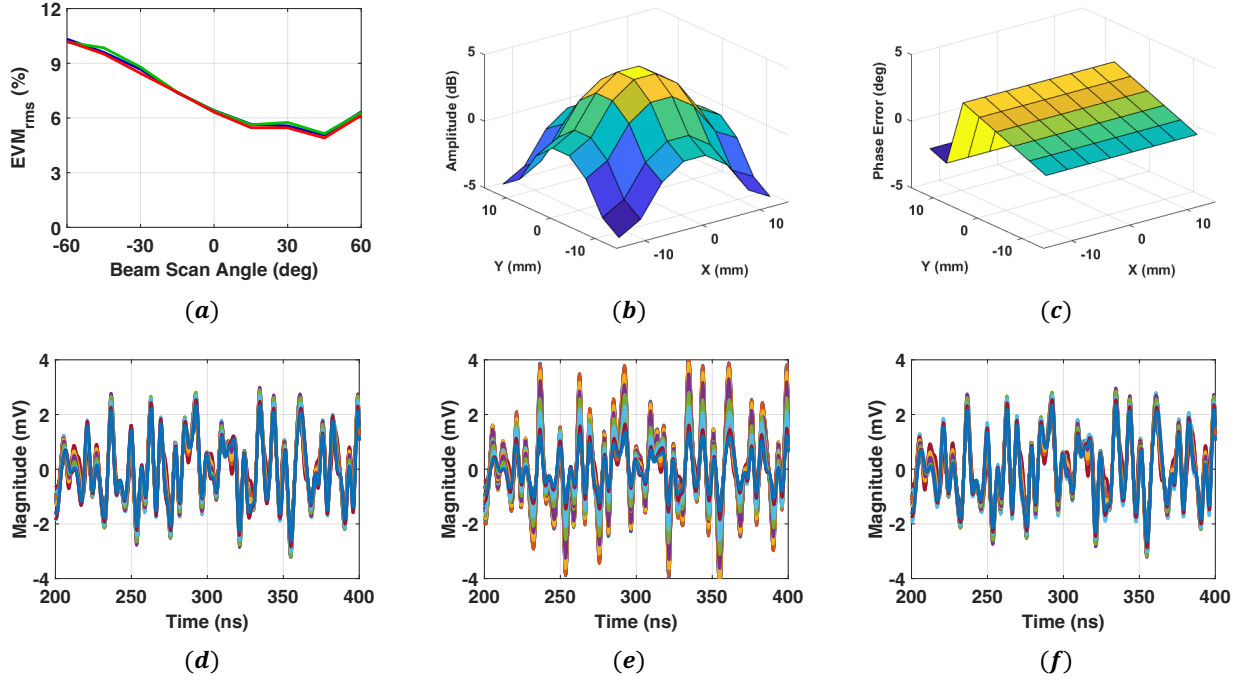


Figure 4.11 **(a)** Un-equalized EVM of the 400 Mbaud 16-QAM test signal resulting from superposition of the simulated array element channels at E-plane beam scan angles  $\theta_s$  with uniform amplitude and no phase error (blue), the 10 dB Taylor amplitude taper shown in **(b)**, and a 6-bit ( $5.6^\circ$ ) phase quantization error (green) shown in **(c)**. Received signals from array elements at  $(\theta_s, \phi_s) = (60^\circ, 180^\circ)$  for the blue, red, and green cases are shown in **(d)**-**(f)**.

complex difference between the received signal sum and the 16-QAM test signal applied to each array element channel  $H_{mn}(f, \theta_s, \phi_s)$ . Results are shown in Fig. 4.11 for three test cases: (1) uniform amplitude and zero phase gradient error, (2) 10 dB Taylor amplitude taper, and (3) uniform amplitude with 6-bit ( $5.6^\circ$ ) phase quantization error. The un-equalized EVM for all three cases are well-correlated, indicating that that array element transfer functions were the dominant source of linear distortion in the far field received signal, just as they were for the simulation of section 4.2.2. Had the phase quantization error been made larger and had the amplitude taper been normalized to 0 dB, as if variable attenuators were used, it is possible that these effects would have had a greater influence on the un-equalized EVM results. The EVM asymmetry across the E-plane scan angles in Fig. 4.11 indicates that the slope of the array elements' amplitude and group delay response across the 16-QAM signal bandwidth is greater at beam scan angles toward the bottom of the array, as displayed in Fig.

4.7, possibly due to the feed positioning. Further analysis is required to determine the source of this asymmetry and means of correcting it in the array design. Nonlinear distortion effects from additional RFIC power amplifiers should also be modeled in conjunction with the linear distortion effects from passive element transmission demonstrated in section 4.2, since the latter can be mitigated with channel equalization and the use of multi-carrier modulation schemes such as OFDM. However, because the complex frequency responses of individual radiating elements as a function of beam scan angle have typically been excluded from phased array EVM simulations, as described in section 4.1, the application of full-wave simulations to phased array EVM simulation models in section 4.2 represents a significant advancement.

### **4.3 Review of Indirect Far Field Measurement Methods for Phased Array EVM Analysis**

The large number, limited size and spacing, and high level of integration of radiating elements with beamforming ICs in large millimeter-wave phased arrays necessitates the use of OTA techniques for measurements of modulated signal quality. This section highlights far field and indirect far field measurement systems that have been used by researchers to perform EVM measurements and enhance their precision and versatility in characterizing the beam scanning performance of millimeter-wave phased arrays.

Far field anechoic test ranges have traditionally been used to measure the radiated electric field magnitude patterns of antennas using CW signals. However, large increases in signal bandwidth and decreases in array element size and spacing at millimeter-wave frequencies have generated interest in characterizing the wideband effects of antennas and arrays on system level performance metrics such as EVM and BER, as described in section 1.2. Controlled OTA test environments are therefore being adapted for these measurements. In [110], the EVM pattern of a 3.5 GHz probe-fed microstrip patch antenna was measured in an anechoic test range. This patch was rotated and received a 50 MHz-wide  $\pi/4$  DQPSK signal transmitted by an identical patch along the broadside direction. In [24], another EVM pattern measurement was taken for a 32-element 28 GHz phased array [111] transmitting an 800 MHz QPSK signal.

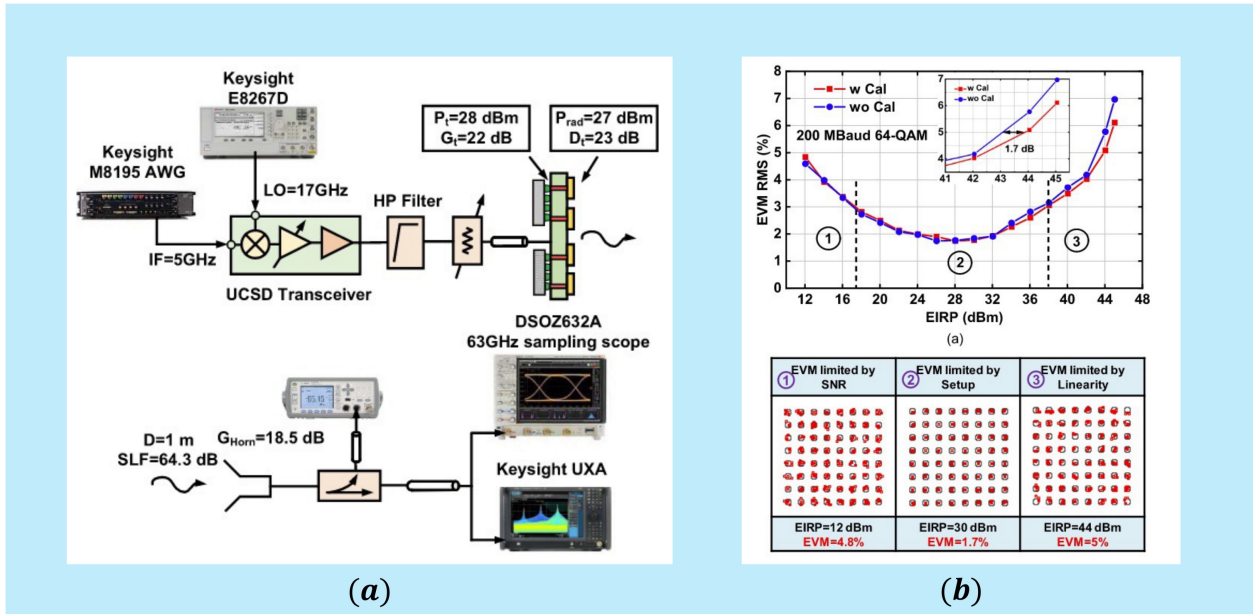


Figure 4.12 Far field EVM measurement system for a 39 GHz 8x8 phased array and probe separated by  $D = 1.0$  m [98]: (a) block diagram of measurement system with AWG and external upconverter for signal generation and real-time scope with VSA software for demodulation of the received signal, and (b) EVM vs. EIRP plot demonstrating the (1) SNR, (2) measurement system, and (3) power amplifier linearity dominated regions.

The EVM pattern was shown to be strongly correlated with the inverted radiated far field pattern, demonstrating that the EVM measured at far field distances is dominated by the SNR when the array amplifiers are not driven into saturation.

The EVM versus RF power of the modulated test signal applied to the common port of the active phased array takes the form of the plot shown in Fig. 4.12(b): At lower EIRP, EVM is dominated by the low SNR resulting from the large free space path loss between antennas and dynamic range limitations of the receiver, which is shown in the representative OTA measurement configuration for the 39 GHz 8x8 phased array of [98] in 4.12(a). At higher EIRP, EVM is dominated by the nonlinear distortion of the phased array power amplifiers. At median EIRP, EVM is limited by the test instrument imperfections such as AWG noise and local oscillator (LO) phase noise [98]. In [112], an OTA measurement system similar to that shown in Fig. 4.3(a) was used to measure the EVM of an analog beamforming front end module with an integrated 4x1 linear array. For the 64-QAM test signal, EVM components



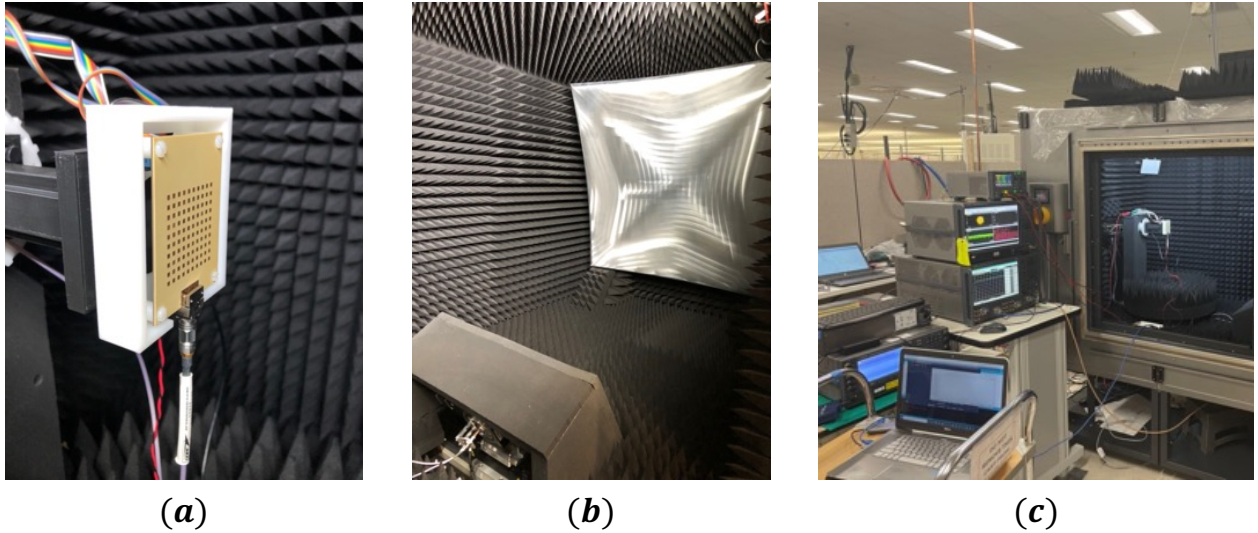


Figure 4.13 Images of a millimeter-wave compact antenna test range and instruments provided by Keysight in Santa Rosa, CA: (a) 39 GHz 8x8 phased array [98] mounted to a roll/azimuth positioner with a custom-designed, 3D-printed bracket that extends the array to quiet zone center, (b) reflector and feed horn enclosure, and (c) exterior view of CATR and instruments.

from independent error sources were estimated to isolate the DUT-based EVM degradation from that of the rest of the test system. Linear distortion in the array link was removed by VSA equalization, and nonlinear distortion from power amplifiers was limited by operating at a 14 dB backoff, such that the authors could approximate the EVM as a root-sum-square of distortion components. The EVM from the module and OTA measurement system errors were estimated at 1.23% and 1.07% respectively. This underscores the difficulty in performing far field EVM measurements with adequate precision.

Limited dynamic range in the VSA receiver and embedded signal generator errors can create EVM comparable with that of the DUT in demodulation-based measurements. As a result, compact test ranges (CATRs) are generally preferable. CATRs utilize a parabolic reflector to transform the spherical plane wave emanating from the feed antenna to a plane wave at the AUT position. This indirect far field method results in smaller test ranges with a lower spatial path loss than direct far field ranges, and it generates a quiet zone in the AUT vicinity where the amplitude and phase variation are minimal [113–116], as described in section 3.4. For example, at 28 GHz, a quiet zone of 27 cm with a 2.0 dB amplitude taper

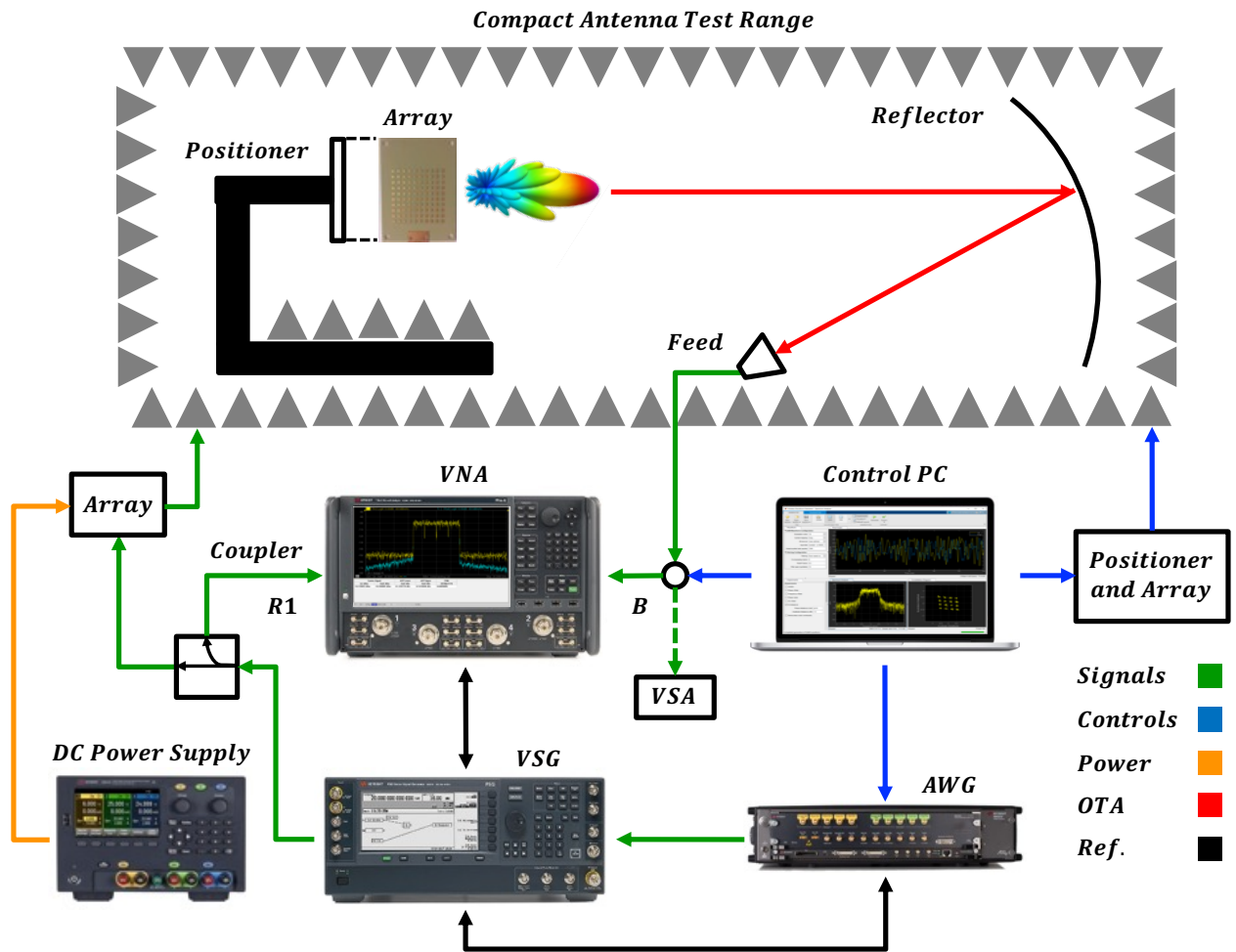


Figure 4.14 Compact test range EVM measurement system diagram highlighting RF signal (green), control (blue), DC power supply (orange), and OTA (red) paths between the PC and test instruments. A 10 MHz reference signal (black) is used for synchronization of the AWG, VSG, and VNA. An Arduino is used as a digital interface between the PC and array.

can be accommodated within a CATR with a maximum dimension of 2.0 meters, but the same quiet zone requires a far field test range dimension  $R \geq 2D^2/\lambda = 13.6$  m and 26 dB of additional path loss [114]. Consequently, CATRs provide a significant improvement in dynamic range which can be leveraged for more precise EVM measurements, especially for large millimeter-wave beamforming arrays. In [116],  $S_{21}$  for a 26 GHz massive MIMO base station array in a CATR was simulated and used to scale each frequency component of a 400 MHz OFDM test signal. The EVM of the was calculated for the  $S_{21}$ -scaled signal after performing a linear equalization to evaluate the CATR's wideband performance. The influence

of AUT gain variation and reflector edge diffraction on CATR links becomes more significant as signal bandwidth increases. Such simulation tools can help engineers examine tradeoffs in CATR reflector design and define the bandwidth and AUT beamforming limitations [116].

Another type of indirect far field measurement system is the plane wave converter (PWC), in which a large array of probe antennas is used to synthesize a spherical quiet zone around the AUT. In [114] and [117], a PWC with 158 wideband Vivaldi antennas was used to measure the EVM of antennas transmitting 100 MHz OFDM signals at 2.4 GHz. At sub-6.0 GHz frequencies, CATR reflectors are prohibitively large and expensive, which makes PWCs an attractive alternative for OTA EVM measurements in these lower frequency bands. However, bandwidth limits imposed by PWC arrays [117] and expensive installation of a large probe arrays [115] at millimeter-wave frequencies suggests that they are less likely to be deployed.

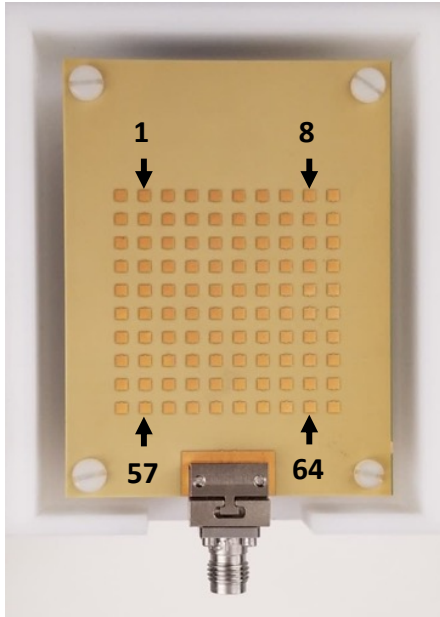
CATRs provide a convenient and controlled OTA test environment for instantaneous EVM measurements at millimeter-wave frequencies, and their limitations are primarily based on the reflector design: It must be made wide enough to generate a quiet zone that fully encloses the AUT, and edge treatments must limit quiet zone amplitude and phase ripple across the test signal bandwidth. An F9650A millimeter-wave CATR from Keysight Technologies, configured for EVM measurements of the 8x8 phased array from [98], is shown in the images of Fig. 4.13 and the block diagram of Fig. 4.14. The EVM measurement system and results for the 8x8 phased array are presented in section 4.4.

#### **4.4 EVM Measurement of an 8x8 Microstrip Patch Phased Array with a Compact Antenna Test Range and Network Analyzer**

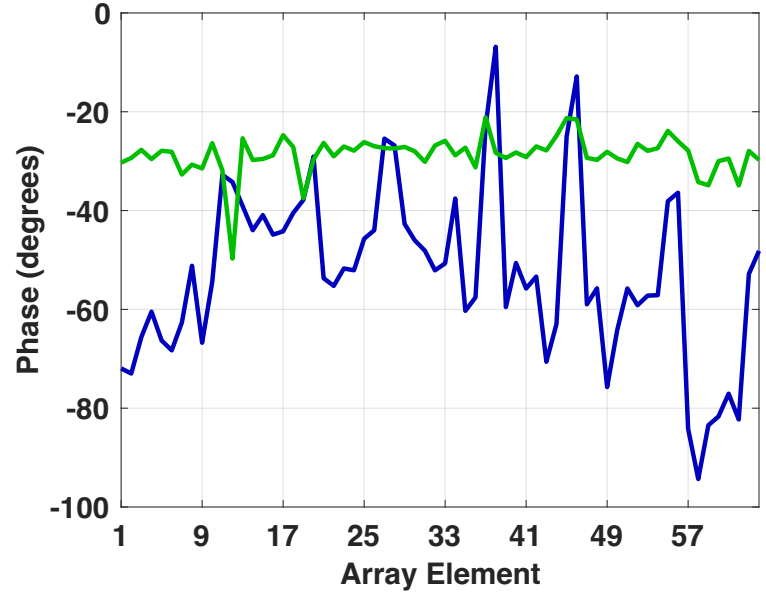
This section presents EVM measurements of the 8x8 phased array from [98] in a millimeter-wave CATR. The measurement system, which is shown in the images of Fig. 4.13 and the block diagram of Fig. 4.14, is identical to the one used for Ka-band horn link measurements described in section 3.4, with the exception of the AUT replacement. The EVM measurements were achieved through spectral correlation on a PNA-X network analyzer. The test equipment was provided by Keysight Technologies and set up at their headquarters in Santa Rosa, CA.

#### 4.4.1 CATR Measurement System and Phased Array Calibration

For details concerning the CATR measurement system of Fig. 4.14 and 16-QAM test signal generation, the reader is referred to section 3.4. For the EVM measurements presented in this section, the 8x8 millimeter-wave phased array that was presented in [98] and developed by researchers at UC San Diego was used as the AUT instead of the Ka-band conical horn antenna shown in Fig. 3.18(a). The AUT has sixty-four stacked microstrip patch elements integrated with sixteen silicon beamforming ICs on a multi-layer PCB. The control PC runs MATLAB scripts designed to perform fully-automated phased array measurement sequences. In addition to sending SCPI commands that synchronize the CATR positioner and network analyzer, as shown in section 3.4, these MATLAB scripts also send pre-programmed commands to an Arduino microcontroller that processes the commands and forwards them to the phased array through its serial peripheral interface (SPI). Therefore, in addition to controlling the test instruments, the MATLAB test automation scripts also control the phased array: They send commands that activate the variable gain amplifiers (VGAs) and update 6-bit phase shift registers for each of the beamforming IC channels to perform calibration, measurements of individual array elements, and measurements of the fully-active array as the beam is scanned. The Arduino board is connected to the PC via USB, and the phased array breakout board is powered through an external DC supply as shown in Fig. 4.14. A phase calibration of the array was performed prior to making the EVM measurements, as highlighted in Fig. 4.15(b), using a custom program for the Arduino microcontroller developed by Keysight Technologies. It automates sequential activation of each array element with the same phase state and VNA triggering to capture the  $S_{21}$  phase at  $f_c = 39$  GHz for each element at boresight. The 6-bit BFIC phase shift registers are then updated to minimize measured phase error relative to that of a specific element, to within  $5.625^\circ$  resolution [98]. Phase error following this calibration is reduced by a factor of three, as shown in Fig. 4.15(b), and results in higher active array gain.



(a)



(b)

Figure 4.15 Phase calibration of array performed at  $f_c = 39$  GHz: (a) enumeration of elements 1-64, which excludes dummy elements, and (b) calibrated (green) and uncalibrated (blue)  $S_{21}$  phase of the array elements with peak-to-peak variations of  $28.5^\circ$  and  $87.5^\circ$  respectively.

#### 4.4.2 EVM Measurement of Individual Phased Array Elements

Following the phase calibration, the modulated gain  $|H_n(f_c)|$  at carrier frequency  $f_c = 39$  GHz, un-equalized  $EVM_{UN}$ , and equalized  $EVM_{EQ}$  of each array element  $n$  was measured in the boresight direction of the phased array  $(\theta_t, \phi_t) = (0^\circ, 0^\circ)$  as a function of the RF output power  $P_{RF}$  from the VSG and as a function of the far field observation angle  $(\theta_t, \phi_t)$  with  $P_{RF} = 15$  dBm. These element-level measurement results are displayed in Fig. 4.16. Fig. 4.17 shows the measured PSD of the input and output signals,  $S_{XX}(f)$  and  $S_{YY}(f)$  respectively, as well as decomposition of  $S_{YY}(f)$  into a linear component with modulated gain  $H(f)$  and nonlinear component  $S_{DD}(f)$  for four representative elements of the 8x8 phased array. Fig. 4.18 shows the equalized and un-equalized EVM and the carrier gain  $|H(f_c)|$  for the same elements, and Fig. 4.19 shows the estimated noise  $EVM_{SNR}$  and intermodulation distortion  $EVM_{IMD}$  components of the equalized EVM from equation (3.22) for elements 13 and 46. In Fig. 4.19, the SNR at the lowest RF output power ( $P_{RF} = -3$  dBm) is calculated from

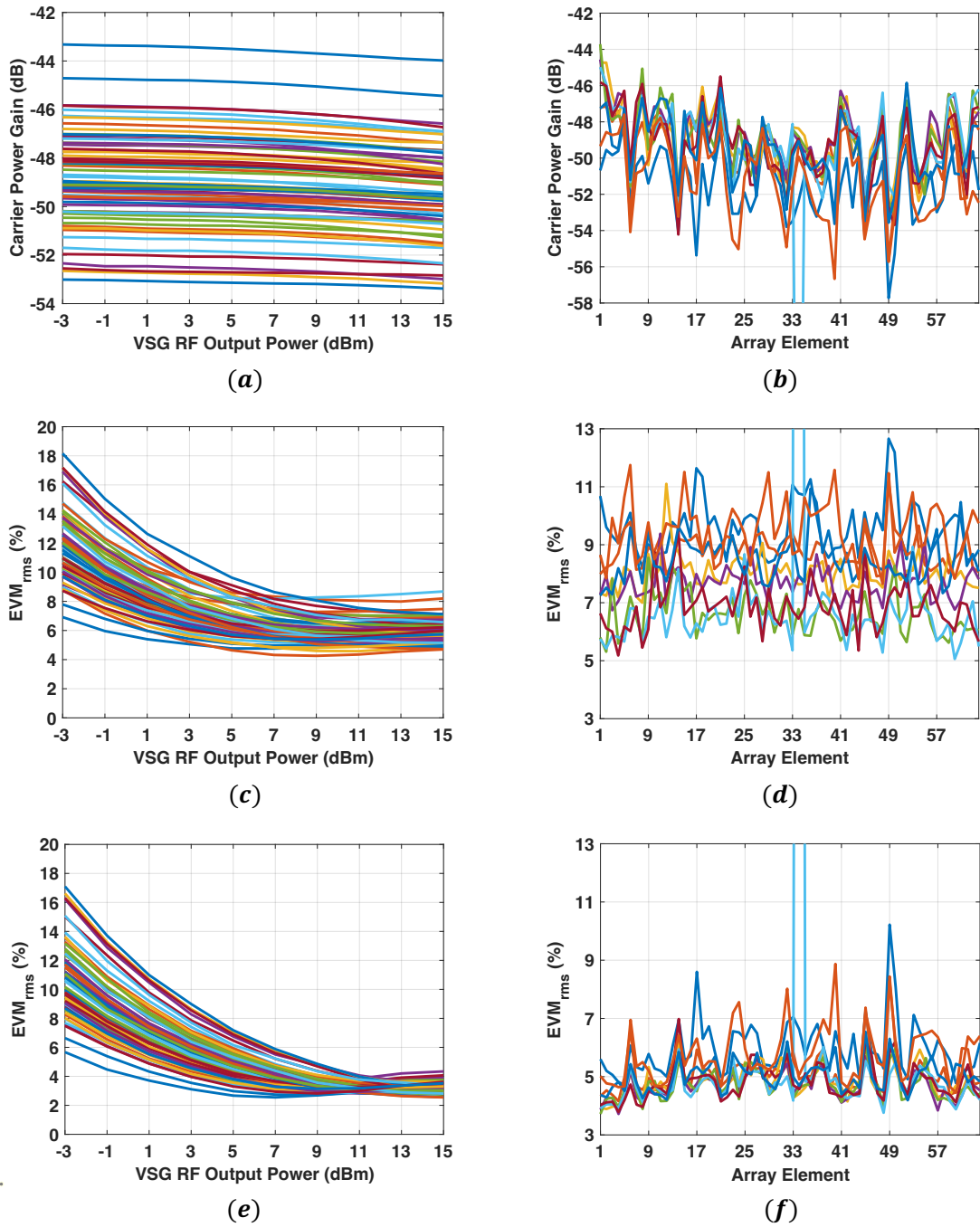


Figure 4.16 RF carrier gain (a)-(b),  $EVM_{UN}$  (c)-(d), and  $EVM_{EQ}$  (e)-(f) of all sixty-four phased array elements. In [(a),(c),(e)], results are plotted at boresight as a function of RF carrier power  $P_{RF}$  from the VSG, and colors represent array elements. In [(b),(d),(f)], results are plotted as a function of array element number with  $P_{RF} = 15$  dBm, and colors represent far field observation angles  $\theta_t$  in the azimuth plane. The anomaly from element 34 for angle  $\theta_t = 15^\circ$  (light blue) in [(b),(d),(f)] is conjectured to result from an Arduino activation failure.

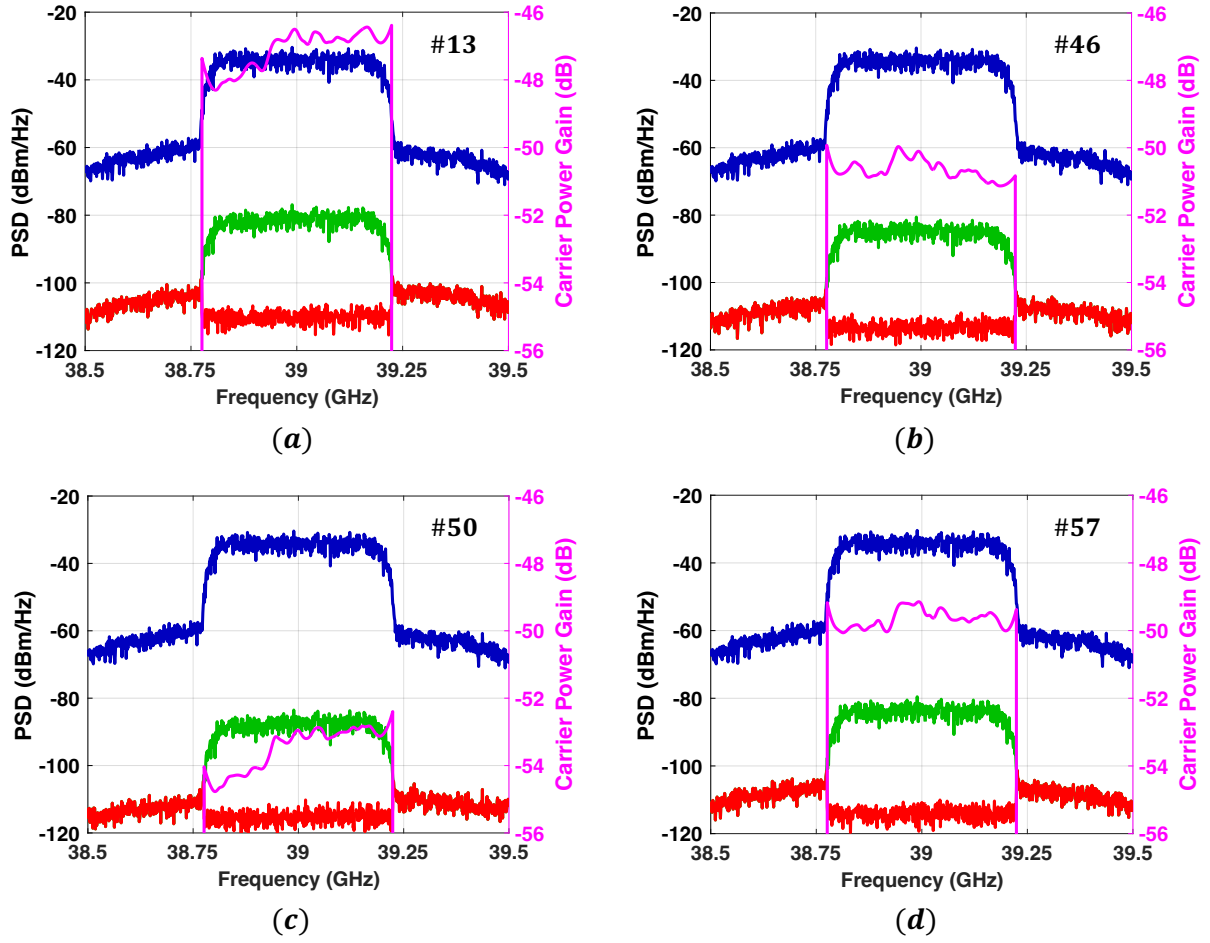


Figure 4.17 Power spectral densities of the modulated stimulus applied to the AUT  $S_{XX}(f)$  (blue) and measured on the PNA-X reference receiver  $R1$ , the received signal from the CATR feed horn  $S_{YY}(f)$  (green) measured on receiver  $B$ , and the distortion spectrum  $S_{DD}(f)$  (red) described in section 2.3, with the corresponding modulated gain  $|H(f)|$  (magenta) overlaid. These results are for array elements (a) 13, (b) 46, (c) 50, and (d) 57.

equation (3.22) by letting  $EVM_{IMD} = 0$ . Remaining SNR values are increased proportionally with  $P_{RF}$  and used to calculate the  $EVM_{IMD}$  using equation (3.22). Finally, Fig. 4.20 shows the EVM for all sixty-four elements of the phased array at the maximum power that could be selected without the source becoming unlevel ( $P_{RF} = 15$  dBm). The following observations can be made by examining the element-level gain and EVM results shown in Figs. 4.16-4.20:

At lower RF output power levels, both the equalized and un-equalized EVM are higher (6-18%) due to a low measurement SNR, and the EVM is dominated by the  $1/SNR$  component

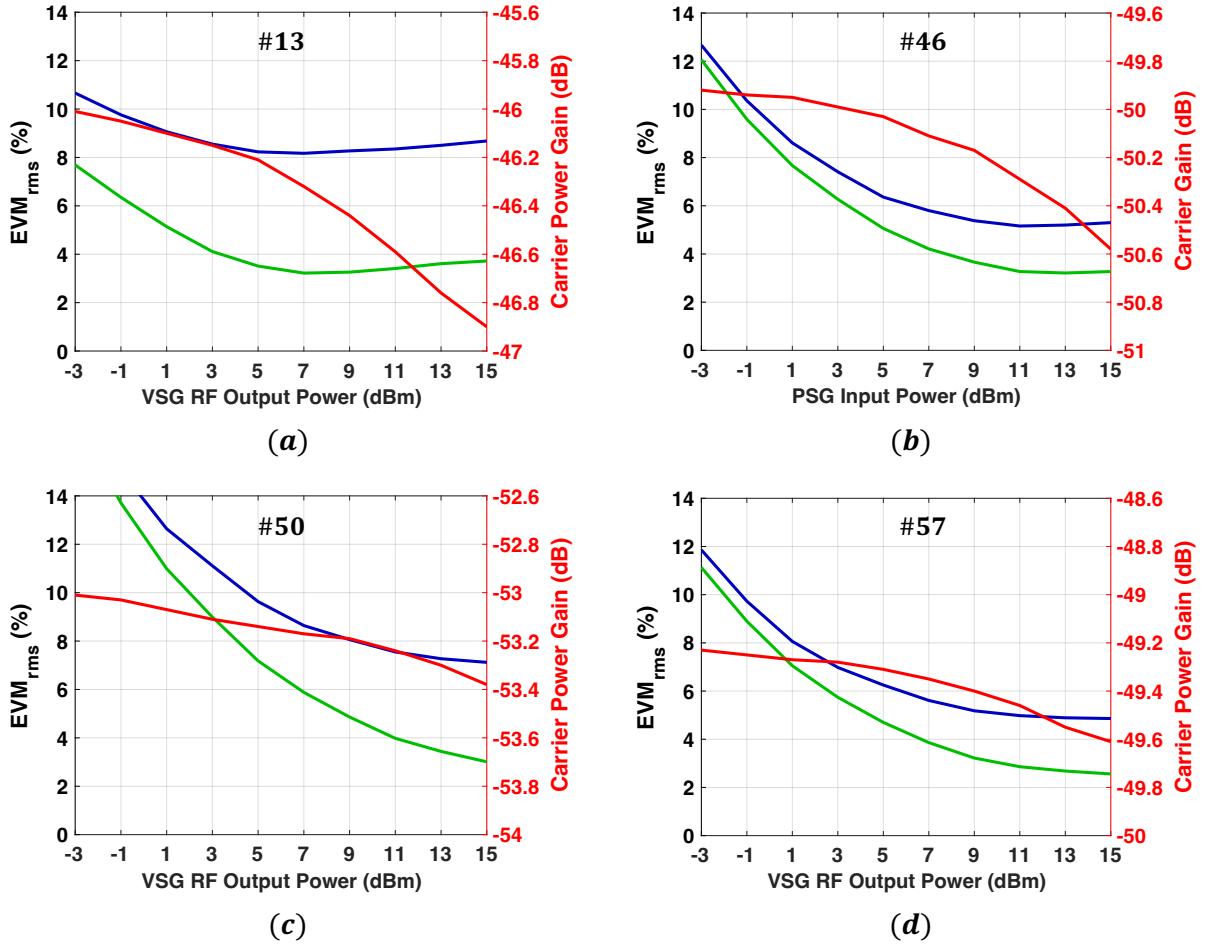


Figure 4.18 Equalized  $EVM_{EQ}$  (green), un-equalized  $EVM_{UN}$  (blue), and carrier gain  $|H(f_c)|$  (red) as a function of RF output power from the VSG for elements (a) 13, (b) 46, (c) 50, and (d) 57.

of equation (3.22). This is shown in Fig. 4.19 for elements 13 and 46. Due to 10 dB variation in uncalibrated gain of the array elements, the SNR likewise varies by 10 dB and causes a larger variation in EVM in this low power region as shown in Fig. 4.16(c) and (e). As RF output power increases, the variation becomes smaller because the EVM starts to be limited by intermodulation  $EVM_{IMD}$  of the BFIC power amplifiers connected to each array element. Because un-equalized EVM includes the amplitude and phase distortion of the array element channels in addition to the noise and nonlinearity from equation (3.22), its variation at the maximum RF output power  $P_{RF} = 15$  dBm (4%) is double that of the equalized EVM (2%),



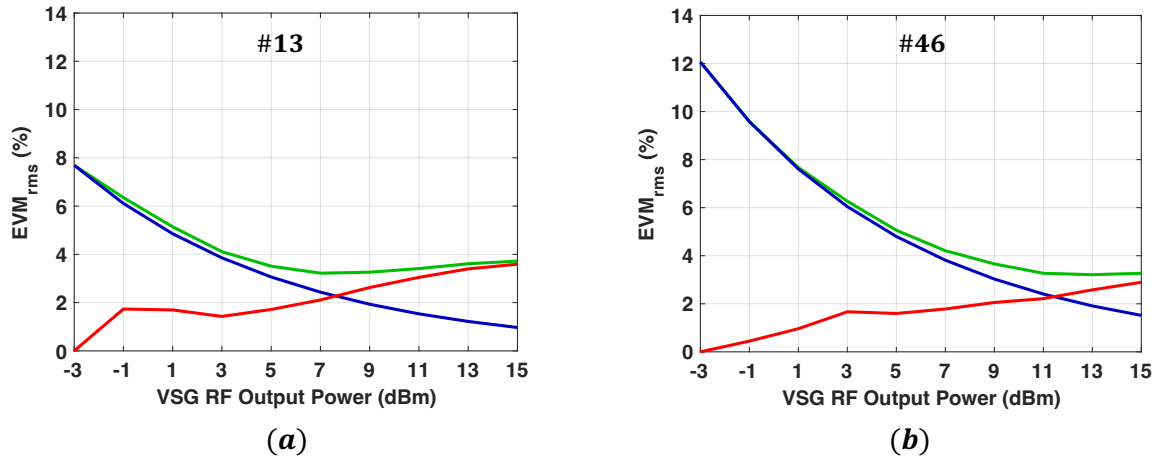


Figure 4.19 Equalized  $EVM_{EQ}$  (green), noise component  $EVM_{SNR}$  (blue), and intermodulation distortion component  $EVM_{IMD}$  (red) from equation (3.22) as a function of VSG RF output power for elements (a) 13 and (b) 46.

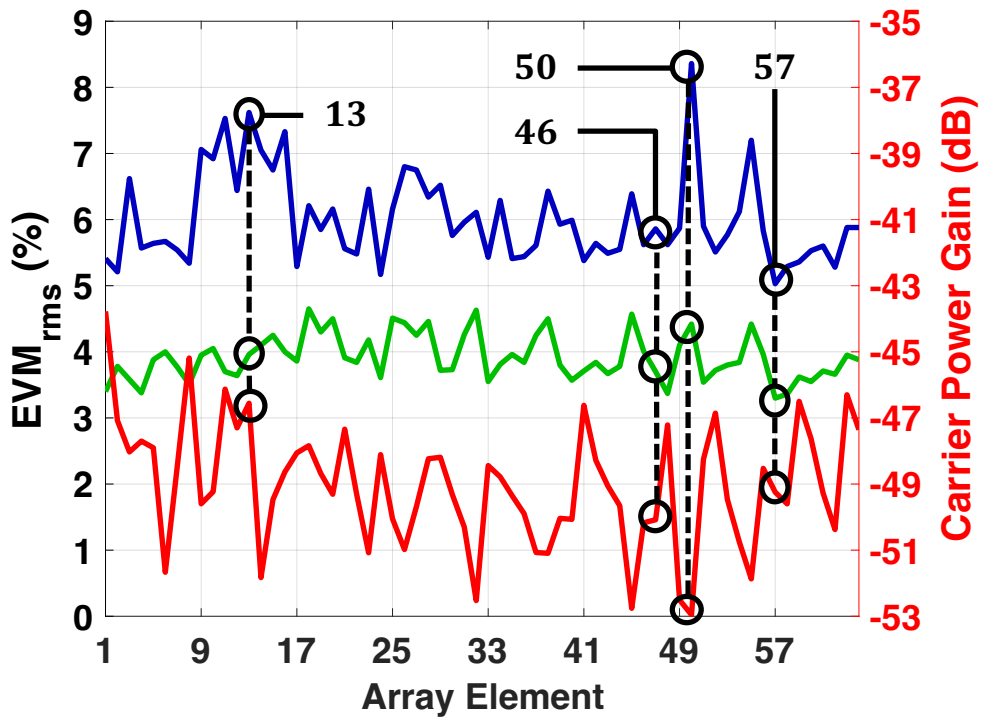


Figure 4.20 Equalized  $EVM_{EQ}$  (green), un-equalized  $EVM_{UN}$  (blue), and carrier gain  $|H(f_c)|$  (red) for all 64 array elements with  $P_{RF} = 15$  dBm. Results for the four array elements from Figs. 4.17 and 4.18 are highlighted for comparison.

and un-equalized EVM is always higher than equalized EVM as shown in Fig. 4.16(c)-(f) and Fig. 4.20. Un-equalized EVM variation as a function of the AUT far field observation angle  $(\theta_t, \phi_t)$  in 4.16(d) is greater than the equalized EVM variation in 4.16(f) because array element frequency response varies with far field angle as demonstrated in the UWB antenna analysis from [118]. The un-equalized EVM is higher at far field angles further from boresight, as highlighted by the dark blue and orange curves representing  $\theta_t = 60^\circ$  and  $\theta_t = 45^\circ$  in Fig. 4.16(d), just as it was for the Ka-band conical horn measurements in section 3.4, due to a higher passband amplitude ripple and group delay variation. Though the equalized EVM in 4.16(f) shows less variation with far field angle, it is likewise higher at large angles due to lower antenna gain and SNR, particularly for elements near the edges (e.g. 17, 24, 40, 49). Comparing results for elements 13 and 46 in Fig. 4.18(a) and (b), equalized EVM at the minimum RF output power  $P_{RF} = -3$  dBm is 4% higher for element 46 as a result of the 3.5 dB lower average modulated gain shown in Fig. 4.17(a) and (b), which increases the SNR. However, the equalized EVM at the maximum RF output power  $P_{RF} = 15$  dBm is slightly lower (-0.4%) for element 46 due to the increased amplifier compression and intermodulation distortion  $EVM_{IMD}$  for element 13, which is observed by comparison of Fig. 4.17(a) and (b). Furthermore, a larger gap exists between the equalized and un-equalized EVM for element 13 than for 46, due to the steeper slope of element 13's modulated gain  $|H_{13}(f)|$  relative to that of element 46  $|H_{46}(f)|$ , as shown in Fig. 4.17(a) and (b). Comparing results for elements 50 and 57 in Figs. 4.17 and 4.18 (c) and (d), both equalized and un-equalized EVM are higher for element 50 at all RF output power levels because its modulated gain  $|H_{50}(f)|$  is 4.0 dB lower and has a larger variation across the 449.1 MHz integration bandwidth than  $|H_{57}(f)|$ .

#### 4.4.3 EVM Measurement of Fully-Activated Phased Array

Section 4.4.2 presented EVM measurements of a 16-QAM test signal distorted by indirect far field links between independent, linearly-polarized active elements of an 8x8 array and a CATR feed horn via spectral correlation on a PNA-X network analyzer. This section presents EVM measurements of the 8x8 array with all elements simultaneously activated as a function of RF source power, symbol rate, and beam scan angle. These array-level measurements were

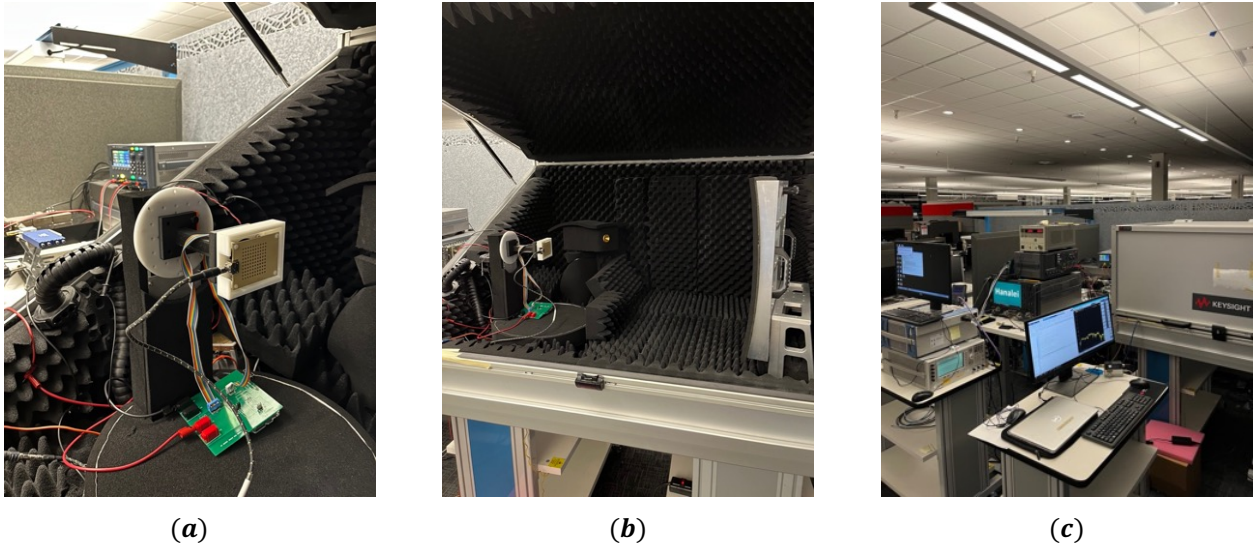


Figure 4.21 Images of another millimeter-wave compact antenna test range and instruments provided by Keysight in Santa Rosa, CA: (a) 39 GHz 8x8 phased array [98] mounted to a roll/azimuth positioner with a custom-designed, 3D-printed bracket that extends the array to quiet zone center, (b) reflector and CATR, and (c) exterior view of CATR and instruments.

performed in a second visit to Keysight’s headquarters in Santa Rosa, CA and implemented with the same OTA test system shown in Fig. 4.14. However, because the F9650A CATR model displayed in Fig. 4.13 was not available during this second visit, the clamshell CATR shown in the images of Fig. 4.21 was used as a substitute. The ports of the dual-polarized feed horn shown in Fig. 4.21(b) were not readily accessible due to the elevated position of the CATR, so the phased array was rotated to match the existing feed polarization as shown in the orientation of Fig. 4.21(a), and measurements were limited to the E-plane of the array by only changing the azimuth position of the AUT. Three different test signals were generated and tested to observe the effects of varying bandwidth and PAPR: a 100 MHz-wide flat tone signal with 1.0 MHz tone spacing and 400 and 800 Mbaud 16-QAM signals with 1600 symbols that were RRC-filtered with rolloff factor  $\alpha = 0.15$ . The modulated gain and normalized group delay of the link between the fully-active phased array and CATR feed horn as a function of the beam scan angle is shown for all three of these test signals in Fig. 4.22(a)-(b) and (c)-(d) respectively. For each beam scan angle shown in the color key of Fig. 4.22, the phased array was measured with the positioner rotated to the scan angle  $\theta_s$ , such that the

| | | | | | |  $(\theta_s, \phi_s) = (45^\circ, 270^\circ), (30^\circ, 270^\circ), (15^\circ, 270^\circ), (0^\circ, 0^\circ), (15^\circ, 90^\circ), (35^\circ, 90^\circ), (45^\circ, 90^\circ)$

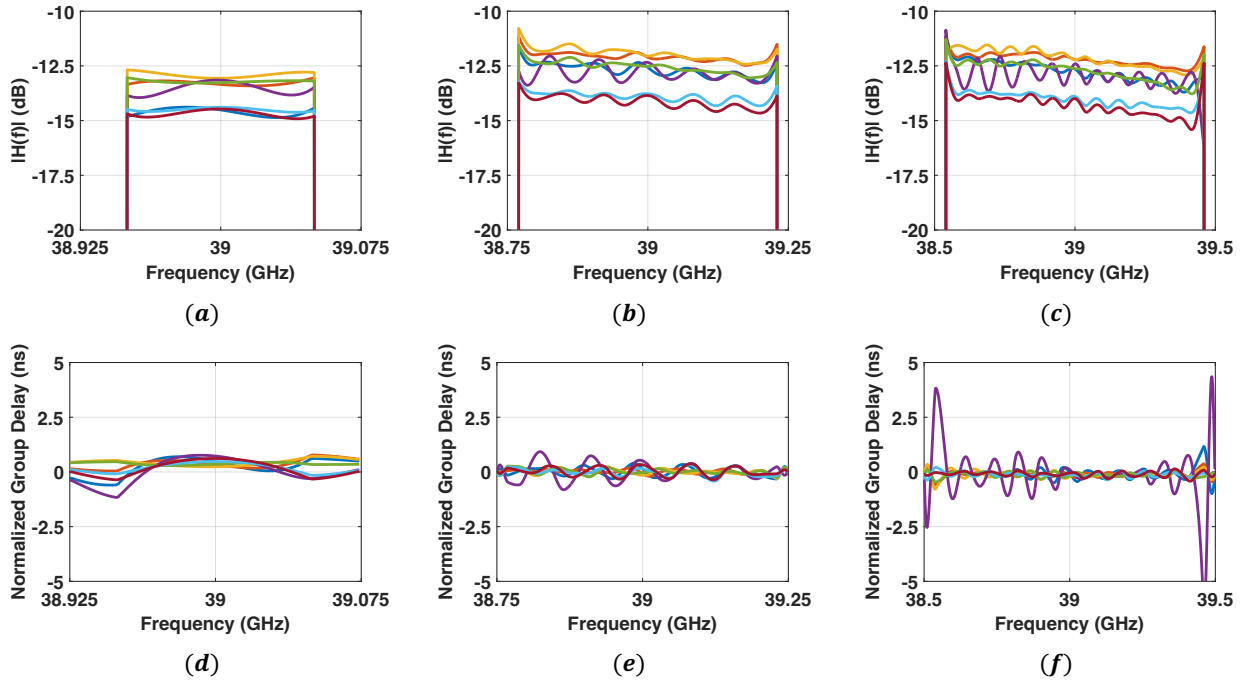


Figure 4.22 Measured modulated channel gain  $|H(f)|$  (a)-(c) and normalized group delay  $t_d(f)$  (d)-(e) of the 8x8 phased array link for a 100 MHz-wide flat tone signal with 1.0 MHz tone spacing [(a),(d)] and 16-QAM signal with 400 Mbaud [(b),(e)] and 800 Mbaud [(c),(f)] symbol rates as a function of E-plane beam scan angle, which is represented by trace color.

beam was expected to point toward the center of the CATR reflector. Because the maximum modulated gain at carrier frequency  $f_c = 39$  GHz occurs at  $(\theta_s, \phi_s) = (15^\circ, 90^\circ)$ , it appears that the positioner was not properly calibrated for alignment along azimuth. Additionally, the modulated gain and group delay ripple measured with the beam scanned to boresight (purple), indicates the possibility of an RF cable calibration error prior to the measurement.

Nonetheless, if the alignment error is accounted for, these measurements show a beam scan loss of 1.8 dB at  $45^\circ$  from the angle of maximum modulated gain at  $f_c = 39$  GHz. This corresponds to a normalized array element pattern of  $\cos^{1.2}(\theta)$  and matches the measured beam scan response of the same phased array presented in [98]. The PSD of the transmitted signal  $S_{XX}(f)$ , received signal  $S_{YY}$ , and distortion component  $S_{DD}(f)$  calculated from the spectral correlation process described in section 2.3 are shown for the three test signals for

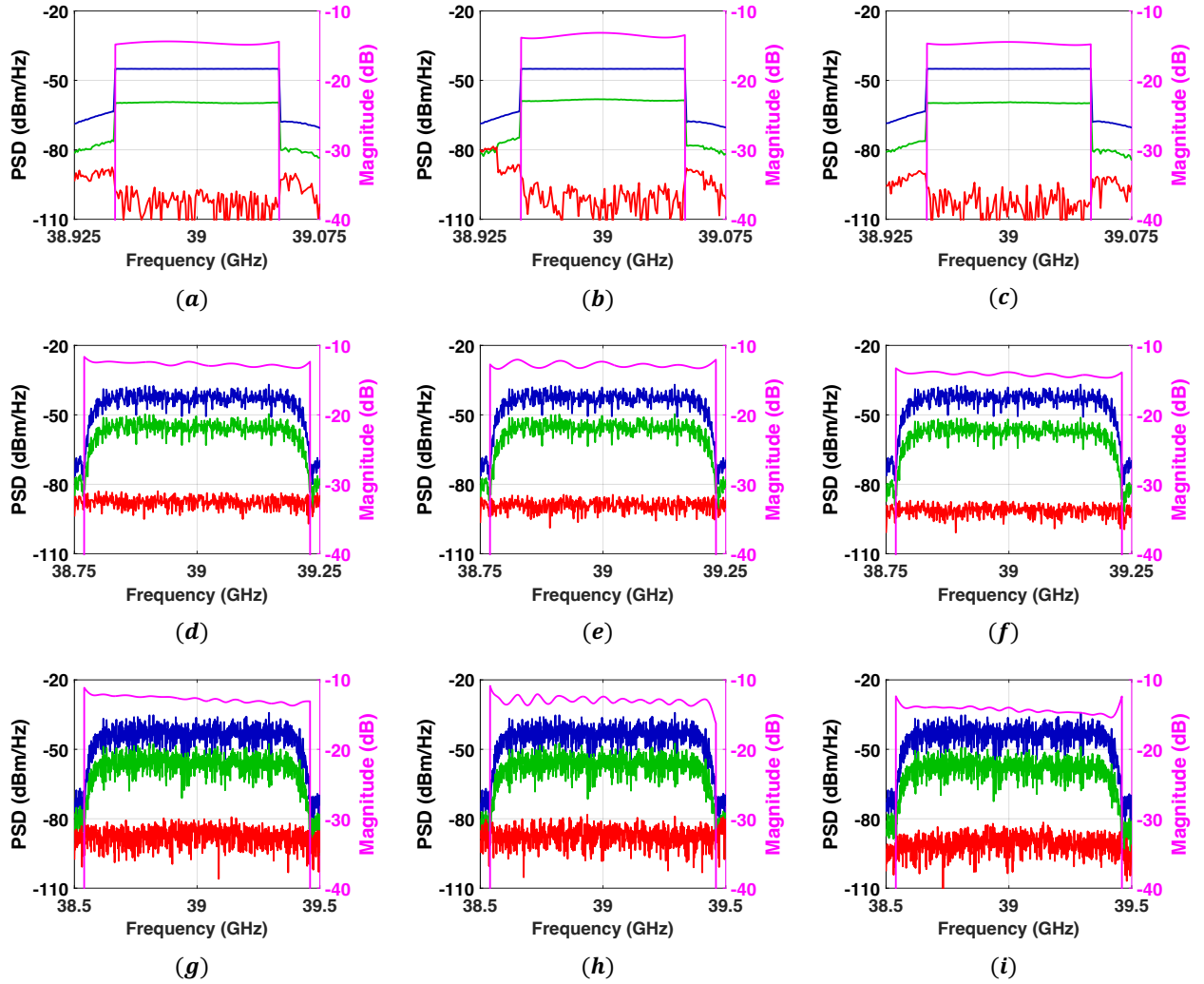


Figure 4.23 Power spectral densities of the modulated stimulus applied to the AUT  $S_{XX}(f)$  (blue) and measured on the PNA-X reference receiver  $R1$ , the received signal from the CATR feed horn  $S_{YY}(f)$  (green) measured on receiver  $B$ , and the distortion spectrum  $S_{DD}(f)$  (red) described in section 2.3, with the corresponding modulated gain  $|H(f)|$  (magenta) overlaid. Results are for a 100 MHz-wide flat tone signal (a)-(c), and a 16-QAM signal with 400 Mbaud (d)-(f) and 800 Mbaud (g)-(i) symbol rates measured at beam scan angles  $(\theta_s, \phi_s) = (45^\circ, 270^\circ)$  [(a),(d),(g)];  $(\theta_s, \phi_s) = (0^\circ, 0^\circ)$  [(b),(e),(h)]; and  $(\theta_s, \phi_s) = (45^\circ, 90^\circ)$  [(c),(f),(i)].

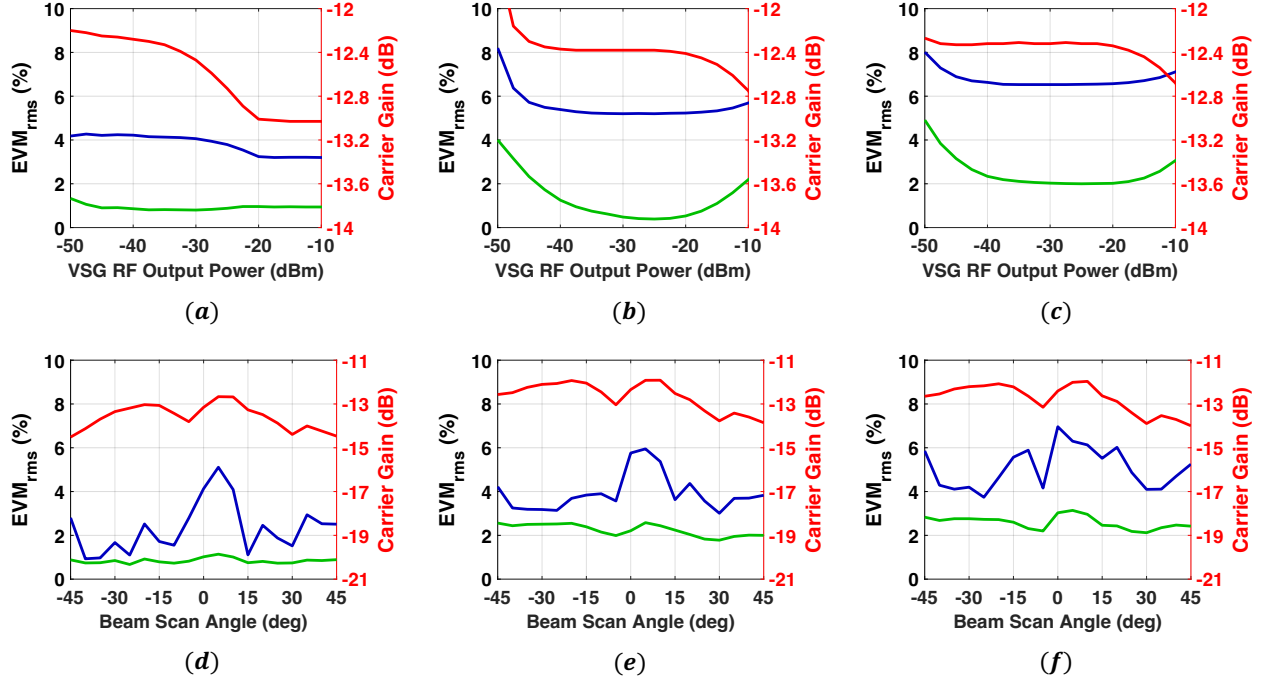


Figure 4.24 Equalized  $EVM_{EQ}$  (green), un-equalized  $EVM_{UN}$  (blue), and carrier gain  $|H(f_c)|$  (red) as a function of RF output power from the VSG (a)-(c) and elevation beam scan angle  $\theta_s = [0^\circ : 15^\circ : 45^\circ]$ ,  $\phi_s = [90^\circ, 270^\circ]$  (d)-(e) for a 100 MHz-wide flat tone signal [(a),(d)] and 16-QAM signals with 400 Mbaud [(b),(e)] and 800 Mbaud [(c),(f)] symbol rates.

three different beam scan angles in Fig. 4.23. While the average modulated gain and power in the distortion spectrum  $S_{DD}(f)$  appear to be relatively stable with beam scan angle, the ripple in modulated gain across the signal bandwidth is greatest when the beam is scanned near boresight  $(\theta_s, \phi_s) = (0^\circ, 0^\circ)$ . Consequently, the equalized EVM remains nearly constant with beam scan angle, while the un-equalized EVM increases near  $\theta_s = 5^\circ$ , as shown in Fig. 4.24(d)-(f). For the 800 Mbaud signal results in Fig. 4.24(d), there is evidence of VGA gain compression, as the equalized EVM variation nearly matches that of the carrier gain  $|H(f_c)|$ .

For the EVM measurements of the 8x8 phased array versus beam scan angle, RF carrier power of the VSG source  $P_{RF}$  was held constant at -10 dBm for the two 16-QAM signals and -25 dBm for the 100 MHz flat tone signal. The EVM was also measured as a function of  $P_{RF}$  with the phased array held stationary and beam scanned to boresight for all three test signals. These results are presented in Fig. 4.24(a)-(b). Due to the higher PAPR of the 100 MHz-wide flat tone signal in Fig. 4.24(a), the VGAs in the phased array beamforming ICs

are in compression, and the carrier gain decreases even near the lowest VSG power levels ( $P_{RF} = -50$  dBm). However, the change in equalized EVM is minimal over the power sweep, and the attenuation settings of the VNA appear to change automatically as power is increased from -20 to -10 dBm to protect its receivers. For the two 16-QAM test signals shown in Fig. 4.24(b)-(c), the equalized EVM takes the form of a bathtub curve and closely approximates the EVM versus EIRP plot in Fig. 4.12(b), which was measured for the same phased array with a 200 Mbaud 64-QAM test signal [98]: At low  $P_{RF}$ , equalized EVM decreases from higher values due to the lower SNR in this region; at median  $P_{RF}$ , where the gain remains constant and SNR is higher, it reaches a minimum value; and at high  $P_{RF}$ , it increases due to increased intermodulation distortion in the transmitted signal from VGA compression. For the measurements of the passive Ka-band horn antenna with no front-end power amplifier, shown in Fig. 3.29, the equalized EVM continues to decrease with increasing  $P_{RF}$  because it remains SNR-limited even in the high power region.

## 4.5 Summary

This chapter presented the modeling, simulation, and measurement of the EVM resulting from wideband modulated signal transmission of active, electronically-scanned arrays (AESAs). Various EVM simulation methods that have been applied to these active arrays and demonstrated in recent literature were reviewed, and limitations of these methods were identified. One limitation was that the linear distortion resulting from the combined effects of the array element frequency response and beam squint had not yet been modeled and simulated. This was addressed by applying phase gradients computed for the same frequency  $f_c = 39$  GHz to arrays of elements with a uniform frequency response (vector effective length magnitude) determined from full-wave simulation of a coax-fed microstrip patch near the center of an 8x8 array and simulating the EVM of 16-QAM signals transmitted at carrier frequencies with offsets  $\Delta f$  from  $f_c$ . The embedded element frequency response was obtained through the same techniques that had been applied to a single microstrip patch antenna in section 3.2. Since only the amplitude distortion of the array elements was modeled in these simulations,

the complex voltage transfer function method applied in section 3.3 was later implemented for each element of this 8x8 array and used to simulate EVM versus beam scan angle. The effects of amplitude tapering and phase quantization, in the absence of a nonlinear distortion model for power amplifiers, were shown to be negligible. A review of indirect far field antenna test systems for EVM measurements of active arrays was presented, and EVM measurements of 16-QAM signals distorted by a millimeter-wave CATR link between the 8x8 phased array from [98] and a wideband WR-28 scalar feed horn [86] were presented. These EVM results were derived from the spectrum of the transmitted and received signals, which were measured simultaneously with a multi-port network analyzer. The calibration and coherent acquisition of narrowband VNA receivers allows noise floor to be lowered enough to capture low-power signals from individual active array element channels in addition to the sum of signals from all array element channels as the beam is scanned. The reduced spatial path loss of the CATR (64.4 dB at  $f_c = 39$  GHz) [93], which is based on the 1.02-meter reflector focal length, further improves the dynamic range. If even greater dynamic range is required and can be tolerated at the expense of longer frequency sweep times, the noise bandwidth (NBW) of the VNA receiver, computed as IF bandwidth times vector averaging factor, can be further reduced to minimize the EVM noise component from equation (3.22) and isolate the harmonic distortion. The EVM of the 8x8 phased array elements measured as a function of RF power at boresight and far field elevation angle and the EVM of the fully-active phased array as a function of RF power at boresight and beam scan angle were presented. Causes of element-to-element variations in EVM were analyzed, and EVM was shown to increase with modulation rate and beamforming IC amplifier intermodulation distortion as the fully-active array was scanned.



## CHAPTER 5

# Far Field EVM Characterization via Planar Near Field to Far Field Transformation

### 5.1 Review of Planar Near Field to Far Field Transformation for Far Field EVM Analysis

Planar near field measurement systems are particularly well-equipped for determining the far field radiation characteristics of large apertures and planar phased arrays with broadside radiation, such as silicon millimeter-wave phased arrays built for base stations and satellites [14–16]. The AUT size is limited by the dimensions of the probe scanning system rather than the those of the reflector quiet zone as it is with a CATR, and the AUT can remain stationary during probe scanning [91]. The reduction in test volume lowers spatial path loss and increases the dynamic range of the measurement as well, which has motivated some researchers to investigate the feasibility of applying planar near-to-far field transformation techniques to the analysis of modulated signal quality metrics such as EVM and BER [19, 114]. The numerous challenges associated with this endeavor have been outlined in recently-published literature. First, the planar near field (PNF) to far field transformation is implemented by calculating a two-dimensional fast Fourier transform (FFT) of the near fields sampled at probe positions with a minimum separation distance of  $\Delta x_0 \leq \lambda/2$  and  $\Delta y_0 \leq \lambda/2$  at discrete wavelengths  $\lambda$  [114, 119], as shown in equations (5.1), (5.2), (5.3), and (5.4), the discrete representations of equations (17-7) and (17-9) from [91]. Equations (5.1) and (5.2) are the  $\hat{x}$  and  $\hat{y}$  components of the plane wave spectrum respectively, where  $N_x$  and  $N_y$  are the number of probe positions along the two dimensions of the PNF scan plane,  $E_x$  and  $E_y$  are the near field components measured in the scan plane at  $z = z_0$ , and  $k_x$  and  $k_y$  are components of the wavenumber

$k = k_x \hat{x} + k_y \hat{y} + k_z \hat{z} = 2\pi/\lambda$  that satisfy the dispersion relation  $k^2 = k_x^2 + k_y^2 + k_z^2$ . Equations (5.3) and (5.4) are orthogonal far field components computed from the plane wave spectrum, where  $(r, \theta, \phi)$  are the spherical coordinates of the far field position at which the radiated fields are evaluated.

$$f_x(k_x, k_y) = \sum_{m=-N_x/2}^{N_x/2} \sum_{n=-N_y/2}^{N_y/2} E_x(m\Delta x_0, n\Delta y_0, z_0) e^{j(k_x m \Delta x_0 + k_y n \Delta y_0)} \Delta x_0 \Delta y_0 \quad (5.1)$$

$$f_y(k_x, k_y) = \sum_{m=-N_x/2}^{N_x/2} \sum_{n=-N_y/2}^{N_y/2} E_y(m\Delta x_0, n\Delta y_0, z_0) e^{j(k_x m \Delta x_0 + k_y n \Delta y_0)} \Delta x_0 \Delta y_0 \quad (5.2)$$

$$E_\theta(r, \theta, \phi) = \frac{jk e^{-jkr}}{2\pi r} (f_x \cos \phi + f_y \sin \phi) \quad (5.3)$$

$$E_\phi(r, \theta, \phi) = \frac{jk e^{-jkr}}{2\pi r} \cos \theta (-f_x \sin \phi + f_y \cos \phi) \quad (5.4)$$

Because the PNF to far field (FF) transformation is predicated on an FFT computation for a plane wave spectrum which is unique for each frequency and planar near field distribution, a large number of FFT computations may be required to acquire wideband radiated far fields of large phased arrays transmitting multicarrier modulated signals such as OFDM [21, 113], and spatial FFTs would have to be calculated for each unique beam state [121]. If multiple beams at large scan angles must be measured within a single PNF scan, the scan plane size must be increased to ensure that the near fields decay to at least 30 dB below the peak magnitude, according to the IEEE recommended practices [122]. This could make the PNF measurement prohibitively time-consuming if a single probe is sequentially moved to each of the planar near field sampling points. Probe positioning errors, especially along the  $\hat{z}$  axis [123], and ambient temperature variations during the PNF scan may reduce the accuracy of the far fields derived

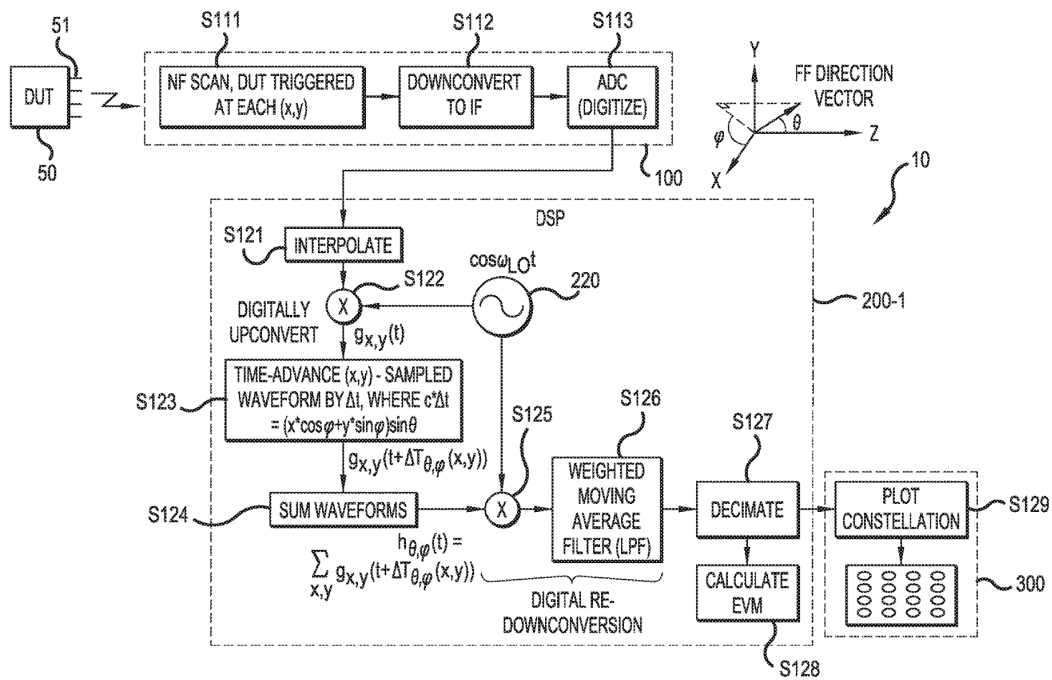


Figure 5.1 A patented procedure for far field EVM estimation from wideband PNF-to-FF transformation [120] based on time advancing the digitized PNF waveforms using eqn. (5.5).

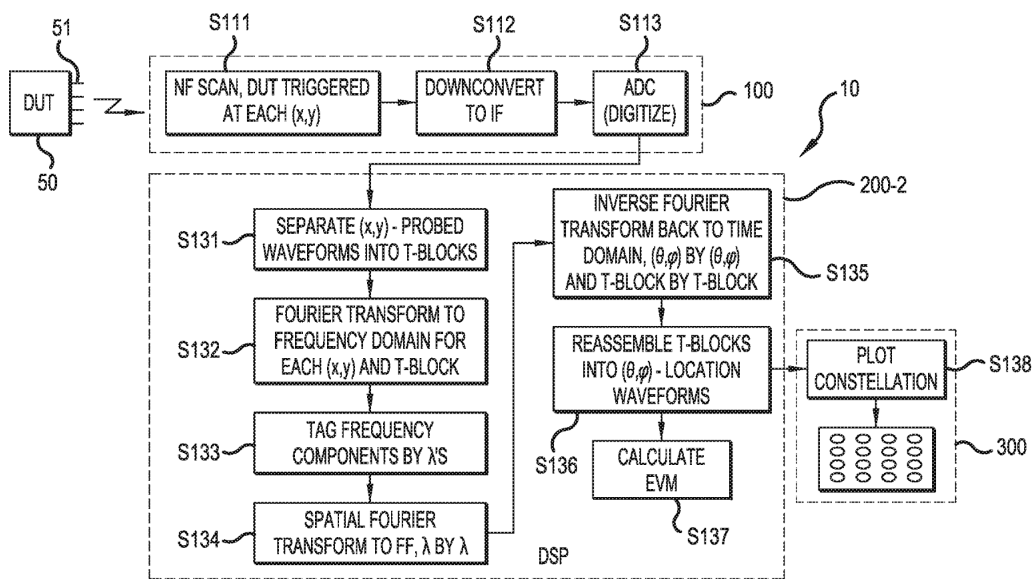


Figure 5.2 A patented procedure for far field EVM estimation from wideband PNF-to-FF transformation [120] based on Fourier transforming multiple PNF waveform time segments and frequency bins.

from the PNF-to-FF transformation as well [19, 113]. For system-embedded millimeter-wave phased arrays that lack ports with direct access to the feed point, a separate stationary probe needs to be included to maintain a phase reference during the PNF scan [113, 119]. Finally, SNR differences between the PNF probe positions and far field positions would have to be determined, which is challenging due to noise figure dependence on PNF probe position [114].

Despite these challenges, researchers have started to develop and patent novel techniques for estimating far field EVM from wideband PNF measurements of modulated test signals, periodically transmitted by the AUT during each PNF probe acquisition [120]. Two representations of the EVM measurement algorithm from [120] are shown in Figs. 5.1 and 5.2. In Fig. 5.1, PNF-sampled signals are down-converted to an intermediate frequency (IF), digitized, interpolated, and upconverted to acquire digital RF signals for sampled planar near fields at each of the probe positions. The propagation to a far field observation point at angle  $(\theta, \phi)$  is modeled by time-advancing the digitized PNF signals by  $\Delta t$  in equation (5.5), where  $(x, y)$  is the PNF probe coordinate and  $c_0$  is the speed of light.

$$\Delta t = [(x \cos \phi + y \sin \phi) \sin \theta] / c_0 \quad (5.5)$$

The superposition of the time-advanced digital RF waveforms represents the far field signal, which is downconverted, filtered, and decimated to calculate the far field EVM. In Fig 5.2, digitized IF near fields from each PNF probe position are partitioned into multiple smaller time segments that are Fourier transformed to the frequency domain. Multiple spatial Fourier transforms are then calculated to obtain the plane wave spectrums for a collection of frequency bins which span the entire modulated signal bandwidth to acquire the wideband far fields for all of the valid far field angles in the upper hemisphere ( $\theta_v \leq 90^\circ$ ). The far fields for each tone are subsequently transformed back to time domain segments that are stitched together to calculate the equivalent far field EVM. The patent holders recommended that the near field time segment durations  $T$  satisfy  $\Delta\omega_{bin}T \geq 50$  and that frequency bins  $\Delta f_{bin}$  satisfy  $\Delta f_{bin} \leq 0.01 * f_c$  to the nearest power of two to facilitate fast and efficient FFT computations.

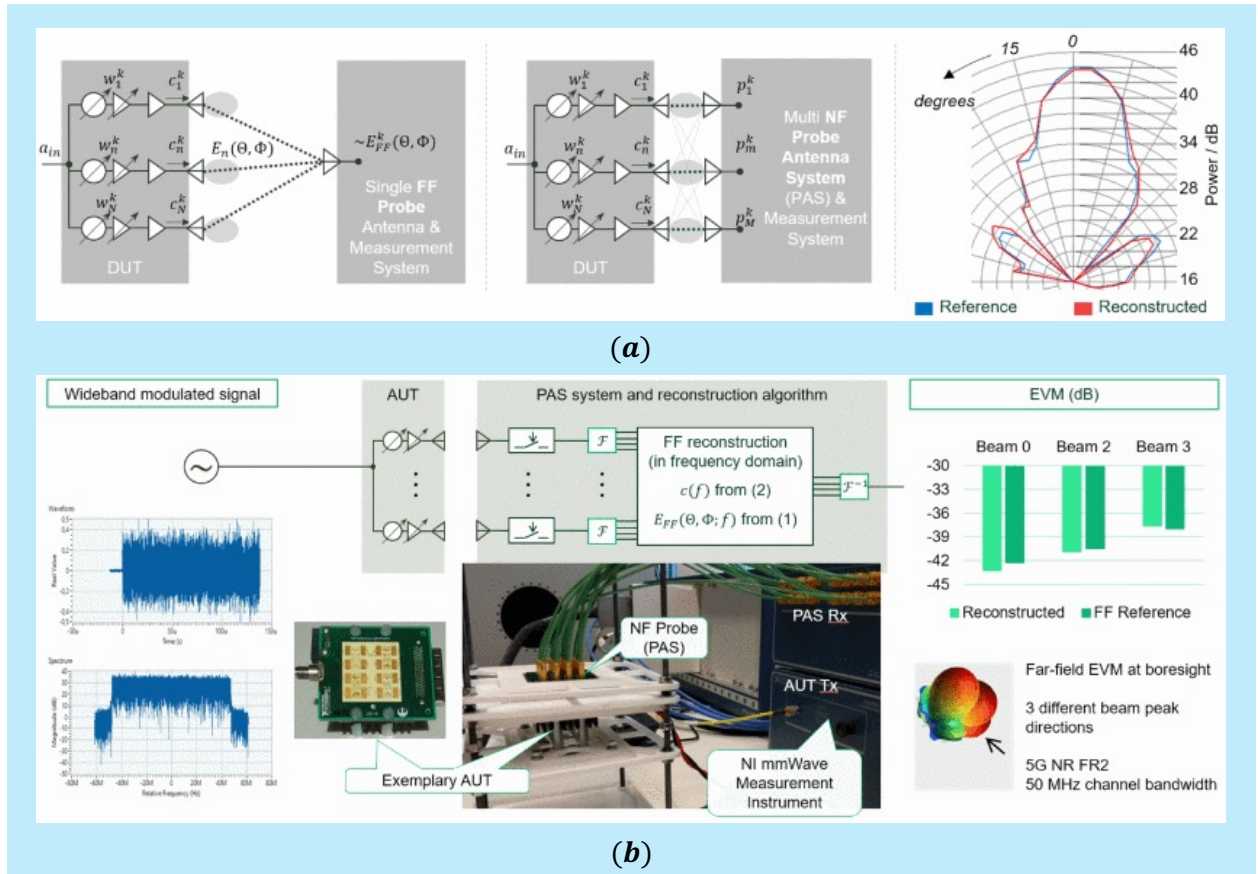


Figure 5.3 Far field EVM estimation from a multi-probe PNF measurement [124]: (a) diagrams of far field calibration and near field measurements and (b) wideband application for EVM.

Another method of determining the far field EVM of a phased array from multi-probe PNF measurements was recently introduced in [124]. In this work, a planar near field to far field mapping matrix  $R$  that transforms the multi-probe PNF measured data  $p$  at each frequency  $f$  to a set of array element pattern scaling coefficients  $c$  is derived by performing both a far field calibration measurement and a multi-probe PNF measurement as highlighted in Fig. 5.3(a) and equations (5.6a)-(5.6b). The PNF probe array and the AUT both had  $N = 16$  antennas, and the PNF probes were assumed to have high cross-isolation ( $\geq 15$  dB) with the AUT antennas based on full-wave simulations from [125]. This method was applied to a 50 MHz wide 5G FR2 test signal, and the EVM of the signal with a frequency spectrum synthesized through PNF measurements and equations (5.6a)-(5.6b) was within 1 dB of the EVM of the signal measured directly in the far field of the AUT for three different beam

states, as shown in Fig. 5.3(b) [124]. While a far field measurement is required to obtain the mapping matrix  $R$  and AUT element patterns  $E_n(\Theta, \Phi, f)$  over the frequency band of interest, this technique takes advantage of the linearity between planar near field and far field measurements to analyze the far field modulated signal quality, which is quantified as EVM.

$$E_{FF}(\Theta, \Phi, f) = \sum_{n=1}^N E_n(\Theta, \Phi, f) \cdot c_n(f) \quad (5.6a)$$

$$\mathbf{c}(\mathbf{f}) = \mathbf{R}(\mathbf{f}) \cdot \mathbf{p}(\mathbf{f}) \quad (5.6b)$$

Some researchers have suggested that EVM measured directly in the near field region of phased arrays may not differ significantly from that measured in the far field [126, 127]. The authors of [126] showed that the closer proximity of the receive probe to the phased array surface in near field measurements yields larger variations in measured group delay, due to larger differences in element path lengths and phase. Despite this, the change in the measured EVM of a 100 MHz 64-QAM signal transmitted by 16-element array was demonstrated to be negligible as probe distance varied from 1-10 wavelengths. In [127], EVM simulation of a four-element linear array transmitting 16 and 64-QAM signals showed that changing the distance between the receive probe and phased array along its normal axis did not change the EVM when the array's beam steering matrix was periodically updated from channel estimates. The early stages of research on the adaptation and application of PNF-to-FF transformation techniques for far field EVM estimation and studies on the relationship between PNF and FF EVM demonstrate the potential for meaningful EVM analysis from measured or simulated near field data. In this chapter, PNF simulations and measurements of the Ka-band conical horn model presented in previous chapters are performed to determine the horn's wideband far field frequency response, and the simulated PNF data is used to predict the far field EVM. Additionally, PNF measurements of a beam-scanning 8x8 millimeter-wave phased array are performed, and measured near field EVM and far field patterns calculated from measured near fields at multiple frequencies are presented. A methodology for estimating far field EVM from PNF measurements of an antenna transmitting wideband modulated test signals is also proposed and demonstrated.

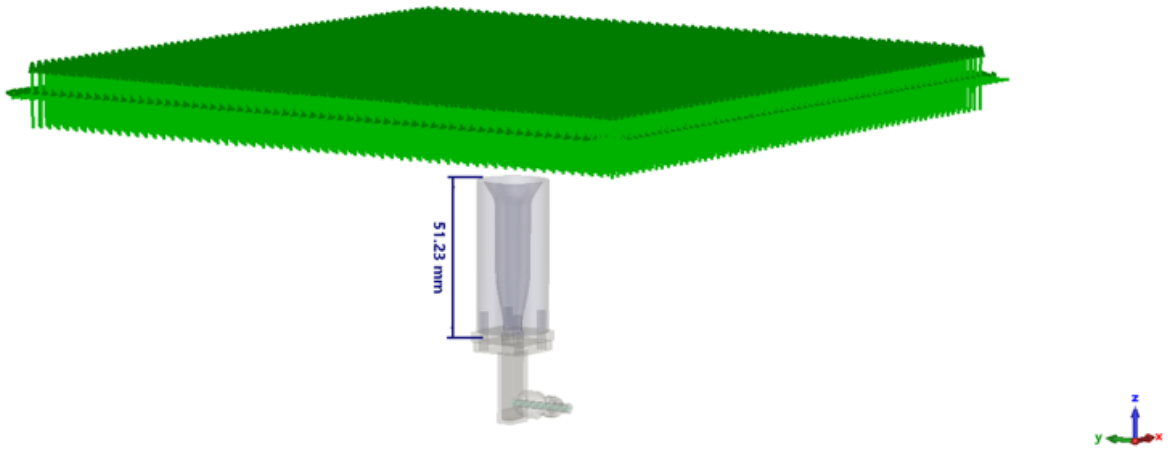


Figure 5.4 Ka-band conical horn antenna model with  $N_x N_y = 4096$  ideal planar near field probes (green) in CST Microwave Studio. Ideal probes have a linear spacing  $\Delta x = \Delta y = \lambda/2$  over the  $32\lambda \times 32\lambda$  scan plane positioned  $z_0 = 5\lambda$  above the horn aperture, where  $\lambda = 6.82$  mm at  $f_{max} = 44$  GHz.

## 5.2 Planar Near Field Simulation and Far Field EVM Prediction for a Ka-band Conical Horn Antenna

### 5.2.1 Introduction

A primary means of achieving high-data rate wireless links in millimeter-wave frequency bands has been the deployment of antennas with high directivity and beam-steering flexibility, such as planar phased arrays. Such antennas help compensate for high over-the-air path loss and mitigate interference. Planar near field (PNF) measurements are favorable for characterizing far field radiation of these antennas due to their minimal space requirements, higher SNR, and computational efficiency of the fast Fourier transform (FFT). In [128], a PNF measurement was emulated in a frequency domain full-wave solver by moving a probe antenna to each PNF sampling point and simulating S21 between the ports of the antenna under test (AUT) and probe. While this approach enables subsequent analysis of the effects of probe patterns and compensation on the Fourier-transformed far fields, running independent simulations for each PNF probe position and frequency may become too time-consuming when (a) the far

fields must be determined at many frequencies and (b) large scan planes with thousands of PNF sampling points are required to obtain near fields that decay to at least 30 dB below the peak magnitude at the edges [122]. The authors were motivated by condition (a) due to an interest in determining the far field modulated signals via PNF simulations. For wide angle beam-steering apertures and phased arrays, condition (b) would also be required to acquire the far field signals for each beam state. Unlike the MLFMM method implemented in [128], the finite integral technique in the CST time domain solver can be used to obtain broadband planar near fields in one simulation, rather than running a full wave simulation for each frequency. The PNF sample position and alignment errors can still be studied using the time domain simulation method shown in this work. The spline-profiled Ka-band conical horn antenna presented in Fig. 5.4 and described in [85] is used to demonstrate this method.

### 5.2.2 Planar Near Field Simulation

An image of the full CST simulation model with the conical horn antenna and planar near field probe objects highlighted in green is shown in Fig. 5.4. A special MATLAB program was developed to synthesize a unique VBA Macro that automates the process of generating each of the ideal PNF probes in CST Microwave Studio for a user-defined scan plane with a valid far field angle  $\theta_v$  in (5.7) [122], where  $L = N_x\Delta x = N_y\Delta y$  is the scan plane dimension,  $D$  is the diameter of the conical horn aperture, and  $z_0$  is the height of the PNF scan plane above the horn aperture.

$$\theta_v = \arctan \frac{L/2 - D/2}{z_0} \quad (5.7)$$

Ideal probe separation  $\Delta x = \Delta y = \lambda/2 = 3.41$  mm was set by the maximum simulated frequency of 44 GHz and  $N_x = N_y = 2^6 = 64$  to facilitate efficient FFT calculations for the far field transformation, which resulted in a large scan plane with dimension  $L = 218.2$  mm and  $\theta_v = 71^\circ$  for  $D = 20$  mm and  $z_0 = 5\lambda = 34$  mm. The PNF scan plane consists of  $N_x N_y = 4096$  ideal probes capturing complex  $\vec{E}_x$  and  $\vec{E}_y$  planar near fields at 1000 frequency



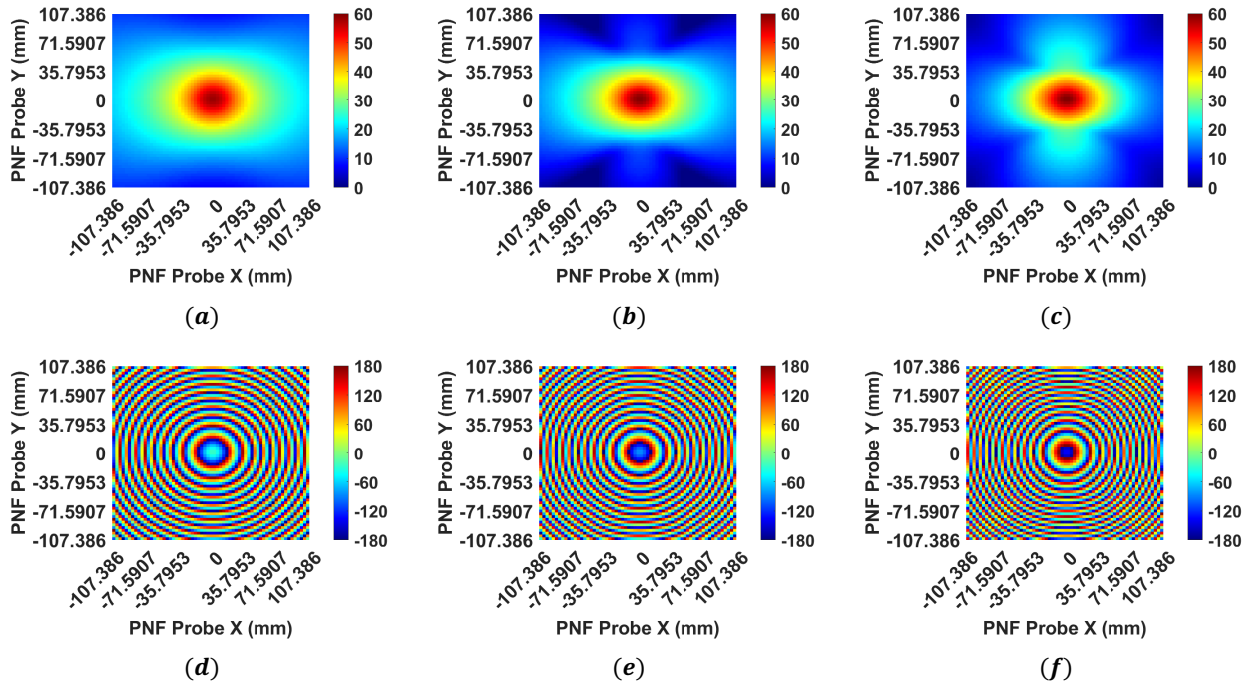


Figure 5.5 Simulated  $\vec{E}_y$  planar near field magnitude (dBV/m) [(a)-(c)] and phase (degrees) [(d)-(f)] at 35 GHz [(a),(d)], 39 GHz [(b),(e)] and 43 GHz [(c),(f)] for Ka-band horn model.

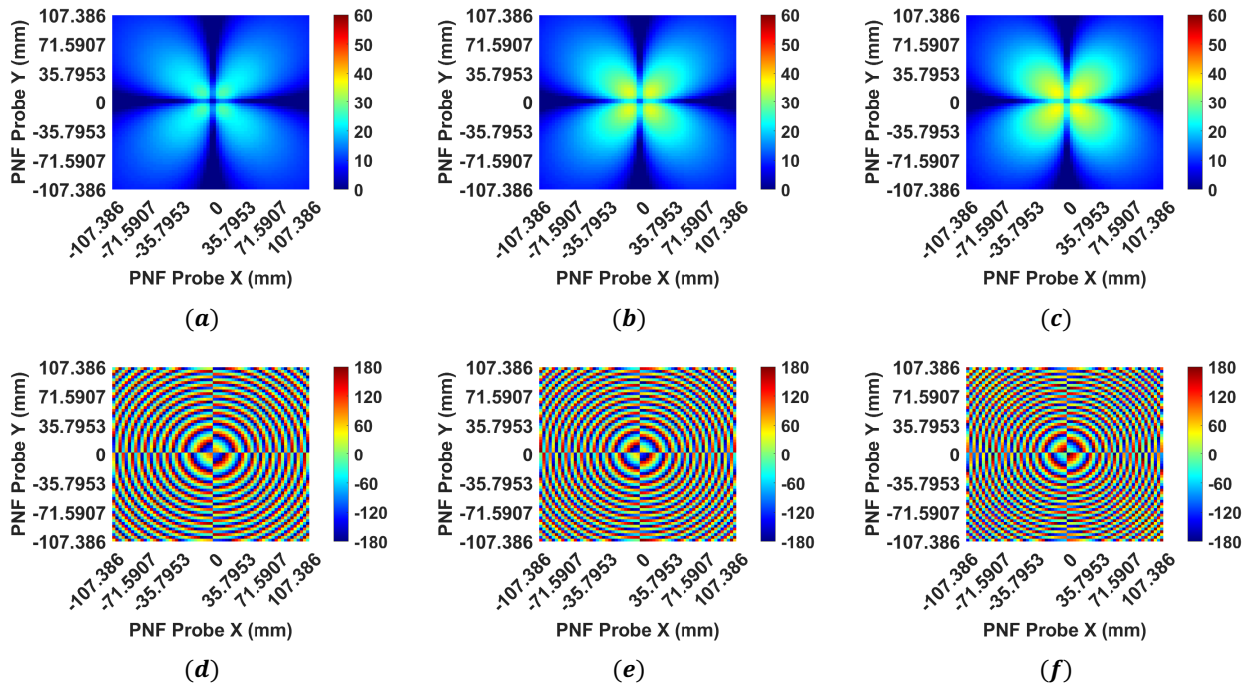


Figure 5.6 Simulated  $\vec{E}_x$  planar near field magnitude (dBV/m) [(a)-(c)] and phase (degrees) [(d)-(f)] at 35 GHz [(a),(d)], 39 GHz [(b),(e)] and 43 GHz [(c),(f)] for Ka-band horn model.

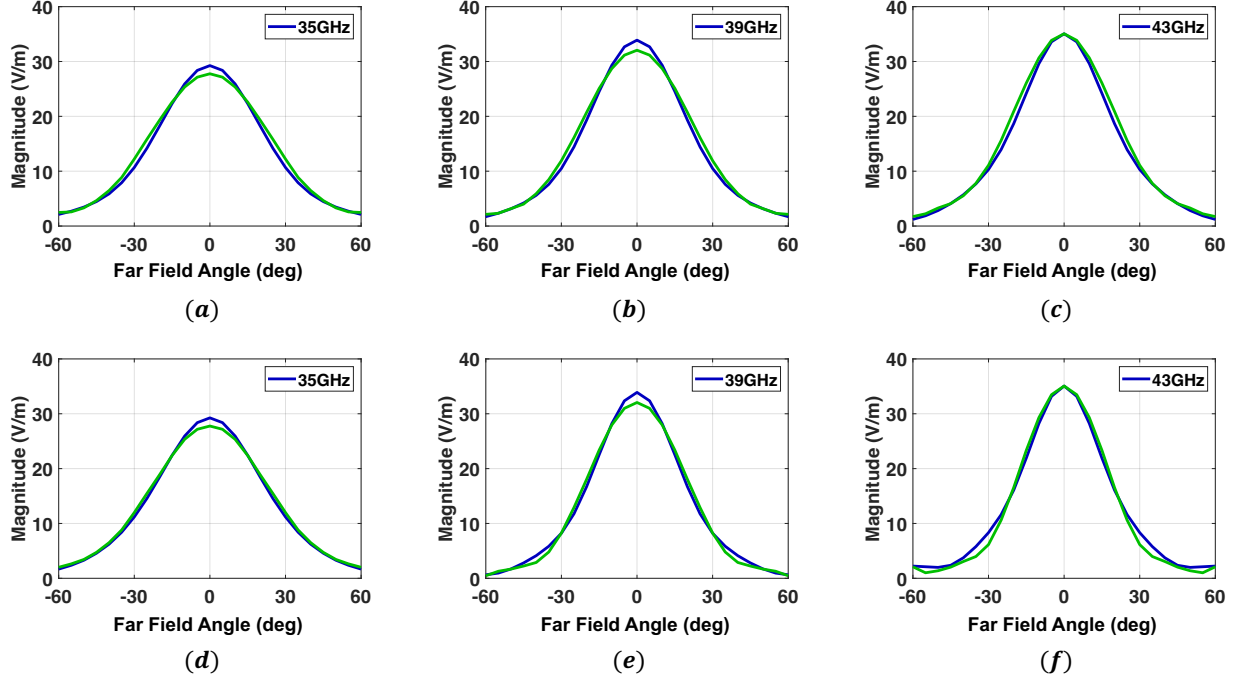


Figure 5.7 Magnitude of vertical Ludwig-3 far field component ( $|\vec{E}_V|$ ) from ideal far field probes (blue) and planar near field to far field transform (green) as a function of the far field angle  $\theta$  in the E-plane [(a)-(b)] and H-plane [(d)-(f)] at 35 GHz [(a),(d)], 39 GHz [(b),(e)] and 43 GHz [(c),(f)]. All  $\theta$  angles are positive (in upper hemisphere): Negative to positive  $\theta$  shifts indicate a  $\phi$  shift of  $(180^\circ, 0^\circ)$  for E-plane and  $(270^\circ, 90^\circ)$  for H-plane.

points spanning 34-44 GHz. The planar near fields were exported from CST with the aid of another VBA Macro that was synthesized from another MATLAB program. The magnitude and phase of simulated planar near fields  $\vec{E}_y$  and  $\vec{E}_x$  at 35 GHz, 39 GHz, and 43 GHz are presented in Figs. 5.5 and 5.6 (a)-(b) and (c)-(d) respectively. For co-polarized planar near fields shown in Fig. 5.5, a uniform phase is present across the circular aperture of the conical horn antenna in (d)-(f), and the decay in  $|\vec{E}_y|$  toward the PNF scan plane edges at 35 GHz (a) is less than that at 39 GHz (b) and 43 GHz (c), indicating a lower horn antenna directivity.

### 5.2.3 Broadband Far Field and EVM Results

The spherical components of the radiated far fields from the Ka-band conical horn antenna  $E_\theta$  and  $E_\phi$  are calculated from the planar near fields exported from the CST time domain

simulation at each of the 1000 frequency points spanning 34-44 GHz using equations (5.1), (5.2), (5.3), and (5.4). The Ludwig 3 vertical far field component  $\vec{E}_V(f, \theta, \phi)$  is then calculated from the spherical far field components using equation (3.14b), and its magnitude is scaled by  $\sqrt{P_{RAD}(f)/P_{PNF}(f)}$ , where  $P_{RAD}(f)$  is the radiated power of the antenna at each frequency  $f$  as reported by the far field monitors from the CST simulation and  $P_{PNF}$  is the radiated power estimated from planar near fields captured within the scan plane as shown in equations (5.8) and (5.9), where  $U(f, \theta, \phi)$  is the radiation intensity,  $r = 1.0$  m is the far field distance,  $\eta = 377\Omega$  is the free space impedance, and  $P_{PNF}$  is obtained from the discrete summation of  $U(f, \theta, \phi)\Delta\theta\Delta\phi$  over all  $(\theta, \phi)$  in the upper hemisphere with a resolution of  $\Delta\theta = \Delta\phi = 1.0^\circ$ .

$$P_{PNF}(f) = \sum_{m=-N_\theta/2}^{N_\theta/2} \sum_{n=-N_\phi/2}^{N_\phi/2} U(f, m\Delta\theta, n\Delta\phi)\Delta\theta\Delta\phi \quad (5.8)$$

$$U(f, \theta, \phi) = \frac{r^2}{2\eta} [ |E_\theta(f, \theta, \phi)|^2 + |E_\phi(f, \theta, \phi)|^2 ] \quad (5.9)$$

The magnitude of Ludwig-3 vertical far field component  $|\vec{E}_V(f, \theta, \phi)|$  as a function of  $\theta$  in two orthogonal planes ( $\phi = 0^\circ, 90^\circ$ ) is presented in Fig. 5.8(a)-(b) and (c)-(d), where the green traces are the far fields derived from the plane wave spectrum of simulated planar near fields and the blue traces are far fields acquired directly from the CST simulation. The far field results for all three frequencies are nearly the same, but because the horn directivity is lower at 35 GHz (-1.6 dB) and 39 GHz (-0.3 dB) relative to 43 GHz, the power of the radiated fields not captured in the PNF scan plane is greater, causing  $|\vec{E}_V|$  from the PNF-transformed far fields to be slightly lower than  $|\vec{E}_V|$  from the CST simulation at these frequencies. Fig. 5.7 presents the results for  $|\vec{E}_V(f, \theta, \phi)|$  versus frequency at far field angles in the same planes as Fig. 5.8. While frequency responses  $|\vec{E}_V(f)|$  from the PNF transformations and CST results are nearly the same at most of the angles, there is greater error at large  $\theta$  angles, particularly in the  $\phi = 90^\circ$  plane (f)-(i), where the amplitude variation is greater. This is likely the result of scan plan truncation, but further analysis is required to make such a determination. The accuracy of wideband far fields derived from these PNF transformations could be enhanced by extending the scan plane edges (for analysis at wide angles) and decreasing the time step

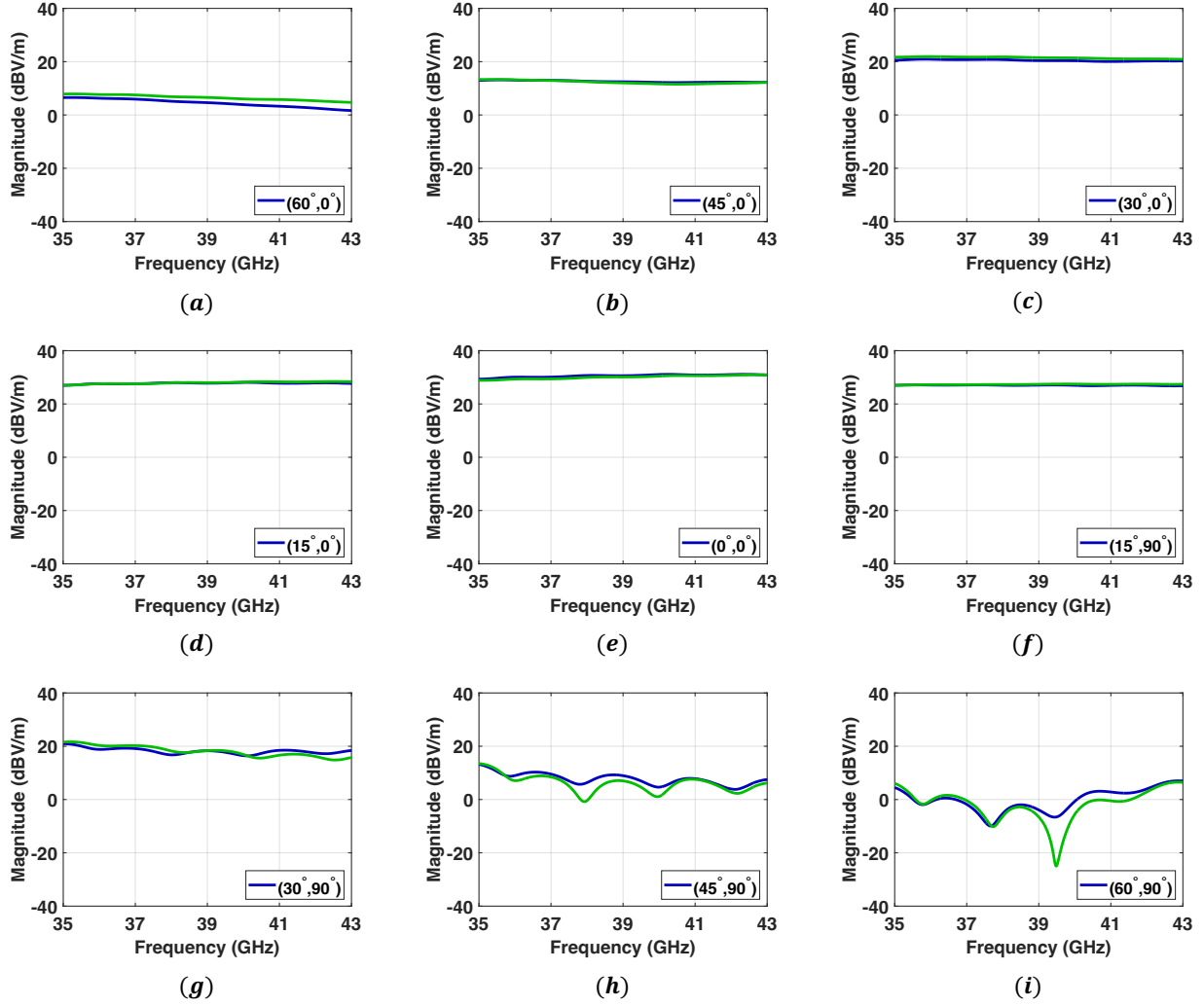


Figure 5.8 Magnitude of vertical Ludwig-3 far field component ( $|\vec{E}_V|$ ) from ideal far field probes (blue) and planar near field to far field transform (green) as a function of frequency at far field angles  $(\theta, \phi) =$  (a)  $(60^\circ, 0^\circ)$ , (b)  $(45^\circ, 0^\circ)$ , (c)  $(30^\circ, 0^\circ)$ , (d)  $(15^\circ, 0^\circ)$ , (e)  $(0^\circ, 0^\circ)$ , (f)  $(15^\circ, 90^\circ)$ , (g)  $(30^\circ, 90^\circ)$ , (h)  $(45^\circ, 90^\circ)$ , and (i)  $(60^\circ, 90^\circ)$ .

of the simulation (for wideband analysis with small separation between individual tones). Nonetheless, these time domain simulations of planar near fields can be used to determine the radiated far fields at a large number of frequencies and over a wide range of angles with reasonable simulation times. This is a critical requirement for estimating the far field EVM from full-wave simulations, especially for millimeter-wave beam-steering antennas and phased arrays transmitting wideband modulated signals. The Ka-band horn far fields derived from these PNF time domain simulations and displayed in Figs. 5.8 and 5.7 were used to estimate

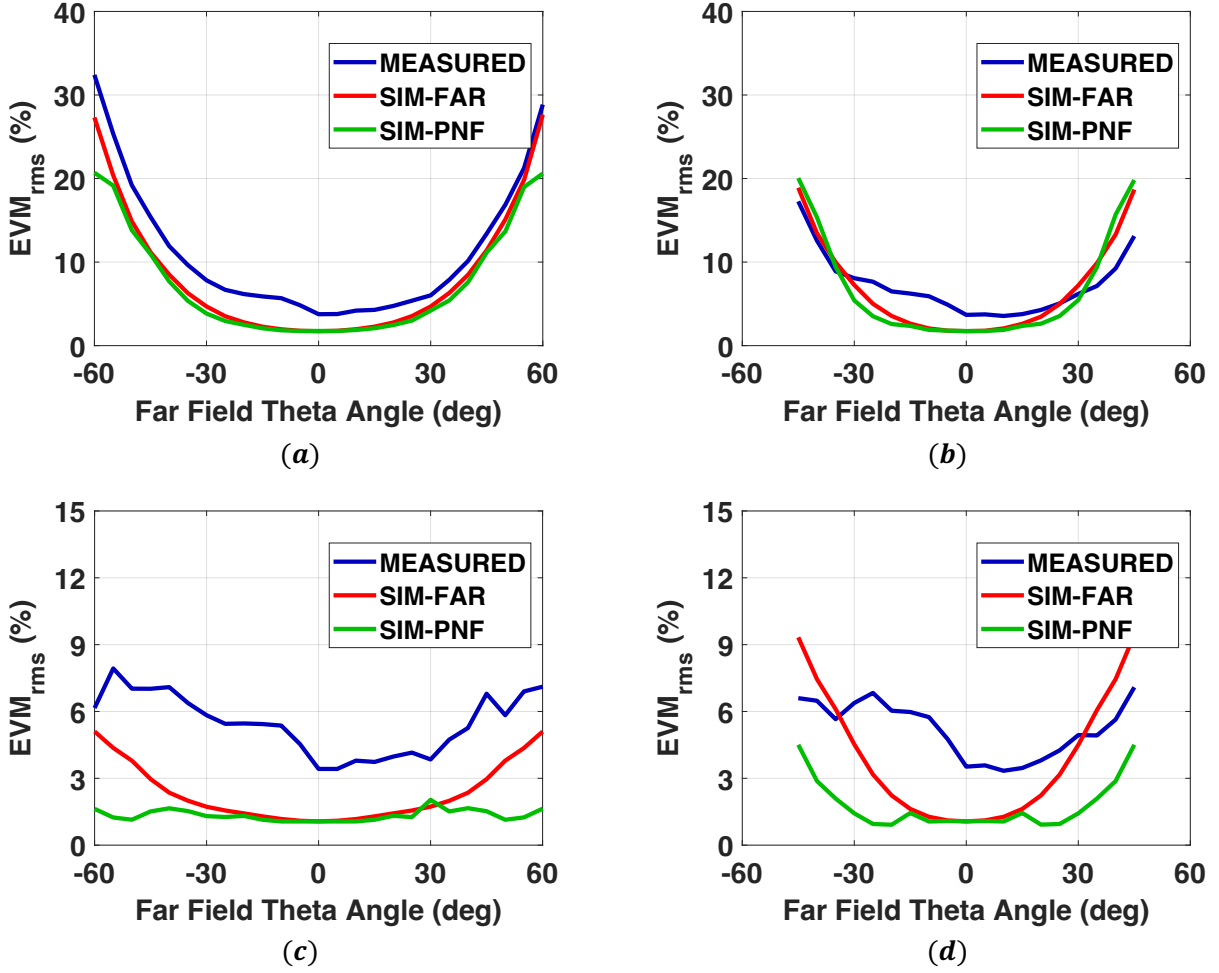


Figure 5.9 Measured (blue) and CST-simulated far field (red), and transformed PNF (green) un-equalized  $EVM_{UN}$  (a)-(b) and linear distortion  $EVM_{H(f)}$  (c)-(d) for Ka-band horn link. Results are shown for E-plane angles ( $\phi = 0^\circ$ ) in (a) and (c) and H-plane angles ( $\phi = 90^\circ$ ) in (b) and (d).  $EVM_{UN}$  results show good agreement except at largest far field angles ( $\theta \geq 45^\circ$ ), while linear distortion  $EVM_{H(f)}$  results only show good agreement for small angles ( $\theta \leq 30^\circ$ ).

the far field EVM using the same antenna link voltage transfer function simulation method, receiving horn antenna, and 16-QAM signal from section 3.3. The un-equalized  $EVM_{UN}$  and linear distortion  $EVM_{H(f)}$  from equation (3.21) that resulted from PNF-transformed far field EVM simulations (green) are compared with the simulations based on ideal far field probe data (red) and CATR measurements, which were presented in Figs. 3.23(a)-(b) and 3.24(a), in Fig. 5.9(a)-(b) and (c)-(d) respectively. Despite the large valid angle  $\theta_v = 71^\circ$  for the PNF simulation,  $EVM_{H(f)}$  values are only similar for  $\theta \leq 30^\circ$  in E-plane and  $\theta \leq 15^\circ$  in H-plane.

This is partially due to differences in the far field amplitude as a function of frequency  $|\vec{E}_V(f)|$ , which are shown in Fig. 5.8 and believed to result from scan plane truncation effects. The differences are greater at larger elevation angles, and as shown in Fig. 5.5, the descent of dominantly-polarized near field  $|\vec{E}_y(f)|$  toward the scan plane edges is not as steep across the H-plane, where there is a greater variation in the far field  $|\vec{E}_V(f)|$ , as it is in the E-plane. However,  $EVM_{H(f)}$  is also sensitive to differences in group delay as a function of frequency, which could also be embedded in the far field link voltage transfer function that was derived from CST time domain simulations of planar near fields. Additional EVM simulations would have to be performed to clearly discern the causes of these discrepancies. For example, if the tone spacing for the PNF to far field transformation was reduced from 10 MHz to 1 MHz, or to a value that more-closely matches the reciprocal of the CST simulation time step, it is plausible that the results would be more-closely matched, since this has an impact on the frequency response resolution and the coefficients of the rational fit function synthesized in MATLAB. When the effect of a finite  $SNR$  is included in the simulation model, as it is for  $EVM_{UN}$  in Fig. 5.9(a)-(b), the results are better-aligned due to the dominating effect of low  $SNR$  at wide angles. Consequently, estimation of far field magnitude versus angle plays a key role in the accuracy of far field EVM predictions from PNF measurements. In this case, the far field magnitude was calculated based on an assumption that the radiated fields of the AUT were entirely contained in the scan plane, resulting in total radiated power  $P_{PNF}(f)$ . Caution must therefore be taken to ensure that the PNF scan plane is wide enough to prevent underestimation of the AUT gain and overestimation of far field EVM, especially if a large scan plane is required to simulate the planar near fields for multiple wide-angle beam scans in a single full wave simulation. While wideband PNF simulations of phased array beam scans were not implemented, these could be accommodated with this automated placement of ideal PNF probes and application of transient techniques such as the FIT. Further experimentation is necessary to fully-validate this method for the purpose of far field EVM estimation and to understand how errors from scan plane truncation, ideal probe positioning, tone spacing, and simulation time steps affect the far field results over wide bandwidths and observation angles.

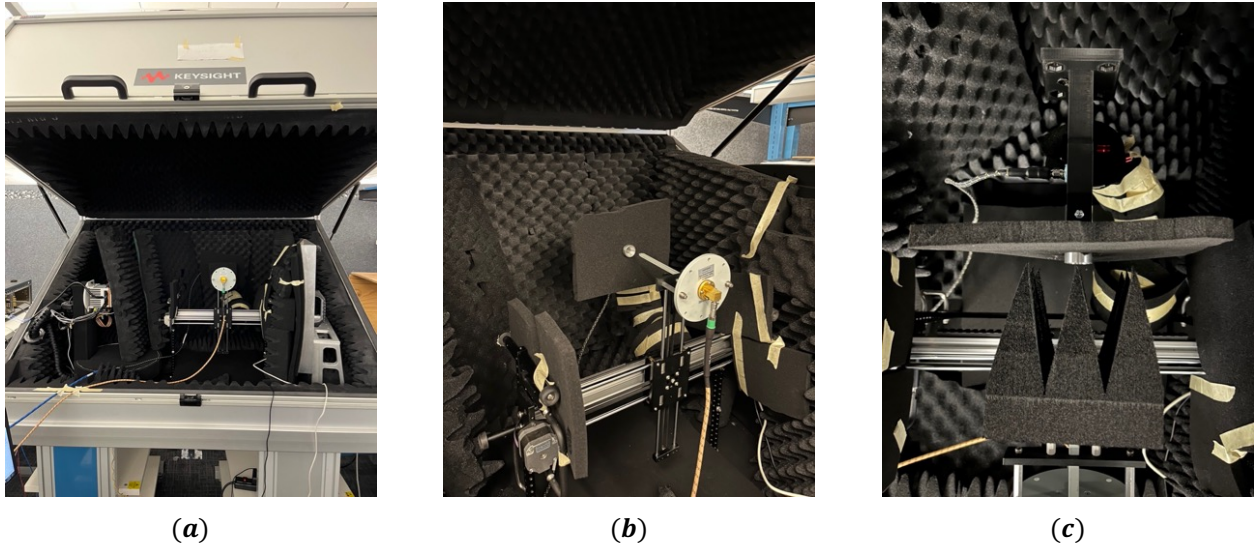


Figure 5.10 Planar near field measurement system for the spline-profiled Ka-band horn: (a) front view of measurement system placed in a shielded millimeter-wave compact antenna test range provided by Keysight in Santa Rosa, CA, with the reflector and AUT positioner covered in absorber, (b) side view of the PNF scanning machine with WR-28 open-ended waveguide probe, and (c) top view of probe and Ka-band horn mounting bracket with absorber covers. This custom PNF measurement system was invented by Dan Slater and presented in [129].

### 5.3 Planar Near Field Measurement and Far Field Pattern Estimation for a Ka-band Conical Horn Antenna

To provide further validation of the planar near field time domain simulation and wideband far field transformation method presented in section 5.2, planar near field measurements of the same Ka-band horn antenna over the same frequency range of 34-44 GHz were implemented with a low-cost miniature PNF probe scanning machine, which was originally developed by Dan Slater and presented in [129]. It is constructed from a two-dimensional robotic scanner with two digitally-controlled servo motors for the  $\hat{x}$  and  $\hat{y}$  axis control, a custom 3D-printed rectangular mounting fixture for the WR-28 waveguide probe, and a commercial off-the-shelf camera mounting bracket for the AUT. Though the reported scan plane size is 31x20 cm [129], the practical scan plane size was limited to 18x18 cm to prevent collision of the probe fixture with the absorber-padded edges of the device shown in Fig. 5.10(b). This is because the scan plane was centered over the AUT, which had to be manually positioned with the supplied

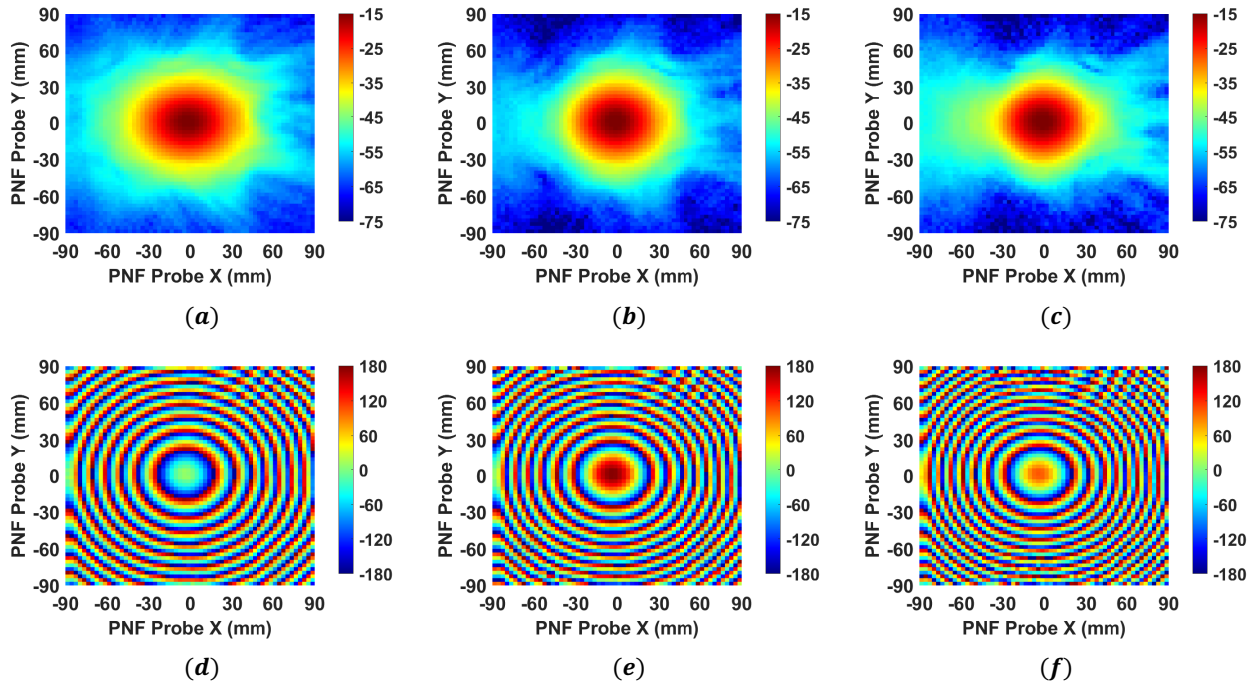


Figure 5.11 Measured  $S_{21y}$  planar near field magnitude (dB) [(a)-(c)] and phase (degrees) [(d)-(f)] at 35 GHz [(a),(d)], 39 GHz [(b),(e)] and 43 GHz [(c),(f)] for Ka-band horn antenna.

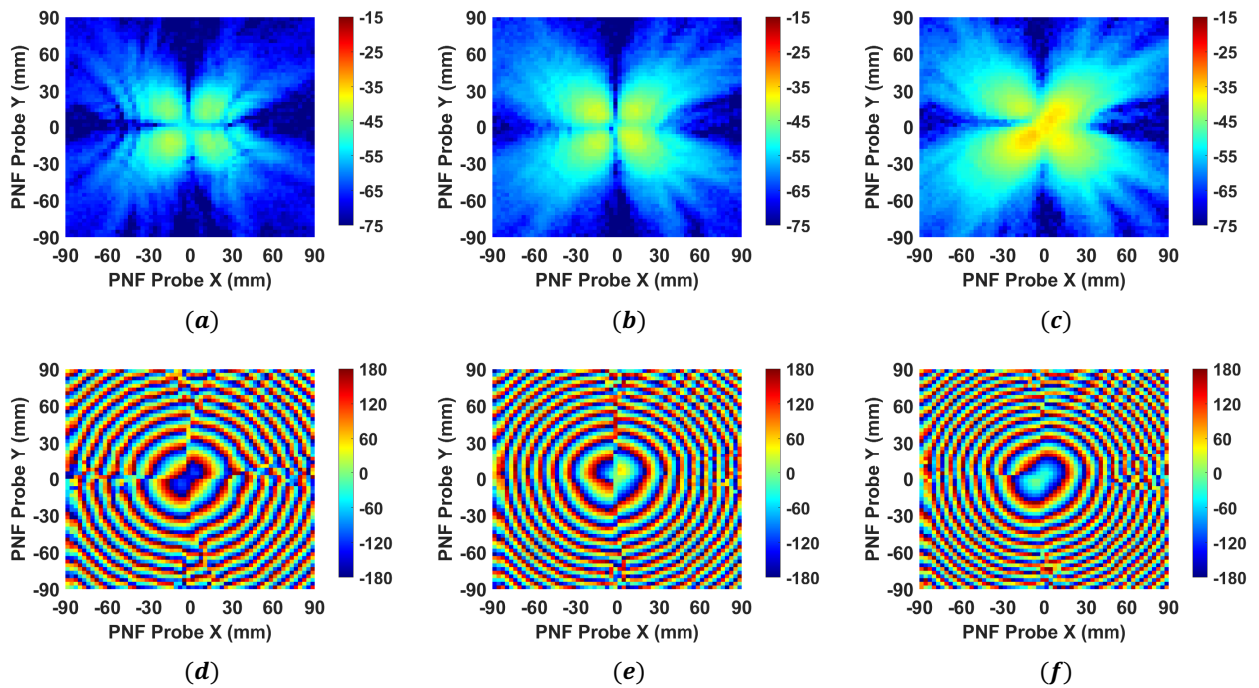


Figure 5.12 Measured  $S_{21x}$  planar near field magnitude (dB) [(a)-(c)] and phase (degrees) [(d)-(f)] at 35 GHz [(a),(d)], 39 GHz [(b),(e)] and 43 GHz [(c),(f)] for Ka-band horn antenna.



camera mounting fixture shown in Fig. 5.10(b)-(c). After manually positioning the Ka-band horn antenna, such that the circular horn aperture was visibly parallel to the PNF scan plane, the center position  $(x_0, y_0)$  of the scan plane was set by adjusting the probe position in 1.0 mm increments until the  $|S_{21}(f_c)|$  measured at  $f_c = 39$  GHz on the PNA-X network analyzer reached a maximum. This position of maximum  $|S_{21}(f_c)|$  was assumed to correspond to the center point of the Ka-band horn aperture in the PNF scan plane. The distance  $z_0$  between the WR-28 waveguide probe aperture (scan plane) and horn aperture was approximately set to  $z_0 = 34$  mm in an effort to match that of the CST simulations from section 5.2, and was measured at  $z_0 = 33$  and  $36$  mm for measurements of  $\vec{E}_y$  and  $\vec{E}_x$  respectively. These two orthogonal near field polarizations were measured by manually rotating the AUT by  $90^\circ$  and rerunning an automated PNF measurement sequence, which is why the two  $z_0$  values differ. This automated measurement sequence was programmed and executed using a customized MATLAB instrument control script similar to the ones that the author developed for the CATR measurements described in sections 3.4 and 4.3: It synchronized the probe positioner movements with frequency sweeps and  $S_{21}$  data file saving on the network analyzer, where  $S_{21}$  was captured for the 34-44 GHz band with a tone spacing of 10 MHz, which matches the CST simulation. The  $S_{21}$  was captured at  $N_x N_y = 61^2 = 3721$  probe positions separated by  $\Delta x = \Delta y = 0.44\lambda_{min} = 3.0$  mm over the usable 18x18 cm scan plane, with IF bandwidth set to 300 Hz and RF output power set to 0 dBm, and measurement duration was approximately two to three hours under these test conditions.

The results of these  $S_{21_y}$  and  $S_{21_x}$  PNF measurements, without any probe compensation, are shown in Figs. 5.11 and 5.12 respectively. Despite a lack of compensation for the WR-28 waveguide probe, which has 7.0 dB of gain at  $f_c = 39$  GHz and 40 dB of cross-polarization isolation according to the manufacturer data sheet [130], the results for the measured  $S_{21}$  for both  $\hat{x}$  and  $\hat{y}$  polarizations are well-correlated with the CST-simulated planar near fields  $\vec{E}_y$  and  $\vec{E}_x$  shown in Figs. 5.5 and 5.6. For all three frequencies shown, the  $S_{21_y}$  magnitude is maximum, and  $S_{21_y}$  phase is uniform across the 20 cm diameter of the Ka-band horn aperture at the center of the scan plane. Additionally,  $|S_{21_y}|$  at the upper and lower scan plane edges is approximately 10 dB higher at 35 GHz than it is at 43 GHz. Similar features are observed

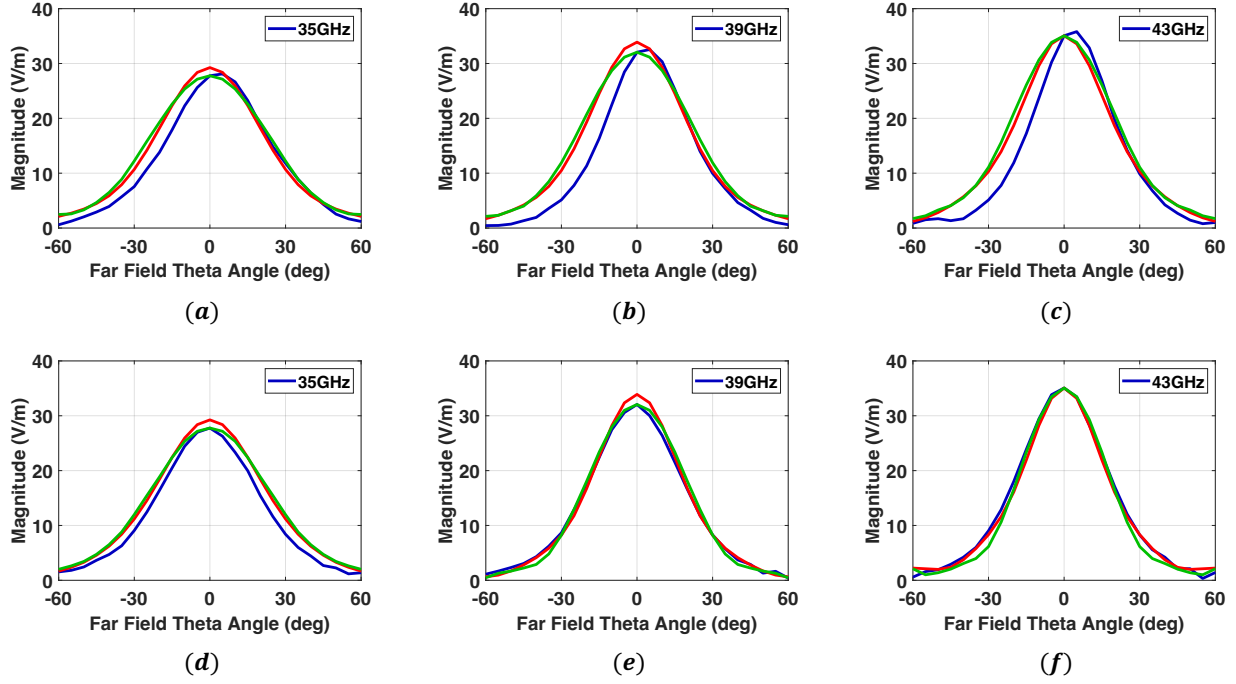


Figure 5.13 Magnitude of vertical Ludwig-3 far field component ( $|\vec{E}_V|$ ) from CST far field ideal probes (red) and simulated (green) and measured (blue) planar near field to far field transforms as a function of the far field angle  $\theta$  in the E-plane [(a)-(b)] and H-plane [(d)-(f)] at 35 GHz [(a),(d)], 39 GHz [(b),(e)] and 43 GHz [(c),(f)]. All  $\theta$  angles are positive (in upper hemisphere): Negative to positive  $\theta$  shifts indicate a  $\phi$  shift of  $(180^\circ, 0^\circ)$  for E-plane and  $(270^\circ, 90^\circ)$  for H-plane.

in the simulated  $\vec{E}_y$ , and the  $S_{21_x}$  results are likewise similar to the corresponding simulated  $\vec{E}_x$  near fields. However, there is less symmetry and uniformity in the measured S21 results for both polarizations across the  $xy$ -plane, likely due to scattering effects of the aluminum scanner chassis, which could not be completely covered with absorber as shown in Fig. 5.10. To facilitate a more meaningful comparison of these simulated and measured planar near field results, improvements in shielding and antenna positioning accuracy would have to be made, and probe compensation would have to be applied. Even so, when the complex S21 data from the PNF probe scan is Fourier transformed to the far field and normalized to the boresight far field magnitude derived from the CST PNF simulations and transformations, these far fields as a function of angle are fairly well-matched for the H-plane as shown in Fig. 5.13(d)-(f). For the E-plane far fields shown Fig. 5.13(a)-(c), the peak magnitude of  $|\vec{E}_V|$  is

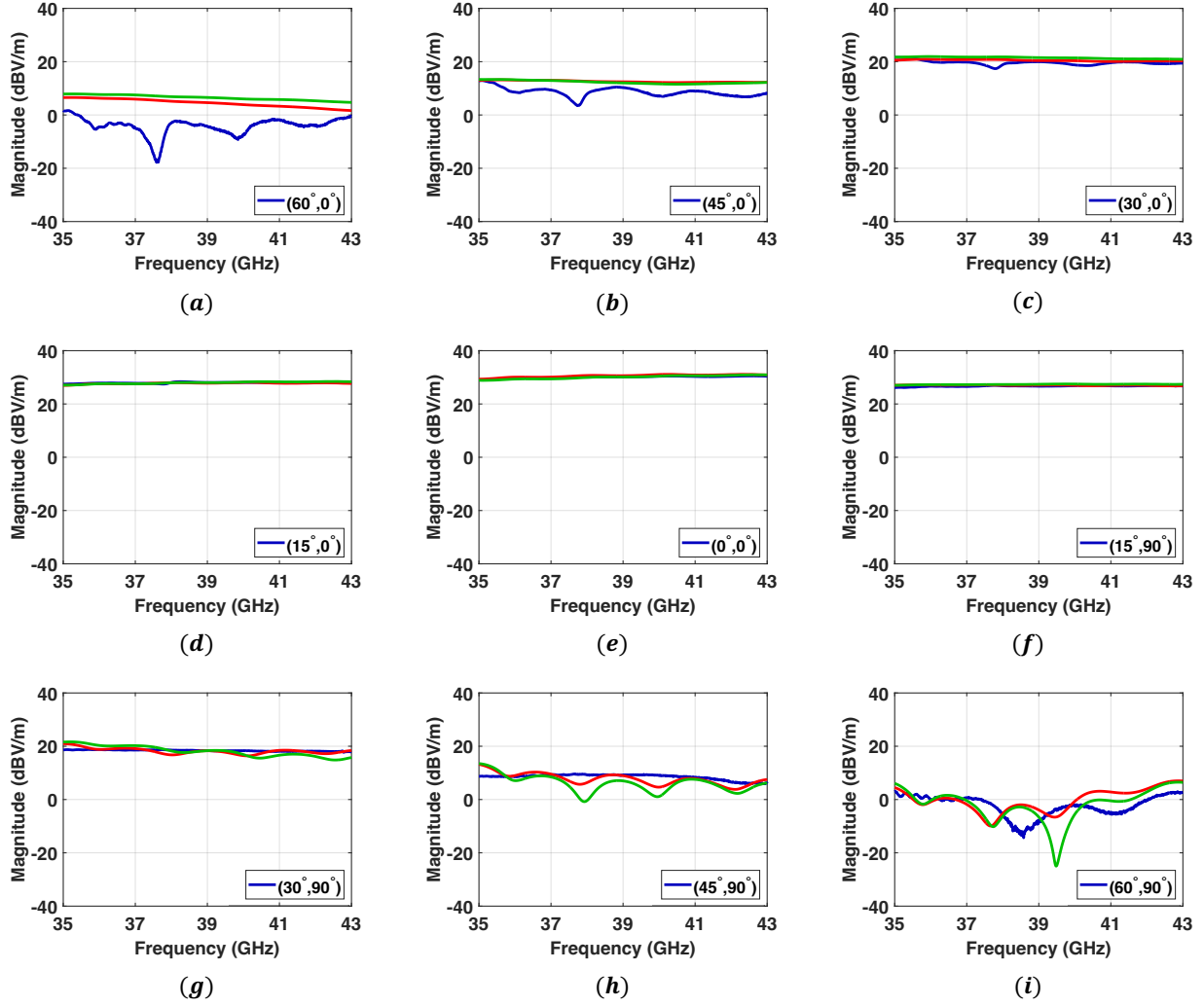
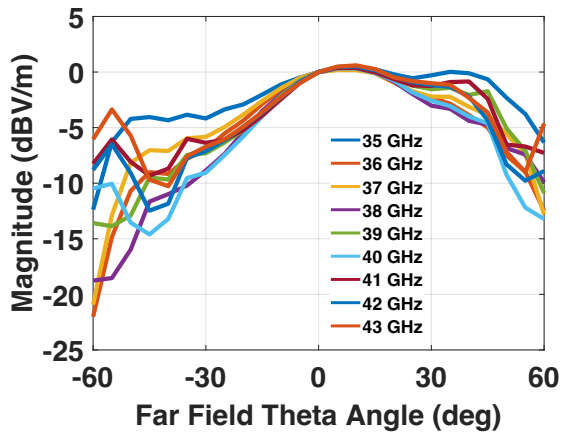


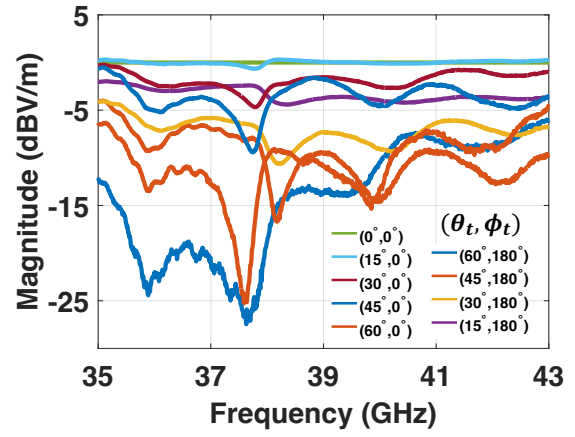
Figure 5.14 Magnitude of vertical Ludwig-3 far field component ( $|\vec{E}_V|$ ) from CST far field ideal probes (red) and simulated (green) and measured (blue) planar near field to far field transforms as a function of frequency at far field angles  $(\theta, \phi) =$  (a)  $(60^\circ, 0^\circ)$ , (b)  $(45^\circ, 0^\circ)$ , (c)  $(30^\circ, 0^\circ)$ , (d)  $(15^\circ, 0^\circ)$ , (e)  $(0^\circ, 0^\circ)$ , (f)  $(15^\circ, 90^\circ)$ , (g)  $(30^\circ, 90^\circ)$ , (h)  $(45^\circ, 90^\circ)$ , and (i)  $(60^\circ, 90^\circ)$ .

at  $\theta = 5^\circ$  rather than  $\theta = 0^\circ$ , likely due to a probe alignment error along the  $\hat{y}$ -axis of the PNF measurement resulting from the imprecise, manual positioning of the AUT and PNF reference point for the scan plane center. The Fourier-transformed far fields from the PNF ideal probe simulation of  $\vec{E}_x$  and  $\vec{E}_y$  in CST and the WR-28 waveguide probe measurement of  $S21_x$  and  $S21_y$  are also compared as a function of frequency in Fig. 5.14, with measured values normalized to simulated values at boresight  $(0^\circ, 0^\circ)$  and center frequency  $f_c = 39$  GHz.

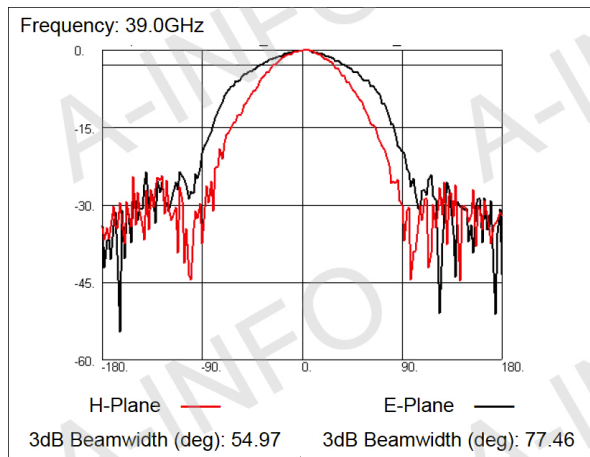
With the exception of far field angles near boresight shown in Fig. 5.14(d)-(f), the WR-28 probe frequency response and scattering effects from the measurement are shown to cause significant error in the transformed far fields, such that the frequency response of the radiated far fields no longer resemble those that were captured in the CST time domain simulations of the same Ka-band horn model. If the differences between the  $|\vec{E}_V(f, \theta, \phi)|$  resulting from PNF full-wave simulation and measurement, displayed in the green and blue traces of Fig. 5.14 respectively, are assumed to be caused exclusively by the WR-28 waveguide probe pattern, the probe patterns as a function of far field angle and frequency can be estimated from these differences. The results of this estimation are shown in Fig. 5.15(a)-(b) next to corresponding measured results published in the data sheet [130] in Fig. 5.15(c)-(d). The probe pattern at 39 GHz and frequency response at boresight in Fig. 5.15(a)-(b) approximate those in Fig. 5.15(c)-(d), but these patterns should not be expected to match since complex interactions between the probe and AUT are ignored. Furthermore, other sources of error such as probe positioning, scattering from the scanner chassis, and RF cable movements could be embedded in the measured S21 data. Thus, before PNF measurements can be used to retrieve the far field frequency response of the AUT with the degree of accuracy required to infer the EVM from the linear distortion generated by that AUT, probe compensation theory [131] must be applied, and a meticulous investigation and elimination of measurement errors must be performed. These remain critical next steps for determining what accuracy and repeatability limitations may exist in the estimation of far field EVM from PNF measurements. However, the EVM of the Ka-band horn antenna was measured directly at the PNF scan plane center as a function of VSG output power and at each PNF probe position with a constant VSG output power for the same three test signals utilized for the 8x8 phased array CATR measurements described in section 4.3, and the results are shown in Fig. 5.16(a)-(c) and (d)-(f) respectively. Because the Ka-band horn antenna is passive, the equalized EVM continues to decrease as the VSG output power increases until it becomes limited by the measurement system, just as it was in the far field measurement of Fig. 3.29, but lower EVM values are captured due to the closer proximity of the WR-28 waveguide probe to the PNF scan plane. For all signals, EVM only falls below 12% when the probe is directly above the circular aperture of the AUT.



(a)



(b)



(c)



(d)

Figure 5.15 Estimate of the normalized WR-28 waveguide probe pattern in the E-plane: (a) as a function of the far field elevation angle  $\theta$  at each of nine frequencies spanning 35-43 GHz, and (b) as a function of frequency at nine elevation angles. Estimates in (a)-(b) are calculated from the difference between  $|\vec{E}_V(f, \theta, \phi)|$  derived from PNF simulation and measurement of the Ka-band conical horn. For comparison, the (c) WR-28 waveguide probe patterns and (d) gain versus frequency profile published in the manufacturer data sheet [130] are also shown.

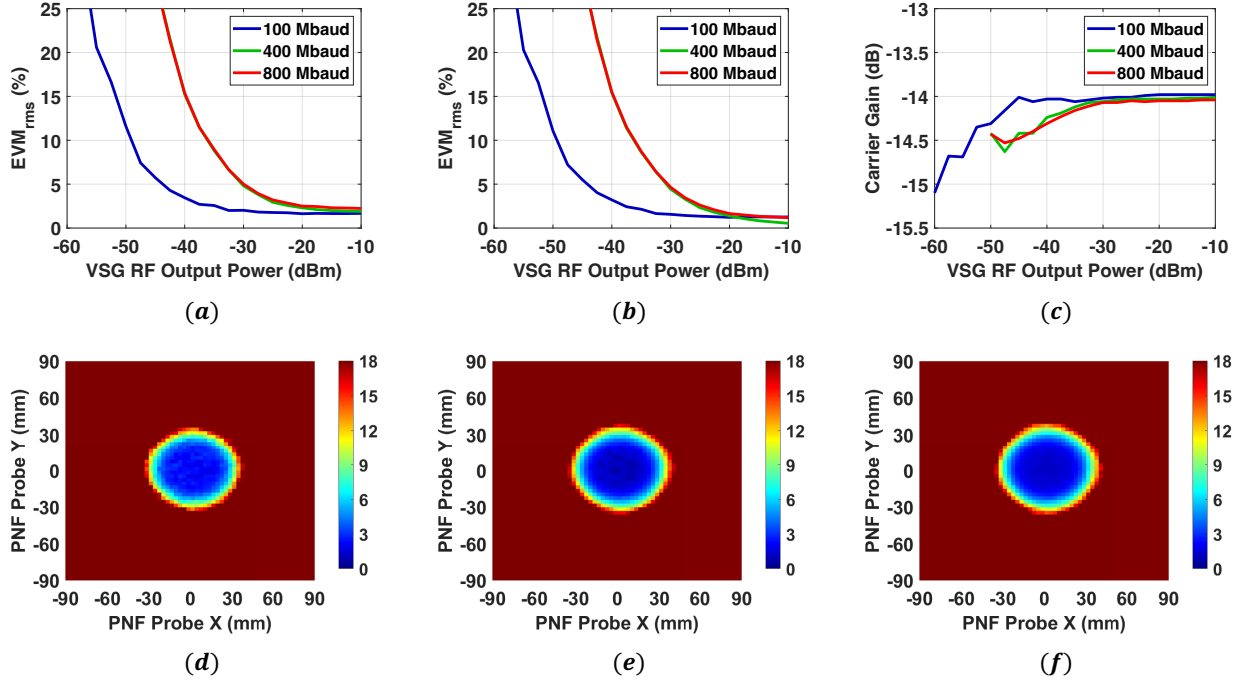


Figure 5.16 Un-equalized  $EVM_{UN}$  (a), equalized  $EVM_{EQ}$  (b), and carrier gain  $|H(f_c)|$  (c) measured at the PNF scan plane center as a function of RF output power from the VSG and equalized  $EVM_{EQ}$  as function of PNF probe position for a 100 MHz-wide flat tone signal (d) and 16-QAM signals with 400 Mbaud (e), and 800 Mbaud (f) symbol rates. In (a)-(c), these three test signals are shown in blue, green, and red respectively. EVM is expressed as a %.

#### 5.4 Planar Near Field Measurement, Far Field Pattern Estimation, and EVM Prediction for an 8x8 Microstrip Patch Phased Array

The same planar near field measurement system [129] was used to measure the 8x8 phased array [98] that was used in the CATR measurements of section 4.4 as it transmitted each of the three modulated test signals from section 4.4.3: a 100 MHz-wide flat tone signal with 1.0 MHz tone spacing and 400 and 800 MBaud 16-QAM signals with 1600 symbols that were RRC-filtered with rolloff factor  $\alpha = 0.15$ . Images of the measurement system setup with the 8x8 phased array are presented in Fig. 5.17. For the PNF modulated signal measurements of the Ka-band horn and 8x8 phased array presented in this chapter, system configurations are the same as those presented in Figs. 3.17 and 4.14 respectively, where the CATR reflector and feed horn are replaced with the PNF scanning machine and WR-28 waveguide probe

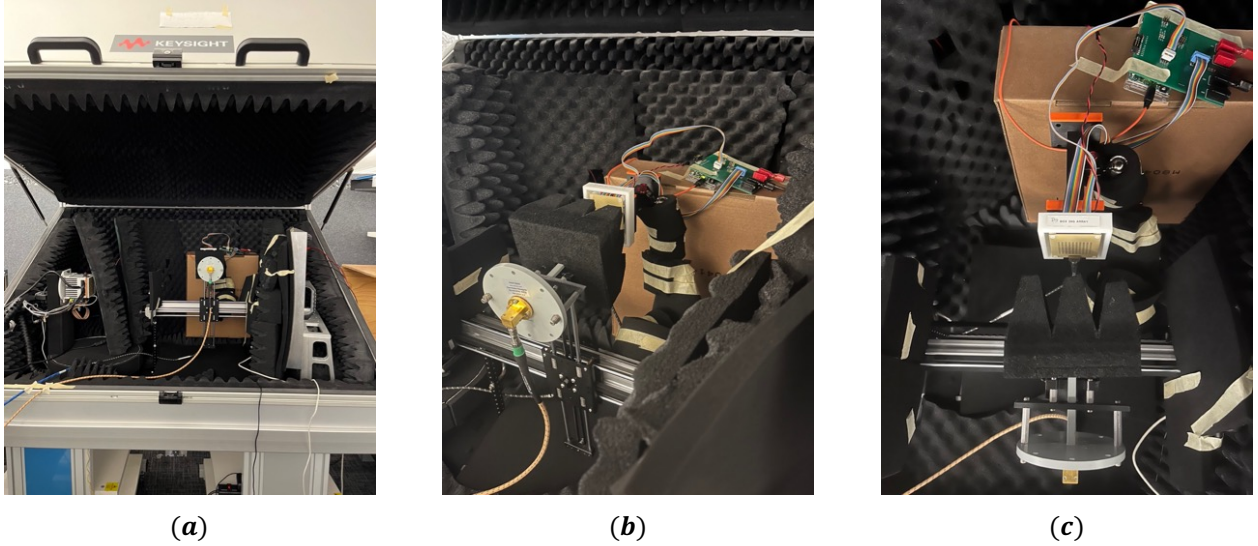


Figure 5.17 Planar near field measurement system for the 8x8 phased array [98]: (a) front view of measurement system placed in a shielded millimeter-wave compact antenna test range provided by Keysight in Santa Rosa, CA, with the Arduino microcontroller and breakout board taped to cardboard box behind the array, (b) side view of PNF scanning machine with WR-28 open-ended waveguide probe, and (c) top view of probe and array mounting bracket. This custom PNF measurement system was invented by Dan Slater and presented in [129].

shown in Figs. 5.10 and 5.17. For the  $S_{21}$  measurements, RF cables to the probe and AUT were connected directly to ports 1 and 2 of the PNA-X network analyzer. The same PNF scan plane dimensions and probe positioning along  $\hat{x}$  and  $\hat{y}$  from the Ka-band horn antenna measurements in section 5.3 were applied to the 8x8 phased array measurements. However, at each of the PNF probe positions, phase gradients were calculated for carrier frequency  $f_c = 39$  GHz and applied to scan beams to far field angles  $\theta_s = [0^\circ : 15^\circ : 45^\circ]$  in elevation ( $\phi_s = 90^\circ, 270^\circ$ ) and azimuth ( $\phi_s = 0^\circ, 180^\circ$ ). The introduction of these beam scans, combined with the increased frequency sweep times for capturing the modulated signal spectrum and EVM statistics at each PNF probe position, dramatically increased the PNF measurement duration relative to that of the Ka-band horn antenna  $S_{21}$  from 34-44 GHz. For example, the PNF probe scan for the 400 Mbaud 16-QAM test signal took approximately 32 hours to complete, and separate scans were required for each of the three test signals. Consequently, only co-polarized ( $\hat{y}$ ) near field data was measured. Measurements of the cross-polarized ( $\hat{z}$ ) near field data would have required  $90^\circ$  rotation of the AUT and repetition of the PNF scan.

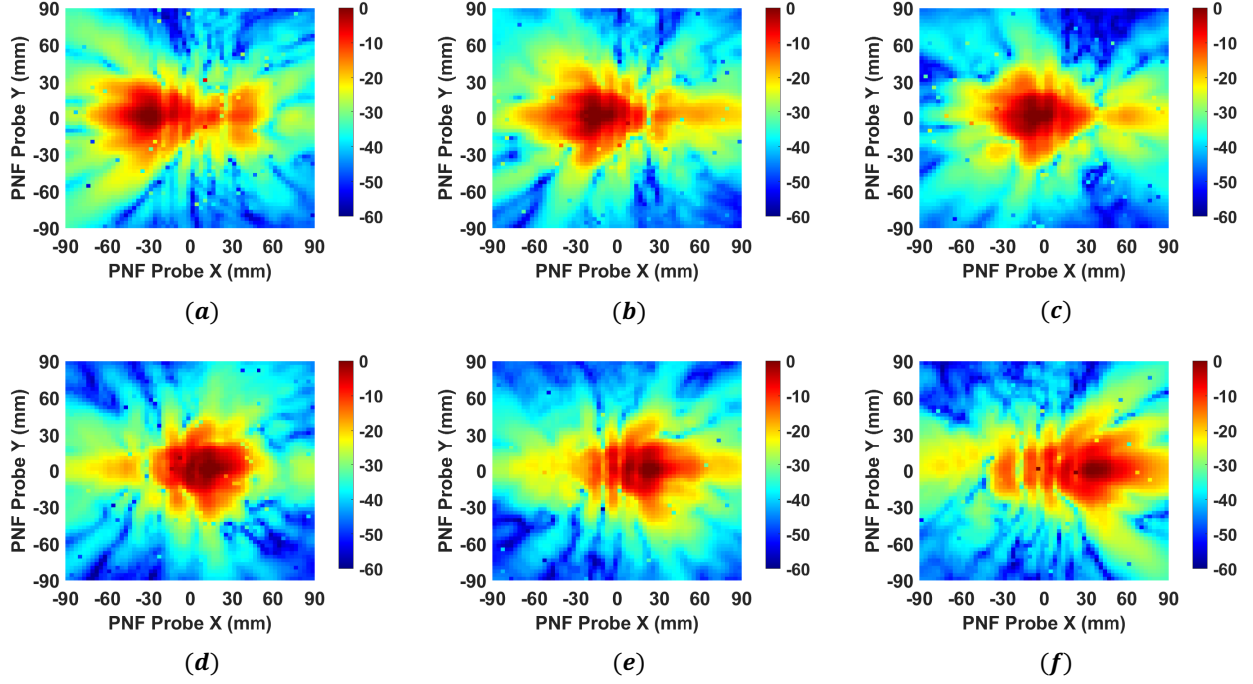


Figure 5.18 Carrier gain  $|H(f_c)|$  of 8x8 phased array transmitting a 16-QAM signal with 400 Mbaud symbol rate, with a VSG output power of -9 dBm and a VNA noise bandwidth of 312 Hz, measured at PNF probe positions with beam scanned to far field angles (a) ( $45^\circ, 180^\circ$ ), (b) ( $30^\circ, 180^\circ$ ), (c) ( $15^\circ, 180^\circ$ ), (d) ( $15^\circ, 0^\circ$ ), (e) ( $30^\circ, 0^\circ$ ), and (f) ( $45^\circ, 0^\circ$ ) at  $f_c = 39$  GHz.

Keeping the AUT stationary between consecutive PNF measurements also has the benefit of eliminating inconsistencies in the AUT orientation and scan plane alignment. Furthermore, the cross-polarization of this 8x8 phased array was measured at  $\leq -40$  dB down with the beam scanned to boresight and  $\leq -30$  dB down with beam scan angles as wide as  $\theta_s = 60^\circ$  in [98], so modulated signal gain is assumed to be zero for the cross-polarization, such that plane wave spectrum component  $f_x$  in equation (5.1) is likewise zero in the far field transformation. The VSG output power was held constant at -25 dBm for PNF scans in which the 100 MHz-wide flat tone signal was applied to the AUT and -9 dBm for scans in which either of the 16-QAM signals were applied. Output power had to be lowered for the flat tone signal due to its higher PAPR, in order to prevent the automatic gain control of the VSG from becoming unstable. The modulated signal gain at  $f_c = 39$  GHz measured at each PNF probe position is shown in Fig. 5.18 and 5.19 for the H-plane (azimuth) and E-plane (elevation) beam scan angles respectively. The un-equalized  $EVM_{UN}$  and equalized  $EVM_{EQ}$  measured at each PNF probe



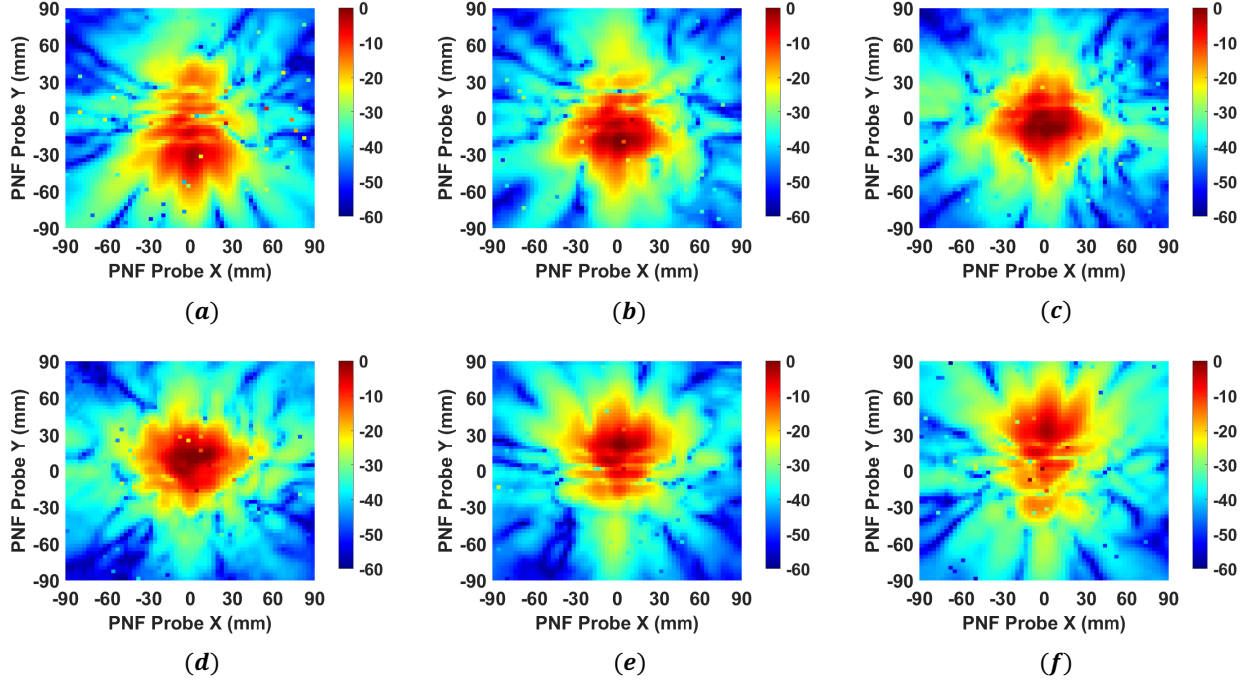


Figure 5.19 Carrier gain  $|H(f_c)|$  of 8x8 phased array transmitting a 16-QAM signal with 400 Mbaud symbol rate, with a VSG output power of -9 dBm and a VNA noise bandwidth of 312 Hz, measured at PNF probe positions with beam scanned to far field angles (a)  $(45^\circ, 270^\circ)$ , (b)  $(30^\circ, 270^\circ)$ , (c)  $(15^\circ, 270^\circ)$ , (d)  $(15^\circ, 90^\circ)$ , (e)  $(30^\circ, 90^\circ)$ , and (f)  $(45^\circ, 90^\circ)$  at  $f_c = 39$  GHz.

position for beams scanned to boresight and the two widest angles ( $\theta_s = 45^\circ$ ) in the H- and E-planes are shown in Fig. 5.20 and 5.21 respectively, for the 400 Mbaud 16-QAM test signal. The carrier gain, un-equalized  $EVM_{UN}$ , and equalized  $EVM_{EQ}$  for PNF scans of each of the three test signals, with the beam scanned to far field angle  $(\theta_s, \phi_s) = (45^\circ, 0^\circ)$ , are presented in Fig. 5.22. These results demonstrate that the peak carrier gain  $|H(f_c)|$  is swept across the PNF scan plane from left to right and bottom to top as the beam is scanned across the two orthogonal planes. Un-equalized EVM is always higher than equalized EVM, but both are proportional to carrier gain as expected. The contours of equalized EVM are nearly identical to those of the carrier gain in both scan planes. While the carrier gain measured across the scan plane is nearly uniform for all three test signals, un-equalized EVM is naturally higher for signals with larger bandwidths. Average  $EVM_{UN}$  measured across the scan plane for the 800 Mbaud signal in Fig. 5.22(f) is greater than that of the 400 Mbaud signal in Fig. 5.22(e), even though both have the same modulation format (16-QAM) and source power (-9 dBm).

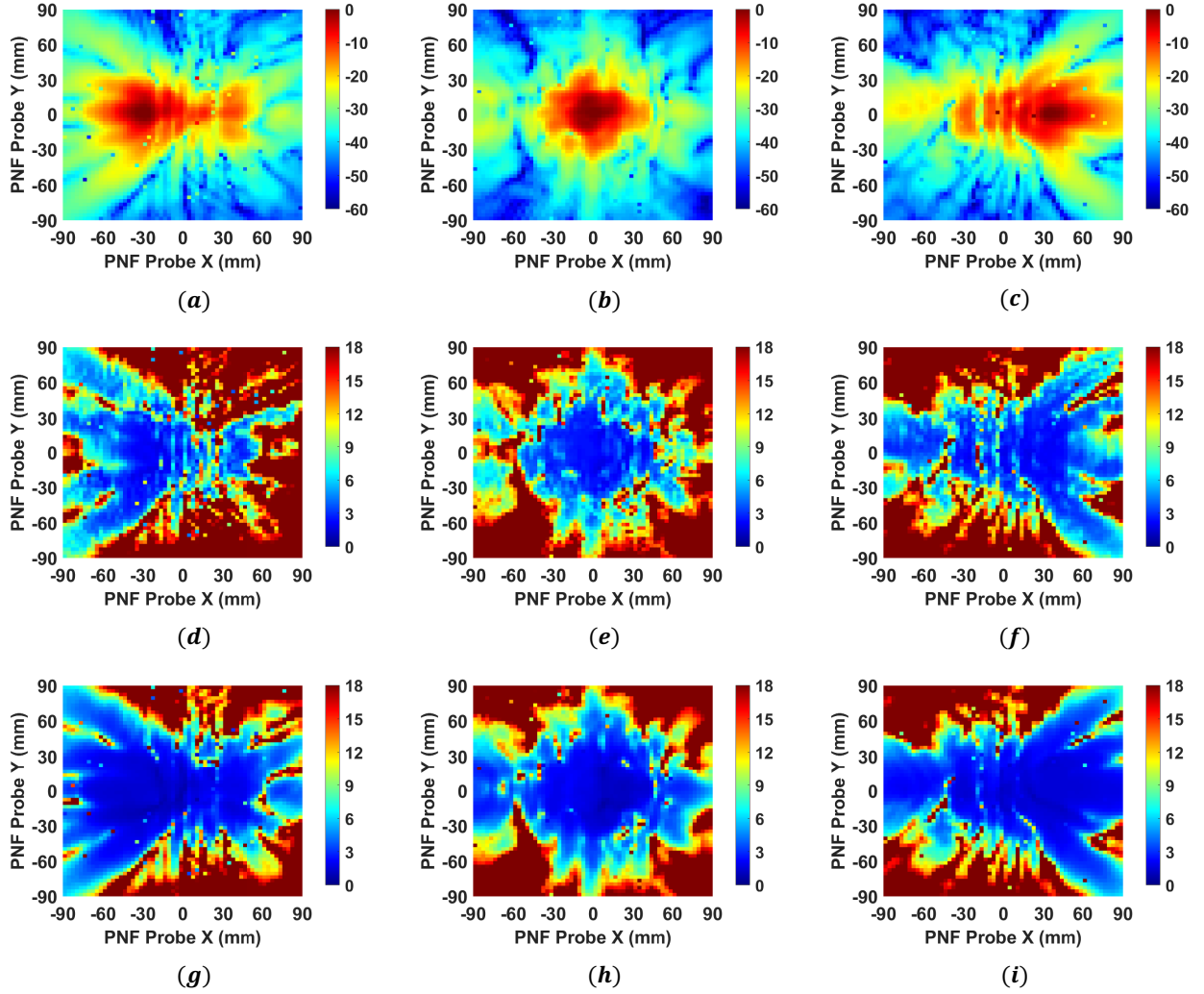


Figure 5.20 Carrier gain  $|H(f_c)|$  in dB [(a)-(c)], un-equalized  $EVM_{UN}$  [(d)-(f)], and equalized  $EVM_{EQ}$  [(g)-(h)] of 8x8 phased array transmitting a 16-QAM signal with 400 Mbaud symbol rate, with a VSG output power of -9 dBm and a VNA noise bandwidth of 312 Hz, measured at PNF probe positions with beam scanned to far field angles [(a),(d),(g)] ( $45^\circ, 180^\circ$ ), [(b),(e),(h)] ( $0^\circ, 0^\circ$ ), and [(c),(f),(i)] ( $45^\circ, 0^\circ$ ). EVM is expressed as a %.

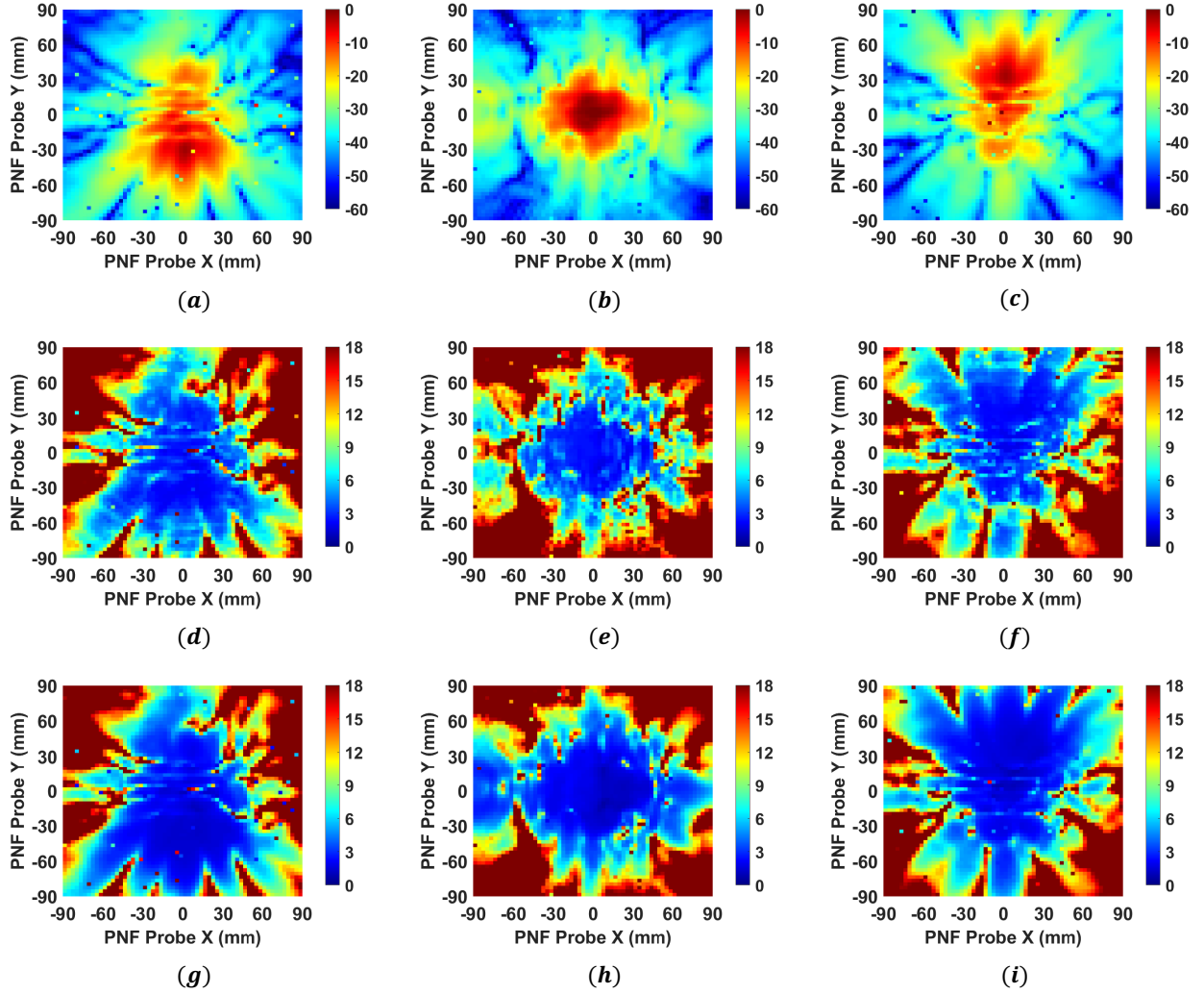


Figure 5.21 Carrier gain  $|H(f_c)|$  in dB [(a)-(c)], un-equalized  $EVM_{UN}$  [(d)-(f)], and equalized  $EVM_{EQ}$  [(g)-(h)] of 8x8 phased array transmitting a 16-QAM signal with 400 Mbaud symbol rate, with a VSG output power of -9 dBm and a VNA noise bandwidth of 312 Hz, measured at PNF probe positions with beam scanned to far field angles [(a),(d),(g)] ( $45^\circ, 270^\circ$ ), [(b),(e),(h)] ( $0^\circ, 0^\circ$ ), and [(c),(f),(i)] ( $45^\circ, 90^\circ$ ). EVM is expressed as a %.

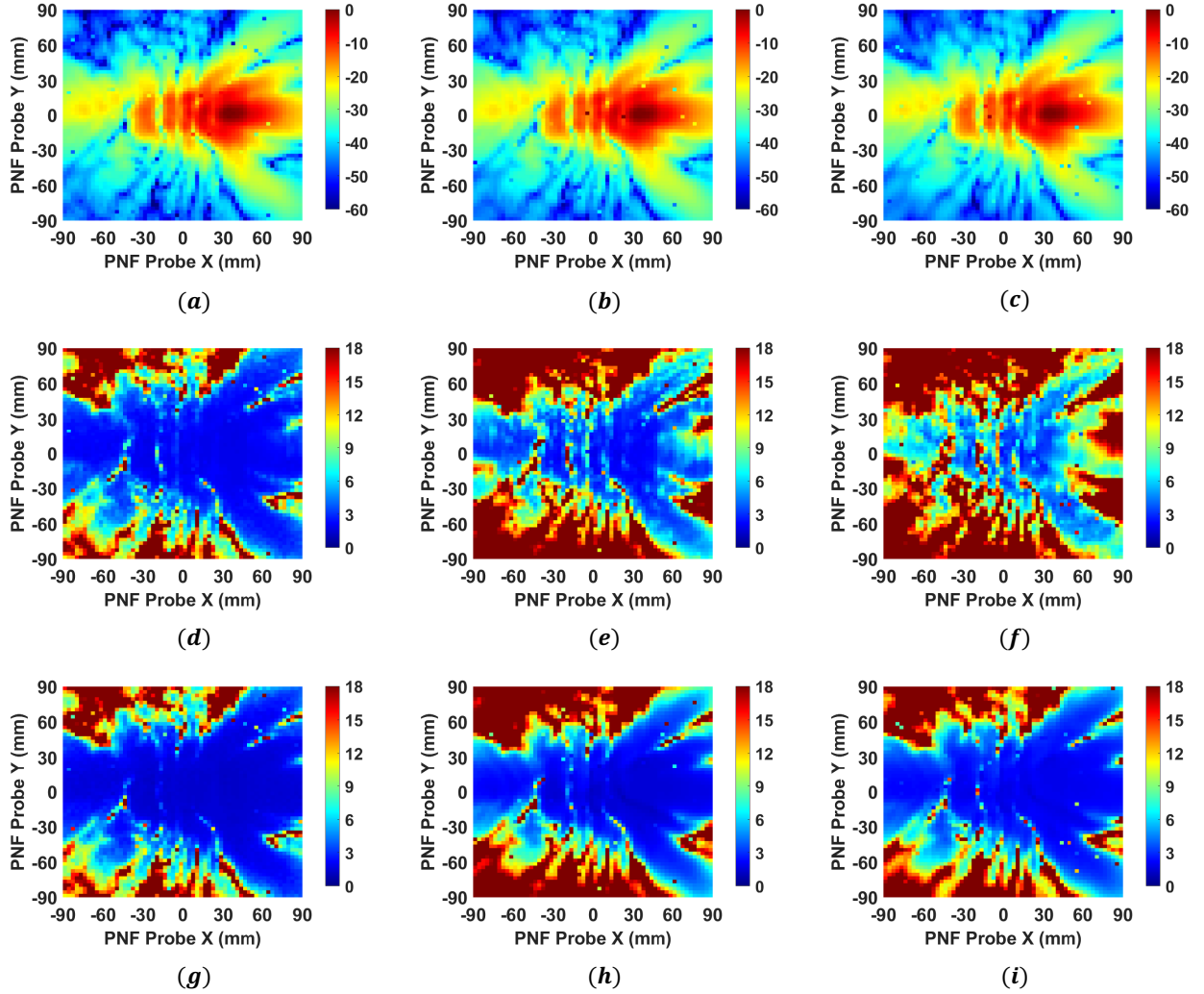


Figure 5.22 Carrier gain  $|H(f_c)|$  in dB [(a)-(c)], un-equalized  $EVM_{UN}$  [(d)-(f)], and equalized  $EVM_{EQ}$  [(g)-(i)] of 8x8 phased array transmitting a 100 MHz-wide flat tone signal [(a),(d),(g)] and 16-QAM signals with 400 Mbaud [(b),(e),(h)] and 800 Mbaud [(c),(f),(i)] symbol rates, measured at PNF probe positions with the beam scanned to far field angle ( $45^\circ, 0^\circ$ ). EVM is expressed as a %.

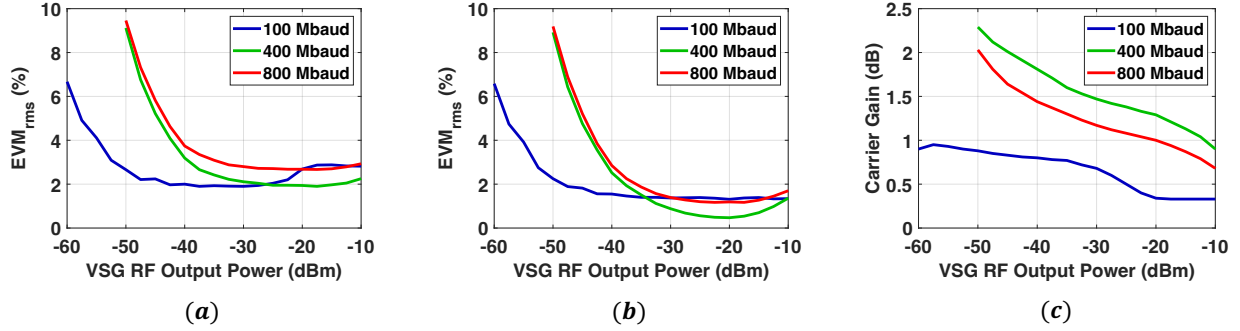


Figure 5.23 Un-equalized  $EVM_{UN}$  (a), equalized  $EVM_{EQ}$  (b), and carrier gain  $|H(f_c)|$  (c) of 8x8 phased array measured at the PNF scan plane center as a function of RF output power from VSG for a 100 MHz-wide flat tone signal (blue), and 16-QAM signals with 400 Mbaud (green), and 800 Mbaud (red) symbol rates.

The carrier gain and EVM were also measured as a function of the VSG output power at the center position of the PNF scan plane for each of the three test signals, as shown in Fig. 5.23. The results are similar to the VSG power sweep measurements of the same AUT that were performed in a CATR and presented in Fig. 4.24: The response of both  $EVM_{UN}$  and  $EVM_{EQ}$  is a bath tub shaped curve in which the EVM increases at higher power levels due to intermodulation distortion from the active RF transmitter paths of each array element, as evidenced by the decreasing carrier gain for the two 16-QAM test signals. The  $EVM_{UN}$  is limited by the amplitude and phase distortion over the modulated signal bandwidth, and therefore has a minimum value higher than that of  $EVM_{EQ}$ . Greater amplitude and group delay variations across the 800 Mbaud signal spectrum, which has double the bandwidth of the 400 Mbaud signal, causes the corresponding  $EVM_{UN}$  to always be lower, as previously described. However, for the 16-QAM test signals, the range of EVM values captured over the same -50 to -10 dBm power sweep ( 9%) is nearly three times as large as the range from the CATR measurements ( 3%). This highlights the potential SNR advantage of measuring the AUT in the near field as opposed to indirect far field, but the relationship between EVM results from these OTA measurements must still be discerned and validated. Some researchers have suggested that the EVM results from near field measurements may be well-correlated with those from direct far field measurements [126, 127], but the planar near field EVM values from this section cannot reasonably be compared with the compact test range EVM values

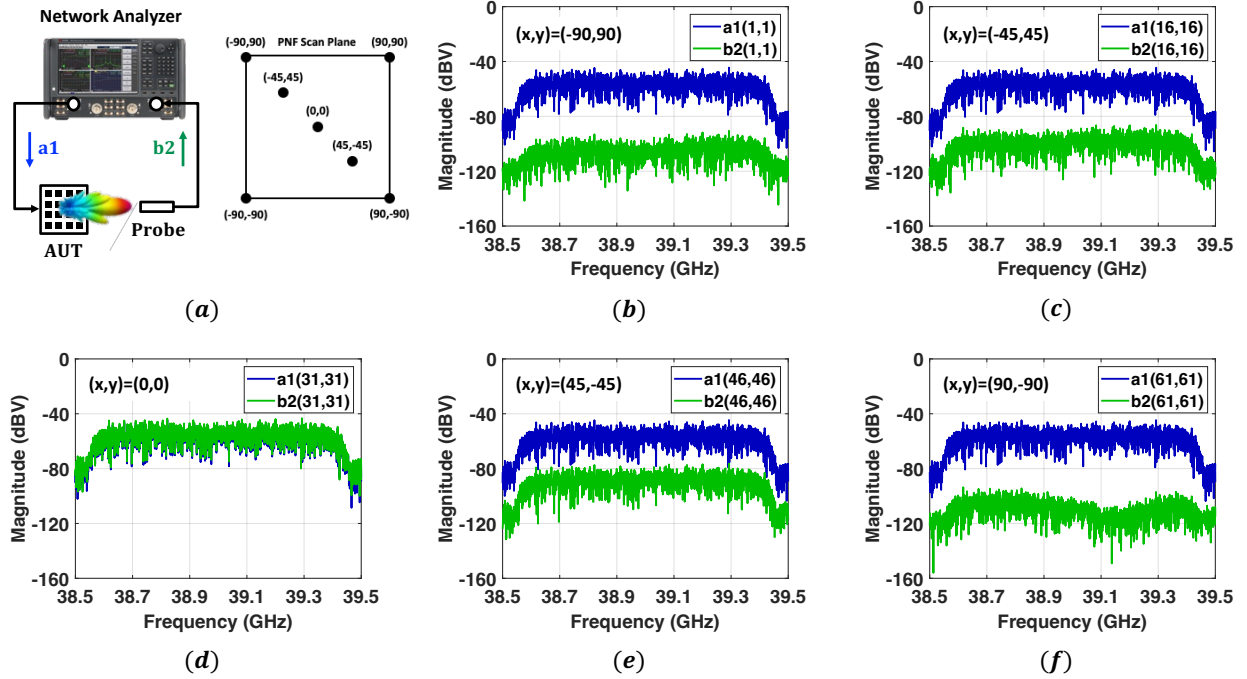


Figure 5.24 Measured spectrum of 16-QAM test signal with 800 Mbaud symbol rate transmitted to the 8x8 phased array port from VNA port #1 (a1, blue) and measured spectrum of the signal received by the probe on VNA port #2 (b2, green) at each of five probe positions along the diagonal of the PNF scan (a), with the beam scanned to boresight  $(\theta_s, \phi_s) = (0^\circ, 0^\circ)$  from section 4.4 in this case due to absence of probe compensation in the former and feed horn calibration in the latter.

Nonetheless, a frequency domain algorithm similar to that which is highlighted in Fig. 5.2 from [120] could be applied to estimate far field EVM from planar near field transformation performed at each frequency in the wideband modulated test signal. The measurement already completes the steps shown in Fig. 5.2 through *S133*: A periodic test signal is transmitted by the AUT, measured at each PNF probe position, digitized, fast Fourier transformed to the frequency domain, and displayed by the multi-port VNA. The spectrum of the signals transmitted by the AUT scanned to boresight and received by the probe at five positions along the scan plane diagonal are shown in Fig. 5.24 for the 800 Mbaud 16-QAM test signal. The next step *S134* is implemented by importing measured PNF probe signal spectrums at each  $(x, y, z_0)$  position into MATLAB and executing the iterative PNF-to-far field transform script that was used for the CST simulation data in section 5.2. Finally, rather than transforming

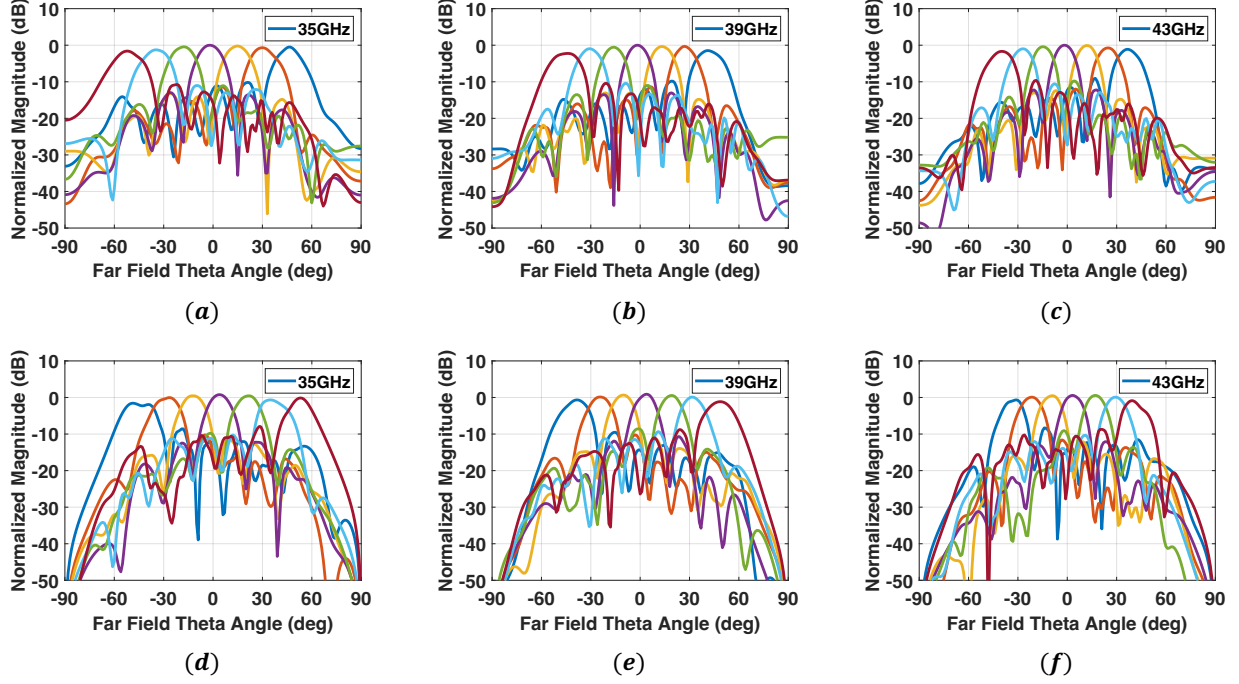


Figure 5.25 Normalized far field patterns  $|\vec{E}_V(\theta)|$  of 8x8 phased array with beams scanned to angles  $\theta_s = [-45^\circ : 15^\circ : 45^\circ]$  in azimuth [(a)-(c)] and elevation [(c)-(f)] at 35 GHz [(a),(d)], 39 GHz [(b),(e)], and 43 GHz [(c),(f)], where negative to positive  $\theta$  shifts indicate  $\phi$  shift of  $(180^\circ, 0^\circ)$  for azimuth and  $(270^\circ, 90^\circ)$  for elevation. Far field patterns are obtained from Fourier transforms of measured modulated complex gain at the specified frequency, as described in section 5.1. Phase gradients are calculated for  $f_c = 39$  GHz, so beam squint effects are shown.

the far fields back to the time domain as suggested in [120], the EVM could be calculated directly in the frequency domain by comparing the far field spectrum at a specific position  $(r, \theta, \phi)$  with the spectrum of the signal applied to the AUT port, which is measured on the multi-port VNA and assumed to remain constant for each of the PNF probe positions in the scan plane. Linear distortion effects generated by a passive receiving antenna at this far field position could also be modeled by taking the dot product of the Fourier-transformed far fields radiated by the AUT with the frequency-dependent vector effective length of this antenna, as described in section 3.1.

Normalized far field patterns of the 8x8 phased array for each of the seven beam scan angles within the E-plane (elevation) and H-plane (azimuth), calculated from the complex  $S_{21}$  measured at the PNF probe positions via the MATLAB far field transformation scripts

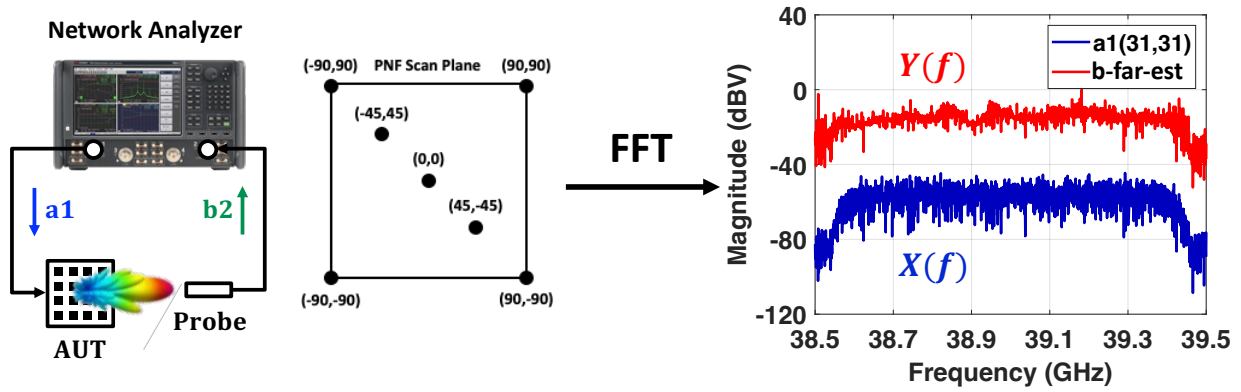


Figure 5.26 Measured spectrum of 16-QAM test signal with 800 Mbaud symbol rate transmitted to the 8x8 phased array port from VNA port #1 (a1, blue) and estimated spectrum of the far field signal received at (1.0 m, 0°, 0°), with the beam scanned to boresight (b, red).

applied in section 5.2, are shown in Fig. 5.25(a)-(c) and (d)-(f) for three different frequencies. Since phase gradients were always calculated for  $f_c = 39$  GHz, the beam pointing directions vary with frequency, and beam squint effects are discernible from a comparison of the beam patterns for 35 and 43 GHz. The pattern distortions for the wide beam scan angles likely result from the 180x180 cm scan plane truncation because Figs. 5.18 and 5.19 show that the amplitude decay is less than 30 dB at the scan plane edges for these beam states. However, distortion could also result from other error sources such as scattering effects that appear to cause random fluctuations in some of the probe measurements shown in Figs. 5.18 and 5.19, or the probe response, which had an effect on the Ka-band horn antenna far fields estimated from measured PNF data in section 5.3. These error sources should be carefully examined and eliminated from the measurement if possible, to ensure that the far fields are accurately characterized over the test signal bandwidth before calculating the EVM. The far field spectrum of the 800 Mbaud 16-QAM test signal transmitted by the 8x8 phased array with the beam scanned to boresight is estimated by Fourier transforming measured planar near fields for each of 2000 tones spanning 38.5-39.5 GHz, which are shown in the (b2, green) plots of Fig. 5.24. The result of these transformations is shown in the ( $Y(f)$ , red) plot of Fig. 5.26, where magnitudes of each far field tone are determined from the directivity calculated from summation of planar near fields as presented in equations (5.8) and (5.9) of section 5.2.



In the absence of any PNF measurement errors, such that  $b_2(f, x, y)$  perfectly represents the amplitude and phase of the AUT-radiated planar near fields at each tone and  $a_1(f, x, y)$  is identical for all probe positions  $(x, y, z_0)$ ,  $Y(f)$  in Fig. 5.26 represents the frequency spectrum of the radiated far fields at position  $(1.0m, 0^\circ, 0^\circ)$  when the beam is scanned to this boresight direction. Therefore, if the far field receiver is considered to be distortionless, the far field EVM can be calculated from the spectral correlation of  $X(f) = a_1(f, x, y)$  and  $Y(f)$  in Fig. 5.26 by applying the techniques described in section 2.3 to distinguish between the linear  $X(f)H(f)$  and nonlinear  $D(f)$  components of  $Y(f)$  and using equation (2.4) with  $N = 2000$ . Since the two-dimensional fast Fourier transform of the plane wave spectrum from equations (5.1) and (5.2) is a linear operator, differences in the EVM between the measured planar near fields and transformed far fields result from changes in  $H(f)$  which affect the degree of amplitude and delay distortion in un-equalized  $EVM_{UN}$  and the SNR in equalized  $EVM_{EQ}$ . Of course, this is based on the assumption that transmitted test signal spectrum  $X(f, x, y)$  and AUT linearity remain constant for each repeated beam state for the complete duration of the PNF scan, which could take many hours and entail significant temperature variations. Further study is required to determine if such an assumption is reasonable and to understand the degree to which various PNF measurement errors influence these far field EVM results.

## 5.5 Summary

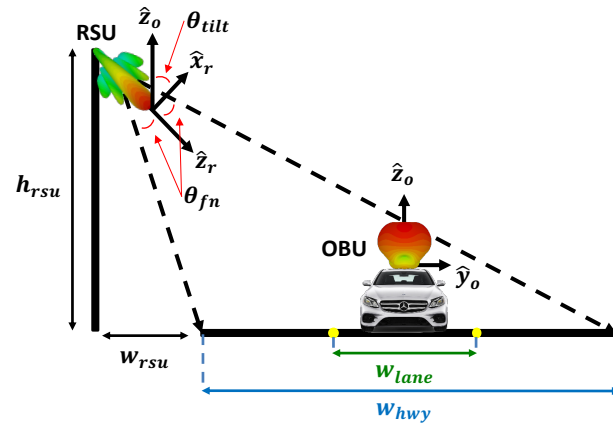
This chapter presented modeling, simulation, and measurement of planar near fields from wide-band modulated signal transmission by a Ka-band conical horn antenna and 8x8 millimeter-wave phased array. PNF measurement theory and published applications for far field EVM analysis were reviewed. A methodology for determining wideband far fields from a single full-wave time domain simulation of an AUT was described and applied to the horn, and far field EVM estimated from a PNF simulation was compared with results from section 3.3. PNF measurements were implemented with MATLAB test scripts designed to synchronize control of a robotic scanner, VNA, and microcontroller. Finally, a framework for estimating far field EVM from PNF data for a beam-scanning phased array was described and applied.

## CHAPTER 6

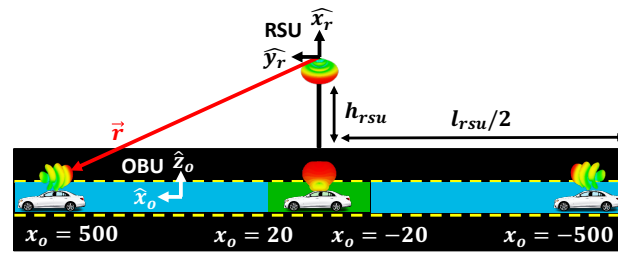
# Vehicle-to-Infrastructure Link Budget Analysis

### 6.1 Introduction

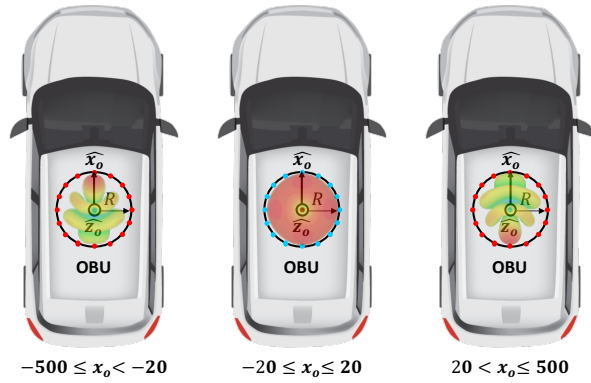
Vehicle-to-infrastructure (V2I) communication systems may soon be deployed to improve the safety and traffic efficiency of highway transportation. For the downlink of a V2I system, roadside unit (RSU) base stations located near highway edges transmit messages to onboard unit (OBU) receivers mounted to vehicle rooftops. The antenna designs for both the RSU and OBU play an important role in maximizing the range of communication and minimizing the co-channel interference between neighboring RSUs. Many advanced antenna arrays and switchable antennas have been developed to achieve specific radiation patterns for the RSU and OBU in V2I applications [132–134]. While fixed-beam phased arrays are suitable for RSUs broadcasting to multiple vehicles in their communication range, switchable beam antennas are likewise suitable for OBUs, as they permit vehicles to receive a sufficiently-powerful signal from a greater distance and are less complex than adaptive arrays. The range extension that results from deployment of switchable-beam arrays reduces the number of RSUs required and the cost of the V2I system. In this section, the power received by this type of OBU antenna is calculated for positions along the length and width of a 1.0 km linear highway segment as the vehicle to which the OBU is mounted passes an RSU base station antenna transmitting from an elevated position near the edge of the highway, such as the top of a security camera pole. This V2I antenna link is shown in the highway model diagram of Fig. 6.1. The simulation results for received power, which are calculated from the Friis equation for free space signal transmission, demonstrate that deploying a switchable-beam array with high gain toward the horizon increases effective link range and decreases RSU interference, as suggested in [134].



(a)



(b)



(c)

Figure 6.1 Front view (a) and side view (b) of the RSU and OBU coordinate systems and (c) top view of the vehicle-mounted OBU circular monopole array beam states at each of the three linear highway segments:  $-500m \leq x_o < 20m$ ,  $-20m \leq x_o \leq 20m$ , and  $20m < x_o \leq 500m$ . See Table 6.1 for linear highway dimensions and RSU and OBU antenna positions.

Table 6.1: RSU Antenna Positions and Highway Dimensions

Dimension	Value
$l_{rsu}$	1000 m
$w_{rsu}$	3.0 m
$h_{rsu}$	11.0 m
$w_{hwy}$	11.0 m
$h_{car}$	1.5 m
$\theta_{tilt}$	50.3°
$\theta_{fn}$	21.0°

## 6.2 RSU and OBU Antenna Array Coordinate Systems

The coordinate systems for the RSU and OBU antennas in the V2I link along the 1.0 km linear highway are presented in Fig. 6.1. A three-lane highway segment of width  $w_{hwy}$  and length  $l_{rsu}$  extending along the  $\hat{x}_o$  axis is used for simulation of the OBU received power. The base of the RSU antenna mounting pole is positioned  $w_{rsu}$  away from the bottom highway edge, and it intersects the highway length midpoint, such that the highway extends to  $l_{rsu}/2$  on opposite sides of the RSU. The RSU antenna is mounted at  $h_{rsu}$  above the highway surface, and the vehicle rooftop is always positioned at  $h_{car}$  above the highway surface regardless of its  $x_o$  position along the length of the highway. The RSU coordinate system tilts down in the  $\hat{y}_o\hat{z}_o$  plane shown in Fig. 6.1(a), such that  $\hat{z}_r$  points to the center lane vehicle rooftop. The vectors that extend from the RSU coordinate system origin to the highway edges in the  $\hat{y}_o\hat{z}_o$  plane form equal angles  $\theta_{fn}$  with the  $\hat{z}_r$  vector that match the gain pattern first null levels of the RSU linear microstrip patch array shown in Fig. 6.2(a). The highway dimension values and first null angles of the RSU patch array  $\theta_{fn}$  are provided in Table 6.1.

## 6.3 RSU and OBU Antenna Array Design Specifications

A linear microstrip patch array of  $N = 4$  elements spaced along the  $\hat{x}_r$  axis is selected for the RSU antenna because it achieves a wide beamwidth in the  $\hat{y}_r\hat{z}_r$  plane, across the length of the highway, and a narrow beamwidth in the  $\hat{x}_r\hat{z}_r$  plane, across the width of the highway.

The number of elements was limited to  $N = 4$  and the spacing between elements was set to  $l_{sp} = 35\text{mm}$  to ensure that the first nulls were pointed to the highway edges at  $\theta_{fn} = 21.0^\circ$ , using the array factor tool in CST Microwave Studio. Thus, the main beam of the microstrip patch array is confined to the cross section of the highway. The RSU linear array is shown in Fig. 6.2(a). Transmitting power for the RSU microstrip patch array was limited to  $P_{RSU} = 10$  dBm to satisfy the EIRP limit of 23 dBm for a 10 MHz DSRC channel [135]. The EIRP is calculated from the sum of  $P_{RSU} = 10$  dBm and  $G_{RSU} = 13$  dB.

A circular monopole array with  $N = 16$  elements and radius  $R = 40.67$  mm centered around the  $\hat{z}_o$  axis is used for the OBU switchable-beam array because it has a high gain in the horizon. When the OBU receiver is not within the immediate vicinity of the RSU transmitter ( $-20\text{m} \leq x_o \leq 20\text{m}$ ), the  $-\hat{r}$  vector pointing from the OBU to the RSU approaches  $\theta_o = 90^\circ$  and  $\phi_o = 0^\circ$  or  $180^\circ$  for vehicle positions  $|x_o| > 20$  m as shown in Fig. 6.1(b). Because these are the two primary directions from which the OBU array receives a signal, only three states are required: two with all elements active and the beams pointing to  $\phi_o = 0^\circ, 180^\circ$  when the vehicle is far from the RSU, and a third omnidirectional state in which only one monopole is active, when the vehicle is close to the RSU. The three beam states for the circular array are shown in Fig. 6.1(c). The circular monopole array has a gain of  $G_{OBU} = 9.5\text{dB}$  at  $\theta_o = 90^\circ$ , which is 3.2 dB lower than the peak gain due to the finite ground plane of the monopole. To obtain beams in  $\phi_o = 0^\circ$  and  $180^\circ$ , element  $n$  phases are set as specified in equation 6.1 [136].

$$\psi(n) = -kR\cos(\phi_0 - n\Delta\phi) \quad (6.1)$$

In equation 6.1,  $k = 2\pi/\lambda_0$  is the wavenumber with free space wavelength  $\lambda_0 = 50.83\text{mm}$ ,  $R$  is the radius of the monopole array,  $\psi_0$  is the desired beam angle within the azimuth plane,  $n$  is the element number, and  $\Delta\phi$  is the rotation angle between elements along the circle with radius  $R$ . Azimuthal beam patterns and monopole array element dimensions are shown in Figs. 6.1(c) and 6.2(b) respectively. Both the RSU and OBU array elements were designed for resonance at  $f_0 = 5.90$  GHz and had  $|S_{11}(f_0)| < -30$  dB with port impedances

Table 6.2: RSU and OBU Phased Array Dimensions

RSU Array	Value	OBU Array	Value
$l_p$	12.4 mm	$l_m$	10.81 mm
$w_p$	16.32 mm	$g_m$	0.49 mm
$l_f$	7.70 mm	$r_m$	0.33 mm
$w_f$	3.11 mm	$s_m$	50.85 mm
$s_g$	30.00 mm	$R$	40.67 mm
$l_{sp}$	35.00 mm	$\Delta\phi$	22.50 deg

$Z_{rsu} = 50\Omega$  and  $Z_{obu} = 36.5\Omega$ , and the dimensions of both arrays are provided in Table 6.2.

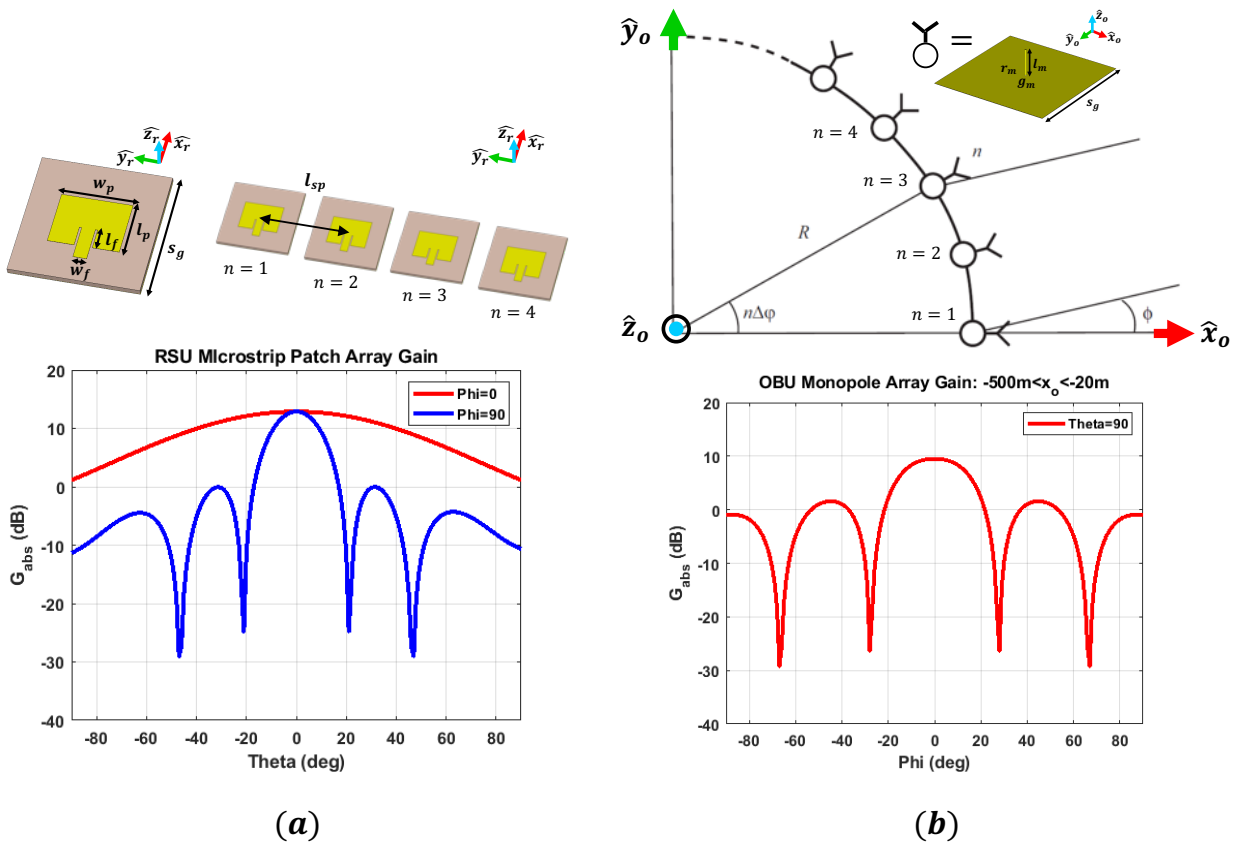


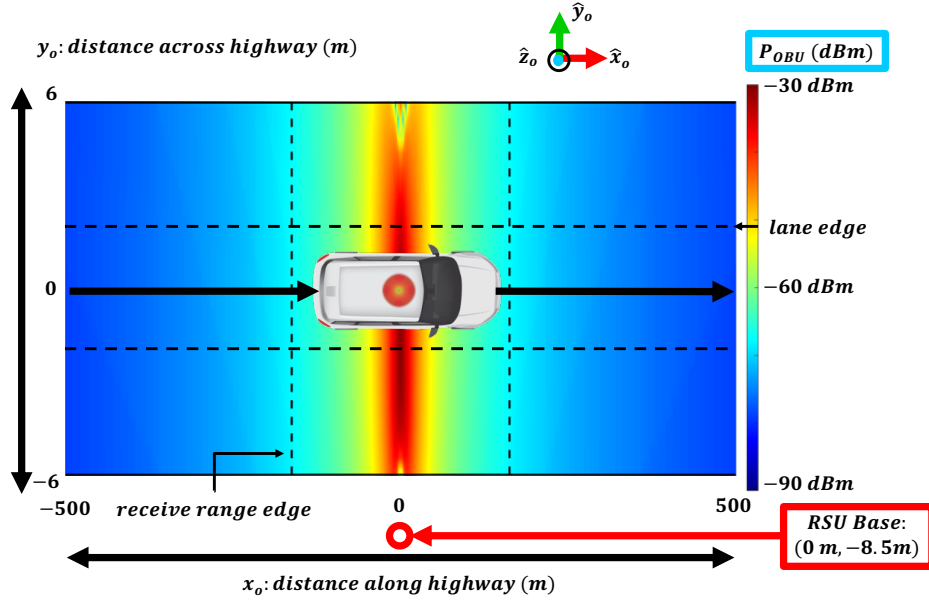
Figure 6.2 (a) RSU linear microstrip patch array with  $N = 4$  elements spaced apart by  $l_{sp}$  and gain patterns with peak  $G_{RSU} = 13.0$  dB at  $\theta_{RSU} = 0^\circ$  and first nulls at  $\theta_{RSU} = \theta_{fn} = 21.0^\circ$  in  $\phi_{RSU} = 90^\circ$  plane. (b) OBU circular monopole array with  $N = 16$  elements spaced apart by  $R\Delta\phi(\pi/180^\circ) = 15.97$  mm along a circle centered at  $\hat{z}_o$  with radius  $R$  and gain pattern in  $\theta_{OBU} = 90^\circ$  plane with peak  $G_{OBU} = 9.5$  dB. The OBU gain pattern shown represents the monopole array state when the vehicle's position along the highway is  $-500m \leq x_o < -20m$ .

## 6.4 OBU Received Power for Multi-Lane Linear Highway

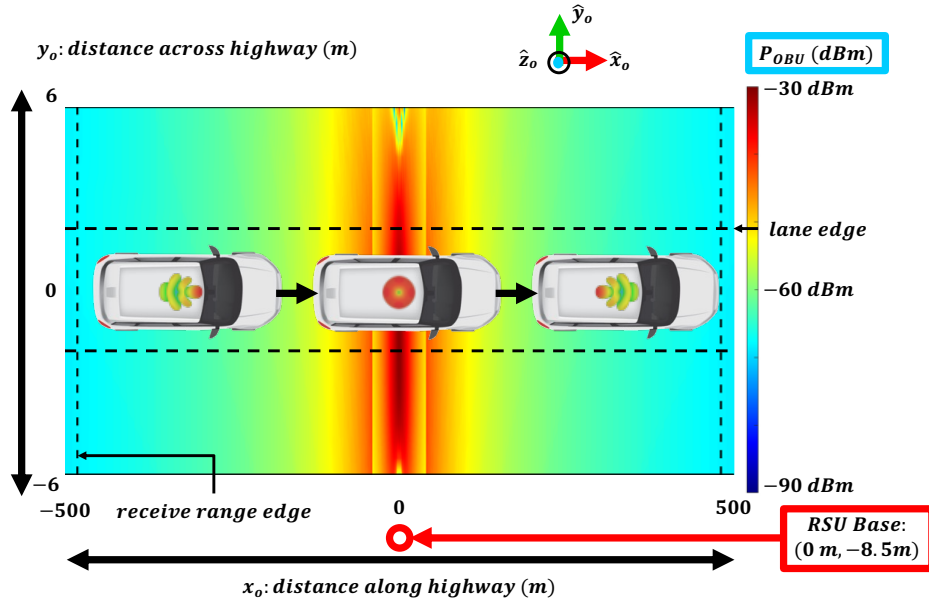
The power received by the OBU circular monopole array at rectilinear grid positions on the 1.0 km-long and 11.0 m-wide linear highway segment shown in Fig. 6.1(b) are estimated from the modified Friis equation for free space transmission between two passive antennas (6.2), with grid resolution of  $\Delta x_o = 1.0$  across the highway length and  $\Delta y_o = 0.5$  m across the highway width. In equation (6.2),  $r$  is the distance between the RSU and OBU arrays and  $|\hat{e}_{RSU} \cdot \hat{h}_{OBU}|$  is a loss factor for polarization mismatch between the plane wave emanating from the transmitting RSU microstrip patch array in Fig. 6.2(a)  $\hat{e}_{RSU}$  and the vector effective length of the receiving OBU circular monopole array in Fig. 6.2(b)  $\hat{h}_{OBU}$ . Array gains  $G_{RSU}$  and  $G_{OBU}$  are obtained through independent full-wave simulations in CST Microwave Studio. The  $\vec{r}$  vectors that point from the stationary RSU to the OBU positions at each grid point  $(x_o, y_o, h_{car})$  are calculated, and the corresponding  $(\theta_{RSU}, \phi_{RSU})$  and  $(\theta_{OBU}, \phi_{OBU})$  angles are obtained by transforming between the two coordinate systems as demonstrated in [137]. The OBU received power results are plotted in a 2D color scale from  $-90dBm \leq P_{OBU} - 30dBm$  in Fig. 6.3(a) for an OBU with only a single monopole and in Fig. 6.3(b) for an OBU with a circular monopole array that switches between three unique states as described in section 6.3.

$$P_{OBU} = \frac{P_{RSU} G_{RSU}(\theta_{RSU}, \phi_{RSU})}{4\pi r^2} \frac{G_{OBU}(\theta_{OBU}, \phi_{OBU}) \lambda_0^2}{4\pi} |\hat{e}_{RSU} \cdot \hat{h}_{OBU}|^2 \quad (6.2)$$

The IEEE 802.11p standard for DSRC communications at 5.9 GHz specifies a minimum receiver sensitivity of -68 dBm for a 1000-byte data packet to be received without error 90 % of the time with a 10 MHz OFDM signal at 27 Mbits/s [138]. When  $P_{OBU} \geq -68$  dBm is applied as a threshold for RSU base station separation in this simulated V2I system, the switchable-beam circular monopole array increases the range of a single RSU from only 325 meters to 961 meters, which reduces the required number of RSUs by a factor of three and dramatically decreases the cost of deploying such a V2I system. Additionally, the 12.2 dB front-to-back ratio of the circular monopole array helps to mitigate co-channel interference



(a)



(b)

Figure 6.3  $P_{OBU}$  at  $f_0 = 5.90$  GHz calculated via equation (6.2) for grid points on a linear highway segment for cases in which (a) OBU has a single monopole antenna and an RSU range of 325 m with a -68 dBm threshold and (c) OBU has a circular monopole array that switches between three beam states as shown in Fig. 6.1(b)-(c) and an RSU range of 961 m with a -68 dBm threshold. The highway is 1.0 km long (along  $\hat{x}_o$ ) and 11.0 m wide (along  $\hat{y}_o$ ).



between adjacent RSUs when vehicles approach mid-points between them, thereby allowing spectral reuse.

The OBU received power for the switchable beam case presented in Fig. 6.3(b) is also plotted as a function of vehicle position along the highway  $x_o$  at the center of each of the three highway lanes along  $y_o$  in Fig. 6.4. The switching of the circular monopole array state, from an azimuth beam pointed toward  $\phi_o = 0^\circ$  for  $-500m \leq x_o < 20m$ , to a single monopole omnidirectional radiation pattern for  $-20m \leq x_o \leq 20m$ , to another azimuth plane beam pointed toward  $\phi_o = 180^\circ$  for  $20m < x_o \leq 500m$ , is clearly observed from the discontinuities in the  $P_{OBU}$  plots for each lane. The  $P_{OBU}$  results presented in Fig. 6.4 are for an RSU array tilt angle  $\theta_{tilt} = 50.25^\circ$  and are reasonably-uniform ( $\pm 5$  dB at  $x_o = 0$ ) for all three lanes of traffic - the one nearest to the base of the RSU, the one furthest from the base of the RSU, and the one at the center. However, as shown in Fig. 6.5, changing  $\theta_{tilt}$  by only  $5.0^\circ$  either up or down causes  $P_{OBU}$  to decrease sharply in the edge lanes and have a lane variation of  $\pm 30$  dB at  $x_o = 0$ . The RSU tilt sensitivity is an important consideration for V2I system design and can be evaluated with this methodology.

## 6.5 Summary

In conclusion, a switchable-beam circular monopole array provides a much high gain toward the horizon and is a good candidate for vehicle-mounted antennas in V2I systems. The use of high gain antenna arrays for both the RSU and OBU can extend the range of communication and minimize the number of RSU base stations required in the network, lowering the cost. The simulation results further indicate that the received power is highly sensitive to RSU tilt angle as changing  $\theta_{tilt}$  by  $5^\circ$  causes the received power to approach the  $P_{OBU} \geq -68$  dBm threshold [138] in the edge lanes. As expected, a precise installation is required for high-gain, fixed-beam RSU arrays to ensure sufficient SNR near the highway edges. More complex RSU aperture designs, such as one with a multi-panel fixed-beam array or adaptive multi-beam phased arrays could potentially be used for the RSU to resolve the tilt sensitivity problem.

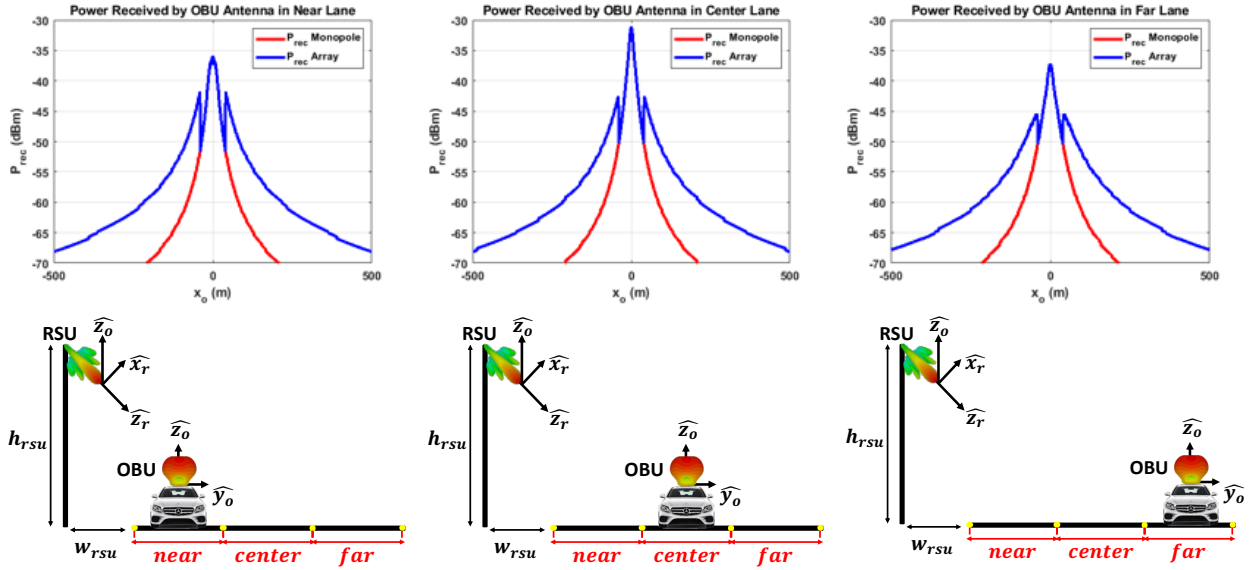


Figure 6.4  $P_{OBU}$  at  $f_0 = 5.90$  GHz calculated via equation (6.2) for grid points on a linear highway segment in (a) near, (b) center, and (c) far lanes with  $\theta_{tilt} = 50.25^\circ$ . See Fig. 6.1(a).

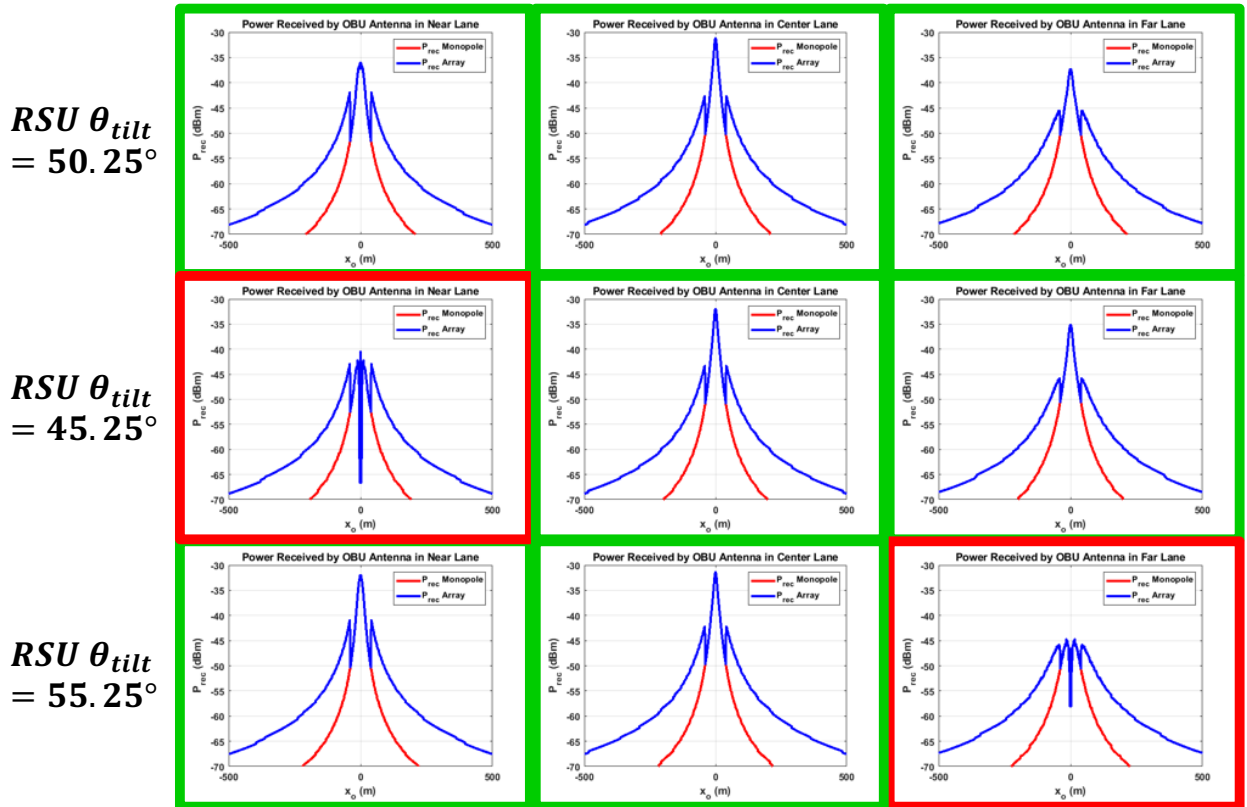


Figure 6.5  $P_{OBU}$  at  $f_0 = 5.90$  GHz calculated via equation (6.2) for grid points on a linear highway segment in all three lanes with different RSU tilt angles  $\theta_{tilt}$ . See Fig. 6.1(a).

# CHAPTER 7

## Conclusion

For many years, antenna measurements have been performed with the aim of characterizing the passive radiation and impedance-matching characteristics such as gain, polarization, and  $S_{11}$  for far field angles and bandwidths of interest. However, modern wireless communication systems operating at millimeter-wave frequencies have brought about a technological evolution in which active, electronically-scanned arrays with a large number of radiating elements are closely-integrated with beamforming integrated circuits and transceivers, such that the passive antenna radiation and active circuit distortion can no longer be characterized independently. The combined response of radiating elements and ICs must now be measured in controlled OTA test environments. Furthermore, the widespread adoption of wideband IQ-modulated signals for increasing data rates has elevated interest in measuring signal quality, which can be quantified as EVM. These trends have introduced numerous measurement challenges. One is determining if and how the far field EVM of these signals could be predicted from planar near field measurements, which have long been used for high gain antennas and phased arrays. The primary objective of this dissertation was to address that challenge, and a secondary objective was to predict the received signal power for a V2I antenna link on a linear highway.

First, a review of IQ signal generation, linear and nonlinear distortion by a generic DUT, and channel equalization was presented in chapter 2, since these details are an integral part of the EVM measurement process. Three different methods of determining EVM were described: (1) time domain demodulation, (2) frequency domain spectral correlation, and (3) continuous wave estimation. The first method is generally implemented with a VSA that demodulates the DUT output signal, but it is susceptible to signal generator errors and wideband thermal noise. The second method, which is detailed in [39] and [139], is implemented with a network

analyzer that measures a periodic, band-limited input signal and output signal for a two-port DUT over multiple coherent acquisitions with a narrowband receiver and calculates EVM from the spectral correlation properties. The advantages of this second method over the first method for EVM analysis of wideband signals were outlined. Finally, a method of estimating EVM from the root sum square of several error terms that are assumed to be uncorrelated and can be extracted from CW stimuli was presented. Chapter 3 presented an UWB model of far field antenna link transmission based on the vector effective length properties of the transmitting and receiving antennas and a simple circuit model. Full wave simulations of amplitude distortion from a 28 GHz microstrip patch antenna were applied to this model using MATLAB to estimate the EVM that results from its far field transmission of a 16-QAM signal. Then full-wave simulations were used to estimate the complex voltage transfer function of a far field link between two Ka-band conical horn antennas, using a rational fit modeling tool within MATLAB, which allowed the effects of both amplitude and group delay distortion to be modeled in the link EVM analysis. These simulations were compared with measured EVM results for the same horn, obtained with a CATR, network analyzer, and customized MATLAB instrument control scripts. Chapter 4 provided an extension from passive antennas to active arrays, starting with a review of EVM simulation and measurement methods that have been used by pioneering researchers. Simulations of 8x8 microstrip patch array elements were applied to phased array signal transmission models to investigate the relative effects of beam squint and element frequency response variations on the far field EVM as the beam is scanned and number of elements increased. Measurements of an 8x8 phased array were also performed with a CATR and network analyzer to determine how EVM varies for elements, beam scan angles, power sweeps, and signal modulation rates. Distortion-dominated EVM measurements of individual active array element channels were achieved, for the first time to the author's knowledge, by lowering VNA IF bandwidth and applying vector averaging. The far field EVM analysis of the Ka-band horn and 8x8 phased array via full-wave simulations and CATR measurements in chapters 3 and 4 provided a foundation and benchmark data for planar near field transformation analysis of these two AUTs in chapter 5. The fundamental principles of PNF measurement theory were presented, and relevant patents and publications

for its application to far field EVM analysis were reviewed. A single time domain simulation of the Ka-band horn planar near fields was performed, and the wideband near fields at each of 4096 ideal probe positions were exported and Fourier-transformed to the far field tone-by-tone. PNF-derived far fields were used to simulate the horn link EVM, and results were compared to those from chapter 3. These results nearly matched when the SNR component of the far field EVM was included, but the EVM predicted from simulated planar near fields for the linear distortion component deviated significantly from the far field simulation results at large elevation angles, indicating that a larger scan plane may be required than that indicated by the valid angle formula in equation (5.7). PNF measurements of the Ka-band horn and 8x8 phased array were also implemented with another customized MATLAB instrument control script. The measured planar near field  $S_{21}$ , EVM versus modulation rate and source power, and transformed far field patterns were presented and included multiple beam scan angles for the phased array. A methodology for estimating EVM of the far field signal from these PNF measurements, similar to that of Fig. 5.2, was defined and partially-demonstrated. Future tasks required to fully characterize the feasibility of determining far field EVM from planar near field measurements were also identified.

While a detailed analysis of CATR and PNF measurement errors was not within the scope of this work due to time constraints in accessing the test equipment, which was provided by Keysight Technologies at their state-of-the-art facilities in northern California, it remains an essential next step in ascertaining the degree of accuracy that can be achieved in predicting the far field EVM from PNF measurements, since this is highly dependent on the specific test conditions and calibration standards that are applied in these measurements (assuming CATR measurements are used as a reference for the far fields transformed from PNF measurements). This area of research is receiving greater attention as the *IEEE Recommended Practice for Estimating the Uncertainty in Error Vector Magnitude of Measured Digitally Modulated Signals for Wireless Communications* was published in November 2022 [140]. Beyond this, alternative PNF measurement techniques such as phaseless measurements [141, 142] and time domain formulations [143, 144] could be explored to determine if these offer speed, accuracy, or computational efficiency advantages when applied to far field EVM estimation.

## REFERENCES

- [1] A. N. Uwaechia and N. M. Mahyuddin, “A Comprehensive Survey on Millimeter Wave Communications for Fifth-Generation Wireless Networks: Feasibility and Challenges,” *IEEE Access*, vol. 8, pp. 62 367–62 414, 2020.
- [2] S. He, Y. Zhang, J. Wang, J. Zhang, J. Ren, Y. Zhang, W. Zhuang, and X. Shen, “A Survey of Millimeter-Wave Communication: Physical-Layer Technology Specifications and Enabling Transmission Technologies,” *Proceedings of the IEEE*, vol. 109, no. 10, pp. 1666–1705, Oct. 2021.
- [3] X. Wang, L. Kong, F. Kong, F. Qiu, M. Xia, S. Arnon, and G. Chen, “Millimeter Wave Communication: A Comprehensive Survey,” *IEEE Communications Surveys Tutorials*, vol. 20, no. 3, pp. 1616–1653, 2018.
- [4] W. Hong, Z. H. Jiang, C. Yu, D. Hou, H. Wang, C. Guo, Y. Hu, L. Kuai, Y. Yu, Z. Jiang, Z. Chen, J. Chen, Z. Yu, J. Zhai, N. Zhang, L. Tian, F. Wu, G. Yang, Z.-C. Hao, and J. Y. Zhou, “The Role of Millimeter-Wave Technologies in 5G/6G Wireless Communications,” *IEEE Journal of Microwaves*, vol. 1, no. 1, pp. 101–122, Jan. 2021.
- [5] M. Giordani, M. Polese, M. Mezzavilla, S. Rangan, and M. Zorzi, “Toward 6G Networks: Use Cases and Technologies,” *IEEE Communications Magazine*, vol. 58, no. 3, pp. 55–61, Mar. 2020.
- [6] U. Gustavsson, P. Frenger, C. Fager, T. Eriksson, H. Zirath, F. Dielacher, C. Studer, A. Pärssinen, R. Correia, J. N. Matos, D. Belo, and N. B. Carvalho, “Implementation Challenges and Opportunities in Beyond-5G and 6G Communication,” *IEEE Journal of Microwaves*, vol. 1, no. 1, pp. 86–100, Jan. 2021.
- [7] K. Hassan, M. Masarra, M. Zwingelstein, and I. Dayoub, “Channel Estimation Techniques for Millimeter-Wave Communication Systems: Achievements and Challenges,” *IEEE Open Journal of the Communications Society*, vol. 1, pp. 1336–1363, 2020.
- [8] S. Sun, T. S. Rappaport, M. Shafi, P. Tang, J. Zhang, and P. J. Smith, “Propagation Models and Performance Evaluation for 5G Millimeter-Wave Bands,” *IEEE Transactions on Vehicular Technology*, vol. 67, no. 9, pp. 8422–8439, Sep. 2018.
- [9] H. Zhang, Y. Zhang, J. Cosmas, N. Jawad, W. Li, R. Muller, and T. Jiang, “mmWave Indoor Channel Measurement Campaign for 5G New Radio Indoor Broadcasting,” *IEEE Transactions on Broadcasting*, pp. 1–14, 2022.
- [10] X. Yu, J. Zhang, M. Haenggi, and K. B. Letaief, “Coverage Analysis for Millimeter Wave Networks: The Impact of Directional Antenna Arrays,” *IEEE Journal on Selected Areas in Communications*, vol. 35, no. 7, pp. 1498–1512, Jul. 2017.
- [11] T. S. Rappaport, *Millimeter Wave Wireless Communications / Theodore S. Rappaport, Robert W. Heath, Robert C. Daniels, James N. Murdock*. Upper Saddle River, NJ: Prentice Hall, 2015.

- [12] S. Ghosh and D. Sen, “An Inclusive Survey on Array Antenna Design for Millimeter-Wave Communications,” *IEEE Access*, vol. 7, pp. 83 137–83 161, 2019.
- [13] G. M. Rebeiz, S.-Y. Kim, O. Inac, W. Shin, O. Gurbuz, Y.-C. Ou, F. Golcuk, T. Kanar, and B.-H. Ku, “Millimeter-wave large-scale phased-arrays for 5G systems,” in *2015 IEEE MTT-S International Microwave Symposium*, May 2015, pp. 1–3.
- [14] D. Zhao, P. Gu, J. Zhong, N. Peng, M. Yang, Y. Yi, J. Zhang, P. He, Y. Chai, Z. Chen, and X. You, “Millimeter-Wave Integrated Phased Arrays,” *IEEE Transactions on Circuits and Systems I: Regular Papers*, vol. 68, no. 10, pp. 3977–3990, Oct. 2021.
- [15] X. Gu, D. Liu, and B. Sadhu, “Packaging and Antenna Integration for Silicon-Based Millimeter-Wave Phased Arrays: 5G and Beyond,” *IEEE Journal of Microwaves*, vol. 1, no. 1, pp. 123–134, Jan. 2021.
- [16] B. Sadhu, X. Gu, and A. Valdes-Garcia, “The More (Antennas), the Merrier: A Survey of Silicon-Based mm-Wave Phased Arrays Using Multi-IC Scaling,” *IEEE Microwave Magazine*, vol. 20, no. 12, pp. 32–50, Dec. 2019.
- [17] P. Choi, D. A. Antoniadis, and E. A. Fitzgerald, “Towards Millimeter-Wave Phased Array Circuits and Systems For Small Form Factor and Power Efficient 5G Mobile Devices,” in *2019 IEEE International Symposium on Phased Array System Technology (PAST)*, Oct. 2019, pp. 1–5.
- [18] J.-C. S. Chieh, E. Yeo, R. Farkouh, A. Castro, M. Kerber, R. B. Olsen, E. J. Merulla, and S. K. Sharma, “Development of flat panel active phased array antennas using 5g silicon rfics at ku-and ka-bands,” *IEEE Access*, vol. 8, pp. 192 669–192 681, 2020.
- [19] Y. Qi, G. Yang, L. Liu, J. Fan, A. Orlandi, H. Kong, W. Yu, and Z. Yang, “5G Over-the-Air Measurement Challenges: Overview,” *IEEE Transactions on Electromagnetic Compatibility*, vol. 59, no. 6, pp. 1661–1670, Dec. 2017.
- [20] K. A. Remley, J. A. Gordon, D. Novotny, A. E. Curtin, C. L. Holloway, M. T. Simons, R. D. Horansky, M. S. Allman, D. Senic, M. Becker, J. A. Jargon, P. D. Hale, D. F. Williams, A. Feldman, J. Cheron, R. Chamberlin, C. Gentile, J. Senic, R. Sun, P. B. Papazian, J. Quimby, M. Mujumdar, and N. Golmie, “Measurement Challenges for 5G and Beyond: An Update from the National Institute of Standards and Technology,” *IEEE Microwave Magazine*, vol. 18, no. 5, pp. 41–56, Jul. 2017.
- [21] S. G. Pannala, “Feasibility and Challenges of Over-The-Air Testing for 5G Millimeter Wave Devices,” in *2018 IEEE 5G World Forum (5GWF)*, Jul. 2018, pp. 304–310.
- [22] W. Fan, P. Kyosti, M. Rumney, X. Chen, and G. F. Pedersen, “Over-the-Air Radiated Testing of Millimeter-Wave Beam-Steerable Devices in a Cost-Effective Measurement Setup,” *IEEE Communications Magazine*, vol. 56, no. 7, pp. 64–71, Jul. 2018.
- [23] J. M. McKinnis, I. Gresham, and R. Becker, “Figures of Merit for Active Antenna Enabled 5G Communication Networks,” in *2018 11th Global Symposium on Millimeter Waves (GSMM)*, May 2018, pp. 1–7.

- [24] M. Millhaem, “Test and Characterization for 5G Phased Array Antenna Systems,” in *2018 IEEE/MTT-S International Microwave Symposium - IMS*, Jun. 2018, pp. 1338–1341.
- [25] K. K. W. Low, S. Zahir, T. Kanar, and G. M. Rebeiz, “A 27-31-GHz 1024-Element Ka-Band SATCOM Phased-Array Transmitter With 49.5-dBW Peak EIRP, 1-dB AR, and  $\pm 70^\circ$  Beam Scanning,” *IEEE Transactions on Microwave Theory and Techniques*, pp. 1–1, 2022.
- [26] X. Luo, J. Ouyang, Z.-H. Chen, Y. Yan, L. Han, Z. Wu, T. Yu, and K. Zheng, “A Scalable Ka-Band 1024-Element Transmit Dual-Circularly-Polarized Planar Phased Array for SATCOM Application,” *IEEE Access*, vol. 8, pp. 156 084–156 095, 2020.
- [27] K. Quzwain, Y. Yamada, K. Kamardin, N. H. A. Rahman, and T. A. Rahman, “Design of Shaped Offset Dual-Reflector Antenna for 5G Mobile Base Station,” in *2018 IEEE International RF and Microwave Conference (RFM)*, Dec. 2018, pp. 5–8.
- [28] O. Quevedo-Teruel, M. Ebrahimpouri, and F. Ghasemifard, “Lens Antennas for 5G Communications Systems,” *IEEE Communications Magazine*, vol. 56, no. 7, pp. 36–41, Jul. 2018.
- [29] W. Hong, Z. H. Jiang, C. Yu, J. Zhou, P. Chen, Z. Yu, H. Zhang, B. Yang, X. Pang, M. Jiang, Y. Cheng, M. K. T. Al-Nuaimi, Y. Zhang, J. Chen, and S. He, “Multi-beam Antenna Technologies for 5G Wireless Communications,” *IEEE Transactions on Antennas and Propagation*, vol. 65, no. 12, pp. 6231–6249, Dec. 2017.
- [30] G. He, X. Gao, L. Sun, and R. Zhang, “A Review of Multibeam Phased Array Antennas as LEO Satellite Constellation Ground Station,” *IEEE Access*, vol. 9, pp. 147 142–147 154, 2021.
- [31] S. Abadal, C. Han, and J. M. Jornet, “Wave Propagation and Channel Modeling in Chip-Scale Wireless Communications: A Survey From Millimeter-Wave to Terahertz and Optics,” *IEEE Access*, vol. 8, pp. 278–293, 2020.
- [32] Z. Iqbal and M. Pour, “Grating lobe reduction in scanning phased array antennas with large element spacing,” *IEEE Transactions on Antennas and Propagation*, vol. 66, no. 12, pp. 6965–6974, 2018.
- [33] A. Ayissi Manga, R. Gillard, R. Loison, I. L. Roy-Naneix, and C. Renard, “A correcting coupling solution to extend the scanning range of large printed phased arrays by means of identical microstrip lines connecting the sources two by two,” in *2019 13th European Conference on Antennas and Propagation (EuCAP)*, 2019, pp. 1–5.
- [34] J. Sombrin and P. Medrel, “Cross-correlation method measurement of error vector magnitude and application to power amplifier non-linearity performances,” in *2016 88th ARFTG Microwave Measurement Conference (ARFTG)*, Dec. 2016, pp. 1–4.



- [35] J. Verspecht, A. Stav, J.-P. Teyssier, and S. Kusano, "Characterizing Amplifier Modulation Distortion Using a Vector Network Analyzer," in *2019 93rd ARFTG Microwave Measurement Conference (ARFTG)*, Jun. 2019, pp. 1–4.
- [36] M. Mckinley, K. Remley, M. Myslinski, J. Kenney, D. Schreurs, and B. Nauwelaers, "EVM calculation for broadband modulated signals," *64th ARFTG Conference*, Jan. 2004.
- [37] R. A. Witte, *Spectrum and network measurements*. IET, 2014, vol. 2.
- [38] R. Hassun, M. Flaherty, R. Matreci, and M. Taylor, "Effective evaluation of link quality using error vector magnitude techniques," in *Proceedings of 1997 Wireless Communications Conference*, Aug. 1997, pp. 89–94.
- [39] J. P. Dunsmore, *Handbook of microwave component measurements: with advanced VNA techniques*. John Wiley & Sons, 2020.
- [40] G. Gibiino, A. Angelotti, A. Santarelli, and P. Traverso, "Vna-based broadband evm measurement of an rf nonlinear pa under load mismatch conditions," in *Proc. IMEKO-TC4 Int. Symp.*, 2020, pp. 65–69.
- [41] K. Gharaibeh, K. Gard, and M. Steer, "Accurate estimation of digital communication system metrics - SNR, EVM and  $\rho$  in a nonlinear amplifier environment," in *64th ARFTG Microwave Measurements Conference, Fall 2004.*, Dec. 2004, pp. 41–44.
- [42] R. A. Shafik, M. S. Rahman, and A. R. Islam, "On the Extended Relationships Among EVM, BER and SNR as Performance Metrics," in *2006 International Conference on Electrical and Computer Engineering*, Dec. 2006, pp. 408–411.
- [43] R. A. Shafik, M. S. Rahman, A. R. Islam, and N. S. Ashraf, "On the error vector magnitude as a performance metric and comparative analysis," in *2006 International Conference on Emerging Technologies*, Nov. 2006, pp. 27–31.
- [44] H. A. Mahmoud and H. Arslan, "Error vector magnitude to SNR conversion for nondata-aided receivers," *IEEE Transactions on Wireless Communications*, vol. 8, no. 5, pp. 2694–2704, May 2009.
- [45] R. Schmogrow, B. Nebendahl, M. Winter, A. Josten, D. Hillerkuss, S. Koenig, J. Meyer, M. Dreschmann, M. Huebner, C. Koos, J. Becker, W. Freude, and J. Leuthold, "Error Vector Magnitude as a Performance Measure for Advanced Modulation Formats," *IEEE Photonics Technology Letters*, vol. 24, no. 1, pp. 61–63, Jan. 2012.
- [46] K. Freiburger, H. Enzinger, and C. Vogel, "A Noise Power Ratio Measurement Method for Accurate Estimation of the Error Vector Magnitude," *IEEE Transactions on Microwave Theory and Techniques*, vol. 65, no. 5, pp. 1632–1645, May 2017.
- [47] J. B. Sombrin, "On the formal identity of EVM and NPR measurement methods: Conditions for identity of error vector magnitude and noise power ratio," in *2011 41st European Microwave Conference*, Oct. 2011, pp. 337–340.

- [48] E. U. T. R. Access, “Base station (bs) radio transmission and reception,” *3gpp ts*, vol. 15, p. 44, 2018.
- [49] S. Ramavath and R. S. Kshetrimayum, “Analytical calculations of cdf for some common papr reduction techniques in ofdm systems,” in *2012 International Conference on Communications, Devices and Intelligent Systems (CODIS)*, 2012, pp. 393–396.
- [50] F. Pancaldi, G. M. Vitetta, R. Kalbasi, N. Al-Dhahir, M. Uysal, and H. Mheidat, “Single-carrier frequency domain equalization,” *IEEE Signal Processing Magazine*, vol. 25, no. 5, pp. 37–56, Sep. 2008.
- [51] H. Wang, P. M. Asbeck, and C. Fager, “Millimeter-Wave Power Amplifier Integrated Circuits for High Dynamic Range Signals,” *IEEE Journal of Microwaves*, vol. 1, no. 1, pp. 299–316, Jan. 2021.
- [52] V. Vasconcellos, G. C. Ornelas, and A. N. Barreto, “Performance of 5g candidate waveforms with non-linear power amplifiers,” in *2017 IEEE 9th Latin-American Conference on Communications (LATINCOM)*. IEEE, 2017, pp. 1–5.
- [53] C. Fager, T. Eriksson, F. Barradas, K. Hausmair, T. Cunha, and J. C. Pedro, “Linearity and Efficiency in 5G Transmitters: New Techniques for Analyzing Efficiency, Linearity, and Linearization in a 5G Active Antenna Transmitter Context,” *IEEE Microwave Magazine*, vol. 20, no. 5, pp. 35–49, May 2019.
- [54] Y. Duroc, “ON THE SYSTEM MODELING OF ANTENNAS,” *Progress In Electromagnetics Research B*, vol. 21, pp. 69–85, 2010.
- [55] W. Sörgel and W. Wiesbeck, “Influence of the Antennas on the Ultra-Wideband Transmission,” *EURASIP Journal on Advances in Signal Processing*, vol. 2005, no. 3, p. 843268, Dec. 2005.
- [56] J. Kunisch and J. Pamp, “Uwb radio channel modeling considerations,” *Proc. of ICEAA*, vol. 3, 2003.
- [57] S. Licul and W. Davis, “Unified frequency and time-domain antenna modeling and characterization,” *IEEE Transactions on Antennas and Propagation*, vol. 53, no. 9, pp. 2882–2888, Sep. 2005.
- [58] B. Razavi, “The decision-feedback equalizer [a circuit for all seasons],” *IEEE Solid-State Circuits Magazine*, vol. 9, no. 4, pp. 13–132, 2017.
- [59] G. P. Gibiino, A. M. Angelotti, A. Santarelli, and P. A. Traverso, “Error vector magnitude measurement for power amplifiers under wideband load impedance mismatch: System-level analysis and vna-based implementation,” *Measurement*, vol. 187, p. 110254, 2022.
- [60] J. Verspecht, T. Nielsen, A. Stav, J. Dunsmore, and J.-P. Teyssier, “Modulation distortion analysis for mixers and frequency converters,” in *2020 95th ARFTG Microwave Measurement Conference (ARFTG)*, 2020, pp. 1–4.

- [61] J.-P. Teyssier, J. Dunsmore, J. Verspecht, and J. Kerr, “Coherent multi-tone stimulus-response measurements with a vna,” in *2017 89th ARFTG Microwave Measurement Conference (ARFTG)*, 2017, pp. 1–3.
- [62] Y. Rolain, M. Zyari, E. Van Nechel, and G. Vandersteen, “A measurement-based error-vector-magnitude model to assess non linearity at the system level,” in *2017 IEEE MTT-S International Microwave Symposium (IMS)*, Jun. 2017, pp. 1429–1432.
- [63] *Create Accurate EVM Measurements with the PNA-X Series Network Analyzer [Application Note]*. Keysight Technologies, 2020.
- [64] J. Pedro and N. Carvalho, “Designing multisine excitations for nonlinear model testing,” *IEEE Transactions on Microwave Theory and Techniques*, vol. 53, no. 1, pp. 45–54, Jan. 2005.
- [65] T.-H. Sang and H.-H. Huang, “EVM simulation of power amplifiers with designed signals in OFDM systems,” in *2011 International Conference on Electric Information and Control Engineering*, Apr. 2011, pp. 5897–5900.
- [66] A. Georgiadis and C. Kalialakis, “Evaluation of error vector magnitude due to combined IQ imbalances and phase noise,” *IET Circuits, Devices & Systems*, vol. 8, no. 6, pp. 421–426, 2014.
- [67] A. Georgiadis, “Gain, phase imbalance, and phase noise effects on error vector magnitude,” *IEEE Transactions on Vehicular Technology*, vol. 53, no. 2, pp. 443–449, Mar. 2004.
- [68] F. Gregorio, J. Cousseau, S. Werner, T. Riihonen, and R. Wichman, “EVM Analysis for Broadband OFDM Direct-Conversion Transmitters,” *IEEE Transactions on Vehicular Technology*, vol. 62, no. 7, pp. 3443–3451, Sep. 2013.
- [69] C. Zhao and R. J. Baxley, “Error Vector Magnitude Analysis for OFDM Systems,” in *2006 Fortieth Asilomar Conference on Signals, Systems and Computers*, Oct. 2006, pp. 1830–1834.
- [70] A. Cheaito, M. Crussière, J.-F. Hélar, and Y. Louët, “Quantifying the Memory Effects of Power Amplifiers: EVM Closed-Form Derivations of Multicarrier Signals,” *IEEE Wireless Communications Letters*, vol. 6, no. 1, pp. 34–37, Feb. 2017.
- [71] A. K. Wang, R. Ligmanowski, J. Castro, and A. Mazzara, “EVM Simulation and Analysis Techniques,” in *MILCOM 2006 - 2006 IEEE Military Communications Conference*, Oct. 2006, pp. 1–7.
- [72] A. Halder and A. Chatterjee, “Low-cost alternate EVM test for wireless receiver systems,” in *23rd IEEE VLSI Test Symposium (VTS’05)*, May 2005, pp. 255–260.
- [73] L. Noel and P. Brousse, “Low-Cost EVM Test Methodology for Wireless Transmitters Applied to W-CDMA,” *IEEE Transactions on Instrumentation and Measurement*, vol. 60, no. 1, pp. 170–175, Jan. 2011.

- [74] V. Natarajan, H. W. Choi, A. Banerjee, S. Sen, A. Chatterjee, G. Srinivasan, F. Taenzler, and S. Bhattacharya, “Low Cost EVM Testing of Wireless RF SoC Front-Ends Using Multitones,” *IEEE Transactions on Computer-Aided Design of Integrated Circuits and Systems*, vol. 31, no. 7, pp. 1088–1101, Jul. 2012.
- [75] J. Van ‘t Hof, C. De Martino, S. Malotiaux, M. Squillante, M. Marchetti, L. Galatro, and M. Spirito, “Vector gain based EVM estimation at mm-wave frequencies,” in *2020 95th ARFTG Microwave Measurement Conference (ARFTG)*, Aug. 2020, pp. 1–5.
- [76] R. K. Goyal and U. S. Modani, “A compact microstrip patch antenna at 28 ghz for 5g wireless applications,” in *2018 3rd International Conference and Workshops on Recent Advances and Innovations in Engineering (ICRAIE)*. IEEE, 2018, pp. 1–2.
- [77] D. Brown and Y. Rahmat-Samii, “Far field evm characterization of antenna frequency response via full-wave analysis,” in *2021 IEEE International Symposium on Antennas and Propagation and USNC-URSI Radio Science Meeting (APS/URSI)*. IEEE, 2021, pp. 1251–1252.
- [78] M. A. Almoteriy, M. I. Sobhy, and J. C. Batchelor, “Antenna Modeling Technique for Digital Communication Systems,” in *2018 15th International Conference on Synthesis, Modeling, Analysis and Simulation Methods and Applications to Circuit Design (SMACD)*, Jul. 2018, pp. 1–48.
- [79] M. El-Hadidy, “UWB antennas: Mathematical presentation, Impulse Response simulation and Electromagnetic modeling,” in *2013 International Conference on High Performance Computing Simulation (HPCS)*, Jul. 2013, pp. 357–361.
- [80] M. El-Hadidy and T. Kaiser, “An UWB Channel Model Considering Angular Antenna Impulse Response and Polarization,” in *The Second European Conference on Antennas and Propagation, EuCAP 2007*, Nov. 2007, pp. 1–5.
- [81] M. A. Almoteriy, M. I. Sobhy, and J. C. Batchelor, “Antenna characterisation and channel effects on digital systems,” in *Loughborough Antennas Propagation Conference (LAPC 2017)*, Nov. 2017, pp. 1–5.
- [82] —, “Characterization of wideband antennas for point-to-point communications,” *IEEE Transactions on Antennas and Propagation*, vol. 66, no. 9, pp. 4466–4473, 2018.
- [83] J. E. Diener, J. Quimby, K. A. Remley, and A. Z. Elsherbeni, “Millimeter-wave frequency FDTD simulation for error vector magnitude of modulated signals,” in *2018 International Applied Computational Electromagnetics Society Symposium (ACES)*, Mar. 2018, pp. 1–2.
- [84] M. E. Leinonen, N. Tervo, M. Jokinen, O. Kursu, and A. Pärssinen, “5g mm-wave link range estimation based on over-the-air measured system evm performance,” in *2019 IEEE MTT-S International Microwave Symposium (IMS)*, 2019, pp. 476–479.

- [85] J. M. Kovitz, V. Manohar, and Y. Rahmat-Samii, “A spline-profiled conical horn antenna assembly optimized for deployable ka-band offset reflector antennas in cubesats,” in *2016 IEEE International Symposium on Antennas and Propagation (APSURSI)*, 2016, pp. 1535–1536.
- [86] *SAF-2334431535-328-S1-280-DP WR-28 DUAL-POLARIZED SCALAR FEED HORN ANTENNA Rev. 01 (Data Sheet)*, SAGE Millimeter, Inc., 2020, <https://www.eravant.com/15-dbi-gain-23-to-44-ghz-40-db-isolation-wr-28-waveguide-dual-polarized-scalar-feed-horn-antenna>.
- [87] Y. Nakatsukasa, O. Sète, and L. N. Trefethen, “The aaa algorithm for rational approximation,” *SIAM Journal on Scientific Computing*, vol. 40, no. 3, pp. A1494–A1522, 2018.
- [88] *Time response for rational objects (timeresp)*, MATLAB, 2022, <https://www.mathworks.com/help/rf/ref/rational.timeresp.html>.
- [89] B. Gustavsen and A. Semlyen, “Rational approximation of frequency domain responses by vector fitting,” *IEEE Transactions on Power Delivery*, vol. 14, no. 3, pp. 1052–1061, 1999.
- [90] J. Verspecht, A. Stav, T. Nielsen, and S. Kusano, “The vector component analyzer: A new way to characterize distortions of modulated signals in high-frequency active devices,” *IEEE Microwave Magazine*, vol. 23, no. 12, pp. 86–96, 2022.
- [91] C. A. Balanis, *Antenna theory: analysis and design*. John wiley & sons, 2015.
- [92] D. M. Pozar, *Microwave engineering*. John wiley & sons, 2011.
- [93] *F9650A Compact Antenna Test Range: Millimeter-Wave Over-The-Air Measurement Chamber (Data Sheet)*, Keysight Technologies, 2020, <https://www.keysight.com/us/en/product/F9650A/compact-antenna-test-range-catr.html>.
- [94] *USB Preamplifiers: U7227/8F 2 to 50 GHz (Technical Overview)*, Keysight Technologies, 2019, <https://www.keysight.com/us/en/product/U7227F/u7227f-usb-preamplifier-2-50-ghz.html?jmpid=zzfindu7227f>.
- [95] H. Wang and H. Zhao, “EVM performance evaluation of array channels’ amplitude and phase errors for DBF phased array antennas,” in *2010 IEEE International Symposium on Phased Array Systems and Technology*, Oct. 2010, pp. 332–334.
- [96] Z. Yong-hua, H. Wen-hua, L. Ping, S. Jian-cang, and Z. Rongwei, “Analysis of Influence of Channel Damage on Phased Array Communication Links\*,” in *2019 IEEE-APS Topical Conference on Antennas and Propagation in Wireless Communications (APWC)*, Sep. 2019, pp. 306–310.
- [97] H. Li, Q. An, K. Jia, H. Wu, and Z. He, “Effects analysis of imperfections on multi-antenna transceiving systems,” *EURASIP Journal on Wireless Communications and Networking*, vol. 2012, no. 1, p. 81, Dec. 2012.

- [98] Y. Yin, S. Zehir, T. Kanar, Q. Ma, H. Chung, L. Gao, and G. M. Rebeiz, “A 37–42-GHz  $8 \times 8$  Phased-Array With 48–51-dBm EIRP, 64-QAM 30-Gb/s Data Rates, and EVM Analysis Versus Channel RMS Errors,” *IEEE Transactions on Microwave Theory and Techniques*, vol. 68, no. 11, pp. 4753–4764, Nov. 2020.
- [99] N. Tervo, M. E. Leinonen, J. Aikio, T. Rahkonen, and A. Pärssinen, “Analyzing the effects of pa variations on the performance of phased array digital predistortion,” in *2018 IEEE 29th Annual International Symposium on Personal, Indoor and Mobile Radio Communications (PIMRC)*, 2018, pp. 215–219.
- [100] B. Rupakula, A. H. Aljuhani, and G. M. Rebeiz, “ACPR Improvement in Large Phased Arrays With Complex Modulated Waveforms,” *IEEE Transactions on Microwave Theory and Techniques*, vol. 68, no. 3, pp. 1045–1053, Mar. 2020.
- [101] R. Argaez-Ramirez, J.-R. Perez-Cisneros, and C. Fager, “Investigation of power amplifier performance under load mismatch conditions,” in *2021 IEEE Topical Conference on RF/Microwave Power Amplifiers for Radio and Wireless Applications (PAWR)*, Jan. 2021, pp. 41–43.
- [102] F. Jalili, D. E. Serup, O. Franek, M. Shen, and G. F. Pedersen, “Antenna Array Inter-Element Coupling impact on Linearization of Active Phased Array,” in *2021 International Symposium on Networks, Computers and Communications (ISNCC)*, Oct. 2021, pp. 1–5.
- [103] C. Fager, K. Hausmair, K. Buisman, K. Andersson, E. Sienkiewicz, and D. Gustafsson, “Analysis of nonlinear distortion in phased array transmitters,” in *2017 Integrated Nonlinear Microwave and Millimetre-wave Circuits Workshop (INMMiC)*, Apr. 2017, pp. 1–4.
- [104] K. Hausmair, S. Gustafsson, C. Sánchez-Pérez, P. N. Landin, U. Gustavsson, T. Eriksson, and C. Fager, “Prediction of Nonlinear Distortion in Wideband Active Antenna Arrays,” *IEEE Transactions on Microwave Theory and Techniques*, vol. 65, no. 11, pp. 4550–4563, Nov. 2017.
- [105] P. Taghikhani, K. Buisman, and C. Fager, “Hybrid Beamforming Transmitter Modeling for Millimeter-Wave MIMO Applications,” *IEEE Transactions on Microwave Theory and Techniques*, vol. 68, no. 11, pp. 4740–4752, Nov. 2020.
- [106] Z. Zhang, Y. Yin, and G. M. Rebeiz, “Intersymbol Interference and Equalization for Large 5G Phased Arrays With Wide Scan Angles,” *IEEE Transactions on Microwave Theory and Techniques*, vol. 69, no. 3, pp. 1955–1964, Mar. 2021.
- [107] Y. Yin, B. Ustundag, K. Kibaroglu, M. Sayginer, and G. M. Rebeiz, “Wideband 23.5–29.5-GHz Phased Arrays for Multistandard 5G Applications and Carrier Aggregation,” *IEEE Transactions on Microwave Theory and Techniques*, vol. 69, no. 1, pp. 235–247, Jan. 2021.

- [108] D. M. Tuan, Y. Cheon, Y. Aoki, and Y. Kim, "Performance comparison of millimeter-wave communications system with different antenna beamwidth," in *2016 10th European Conference on Antennas and Propagation (EuCAP)*, Apr. 2016, pp. 1–5.
- [109] H. Holter and H. Steyskal, "On the size requirement for finite phased-array models," *IEEE Transactions on Antennas and Propagation*, vol. 50, no. 6, pp. 836–840, 2002.
- [110] G. Huff, N. Soldner, W. Palmer, and J. Bernhard, "Study of error vector magnitude patterns (EVRP) for a transmit/receive pair of microstrip patch antennas," in *2006 IEEE Antennas and Propagation Society International Symposium*, Jul. 2006, pp. 449–452.
- [111] K. Kibaroglu, M. Sayginer, and G. M. Rebeiz, "A Low-Cost Scalable 32-Element 28-GHz Phased Array Transceiver for 5G Communication Links Based on a  $2 \times 2$  Beamformer Flip-Chip Unit Cell," *IEEE Journal of Solid-State Circuits*, vol. 53, no. 5, pp. 1260–1274, May 2018.
- [112] S. Spira, K. Blau, R. Thomä, and M. A. Hein, "5G mm-Wave Over-The-Air Measurements of an Agile Multi-Beam Front-End," in *2020 50th European Microwave Conference (EuMC)*, Jan. 2021, pp. 153–156.
- [113] B. T. Walkenhorst, "Test Environments for 5G Millimeter-Wave Devices," in *2019 13th European Conference on Antennas and Propagation (EuCAP)*, Mar. 2019, pp. 1–5.
- [114] B. Derat, C. Rowell, and A. Tankielun, "Promises of Near-Field Software and Hardware Transformations for 5G OTA," in *2018 IEEE Conference on Antenna Measurements Applications (CAMA)*, Sep. 2018, pp. 1–4.
- [115] L. M. Tancioni, A. Jernberg, P. Noren, A. Giacomini, A. Scannavini, L. Foged, R. Braun, M. Boumans, F. Hirn, B. Horrocks, and C. Schröter, "Over-the-Air testing of Active Antenna System Base Stations in Compact Antenna Test Range," in *2019 13th European Conference on Antennas and Propagation (EuCAP)*, Mar. 2019, pp. 1–5.
- [116] S. Gregson and C. Parini, "Use of OTA System Performance Metrics in the Design and Optimization of CATRs for 5G Testing," in *2019 Antenna Measurement Techniques Association Symposium (AMTA)*, Oct. 2019, pp. 1–6.
- [117] H. Bartko, A. Tankielun, and B. Derat, "New Measurements Concept of Electrically Large Active Antenna Systems in Compact Test Chambers," in *2019 8th Asia-Pacific Conference on Antennas and Propagation (APCAP)*, Aug. 2019, pp. 599–600.
- [118] W. Q. Malik, D. J. Edwards, and C. J. Stevens, "Angular-spectral antenna effects in ultra-wideband communications links," *Proc. Inst. Elect. Eng. Commun.*, pp. 99–106, 2006.
- [119] M. Alonso-delPino, M. di Rosa, M. Simeoni, M. Spella, C. De Martino, and M. Spirito, "A Planar Near-Field Setup for Millimeter-Wave System-Embedded Antenna Testing," *IEEE Antennas and Wireless Propagation Letters*, vol. 16, pp. 83–86, 2017.

- [120] G. S. Lee, G. D. VanWiggeren, and C. Coleman, “Determining far field error vector magnitude (evm) of a device under test over the air (ota),” Feb. 13 2018, uS Patent 9,893,819.
- [121] MVG, “Fast, spherical near-field antenna measurements for satellites,” *Microwave Journal*, 2021. [Online]. Available: [www.microwavejournal.com/articles/36138-fast-spherical-near-field-antenna-measurements-for-satellites](http://www.microwavejournal.com/articles/36138-fast-spherical-near-field-antenna-measurements-for-satellites)
- [122] “Ieee recommended practice for near-field antenna measurements,” *IEEE Std 1720-2012*, pp. 1–102, 2012.
- [123] S. F. Razavi and Y. Rahmat-Samii, “Resilience to probe-positioning errors in planar phaseless near-field measurements,” *IEEE Transactions on Antennas and Propagation*, vol. 58, no. 8, pp. 2632–2640, 2010.
- [124] M. Löhning, T. Deckert, V. Kotzsch, and M. V. Bossche, “A novel ota near-field measurement approach suitable for 5g mmwave wideband modulated tests,” in *2022 IEEE/MTT-S International Microwave Symposium - IMS 2022*, 2022, pp. 856–858.
- [125] M. Laabs, D. Plettemeier, T. Deckert, V. Kotzsch, and M. Vanden Bossche, “A novel ota near-field measurement approach suitable for 5g mmwave validation and test,” in *2021 51st European Microwave Conference (EuMC)*, 2022, pp. 564–567.
- [126] H. Noda, “Observations on Near-Field Evaluation of 5G Signal Quality,” in *2020 International Symposium on Antennas and Propagation (ISAP)*, Jan. 2021, pp. 427–428.
- [127] H. Saito and H. Arai, “Near field EVM estimation in OTA test,” *IEICE Communications Express*, vol. 10, no. 9, pp. 677–680, Sep. 2021.
- [128] V. Manohar and Y. Rahmat-Samii, “Mimicking antenna near-field measurements using full wave solvers for error characterization,” in *2019 IEEE International Symposium on Antennas and Propagation and USNC-URSI Radio Science Meeting*, 2019, pp. 1851–1852.
- [129] D. Slater, “Personal near-field system 1987, radio camera 2019,” in *2019 Antenna Measurement Techniques Association Symposium (AMTA)*, 2019, pp. 1–5.
- [130] *EWG28 26.5-40.0 GHz Open Ended Waveguide Probe (Technical Specification)*, A-INFO, <http://www.ainfoinc.com.cn/en/product/h'oewg.asp>.
- [131] D. M. Kerns, *Plane-wave scattering-matrix theory of antennas and antenna-antenna interactions*. US Department of Commerce, National Bureau of Standards, 1981, vol. 162.
- [132] D. Inserra, W. Hu, and G. Wen, “Antenna array synthesis for rfid-based electronic toll collection,” *IEEE Transactions on Antennas and Propagation*, vol. 66, no. 9, pp. 4596–4605, 2018.



- [133] T. Varum, J. N. Matos, P. Pinho, and R. Abreu, “Nonuniform broadband circularly polarized antenna array for vehicular communications,” *IEEE Transactions on Vehicular Technology*, vol. 65, no. 9, pp. 7219–7227, 2016.
- [134] L. Huang and Y. Lu, “A switchable or mimo antenna for v2x communication,” in *2019 IEEE International Conference on Computational Electromagnetics (ICCEM)*, 2019, pp. 1–2.
- [135] A. Chachich, V. Fessmann, J. Arnold, D. Thompson, W. Fehr, and S. Stasko, “Dsrc-unlicensed device test plan: To characterize the existing radio frequency signal environment and identify the impacts to dsrc operations of unlicensed devices operating in the 5850-5925 mhz band and adjacent bands,” *The National Academies of Sciences, Engineering, and Medicine: Transportation Research Board*, 2015.
- [136] L. Josefsson and P. Persson, *Conformal array antenna theory and design*. John wiley & sons, 2006, vol. 29.
- [137] Y. Rahmat-Samii, “Useful coordinate transformations for antenna applications,” *IEEE Transactions on Antennas and Propagation*, vol. 27, no. 4, pp. 571–574, 1979.
- [138] J. B. Kenney, “Dedicated short-range communications (dsrc) standards in the united states,” *Proceedings of the IEEE*, vol. 99, no. 7, pp. 1162–1182, 2011.
- [139] J. Verspecht, A. Stav, T. Nielsen, and S. Kusano, “The vector component analyzer: A new way to characterize distortions of modulated signals in high-frequency active devices,” *IEEE Microwave Magazine*, vol. 23, no. 12, pp. 86–96, 2022.
- [140] “Ieee recommended practice for estimating the uncertainty in error vector magnitude of measured digitally modulated signals for wireless communications,” *IEEE Std 1765-2022*, pp. 1–105, 2022.
- [141] S. F. Razavi and Y. Rahmat-Samii, “Resilience to probe-positioning errors in planar phaseless near-field measurements,” *IEEE Transactions on Antennas and Propagation*, vol. 58, no. 8, pp. 2632–2640, 2010.
- [142] V. Manohar and Y. Rahmat-Samii, “An in-depth understanding of salient features of antenna near-field measurements through full wave simulations : (invited paper),” in *2020 14th European Conference on Antennas and Propagation (EuCAP)*, 2020, pp. 1–4.
- [143] T. Hansen and A. Yaghjian, “Planar near-field scanning in the time domain .1. formulation,” *IEEE Transactions on Antennas and Propagation*, vol. 42, no. 9, pp. 1280–1291, 1994.
- [144] —, “Planar near-field scanning in the time domain .2. sampling theorems and computation schemes,” *IEEE Transactions on Antennas and Propagation*, vol. 42, no. 9, pp. 1292–1300, 1994.